

DISS. ETH NO. 29104

# **Understanding the Mechanism of Preferential Carbon Monoxide Oxidation over Pt-Fe Catalysts: an Operando Spectroscopy Approach**

A thesis submitted to attain the degree of

DOCTOR OF SCIENCES of ETH ZURICH

(Dr. sc. ETH Zurich)

presented by

**ILIA SADYKOV**

MSc in Chemistry, Lomonosov Moscow State University, Russian Federation

born on 07.01.1994.

citizen of Russian Federation

accepted on the recommendation of

Prof. Dr. J. A. van Bokhoven, examiner

Prof. Dr. J. Pérez-Ramírez, co-examiner

Dr. O. Safonova, co-examiner

2023



*“I would rather have questions that can't be answered  
than answers that can't be questioned.”*

*Richard P. Feynman*





# TABLE OF CONTENTS

1 Introduction .....	11
1.1 Industrial Production and Purification of Hydrogen .....	11
1.2 Preferential Carbon Monoxide Oxidation .....	13
1.3 Preferential Carbon Monoxide Oxidation over Pt-Fe catalysts .....	18
1.4 References.....	22
2 Motivation and Strategy .....	27
2.1 Time-Resolved XAS Study of Carbon Monoxide Oxidation over a Bimetallic $\gamma$ -Al <sub>2</sub> O <sub>3</sub> -Supported Platinum-Iron Catalyst.....	27
2.2 An Operando XAS Study of Preferential Carbon Monoxide Oxidation over $\gamma$ -Al <sub>2</sub> O <sub>3</sub> and SiO <sub>2</sub> -Supported Platinum-Iron Catalysts Active at Ambient Temperature .....	27
3 Time-Resolved XAS Study of Carbon Monoxide Oxidation over a Bimetallic $\gamma$ -Al <sub>2</sub> O <sub>3</sub> -Supported Pt-Fe Catalyst.....	28
3.1 Abstract.....	29
3.2 Introduction.....	30
3.3 Results and Discussion.....	32
3.3.1 Structure of the Catalysts .....	32
3.3.2 Carbon Monoxide Oxidation Activity and Kinetics.....	33
3.3.3. Platinum and Iron States During the Pretreatment in Hydrogen .....	34
3.3.4 Platinum State under Reaction Conditions.....	38
3.3.5 Iron State under Reaction Conditions .....	38
3.3.6 Mechanism of Carbon Monoxide Oxidation over Pt <sub>2.1</sub> Fe <sub>0.7</sub> -Al <sub>2</sub> O <sub>3</sub> -673-5.....	39
3.4 Conclusions.....	43
3.5 Methodology of XAS.....	44
3.5.1 In situ/operando XAS Experiments .....	44
3.5.2 XANES Analysis.....	45
3.5.3 Pt L <sub>3</sub> -edge EXAFS Analysis.....	45
3.5.4 Fe K-edge EXAFS Analysis .....	46
3.6 References.....	47

4 An Operando XAS Study of Preferential Carbon Monoxide Oxidation over $\gamma$ -Al <sub>2</sub> O <sub>3</sub> and SiO <sub>2</sub> -Supported Pt-Fe Catalysts Active at Ambient Temperature .....	51
4.1 Abstract .....	52
4.2 Introduction .....	53
4.3 Results and Discussion .....	55
4.3.1 Pretreatment Strategies .....	55
4.3.2 In situ FTIR .....	58
4.3.3 In situ XAS after Reduction .....	60
4.3.4 Operando XAS under Preferential Carbon Monoxide Oxidation Conditions .....	62
4.3.5 Mechanism of Preferential Carbon Monoxide Oxidation .....	65
4.4 Conclusions .....	67
4.5 References .....	68
5 Role of Water in the Promotion of Preferential Carbon Monoxide Oxidation over $\gamma$ -Al <sub>2</sub> O <sub>3</sub> - and SiO <sub>2</sub> -Supported Platinum-Iron Catalysts .....	71
5.1 Abstract .....	72
5.2 Introduction .....	73
5.3 Results and Discussion .....	75
5.3.1 Water Pretreatment Strategies .....	75
5.3.2 Water Influence on Reaction Kinetics .....	78
5.3.3 <sup>18</sup> O-labeling Experiments .....	79
5.3.4 Operando Fe K-edge XAS Experiments .....	81
5.3.5 Operando DRIFTS Experiments .....	84
5.3.6 Water Influence on Reaction Mechanism .....	86
5.4 Conclusions .....	89
5.5 References .....	90
6 Conclusions and Outlook .....	93
7 Materials and methods .....	97
7.1 Gases .....	97
7.2 Catalysts Supports .....	97
7.3 Main Characterization Methods .....	97
7.3.1 Elemental Analysis .....	97

7.3.2 Carbon Monoxide Chemisorption .....	97
7.3.3 Electron Microscopy .....	98
7.3.4 X-ray Absorption Spectroscopy .....	98
7.3.5 In situ Fourier Transform Infrared Spectroscopy .....	99
7.3.6 Conversion and Selectivity Estimation .....	99
7.4 References.....	100
Supporting Information .....	101
S1. Time-Resolved XAS Study of Carbon Monoxide Oxidation over a Bimetallic $\gamma$ -Al <sub>2</sub> O <sub>3</sub> - Supported Pt-Fe Catalyst (Chapter 3) .....	102
S2. An Operando XAS Study of Preferential Carbon Monoxide Oxidation over $\gamma$ -Al <sub>2</sub> O <sub>3</sub> and SiO <sub>2</sub> - Supported Pt-Fe Catalysts Active at Ambient Temperature (Chapter 4) .....	131
S3. Role of Water in the Promotion of Preferential Carbon Monoxide Oxidation over $\gamma$ -Al <sub>2</sub> O <sub>3</sub> - and SiO <sub>2</sub> -Supported Platinum-Iron Catalysts (Chapter 5) .....	168
CURRICULUM VITAE .....	195

# ABSTRACT

Hydrogen production and purification is a cornerstone of the modern chemical industry and a future renewable hydrogen-based economy. Widely spread hydrogen purification from catalyst-poisoning carbon monoxide impurities by means of methanation and pressure swing adsorption is inextricably tied to the industrial synthesis of ammonia and fertilizers. Despite being highly efficient, these purification processes can only recover 70-90% of initially supplied hydrogen, and an alternative hydrogen purification method has become a necessity. This alternative method is preferential carbon monoxide oxidation. It avoids hydrogen losses by selectively oxidizing carbon monoxide impurities in the hydrogen stream. Successful implementation of this hydrogen purification process primarily depends on a heterogeneous catalyst having enough activity and selectivity toward carbon monoxide oxidation. Currently used platinum-based catalysts suffer from carbon monoxide poisoning and deactivation, and their activities can be significantly improved through promotion with iron or combination with other catalysts. At the same time, the lack of knowledge on how iron influences activity and selectivity deprives us of the ability to fully realize the potential of Pt-Fe catalysts and allow their widespread use.

A review of the preferential carbon monoxide oxidation and the current status of the research on the role of iron as a platinum promoter is presented in Chapter 1. Chapter 2 sets the scene by defining the research goals and the research strategy.

Chapter 3 is dedicated to uncovering the role of iron and platinum in the catalytic carbon monoxide oxidation in the absence of hydrogen by means of operando / in situ X-ray absorption and infrared spectroscopies aiming at understanding the mechanism of oxygen activation on iron sites and the state of these sites under reaction conditions. A combination of X-ray absorption spectroscopy with mass spectrometry (operando XAS) performed in real time allowed a quantitative correlation of the reaction kinetics and the catalytic structure. The chemometric data analysis methods were employed to extract information about the active species responsible for carbon monoxide and oxygen activation. These methods showed that  $\text{Fe}^{2+}/\text{Fe}^{3+}\text{O}_x$  surface oligomers in close proximity to metallic platinum nanoparticles could enable to circumvent oxygen activation on the platinum surface, which is difficult due to a complete saturation with carbon monoxide under reaction conditions. Electrophilic oxygen species on these oxidic iron sites were found to be the key intermediates in the oxidation of carbon monoxide.

Chapter 4 reports a study of preferential carbon monoxide oxidation over supported Pt-Fe catalysts, in the presence of hydrogen, using operando / in situ X-ray absorption and infrared spectroscopies. Compared to Chapter 3, iron concentration was increased, catalysts activities towards carbon monoxide oxidation were optimized, and the significant role of reduction pretreatment was revealed. The formation of a platinum-iron alloy or atomically-dispersed platinum was shown to have no significant influence on catalytic activity. Instead, enhanced catalytic activity close to ambient temperature was found to be directly proportional to the number of  $\text{Fe}^{+2}\text{O}$  sites located at the interface with the metallic platinum nanoparticles. Their irreversible oxidation and aggregation were shown to be the leading

cause of catalyst deactivation. Hydrogen pressure during pretreatment determined the concentration of active  $\text{Fe}^{+2}\text{O}$  sites and, thus, the catalytic activity.

Chapter 5 demonstrates how water, which is always present in the commercial preferential carbon monoxide oxidation process, can affect active  $\text{Fe}^{+2}\text{O}$  sites and create even more active  $\text{FeO}_x(\text{OH})_y$  species at the interface with the metallic platinum nanoparticles. Reduction of supported Pt-Fe catalysts under pure hydrogen in the presence of steam yielded a  $\text{FeO}_x(\text{OH})_y/\text{Pt}$  catalyst with one of the highest reported activities to date. Following the kinetics of PROX in  $^{18}\text{O}$ -labeled water experiments, mass-spectrometry showed that adsorbed water and iron-associated hydroxyl groups are directly involved in the catalytic cycle of carbon monoxide oxidation. Operando X-ray absorption and infrared spectroscopies uncovered that steam hydroxylates existing active interfacial  $\text{Fe}^{+2}\text{O}$  sites and creates active iron-associated hydroxyl groups. Real-time correlations between the catalytic activity and the iron structure derived from X-ray absorption spectroscopy showed that hydroxylated  $\text{FeO}_x(\text{OH})_y/\text{Pt}$  increase the catalytic turnover frequency of individual iron  $\text{Fe}^{2+}$  sites.

Finally, Chapter 6 summarizes the main findings and provides an understanding of the structure-performance relationships for Pt-Fe preferential carbon monoxide oxidation catalysts obtained in this study. We further discuss different hypotheses on how to improve the existing Pt-Fe catalysts and come one step closer to a more efficient practical realization of the preferential carbon monoxide oxidation process in the chemical industry. Chapter 7, as well as Supporting information S1, S2, and S3 provide technical details.

# ZUSAMMENFASSUNG

Die Herstellung und Reinigung von Wasserstoff ist ein Eckpfeiler der modernen chemischen Industrie und einer wasserstoffbasierten Erneuerbare Wirtschaft der Zukunft. Die weit verbreitete Wasserstoffreinigung von katalysatorvergiftenden Kohlenmonoxidverunreinigungen mittels Methanisierungsreaktion und Druckwechsel-Adsorption ist untrennbar mit der industriellen Synthese von Ammoniak und Düngemitteln verbunden. Obwohl die Methanisierung hocheffizient ist, diese Reinigungsverfahren können nur 70-90 % des ursprünglich gelieferten Wasserstoff zurückgewinnen, so dass eine alternative Methode zur Wasserstoffreinigung erforderlich geworden ist. Diese alternative Wasserstoffreinigungsmethode ist die bevorzugte Oxidation von Kohlenmonoxid. Es vermeidet Wasserstoffverluste durch selektives Oxidieren von Kohlenmonoxidverunreinigungen im Wasserstoffstrom. Die erfolgreiche Umsetzung dieses Wasserstoffreinigungsverfahrens hängt in erster Linie von heterogenen Katalysatoren ab, die über eine ausreichende Aktivität und Selektivität für die Oxidation von Kohlenmonoxid verfügen. Die derzeit verwendeten Katalysatoren auf Platinbasis leiden an einer Kohlenmonoxidvergiftung und Deaktivierung, und ihre Aktivität kann durch die Promotion mit Eisen oder durch Kombination mit anderen Katalysatoren deutlich gesteigert werden. Gleichzeitig hindert uns das mangelnde Wissen über den Einfluss von Eisen auf Aktivität und Selektivität, das Potenzial von Pt-Fe-Katalysatoren voll auszuschöpfen und ihre großflächige Nutzung zu ermöglichen.

In Kapitel 1 finden Sie einen Überblick über die bevorzugte Kohlenmonoxid-Oxidation und den aktuellen Stand der Forschung zur Rolle von Eisen als Platinpromotor. Kapitel 2 legt die Ziele und die Forschungsstrategie fest.

Kapitel 3 beschäftigt sich mit der Rolle von Eisen und Platin bei der katalytischen Oxidation von Kohlenmonoxid ohne die Anwesenheit von Wasserstoff mit Hilfe von operando / in situ Röntgenabsorptions- und Infrarotspektroskopie. Diese zielt darauf ab, Mechanismus der Sauerstoffaktivierung an Eisenzentren und Zustand dieser Seiten unter Reaktionsbedingungen zu verfolgen. Eine Kombination von operando-Röntgenabsorptionsspektroskopie mit Massenspektrometrie in Echtzeit ermöglichte eine quantitative Korrelation der Reaktionskinetik und der katalytischen Struktur. Die chemometrischen Methoden machten es möglich, die Informationen über die aktiven Spezies zu extrahieren, die für die Aktivierung von Kohlenmonoxid und Sauerstoff verantwortlich sind. Die Ergebnisse zeigen, dass  $\text{Fe}^{2+}/\text{Fe}^{3+}\text{O}_x$ -Oberflächenoligomere in unmittelbarer Nähe zu metallischen Platin-Nanopartikeln die Sauerstoffaktivierung auf der Platinoberfläche, die unter den Reaktionsbedingungen vollständig mit Kohlenmonoxid gesättigt ist, umgehen können. Es hat sich gezeigt, dass electrophile Sauerstoffspezies auf diesen oxidischen Eisenstellen die wichtigsten Zwischenstufen bei der Oxidation von Kohlenmonoxid sind.

In Kapitel 4 wird die bevorzugte Oxidation von Kohlenmonoxid an Pt-Fe-Trägerkatalysatoren, in Gegenwart von Wasserstoff, mit Hilfe von operando / in situ Röntgenabsorption und Infrarotspektroskopie untersucht. Im Vergleich zu Kapitel 3 wurden die Aktivitäten der Katalysatoren optimiert, Eisenkonzentration erhöht, und die bedeutende Rolle der Reduktionsvorbehandlung kam zum Vorschein. Es zeigte sich, dass die Bildung einer Platin-Eisen-Legierung bzw. von atomar

dispergiertem Platin keinen signifikanten Einfluss auf die katalytische Aktivität hat. Stattdessen wurde festgestellt, dass die verbesserte katalytische Aktivität nahe Umgebungstemperatur direkt proportional zur Anzahl der  $\text{Fe}^{+2}\text{O}$ -Stellen ist, die sich an der Grenzfläche der metallischen Platin-Nanopartikel befinden. Deren irreversible Oxidation und Aggregation wurde als Hauptursache für die Deaktivierung des Katalysators nachgewiesen. Der Wasserstoffdruck während der Vorbehandlung bestimmt die Konzentration der aktiven  $\text{Fe}^{+2}\text{O}$ -Stellen und somit, die katalytische Aktivität.

Das Kapitel 5 demonstriert, wie Wasser, das im kommerziellen, bevorzugten Kohlenmonoxid-Oxidationsprozess immer vorhanden ist, die  $\text{Fe}^{+2}\text{O}$ -Stellen beeinflussen und noch aktivere  $\text{FeO}_x(\text{OH})_y$ -Spezies an der Grenzfläche von metallischen Platin-Nanopartikeln erzeugen kann. Die Reduktion von geträgerten Pt-Fe-Katalysatoren unter reinem Wasserstoff in Gegenwart von Wasserdampf ergab den  $\text{FeO}_x(\text{OH})_y/\text{Pt}$ -Katalysator mit einer der höchsten gemeldeten Aktivitäten. Im Anschluss an die Kinetik der PROX unter Verwendung von  $^{18}\text{O}$ -markiertem Wasser ergab die Massenspektrometrie, dass adsorbiertes Wasser und eisenassoziierte Hydroxylgruppen direkt in den katalytischen Zyklus der Kohlenmonoxidoxidation eingebunden sind. Operando-Röntgenabsorptions- und Infrarotspektroskopien deckten auf, dass Wasserdampf bestehende aktive  $\text{Fe}^{+2}\text{O}$ -Grenzflächen hydroxyliert und aktive eisenassoziierte Hydroxylgruppen erzeugt. Echtzeit-Korrelationen zwischen der katalytischen Aktivität und der Eisenstruktur, die aus der Röntgenabsorptionsspektroskopie abgeleitet wurden, zeigten, dass hydroxyliertes  $\text{FeO}_x(\text{OH})_y/\text{Pt}$  die katalytische Umsatzfrequenz einzelner  $\text{Fe}^{2+}$ -Eisenstellen erhöht.

In Kapitel 6 schließlich werden die Ergebnisse dieser Studie zusammengefasst und unser Verständnis der Struktur-Leistungs-Beziehungen für Pt-Fe-Katalysatoren dargelegt. Wir erörtern, wie wir die bestehenden Pt-Fe-Katalysatoren optimieren und der effizienten, praktischen Anwendung des bevorzugten Kohlenmonoxid-Oxidationsprozesses in der chemischen Industrie einen Schritt näher kommen können. Kapitel 7 sowie die unterstützenden Informationen S1, S2 und S3 enthalten technische Details.

## ACKNOWLEDGEMENTS

The research presented in this thesis would not have been possible without the support, guidance, dedication, belief, and contribution of many colleagues, friends, and family. I am grateful to everyone who supported this work in any way, even if not specifically mentioned here.

Olga, Jeroen, and Maarten, you are the best supervisors I have ever had. Your constant support and passion for our research gave me the confidence to continue through all the struggles that we had in recent years. You are excellent scientists and deserve the utmost respect.

Olga, I wish that every student had such a supervisor and mentor as you. I can truly say that you take your responsibilities as a supervisor very seriously. Not only are you a great colleague, but you are also able to train a scholar and a scientist as a good teacher. Scientific progress is based on the people like you, and I sincerely thank you for all your work and support. So many people depend on you, and yet, you always find time for me, and I really appreciate that. If your family reads this, I would like them to know how good a scientist and person you are.

Jeroen, superbedankt! Without your support, ideas, and propositions, I would not be able to perform this research. Every time I spoke to you, I felt so much more optimistic and well-determined. I see in you the ideal of a scientist able to solve even the most complicated puzzles that nature gives us. Whenever I hit a dead end, you helped me find a way out. You created your own scientific school and organized a cooperative team of experts as an experienced leader. Thanks to you, I made many new friends and colleagues who supported me during my PhD.

Professor Pérez-Ramírez, thank you for co-refereeing my dissertation. I greatly admire your work and cutting-edge research. It is a great pleasure to have you on the examination committee.

Maarten, dankuwel! I can be proud of a boss like you, thanks to your support I was always confident in the success of our experiments. You are a very kind person, a great scientist, and organizer. I think this is the reason why you were able to create absolutely the best beamline, no competition.

Adam, you are the best colleague I could wish for. You are a great sympathetic person and always care for the people around you. Your software is as fast as your bike, I hope it will be installed at all the beamlines all over the globe.

Maxim and Anna, I could not thank you more for your help. Wish a successful, victorious year and the fulfilment of all desires for you and your family.

Frank, Hannes, and Arik, you are great scientists and supporters of this work. Before meeting you, I could have never imagined that people could do such precise imaging. Besten Dank!

Vitaly, Davide, and Rob, I sincerely thank you for your help with the infrared spectroscopy experiments. You have a really broad spectrum of expertise, and I sincerely enjoyed our time together.



Dennis, thank you for your help and great ideas, we really miss you here. You mastered not only energy slopes but the mountain slopes as well.

Stephan and Stephan, Seline, Urs, Anna, and Dominik, thank you for your help at the beamline and your inspiration!

Sergei Kuzin and Prof. Dr. Gunnar Jeschke, thank you! I hope one day we could catch those elusive radicals. I would like to include your EPR results in our new manuscript.

Dr. Luca Artiglia and Xiansheng Li, you are great scientists who volunteered to help me even after work, for which I will always be grateful. Hope we can publish our results soon.

The people who made operando experiments possible are Dr. Miren Agote Arán, Dr. Anna Zabilska, Mikalai Artsiusheuski, Dr. Rob Jeremiah Nuguid, Luca Maggiulli, Dr. Maneka Claire Roger, Filippo Buttignol, Jan Alfke, Jingfeng Chen, Dr. Igor Plokhikh, Patrick Gäumann, Sumant Phadke and Lunhan Chen. I will never forget that you agreed to help me day and night and fully supported me.

I am grateful to Dr. Alexey Fedorov and Dr. Sung Min Kim for their help with chemisorption measurements.

I am deeply grateful to my family for their unconditional support in all my endeavours. Many thanks to my parents, Olga Sadykova and Igor Sadykov, who raised me, taught me mathematical thinking, and invested so much in me. My sister Anastasia, you are the best psychologist, high five!

To all my colleagues and friends at Paul Scherrer Institute and ETH Zurich, thank you all for your support, your help, and a lot of fun we had together! PS!comiao!

I want to extend my gratitude to the Swiss National Science Foundation for funding my research. The allocation of beamtime at the SuperXAS beamline at the Swiss Light Source is appreciatively acknowledged (Proposals 20191322, 20210434, 20212208). The help of the Scientific Center for Optical and Electron Microscopy at ETH Zürich is gratefully acknowledged. The authors acknowledge the use of computational resources of DelftBlue supercomputer, provided by Delft High Performance Computing Centre.

# LIST OF ABBREVIATIONS

PROX	Preferential carbon monoxide oxidation
XAS	X-ray absorption spectroscopy
BET	Brunauer–Emmett–Teller (theory)
PIPS	passivated implanted planar silicon detector
MS	mass spectrometer
TPR	temperature-programmed reduction
MCR-ALS	multivariate curve resolution-alternating least squares
SVD	singular value decomposition
EXAFS	extended X-ray absorption fine structure
FT	Fourier transform
HAADF-STEM	high-angle annular dark-field scanning transmission electron microscopy
STEM	scanning transmission electron microscopy
TEM	transmission electron microscopy
XRD	X-ray diffraction
FTIR	Fourier transform infrared spectroscopy
DTGS	deuterated triglycine sulfate
ALD	atomic layer deposition
XANES	X-ray absorption near-edge structure
LCF	linear combination fitting
DRIFTS	diffuse reflectance infrared Fourier transform spectroscopy
vol. %	volumetric percentage
mol. %	molar percentage
TPD	temperature-programmed desorption

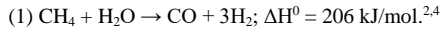
# 1 Introduction

## 1.1 Industrial Production and Purification of Hydrogen

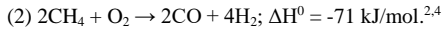
Hydrogen is an essential part of the modern industrialized world, and its influence is only expected to grow. The overall pure hydrogen market is estimated to be about 75 million tons per year as of 2022.<sup>1</sup> An overview of hydrogen production released in 2014 showed that approximately half of the obtained hydrogen was utilized to produce ammonia and methanol, and about 30% was used directly at refineries for hydrocracking and hydrotreating.<sup>2</sup> Production of metal, polymers, oxo-alcohols, fatty acids, and synthetic natural gas accounted for another 10%.<sup>2</sup> Some processing industries required about 6% of produced hydrogen for the direct reduction of iron ore and glass production.<sup>2</sup> On top of that, hydrogen could be used as an energy carrier for fuel cells and energy storage systems that emerged in the last decade.<sup>3</sup>

Hydrogen production is dominated by the steam reforming of methane and other hydrocarbons, responsible for approximately 48% of the overall production of molecular hydrogen in the world.<sup>1,2</sup> The partial catalytic oxidation of methane and methane pyrolysis are alternative pathways for the production of hydrogen.<sup>2,4</sup> These processes are attractive and can be a cheaper option for hydrogen production because they minimize the amount of expensive superheated steam.<sup>2,4</sup> When partial oxidation and steam reforming are combined in the same reactor, a new route for hydrogen production appears, known as autothermal reforming.<sup>2,4</sup> Hydrogen produced by these approaches is generally designated as “grey hydrogen” or “blue hydrogen”; the latter corresponds to processes when the released carbon dioxide is captured.<sup>5</sup> While natural gas is the most common feedstock for steam reforming, this process can also be applied to the refinery of bio-derived fuels, off-gases, and liquefied petroleum gas as feedstocks.<sup>2,4,6</sup> For instance, supercritical water gasification of biomass involves similar production steps and allows achieving low environmental costs by taking advantage of natural renewable feedstock.<sup>6</sup> Another modern way to minimize the environmental impact of hydrogen production is water electrolysis powered by renewable energy sources (“green hydrogen”), which constituted about 4% of the global production in 2022.<sup>1</sup> The same water electrolysis yields “purple hydrogen” when energy for electrolysis comes from a nuclear power plant. Around 1% of hydrogen originates from chlorine production plants as a by-product.<sup>2,4</sup>

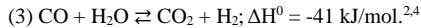
Despite a large variety of hydrogen production methods, the method of choice is typically dictated by the final application of hydrogen due to the high transportation hazards.<sup>2,4</sup> These risks dictate the on-site production of hydrogen for both ammonia and methanol production plants. In particular, on-site steam reforming of natural gas for further ammonia synthesis is one of the largest hydrogen production processes.<sup>2,4</sup> The generalized scheme of hydrogen production via steam reforming is presented in **Figure 1-1**.<sup>2</sup> As the reforming reaction is endothermic (equation 1), it requires significant heat supply via the high-temperature steam as well as via external burning of off-gases and natural gas:



Generally, this reaction is performed over a nickel-based catalyst at the temperature from 1023 K to 1173 K, while pressure varies from 3 to 25 bar, depending on the process design.<sup>2</sup> Steam reforming can also include an additional catalytic partial oxidation process:



To further increase the concentration of hydrogen, the resulting synthesis gas after the reforming step is then subjected to a set of shift-conversion reactions (water-gas shift) with added steam to increase the H<sub>2</sub>:CO ratio:



High (673 K) and low-temperature (573 K) water-gas shift reactors enable plants to reduce carbon monoxide content to about 0.5-1% CO.<sup>2,4</sup> The residual carbon dioxide can be removed from the process gas in an absorber (acid gas removal, **Figure 1-1**) using a solvent. After the absorber, the gas stream contains mainly hydrogen, nitrogen, as well as traces of carbon monoxide. Further purification of hydrogen from traces of carbon monoxide is necessary whenever a high standard of hydrogen purity is required, primarily for the production of ammonia but also for hydrogen fuel applications, namely proton-exchange membrane fuel cells.<sup>2,4,7</sup> Even traces of carbon monoxide (>300 ppm) present in hydrogen before purification can poison catalysts for these processes and disrupt their regular operation.

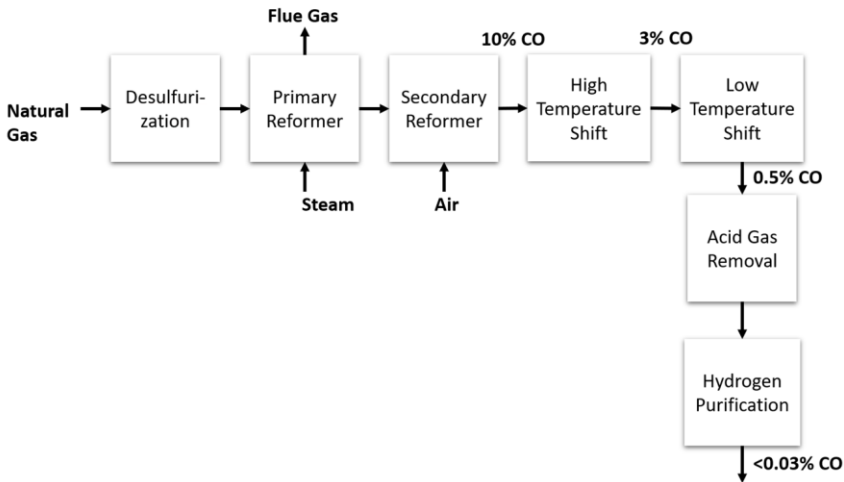
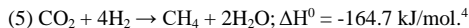
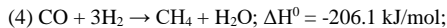


Figure 1-1. Generalized scheme of hydrogen production via steam reforming.  
Adapted from Refs. 2 and 4.

The most mature technologies for carbon monoxide traces removal are methanation and absorption.<sup>2,4</sup> Both processes require significant energy inputs as they operate at elevated temperatures and pressures.<sup>2,4</sup> Moreover, methanation consumes ca. 5% of hydrogen (equation 4), but actual losses can reach 15% due to the unselective methanation of carbon dioxide (equation 5):

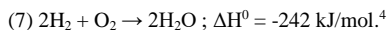
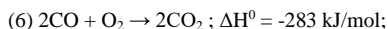


Pressure swing adsorption requires large low flow rates, which reduces throughput and limits hydrogen recovery to 70-90%.<sup>4</sup> Commonly used pressure swing adsorption systems require hot valves able to divert the reformat flow from one bed to another. These valves add a problem for component failure. On the other hand, a scrubber installed after the water-gas shift unit can solve the problem. However, it needs a regular replacement of an adsorbent, which does not allow continuous operation. Even membranes cannot be used on a large-scale plant due to low processing speeds.

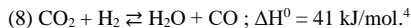
Preferential carbon monoxide oxidation (PROX) is an alternative technology that enables to selectively remove traces of carbon monoxide from reformat using a dedicated catalyst. This method is based on the catalytic oxidation of carbon monoxide to carbon dioxide and thus can be operated on a truly continuous basis. The amount of oxygen needed for carbon monoxide oxidation is fed to the PROX reactor via an air blower consuming only a small amount of energy. Another potential for energy savings is the absence of heating and pressurization, as PROX catalysts, ideally, should be able to operate close to ambient temperature and pressure.<sup>4</sup>

## 1.2 Preferential Carbon Monoxide Oxidation

The shifted reformat gas after the low-temperature shift reactor (**Figure 1-1**) at the inlet of the preferential carbon monoxide oxidation reactor typically contains ~0-31 mol.% H<sub>2</sub>O, ~0.5 mol.% CO, 0-3 mol.% CH<sub>4</sub>, and the balance hydrogen: additional ~0.6-2 mol.% O<sub>2</sub>, N<sub>2</sub> are obtained by blowing air into the stream, additional 0-14 mol.% CO<sub>2</sub> is present or not depending on the acid gas unit.<sup>4,7</sup> The gas feed is usually supplied at ambient conditions but can have elevated pressure or temperature as well. Concentrations of these gases depend on many parameters, and a simulated reformat mixture (0.5-2 % CO, 0.5-5 % O<sub>2</sub>, 0-4 % H<sub>2</sub>O, H<sub>2</sub>, and N<sub>2</sub>) is often used to represent the reactor feed when testing PROX catalysts. According to equilibrium calculations for 52.6 mol.% H<sub>2</sub>, 0.5 mol.% CO, 13 mol.% CO<sub>2</sub>, 2.4 mol.% CH<sub>4</sub>, 0.8 mol.% N<sub>2</sub>, 30.2 mol.% H<sub>2</sub>O, and 0.6% O<sub>2</sub>, such a mixture is thermodynamically unstable.<sup>4</sup> Thermodynamics predict that most of the oxygen should be consumed by both hydrogen and carbon monoxide already at 298 K according to the following reactions (**Figure 1-2a**):



Predicted hydrogen losses gradually increase from 0.7% at 298 K to 2% at 523 K (**Figure 1-2a**) with the concurrent decrease in carbon monoxide conversion (**Figure 1-2b**). Hydrogenation of carbon dioxide (reverse water-gas shift reaction) works against the reactor designer to reach 100% conversion of carbon monoxide:



The contribution of the reverse water-gas shift reaction is so substantial at high temperatures that the system can start to produce carbon monoxide above 483 K instead of consuming it. The methanation reaction (equation 4) additionally complicates this set of reactions.

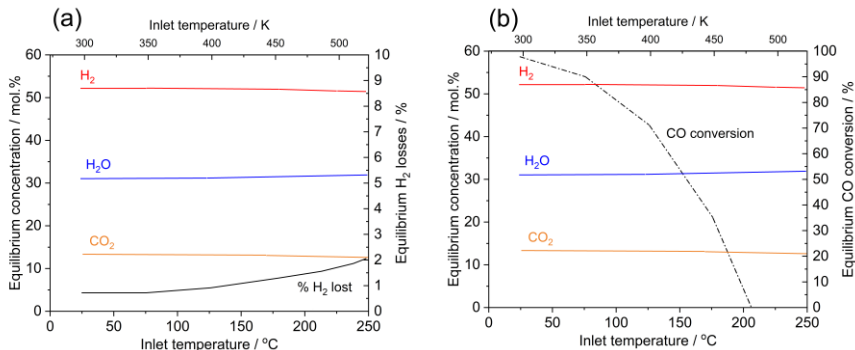


Figure 1-2. Calculated equilibrium molar concentrations of hydrogen, water, and carbon dioxide (left axis) compared to hydrogen losses (right axis, a) and carbon monoxide conversion (right axis, b). The initial mixture contains 52.6 mol.% H<sub>2</sub>, 0.5 mol.% CO, 13 mol.% CO<sub>2</sub>, 2.4 mol.% CH<sub>4</sub>, 0.8 mol.% N<sub>2</sub>, 30.2 mol.% H<sub>2</sub>O, and 0.6 mol.% O<sub>2</sub>. Reproduced from Ref. 4.

Clearly, a heterogeneous catalyst capable of deviating chemistry away from equilibrium is essential for the successful implementation of preferential carbon monoxide oxidation reaction. PROX selectivity to carbon monoxide oxidation (carbon monoxide selectivity) can be defined from equations 6 and 7 as:

$$(9) \text{CO selectivity (\%)} = \frac{[\text{CO}_2]_{\text{out}}}{2 \cdot [\text{O}_2]_{\text{in}}} \cdot 100\%,$$

where [CO<sub>2</sub>]<sub>out</sub> and [O<sub>2</sub>]<sub>in</sub> are the concentrations of carbon dioxide and oxygen at the outlet and the inlet of the PROX reactor, respectively.

The main criterion for selecting a catalyst for PROX is the rate of carbon monoxide oxidation. The carbon monoxide oxidation rate is affected by the nature of carbon monoxide and oxygen adsorption on the catalyst surface. Noble 4d- and 5d-metals in the form of supported nanoparticles are the first candidates for PROX catalysts as they can selectively chemisorb carbon monoxide in the presence of oxygen. Energies of carbon monoxide adsorption (kJ mol<sup>-1</sup>) on (211) noble metal surfaces representing nanoparticles or clusters edges are subject to the following relation: Ir (189) > Pt (182) > Rh (173) > Ru (171) > Pd (168) >> Au (34) as calculated by density functional theory.<sup>8</sup> Experimental carbon monoxide adsorption heat follows the same trend.<sup>9</sup> The calculated energy of dissociative oxygen adsorption (kJ mol<sup>-1</sup>) on (211) surfaces shows a different trend: Ir (449) ≈ Ru (446) > Rh (389) > Pt (209) > Pd (116) > Ag (63) >> Au (-52) and also agrees with the chemisorption heat of oxygen measured experimentally for metal foils, except for Pd.<sup>8</sup> Clearly, iridium strongly adsorbs both carbon monoxide

and oxygen; on the other hand, adsorption of carbon monoxide on gold is weak, and dissociative adsorption of oxygen on gold close to ambient temperature is thermodynamically unlikely. These low adsorption energies can increase for small clusters or nanoparticles of gold, even though platinum and palladium nanoparticles still show significantly higher oxygen and carbon monoxide adsorption energies.<sup>10</sup> Carbon monoxide oxidation rate calculated for optimal coverage of both oxygen and carbon monoxide follows a particular trend for atomic clusters at 273 K: Au > Pd > Ag > Pt > Cu and another trend at 600 K: Pd > Au > Ag > Pt > Cu.<sup>10</sup> An almost irreversible chemisorption of carbon monoxide and oxygen on platinum, iridium, and ruthenium hinders rapid reaction. At the same time, gold is able to keep the gas phase in equilibrium with weakly chemisorbed surface species.<sup>10</sup>

The observed properties of gold nanoparticles containing coordinatively unsaturated gold sites explain why catalysts based on gold nanoparticles and clusters were also extensively investigated from the perspective of PROX applications.<sup>11</sup> At the same time, the dissociative chemisorption of hydrogen occurs for all mentioned metals as hydrogen chemisorption energy changes according to the following trend: Ru > Ir  $\approx$  Pd  $\approx$  Rh > Pt > Au.<sup>12</sup> The possibility of hydrogen activation complicates the catalyst selection, as hydrogen oxidation reaction over supported gold, platinum, and palladium is known to occur already at room temperature.<sup>13</sup>

The catalytic oxidation of hydrogen can adversely affect PROX selectivity towards carbon monoxide oxidation and lead to significant hydrogen losses, even higher than those predicted by thermodynamic equilibrium. As the possibility of side reactions, such as the reverse water-gas shift and methanation, only increases with temperature, it is beneficial to operate PROX at the temperatures below 373 K. At the same time, not many catalysts are able to show both high carbon monoxide conversion and selectivity below 423 K. Most of the noble metals are only active in carbon monoxide oxidation above 373 K, including the most widely studied platinum on inert oxides (SiO<sub>2</sub>, Al<sub>2</sub>O<sub>3</sub>).<sup>14,15</sup> The reactivity of supported platinum and iridium nanoparticles is limited by high carbon monoxide adsorption energies that result in a complete blockage and poisoning of the surface with carbon monoxide.<sup>16,17</sup> Ruthenium possesses intermediate carbon monoxide adsorption energy and, thus, can be more active in PROX than platinum.<sup>17</sup> Nonetheless, ruthenium still requires elevated temperatures above  $\sim$ 423 K, at which it is also active in the unwanted methanation reaction.<sup>17</sup> The ability of palladium to form  $\beta$ -hydrides, which can be further oxidized by stable PdO<sub>2</sub> species, makes it impossible to use palladium for selective oxidation of carbon monoxide.<sup>17</sup> Since PROX catalyst is required to reduce carbon monoxide slip under 300 ppm, hydrogen concentration under the maximum conversion can be at least three orders of magnitude higher than carbon monoxide concentration.<sup>4,17</sup> This inevitably leads to hydrogen chemisorption and its subsequent catalytic oxidation by the aforementioned noble metals. Only gold is capable of low-temperature PROX operation, while other noble metals require additional promoters to shift reaction to lower temperatures where hydrogen oxidation can be mitigated at the full carbon monoxide conversion.<sup>11,17</sup> Gold nanoparticles supported on Fe<sub>2</sub>O<sub>3</sub>, CeO<sub>2</sub>, CeO<sub>2</sub>-Al<sub>2</sub>O<sub>3</sub>, and Zn-doped CeO<sub>2</sub> were able to achieve carbon monoxide conversion >98% with the corresponding CO slip under 300 ppm.<sup>18-20</sup> The most active state-of-the-art catalysts presented so far are water-treated Au/Al<sub>2</sub>O<sub>3</sub>, Au/CeO<sub>2</sub>-Al<sub>2</sub>O<sub>3</sub>, Pt-Fe/ $\gamma$ -Al<sub>2</sub>O<sub>3</sub>, and Pt-Fe-Ni/TiO<sub>2</sub> capable of achieving highest activities even at ambient temperature.<sup>11,21</sup> All state-of-the-art catalysts that were shown to reduce carbon monoxide content below 200 ppm in the presence of hydrogen at low temperatures are presented in **Table 1-1**.

Table 1-1. Maximum reported oxygen activity and selectivity towards carbon monoxide oxidation for catalysts previously investigated under PROX tested at the minimum temperature required to reduce the carbon monoxide content below 200 ppm. The estimated reaction rate corresponds to the highest reported conversion at a indicated temperature weighted by the noble metal amount or mass and the carbon monoxide flow rate ("NM": Au, Pt, Ru, Ir, and Cu). Carbon dioxide and methane were not present in reaction feed.

\*Pt-Ru reaction rate is weighted by a sum of Pt and Ru masses.

Catalyst	T / °C	T / K	CO feed / mol. %	O <sub>2</sub> feed / mol. %	CO conversion / %	O <sub>2</sub> selectivity to CO / %	Estimated rate / mol <sub>CO</sub> g <sub>NM</sub> <sup>-1</sup> h <sup>-1</sup>	Estimated rate / mol <sub>CO</sub> mol <sub>NM</sub> <sup>-1</sup> min <sup>-1</sup>	Ref.
<b>Au/Al<sub>2</sub>O<sub>3</sub></b>	<b>40</b>	<b>313</b>	<b>1</b>	<b>1.4</b>	<b>~99.7</b>	<b>~50</b>	<b>5.6</b>	<b>18.3</b>	<b>11</b>
Au/Fe <sub>2</sub> O <sub>3</sub>	80	353	0.9	0.9	~99.8	~40	0.1	0.3	18
Au/Fe <sub>2</sub> O <sub>3</sub>	100	373	1	1.25	~99.5	~45	1.7	5.5	19
Au/ ZnO-CeO <sub>2</sub>	67	340	1	1.25	~98	~63	1.6	5.2	20
<b>Au/ CeO<sub>2</sub>-Al<sub>2</sub>O<sub>3</sub></b>	<b>50</b>	<b>323</b>	<b>2</b>	<b>2</b>	<b>~99</b>	<b>~55</b>	<b>6.4</b>	<b>20.9</b>	<b>22</b>
Au/ CeO <sub>2</sub> -Fe <sub>2</sub> O <sub>3</sub>	30	303	1	2	~100	~25	0.5	1.6	23
Au/TiO <sub>2</sub>	60	333	1	2	~98.5	~85	0.8	2.6	24
<b>Pt-Fe-Ni/ TiO<sub>2</sub></b>	<b>25</b>	<b>298</b>	<b>1</b>	<b>1</b>	<b>~100</b>	<b>~50</b>	<b>50.9</b>	<b>165.4</b>	<b>21</b>
<b>Pt-Fe/ γ-Al<sub>2</sub>O<sub>3</sub></b>	<b>30</b>	<b>303</b>	<b>1</b>	<b>1</b>	<b>~100</b>	<b>~50</b>	<b>12.4</b>	<b>40.3</b>	<b>25</b>
<b>Pt-Fe(OH)<sub>3</sub>/ SiO<sub>2</sub></b>	<b>27</b>	<b>300</b>	<b>1</b>	<b>0.5</b>	<b>~100</b>	<b>~100</b>	<b>5.6</b>	<b>18.2</b>	<b>26</b>
Pt-Fe/SiO <sub>2</sub>	27	300	1	0.5	~100	~100	0.4	1.2	27
Pt-Fe/ γ-Al <sub>2</sub> O <sub>3</sub>	25	298	1	1	~100	~55	1.1	3.7	28
Pt-Fe/ mordenite	80	353	1	0.5	~100	~100	1.2	3.9	29
Pt-Fe/ mordenite	100	373	1	1	~100	~50	1.0	3.1	30
Pt-Fe/ Carbon black	30	303	1	0.5	~100	~100	0.3	1.0	31
Cu@Pt-Fe/ Carbon black	30	303	1	0.5	~100	~100	1.3	4.4	32
Pt-Co/YSZ	57	330	1	1	~100	~50	4.8	15.8	33
Pt-Co/CNT	40	313	1	1	~100	~55	0.3	1.0	34
Pt-Co/APO-5	65	338	1	1	~100	~50	1.0	3.2	35
Pt-Co/ γ-Al <sub>2</sub> O <sub>3</sub>	117	390	1	1	~100	~50	2.4	7.9	36
<b>Pt-Ru/SiO<sub>2</sub>*</b>	<b>110</b>	<b>383</b>	<b>0.5</b>	<b>0.5</b>	<b>~100</b>	<b>~50</b>	<b>-</b>	<b>2.7*</b>	<b>37</b>
Ir/Fe(OH) <sub>x</sub>	27	300	1	1	~100	~50	0.5	1.6	38
CuO-CeO <sub>2</sub>	104	377	1	1	~100	~95	0.2	0.2	39
CuO-CeO <sub>2</sub>	140	413	0.5	0.5	~100	~75	1.0	1.0	40
CuO/CeO <sub>2</sub> / γ-Al <sub>2</sub> O <sub>3</sub>	200	473	0.6	0.6	~99	~80	0.1	0.1	41



At high conversion, the concentration of carbon monoxide approaches zero and even more surface sites on the noble metal surface become available for hydrogen activation, causing a decrease in selectivity. This is incredibly profound for some Au-based and Pt-Co catalysts, whose selectivity towards carbon monoxide oxidation can fall below 50% and even down to 25%. The observed difference in selectivity can be, in part, explained by the different oxygen-carbon monoxide ratios. The parameter  $\lambda = 2[\text{O}_2]_{\text{in}}/[\text{CO}]_{\text{in}}$  describes oxygen excess in the inlet PROX feed and sets the lower boundary for selectivity at 100% carbon monoxide conversion as derived from equations 6, 7, and 9:

$$(10) \text{ CO selectivity } (\%) = \frac{[\text{CO}_2]_{\text{out}}}{2 \cdot [\text{O}_2]_{\text{in}}} \cdot 100\% = \frac{1}{\lambda} \cdot 100\%.$$

As shown in **Figure 1-3**, for many catalysts, selectivity to carbon monoxide at ~100% conversion is close to its smallest possible value determined by  $1/\lambda$ . This implies that for those materials (mainly platinum-based PROX catalysts), the fraction of the catalyst not involved in carbon monoxide oxidation will inevitably react almost all available oxygen with hydrogen, leading to significant hydrogen losses. However, some catalysts, such as Au/CeO<sub>2</sub>-Fe<sub>2</sub>O<sub>3</sub>, Au/Al<sub>2</sub>O<sub>3</sub>, and CuO/CeO<sub>2</sub>, are able to preserve hydrogen from reacting with residual oxygen.<sup>11,23,39-41</sup> This is related to the intrinsically higher activity of these catalysts for carbon monoxide oxidation in comparison to hydrogen oxidation.

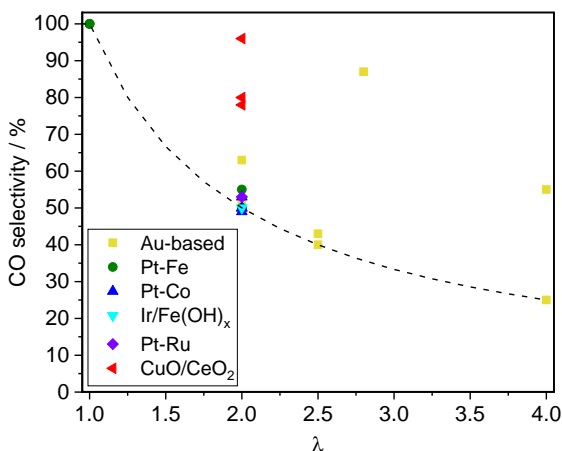


Figure 1-3. Correlation between the selectivity to carbon monoxide oxidation and the oxygen excess ( $\lambda = 2\text{O}_2/\text{CO}$ ) for catalysts from Table 1 operating at ~100% carbon monoxide conversion. Dashed line sets the lower boundary for selectivity defined by  $\lambda = 2[\text{O}_2]_{\text{in}}/[\text{CO}]_{\text{in}}$ .

Preferential carbon monoxide oxidation over these highly selective gold- and copper-based catalysts was extensively investigated, leading to a deep understanding of underlying catalytic mechanisms. Highly selective Au/CeO<sub>2</sub>-Fe<sub>2</sub>O<sub>3</sub> catalysts consist of gold nanoparticles supported on the CeO<sub>2</sub>-Fe<sub>2</sub>O<sub>3</sub> solid solution. Simple water vapor treatment of Au/Al<sub>2</sub>O<sub>3</sub> also yields a highly selective and active

catalyst.<sup>11,23</sup> It was suggested that gold nanoparticles in the presence of water facilitate the formation of -OOH hydroperoxide species able to rapidly react with adsorbed carbon monoxide to form -COOH carboxyl intermediates that can further decompose with the release of carbon dioxide.<sup>11,42</sup> Oxidation of hydrogen by Au-OOH has higher activation energy than the oxidation of carbon monoxide, which is the main reason for high selectivity.<sup>11</sup> As far as active supports are concerned, FeO<sub>x</sub> and CeO<sub>2</sub> are able to undergo reversible redox changes under carbon monoxide oxidation conditions providing active peroxidic O<sub>2</sub><sup>2-</sup> species at the interface with gold.<sup>43</sup> These properties of CeO<sub>2</sub> make direct oxygen supply to the CuO interface possible for highly selective CuO/CeO<sub>2</sub> catalysts, which allows active Cu<sup>2+</sup> species to reversibly access oxygen from the CeO<sub>2</sub> lattice.<sup>39</sup> The complete oxidation of metallic Cu<sup>0</sup> under PROX limits hydrogen and carbon monoxide activation, which is why copper-based catalysts demonstrate high selectivity (**Table 1-1**). At the same time, Pt-Fe-based compositions can achieve much higher activities and possess reasonable selectivity at intermediate conversion levels.

As evident from **Table 1-1**, Pt-Fe-Ni/TiO<sub>2</sub> (PROX rate 165.4 mol<sub>CO</sub> mol<sub>Pt</sub><sup>-1</sup> min<sup>-1</sup> at 298 K) catalysts prepared by depositing Pt-Fe-Ni nanoparticles onto TiO<sub>2</sub>, as well as Pt-Fe/ $\gamma$ -Al<sub>2</sub>O<sub>3</sub> (40.3 mol<sub>CO</sub> mol<sub>Pt</sub><sup>-1</sup> min<sup>-1</sup> at 303 K) prepared by precipitation from aqueous solution, demonstrate the highest reported carbon monoxide oxidation rate among other studied PROX catalysts, which is much higher than for pure Pt/SiO<sub>2</sub> (0.2 mol<sub>CO</sub> mol<sub>Pt</sub><sup>-1</sup> min<sup>-1</sup> at 300 K).<sup>21,25,26</sup> On the other hand, other reported Pt, Pt-Fe, and Pt-Co catalysts have vastly different activities. It is unclear why promotion with iron can yield different catalytic activities, changing by three orders of magnitude. To unlock the great potential of Pt-Fe catalysts and to understand the observed conversion-selectivity relationships, we decided to dive deeper into the hidden nature of Pt-Fe catalysts.

### 1.3 Preferential Carbon Monoxide Oxidation over Pt-Fe catalysts

Historically, Korotkikh and Farrauto were the first to report the promotional effect of iron for carbon monoxide oxidation over Pt/ $\gamma$ -Al<sub>2</sub>O<sub>3</sub>.<sup>44</sup> PROX catalyst in the form of platinum nanoparticles supported on  $\gamma$ -Al<sub>2</sub>O<sub>3</sub> and promoted with a 3d-metal oxide is commercially available under the Selectoxo name.<sup>44</sup> In the light of commercial applications, many studies were performed on iron-doped platinum nanoparticles supported on  $\gamma$ -Al<sub>2</sub>O<sub>3</sub> prepared by various synthetic methods, including wet impregnation, wet precipitation, and sol-gel methods. However, no information on the structure of active iron species and their role in catalysis was provided. It also remained unclear why simple wet precipitation of Pt-Fe on  $\gamma$ -Al<sub>2</sub>O<sub>3</sub> allows achieving much higher activities than other methods.<sup>25,44,45</sup>

Several groups developed new mordenite-supported Pt-Fe catalysts with platinum nanoparticles of about 1 nm in size, having activities far superior to the conventional Pt/Al<sub>2</sub>O<sub>3</sub> and Pt/mordenite (**Table 1-1**).<sup>29,30</sup> Platinum and iron salt precursors were also successfully deposited onto silica particles functionalized with (3-aminopropyl)triethoxysilane, creating iron-promoted platinum nanoparticles.<sup>27</sup> However, these catalysts were less active than the state-of-the-art Pt-Fe/ $\gamma$ -Al<sub>2</sub>O<sub>3</sub>.<sup>21,25,27</sup>

Several groups proposed using iron oxide itself as a support for platinum. For instance, FeO<sub>x</sub> species were able to form an interface with platinum nanoparticles in Pt/Fe<sub>2</sub>O<sub>3</sub> and further encapsulate them during reduction above 573 K.<sup>46</sup> PROX catalytic tests showed that observed strong metal-support interaction influenced catalytic activity and the reduction at 373 K under hydrogen was optimal to stabilize several monolayers of FeO on top of ~2-3 nm platinum nanoparticles. The reduction at higher temperatures led to encapsulation with multiple iron oxide layers and a significant activity loss.<sup>46</sup> Due to the larger size of platinum nanoparticles of about 2 nm, Pt/Fe<sub>2</sub>O<sub>3</sub> also possessed relatively low carbon monoxide oxidation activity of approximately 0.6 mol<sub>CO</sub> mol<sub>Pt</sub><sup>-1</sup> min<sup>-1</sup> at 300 K.<sup>46</sup> Co-precipitation of Fe<sub>2</sub>O<sub>3</sub> and atomically-dispersed platinum (0.17 wt.% Pt) enabled to achieve higher activities of about

2.2 mol<sub>CO</sub> mol<sub>Pt</sub><sup>-1</sup> min<sup>-1</sup> at 300 K.<sup>47</sup> Selective atomic layer deposition of iron oxide on top of platinum boosted reaction rate to 1.3 mol<sub>CO</sub> mol<sub>Pt</sub><sup>-1</sup> min<sup>-1</sup> at 300 K, which still pales before the activity of Pt-Fe/γ-Al<sub>2</sub>O<sub>3</sub> prepared by wet precipitation (40.3 mol<sub>CO</sub> mol<sub>Pt</sub><sup>-1</sup> min<sup>-1</sup> at 303 K).<sup>25,26</sup>

The formation of Pt-Fe alloy is often considered to be crucial to reach the high carbon monoxide oxidation activity, as was shown in several publications.<sup>14,48</sup> The structure of Pt-Fe alloy can change upon further oxidative treatment and lead to the formation of Pt(core)@Fe<sub>3</sub>O<sub>4</sub>(shell) structures, as was shown by Silva et al.<sup>49</sup> Reduction treatment can rearrange Pt-Fe@FeO<sub>x</sub> and collapse iron oxide shell with the formation of voids inside, thereby freeing alloy surface and increasing the catalytic activity. Various Pt-Fe alloys deposited on amorphous carbon indeed demonstrated high activities (**Table 1-1**), but no precise mechanism explaining the role of iron was proposed.<sup>31,32</sup> Acid leaching of these alloys demonstrated that iron was present both on the surface and inside platinum nanoparticles.<sup>31</sup> Nonetheless, only the surface iron sites were shown to be active in PROX.<sup>31</sup>

The question of whether alloy or core-shell structures are responsible for high PROX activity is still not answered. In fact, the Pt-Fe/γ-Al<sub>2</sub>O<sub>3</sub> catalyst mentioned previously can have much higher activities than any reported Pt-Fe alloy, atomically dispersed platinum on Fe<sub>2</sub>O<sub>3</sub> or core-shell structures.<sup>25</sup> Whether these structures can exist in commercial Pt/γ-Al<sub>2</sub>O<sub>3</sub> doped with iron and whether these structures are necessary for high PROX activities and selectivities is yet to be answered. Highly active Pt-Fe catalysts tend to contain small platinum nanoparticles of <3 nm, which makes their investigation by electron microscopy or X-ray diffraction very challenging, as iron phases and platinum-iron interface are barely visible.<sup>25</sup> This is the reason why no previous work demonstrated clear evidence of the structure of active sites, and discussions on the role of iron remain hypothetical. At the same time, the lack of deep understanding of Pt-Fe catalyst structure influenced by synthetic and pretreatment procedures significantly hinders commercial development of PROX.

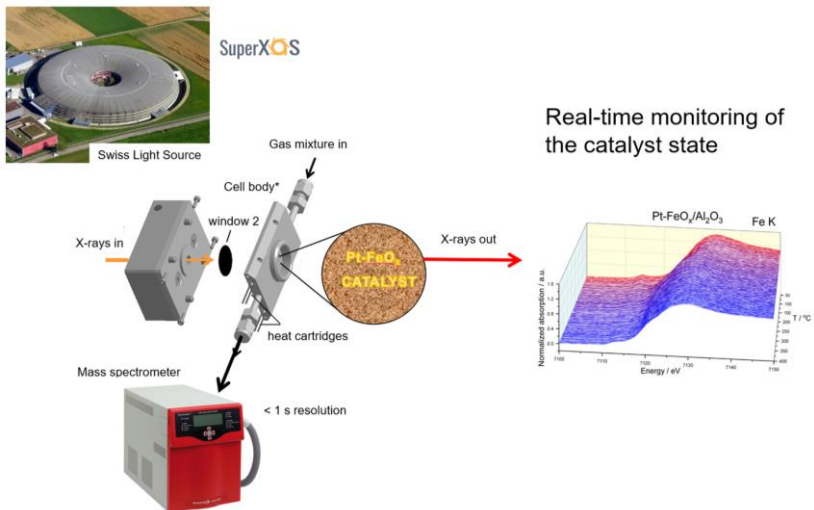
Density functional theory calculations, together with model experiments using scanning tunneling microscopy, scrutinized model FeO islands on Pt(111) surface.<sup>27,50,51</sup> Iron atoms located at the interface with platinum were shown to be redox-active and sensitive to the concentration of gas phase oxygen. Their oxygen coordination environment was sensitive to the presence of carbon monoxide, oxygen, or hydrogen in the 10<sup>-6</sup>-10<sup>-8</sup> mbar pressure range.<sup>51</sup> Added water could dissociate on the surface of these islands, supposedly forming iron-bound hydroxyl groups, which resulted in a higher amount of reacted carbon monoxide.<sup>52-54</sup> These modeling studies suggest that the structure of iron under reaction conditions is dynamic and depends on many parameters. That is why methods capable of following the structural changes of iron and platinum active sites are necessary to understand the role of iron in the promotion of platinum.

The only methods capable of following the structure of platinum and iron species in the state-of-the-art Pt-Fe PROX catalysts under real catalytic conditions are in situ X-ray absorption spectroscopy (XAS) and infrared spectroscopy. Element-specific XAS methods are sensitive to the average local structure of materials (e.g., oxidation state of elements, nature of the neighbors in the first and second coordination shells), even for amorphous materials, therefore, they are suitable for structural analysis of small nanoparticles, clusters, and highly dispersed surface species. Furthermore, the application of this technique, as well as in situ infrared spectroscopy, is possible at high temperatures and pressures. Both XAS and infrared spectroscopy methods do not require a vacuum environment, and, thus, XAS studies can be performed in dedicated in situ reactors in the flow of relevant gas atmospheres, mimicking the conditions applied in laboratory and industrial reactors. These advantages make X-ray absorption and infrared spectroscopies ideal tools for mechanistic research in catalysis. At the same time, XAS also has certain limitations. As shown before, in situ XAS can only detect the average state of iron and platinum in Pt-Fe catalysts but cannot distinguish per se, which iron species are directly involved in the catalytic cycle and which of them (typically the majority) are inactive spectators.<sup>27,55</sup>

Similarly, infrared spectra are generally dominated by the signal of the support and provide infrared absorption peaks associated mainly with adsorbed water and carbon monoxide adsorbed on spectator sites.<sup>14,56,57</sup>

The so-called operando approach makes it possible to follow both the structure and catalytic activity using XAS or infrared spectroscopy, in combination with other methods able to follow catalytic conversion and selectivity in real-time, such as mass spectrometry.<sup>58</sup> Quick XAS measurements on a time scale of seconds available at modern synchrotron facilities are particularly useful for such studies. By directly correlating the activity and the structural evolution trends monitored by XAS, one can distinguish the active metal species from spectators. We decided to employ these powerful tools to understand the mechanism of carbon monoxide oxidation over Pt-Fe catalysts, investigate how the structure of Pt-Fe catalysts changes under PROX conditions, and, most importantly, which species and intermediates are responsible for such high activities of the state-of-the-art Pt-Fe catalysts. Monitoring key intermediates was vital for proposing realistic carbon monoxide oxidation mechanisms. Operando diffuse reflectance infrared Fourier transform spectroscopy (DRIFTS) was able to correlate real-time production of carbon dioxide and concentrations of active intermediates.

**Scheme 1-1** demonstrates the operando approach used in this thesis. We constructed the operando reactor cell with graphite windows enabling multimodal operando experiments where XAS and catalytic activity were measured simultaneously with satisfactory time resolution (on the scale of seconds). The qualification of the catalytic activity is possible via a mass spectrometer. Synchrotron-generated X-rays pass through the cell containing a catalyst, and the corresponding Fe K-edge and Pt L<sub>3</sub>-edge absorption spectra can be acquired. These XAS data contain both X-ray absorption near-edge structure (XANES) and extended X-ray absorption fine structure (EXAFS), which carry information about both the local structure and the chemical state of iron and platinum. A similar approach was used for operando and in situ infrared experiments. These techniques helped us understand the role of iron in preferential carbon monoxide oxidation and reveal its influence on the reaction mechanism.



Scheme 1-1. Scheme of the experimental operando XAS setup and operando approach.<sup>59</sup> Image of the Swiss Light Source is a courtesy of Paul Scherrer Institute, Villigen PSI, Switzerland.

## 1.4 References

1. International Renewable Energy Agency. Hydrogen overview. <https://www.irena.org/Energy-Transition/Technology/Hydrogen> (accessed January 2023).
2. (a) Speight, J. G. Hydrogen in refineries. In *Hydrogen science and engineering: materials, processes, systems and technology*, First Edition. Stolten, D. and Emonts, B., Ed.; Wiley, 2016; pp. 3-18. (b) Ausfelder, F. and Bazzanella, A. Hydrogen in the chemical industry. In *Hydrogen science and engineering: materials, processes, systems and technology*, First Edition. Stolten, D. and Emonts, B., Ed.; John Wiley & Sons, Inc., 2016; pp. 19-39.
3. Pei, P.; Wang, M.; Chen, D.; Ren, P. and Zhang, L. Key technologies for polymer electrolyte membrane fuel cell systems fueled impure hydrogen. *Prog. Nat. Sci.* 2020, 30, 751-76.
4. Liu, K.; Song, C. and Subramani, V., Ed. Hydrogen and syngas production and purification technologies.; John Wiley & Sons, Inc., 2010; pp. 127-155. (b)
5. (a) Newborough, M. and Cooley, G. Developments in the global hydrogen market: the spectrum of hydrogen colours. *Fuel Cells Bul.* 2020, 11, 16-22. (b) Germscheidt, R.L.; Moreira, D.E.; Yoshimura, R.G.; Gasbarro, N.P.; Datti, E.; dos Santos, P.L. and Bonacin, J.A. Hydrogen environmental benefits depend on the way of production: an overview of the main processes production and challenges by 2050. *Adv. Energy Sustainability Res.* 2021, 2, 2100093.
6. Fang, Z.; Smith, R. L. and Qi, X. Ed. Production of hydrogen from renewable resources. *Biofuels and biorefineries series*, Volume 5. Springer, 2015.
7. EG&G Services Parsons, Inc. Science Applications International Corporation. Fuel cell handbook. Fifth Edition, 2000.
8. Royer, S. and Duprez, D. Catalytic oxidation of carbon monoxide over transition metal oxides. *ChemCatChem* 2011, 3, 24-65.
9. Campbell, C. T. and Lytken, O. Experimental measurements of the energetics of surface reactions. *Surf. Sci.* 2009, 603, 1365-1372.
10. Falsig, H.; Hvolbæk, B.; Kristensen, I. S.; Jiang, T.; Bligaard, T.; Christensen, C. H. and Nørskov, J. K. Trends in the catalytic CO oxidation activity of nanoparticles. *Angew. Chem. Int. Ed.* 2008, 120, 4913-4917.
11. Saavedra, J.; Whittaker, T.; Chen, Z.; Pursell, C.J.; Rioux, R.M. and Chandler, B.D. Controlling activity and selectivity using water in the Au-catalysed preferential oxidation of CO in H<sub>2</sub>. *Nature Chem.* 2016, 8, 584-589.
12. Nordlander, P.; Holloway, S. and Nørskov, J. K. Hydrogen adsorption on metal surfaces. *Surf. Sci.* 1984, 136, 59-81.
13. (a) Haruta, M.; Yamada N.; Kobayashi T. and Iijima S. Gold catalysts prepared by coprecipitation for low-temperature oxidation of hydrogen and of carbon monoxide. *J. Catal.* 1989, 115, 301-309. (b) Hanson, F. V. and Boudart, M. The Reaction between H<sub>2</sub> and O<sub>2</sub> over supported platinum catalysts. *J. Catal.* 1978, 53, 56-67. (c) Radkevich, V. Z.; Senko T. L.; Wilson K.; Grishenko L. M.; Zaderko A. N. and Diyuk V. Y. The influence of surface functionalization of activated carbon on palladium dispersion and catalytic activity in hydrogen oxidation. *Applied Catalysis A: General.* 2008, 8, 241-251.

14. Siani, A.; Captain, B.; Alexeev, O. S.; Stafyla, E.; Hungria, A. B.; Midgley, P. A.; Thomas, J. M.; Adams, R.D. and Amiridis, M. D. Improved CO oxidation activity in the presence and absence of hydrogen over cluster-derived PtFe/SiO<sub>2</sub> catalysts. *Langmuir* **2006**, *22*, 5160-5167.
15. Kahlich, M. J.; Gasteiger, H. A. and Behm R. J. Kinetics of the selective CO oxidation in H<sub>2</sub>-rich gas on Pt/Al<sub>2</sub>O<sub>3</sub>. *J. Catal.* **1997**, *171*, 93-105.
16. Berlowitz, P.J.; Peden, C.H. and Goodman, D.W. Kinetics of carbon monoxide oxidation on single-crystal palladium, platinum, and iridium. *J. Phys. Chem.* **1988**, *92*, 5213-5221.
17. Liu, K.; Wang, A. and Zhang, T. Recent advances in preferential oxidation of CO reaction over platinum group metal catalysts. *ACS Catal.* **2012**, *2*, 1165-78.
18. Landon, P.; Ferguson, J.; Solsona, B.E.; Garcia, T.; Al-Sayari, S.; Carley, A.F.; Herzing, A.A.; Kiely, C.J.; Makkee, M.; Moulijn, J.A. and Overweg, A. Selective oxidation of CO in the presence of H<sub>2</sub>, H<sub>2</sub>O and CO<sub>2</sub> utilising Au/ $\alpha$ -Fe<sub>2</sub>O<sub>3</sub> catalysts for use in fuel cells. *J. Materials Chem.* **2006**, *16*, 199-208.
19. Avgouropoulos, G.; Ioannides, T.; Papadopoulou, C.; Batista, J.; Hocevar, S. and Matralis, H.K. A comparative study of Pt/ $\gamma$ -Al<sub>2</sub>O<sub>3</sub>, Au/ $\alpha$ -Fe<sub>2</sub>O<sub>3</sub> and CuO-CeO<sub>2</sub> catalysts for the selective oxidation of carbon monoxide in excess hydrogen. *Catal. Today* **2002**, *75*, 157-167.
20. Avgouropoulos, G.; Manzoli, M.; Boccuzzi, F.; Tabakova, T.; Papavasiliou, J.; Ioannides, T. and Idakiev, V. Catalytic performance and characterization of Au/doped-ceria catalysts for the preferential CO oxidation reaction. *J. Catal.* **2008**, *256*, 237-247.
21. Chen, G.; Zhao, Y.; Fu, G.; Duchesne, P.N.; Gu, L.; Zheng, Y.; Weng, X.; Chen, M.; Zhang, P.; Pao, C.W. and Lee, J.F. Interfacial effects in iron-nickel hydroxide-platinum nanoparticles enhance catalytic oxidation. *Science* **2014**, *344*, 495-499.
22. Fonseca, J.D.S.L.; Ferreira, H.S.; Bion, N.; Pirault-Roy, L.; do Carmo Rangel, M.; Duprez, D. and Epron, F. Cooperative effect between copper and gold on ceria for CO-PROX reaction. *Catal. Today* **2012**, *180*, 34-41.
23. Liao, X.; Chu, W.; Dai, X. and Pitchon, V. Promoting effect of Fe in preferential oxidation of carbon monoxide reaction (PROX) on Au/CeO<sub>2</sub>. *Appl. Catal. A: General* **2012**, *449*, 131-138.
24. Galletti, C.; Fiorot, S.; Specchia, S.; Saracco, G. and Specchia, V., Catalytic performance of Au-TiO<sub>2</sub> catalysts prepared by deposition-precipitation for CO preferential oxidation in H<sub>2</sub>-rich gases. *Chem. Eng. J.* **2007**, *134*, 45-50.
25. Lou, Y. and Liu, J. A highly active Pt-Fe/ $\gamma$ -Al<sub>2</sub>O<sub>3</sub> catalyst for preferential oxidation of CO in excess of H<sub>2</sub> with a wide operation temperature window. *Chem. Comm.* **2017**, *53*, 9020-9023.
26. Cao, L.; Liu, W.; Luo, Q.; Yin, R.; Wang, B.; Weissenrieder, J.; Soldemo, M.; Yan, H.; Lin, Y.; Sun, Z. and Ma, C. Atomically dispersed iron hydroxide anchored on Pt for preferential oxidation of CO in H<sub>2</sub>. *Nature* **2019**, *565*, 631-635.
27. Fu, Q.; Li, W.X.; Yao, Y.; Liu, H.; Su, H.Y.; Ma, D.; Gu, X.K.; Chen, L.; Wang, Z.; Zhang, H. and Wang, B., Interface-confined ferrous centers for catalytic oxidation. *Science* **2010**, *328*, 1141-1144.

28. Zhang, H.; Liu, X.; Zhang, N.; Zheng, J.; Zheng, Y.; Li, Y.; Zhong, C.J. and Chen, B.H. Construction of ultrafine and stable PtFe nano-alloy with ultra-low Pt loading for complete removal of CO in PROX at room temperature. *Appl. Catal. B: Environ.* **2016**, *180*, 237-245.
29. Watanabe, M.; Uchida, H.; Ohkubo, K. and Igarashi, H. Hydrogen purification for fuel cells: selective oxidation of carbon monoxide on Pt-Fe/zeolite catalysts. *Appl. Catal. B: Environ.* **2003**, *46*, 595-600.
30. Maeda, N.; Matsushima, T.; Uchida, H.; Yamashita, H. and Watanabe, M. Performance of Pt-Fe/mordenite monolithic catalysts for preferential oxidation of carbon monoxide in a reformat gas for PEFCS. *Appl. Catal. A: General* **2008**, *341*, 93-97.
31. Xu, H.; Fu, Q.; Yao, Y. and Bao, X. Highly active Pt-Fe bicomponent catalysts for CO oxidation in the presence and absence of H<sub>2</sub>. *Energ. & Environ. Sci.* **2012**, *5*, 6313-6320.
32. Guo, X.; Fu, Q.; Ning, Y.; Wei, M.; Li, M.; Zhang, S.; Jiang, Z. and Bao, X. Ferrous centers confined on core-shell nanostructures for low-temperature CO oxidation. *JACS* **2012**, *134*, 12350-12353.
33. Ko, E.Y.; Park, E.D.; Lee, H.C.; Lee, D. and Kim, S. Supported Pt-Co Catalysts for Selective CO Oxidation in a Hydrogen-Rich Stream. *Angew. Chem. Int. Ed.* **2007**, *46*, 734-737.
34. Wang, C.; Li, B.; Lin, H. and Yuan, Y. Carbon nanotube-supported Pt-Co bimetallic catalysts for preferential oxidation of CO in a H<sub>2</sub>-rich stream with CO<sub>2</sub> and H<sub>2</sub>O vapor. *J. Power Sources* **2012**, *202*, 200-208.
35. Wang, C.; Zhang, L. and Liu, Y. Aluminumphosphate molecular sieves supported Pt-Co catalysts for the preferential oxidation of CO in H<sub>2</sub>-rich gases. *Appl. Catal. B: Environ.* **2013**, *136*, 48-55.
36. Ko, E.Y.; Park, E.D.; Seo, K.W.; Lee, H.C.; Lee, D. and Kim, S. Nanosized Pt-Co catalysts for the preferential CO oxidation. *J. Nanosci. Nanotech.* **2006**, *6*, 3567-3571.
37. Chin, S.Y.; Alexeev, O.S. and Amiridis, M.D. Structure and reactivity of Pt-Ru/SiO<sub>2</sub> catalysts for the preferential oxidation of CO under excess H<sub>2</sub>. *J. Catal.* **2006**, *243*, 329-339.
38. Lin, J.; Qiao, B.; Liu, J.; Huang, Y.; Wang, A.; Li, L.; Zhang, W.; Allard, L.F.; Wang, X. and Zhang, T. Design of a highly active Ir/Fe(OH)<sub>x</sub> catalyst: versatile application of Pt-group metals for the preferential oxidation of carbon monoxide. *Angew. Chem.* **2012**, *124*, 2974-2978.
39. Wang, F.; Buchel, R.; Savitsky, A.; Zalibera, M.; Widmann, D.; Pratsinis, S.E.; Lubitz, W. and Schüth, F. In situ EPR study of the redox properties of CuO-CeO<sub>2</sub> catalysts for preferential CO oxidation (PROX). *ACS Catal.* **2016**, *6*, 3520-3530.
40. Caputo, T.; Lisi, L.; Pirone, R. and Russo, G. Kinetics of the preferential oxidation of CO over CuO/CeO<sub>2</sub> catalysts in H<sub>2</sub>-rich gases. *Industrial & Eng. Chem. Res.* **2007**, *46*, 6793-6800.
41. Moretti, E.; Lenarda, M.; Storaro, L.; Talon, A.; Montanari, T.; Busca, G.; Rodríguez-Castellón, E.; Jiménez-López, A.; Turco, M.; Bagnasco, G. and Frattini, R. One-step synthesis of a structurally organized mesoporous CuO-CeO<sub>2</sub>-Al<sub>2</sub>O<sub>3</sub> system for the preferential CO oxidation. *Appl. Catal. A: General* **2008**, *335*, 46-55.
42. Saavedra, J.; Pursell, C.J. and Chandler, B.D. CO oxidation kinetics over Au/TiO<sub>2</sub> and Au/Al<sub>2</sub>O<sub>3</sub> catalysts: evidence for a common water-assisted mechanism. *JACS* **2018**, *140*, 3712-3723.



43. Lohrenscheid, M. and Hess, C. Direct evidence for the participation of oxygen vacancies in the oxidation of carbon monoxide over ceria-supported gold catalysts by using operando Raman spectroscopy. *ChemCatChem* **2016**, *8*, 523-526.
44. Liu, X.; Korotkikh, O. and Farrauto, R. Selective catalytic oxidation of CO in H<sub>2</sub>: structural study of Fe oxide-promoted Pt/alumina catalyst. *Appl. Catal. A: General* **2002**, *226*, 293-303.
45. Tomita, A.; Shimizu, K.I. and Tai, Y. Effect of metal oxide promoters on low temperature CO oxidation over water-pretreated Pt/alumina catalysts. *Catal. Lett.* **2014**, *144*, 1689-1695.
46. Xu, X.; Fu, Q.; Gan, L.; Zhu, J. and Bao, X. Interface-confined FeO<sub>x</sub> adlayers induced by metal support interaction in Pt/FeO<sub>x</sub> catalysts. *J. Phys. Chem. B* **2018**, *122*, 984-990.
47. Qiao, B.; Wang, A.; Yang, X.; Allard, L.F.; Jiang, Z.; Cui, Y.; Liu, J.; Li, J. and Zhang, T. Single-atom catalysis of CO oxidation using Pt1/FeO<sub>x</sub>. *Nature Chem.* **2011**, *3*, 634-641.
48. Yin, J.; Wang, J.; Zhang, T. and Wang, X. Novel alumina-supported PtFe alloy nanoparticles for preferential oxidation of carbon monoxide in hydrogen. *Catal. Lett.* **2008**, *125*, 76-82.
49. Da Silva, T.L.; Da Silva, A.H.M. and Assaf, J.M. Preparation of core-shell Pt@Fe<sub>3</sub>O<sub>4</sub>@SiO<sub>2</sub> nanostructures by oxidation of core-shell FePt@SiO<sub>2</sub> nanoflowers and their performance in preferential CO oxidation reaction. *Materials Res. Expr.* **2018**, *6*, 015042.
50. Wang, Y.; Zhang, H.; Yao, X.; Zhao, X. J. Edges of FeO/Pt(111) interface: A first-principle theoretical study. *Phys. Chem. C* **2013**, *117*, 1672-1676.
51. Kudernatsch, W.; Peng, G.; Zeuthen, H.; Bai, Y.; Merte, L. R.; Lammich, L.; Besenbacher, F.; Mavrikakis, M. and Wendt, S. Direct visualization of catalytically active sites at the FeO-Pt (111) interface. *ACS Nano* **2015**, *9*, 7804-7814.
52. Wang, W.; Zhang, H.; Wang, W.; Zhao, A.; Wang, B. and Hou, J.G. Observation of water dissociation on nanometer-sized FeO islands grown on Pt (111). *Chem. Phys. Lett.* **2010**, *500*, 76-81.
53. Ringleb, F.; Fujimori, Y.; Wang, H.F.; Ariga, H.; Carrasco, E.; Sterrer, M.; Freund, H.J.; Giordano, L.; Pacchioni, G. and Goniakowski, J. Interaction of water with FeO (111)/Pt (111): environmental effects and influence of oxygen. *J. Phys. Chem. C* **2011**, *115*, 19328-19335.
54. Xu, L.; Wu, Z.; Zhang, W.; Jin, Y.; Yuan, Q.; Ma, Y. and Huang, W. Oxygen vacancy-induced novel low-temperature water splitting reactions on FeO (111) monolayer-thick film. *J. Phys. Chem. C* **2012**, *116*, 22921-22929.
55. Tomita, A.; Shimizu, K.I.; Kato, K.; Akita, T. and Tai, Y. Mechanism of low-temperature CO oxidation on Pt/Fe-containing alumina catalysts pretreated with water. *J. Phys. Chem. C* **2013**, *117*, 1268-1277.
56. Li, S.; Jia, M.; Gao, J.; Wu, P.; Yang, M.; Huang, S.; Dou, X.; Yang, Y. and Zhang, W. Infrared studies of the promoting role of water on the reactivity of Pt/FeO<sub>x</sub> catalyst in low-temperature oxidation of carbon monoxide. *J. Phys. Chem. C* **2015**, *119*, 2483-2490.
57. Zheng, B.; Liu, G.; Geng, L.; Cui, J.; Wu, S.; Wu, P.; Jia, M.; Yan, W. and Zhang, W. Role of the FeO<sub>x</sub> support in constructing high-performance Pt/FeO<sub>x</sub> catalysts for low-temperature CO oxidation. *Catal. Sci. & Tech.* **2016**, *6*, 1546-1554.

58. Weckhuysen, B.M. Determining the active site in a catalytic process: Operando spectroscopy is more than a buzzword. *PCCP* **2003**, *5*, 4351-4360.

59. Chiarello, G. L.; Nachtegaal, M.; Marchionni, V.; Quaroni, L. and Ferri, D. Adding diffuse reflectance infrared Fourier transform spectroscopy capability to extended x-ray-absorption fine structure in a new cell to study solid catalysts in combination with a modulation approach. *Rev. Sci. Instrum.* **2014**, *85*, 074102.

## 2 Motivation and Strategy

The aim of the present research is to understand the role of iron in the promotion of preferential carbon monoxide oxidation catalysts based on supported platinum nanoparticles. We endeavor to uncover the structure of iron species in the catalysts depending on different synthetic and pretreatment conditions to understand their interaction with platinum, and distinguish which iron and platinum species are actively involved in carbon monoxide oxidation. This is made possible through careful experimental design and the use of advanced experimental methods, including in situ/operando X-ray absorption spectroscopy, in situ/operando infrared spectroscopy, kinetic methods, scanning transmission electron microscopy, as well as other methods.

### 2.1 Time-Resolved XAS Study of Carbon Monoxide Oxidation over a Bimetallic $\gamma$ -Al<sub>2</sub>O<sub>3</sub>-Supported Platinum-Iron Catalyst

The preferential carbon monoxide oxidation process takes place in a complex gas atmosphere. To initially isolate the reactivity of oxygen and carbon monoxide, we decided to focus our first research on carbon monoxide oxidation in the absence of hydrogen and water. To be closer to the industrial (Selectoxo) catalysts, we used  $\gamma$ -Al<sub>2</sub>O<sub>3</sub> support with highly dispersed platinum and iron components and studied the carbon monoxide oxidation mechanism using time-resolved operando X-ray absorption (XAS) and infrared spectroscopies. The catalysts were promoted with a small amount of iron (corresponding to Pt:Fe molar ratio of  $\sim 1$ ) to enhance the fraction of active iron sites and minimize the fraction of spectators. This study is presented in Chapter 3.

### 2.2 An Operando XAS Study of Preferential Carbon Monoxide Oxidation over $\gamma$ -Al<sub>2</sub>O<sub>3</sub> and SiO<sub>2</sub>-Supported Platinum-Iron Catalysts Active at Ambient Temperature

The next goal was to systematically explore which parameters are responsible for the ambient temperature catalytic activity of supported platinum-iron catalysts under realistic conditions of PROX reaction. To achieve this goal, we compared  $\gamma$ -Al<sub>2</sub>O<sub>3</sub> and SiO<sub>2</sub> supports, varied concentration of iron, and, most importantly, conditions of the reduction pretreatment. Compared to Chapter 1, impregnation strategy and iron concentrations were slightly optimized to achieve higher carbon monoxide oxidation activities. The pretreatment under hydrogen stream created active sites that were not present in the catalysts described in Chapter 3 at ambient temperature. The use of operando time-resolved XAS allowed us to expose the nature of the minority of active iron species at the interface with platinum nanoparticles involved in carbon monoxide oxidation and distinguish them from inactive spectators. In addition, we uncovered the reasons behind the PROX catalysts deactivation. These results are described in detail in Chapter 4.

As water vapor is one of the main components of the reformat gas and, according to the literature, water can be involved in the PROX catalytic cycle, we completed our research focusing on the role of water and explored how water can enhance PROX activity and affect the structure of the active sites. Chapter 5 describes this research pointing out the multiple roles of water involving the modification of the structure of active iron sites and the participation of surface hydroxyl groups in the catalytic cycle.

### 3 Time-Resolved XAS Study of Carbon Monoxide Oxidation over a Bimetallic $\gamma$ -Al<sub>2</sub>O<sub>3</sub>-Supported Pt-Fe Catalyst

Chapter 3 is based on the article from Ilia I. Sadykov, Maxim Zabilskiy, Adam H. Clark, Frank Krumeich, Vitaly L. Sushkevich, Jeroen A. van Bokhoven, Maarten Nachtegaal and Olga V. Safonova, *ACS Catal.*, **2021**, *11*, *18*, 11793-11805.

#### *Author contributions:*

*Ilia I. Sadykov and Olga V. Safonova conceived this study. Ilia I. Sadykov and Maxim Zabilskiy synthesized catalysts and characterized their catalytic activity. Ilia I. Sadykov, Olga V. Safonova, and Adam H. Clark designed and performed X-ray absorption experiments. Vitaly L. Sushkevich assisted with in situ Fourier transform infrared spectroscopy experiments. Frank Krumeich performed electron microscopy characterization of the catalysts. Ilia I. Sadykov analyzed the X-ray absorption spectroscopy data. Ilia I. Sadykov, Olga V. Safonova, Jeroen A. van Bokhoven, and Maarten Nachtegaal were involved in the research design and helped to connect individual parts of the research.*

### 3.1 Abstract

Reducible oxides are effective aerobic oxidation catalysts being able to activate molecular oxygen. This ability is generally attributed to the high concentration of oxygen vacancies serving as oxygen activation sites. At the same time, the mechanism of oxygen activation remains to be determined since surface oxygen activation sites cannot be easily detected using conventional methods. In this work, we unraveled the mechanism of oxygen activation over iron sites of Pt-FeO<sub>x</sub>/Al<sub>2</sub>O<sub>3</sub> during carbon monoxide oxidation using a combination of in situ and operando methods. In situ/operando XAS at the Pt L<sub>3</sub> and Fe K-edges, in situ Fourier transform infrared (FTIR) spectroscopy, and carbon monoxide chemisorption showed that carbon monoxide activation takes place at metallic platinum sites and is not affected by the presence of cationic iron species. Operando time-resolved Fe K-edge X-ray absorption spectroscopy (XAS) demonstrated that the Fe<sup>2+</sup>/Fe<sup>3+</sup> redox pair is directly involved in the mechanism of oxygen activation over Pt-FeO<sub>x</sub>/Al<sub>2</sub>O<sub>3</sub>. The detailed analysis of oxygen cut-off experiments demonstrated that after switching off oxygen, approximately one carbon dioxide molecule was formed for each Fe<sup>3+</sup> ion reduced to produce Fe<sup>2+</sup>. At the same time, the steady-state carbon dioxide formation rate was about twice higher than the initial rate of Fe<sup>2+</sup> formation after the cut-off of oxygen from the catalytic feed. These experiments allude to a catalytic cycle involving electrophilic oxygen species adsorbed on iron centers as reaction intermediates. Similar mechanisms might be expected for other catalytic oxidation reactions over cationic iron of both chemical and biological importance.

### 3.2 Introduction

Molecular oxygen is considered an ideal oxidant, especially for green chemistry processes, owing to its natural abundance and nontoxicity.<sup>1</sup> Catalytic molecular oxygen activation can be effectively realized over reducible oxides due to their relatively low oxygen vacancy formation energy.<sup>2</sup> It is generally accepted that selective oxidation catalysis over reducible oxides proceeds via the Mars and van Krevelen-type mechanism.<sup>3</sup> During the oxidation of a reactant, lattice oxygen ( $O^{2-}$ ) is removed from the surface, resulting in the formation of an oxygen vacancy, which is then replenished via reaction with molecular oxygen filling the vacancy and completing the catalytic cycle.<sup>3</sup> Lattice oxygen is considered nucleophilic, in contrast to electrophilic peroxy ( $O_2^{2-}$ ,  $O^-$ ) and superoxy ( $O_2^-$ ) species, which may also exist on the surface of the reducible oxide.<sup>4,5</sup> The formation of such charged oxygen species is accompanied by a change in the charge state of specific metal sites of the metal oxides. The concentration and reactivity of various oxygen species on the surface determine the catalytic activity.<sup>4,6</sup>

Activation of oxygen by oxides can be affected by metal nanoparticles, which are typically added to oxidation catalysts to facilitate the activation of molecules reacting with oxygen.<sup>7,8</sup> The resulting catalysts are bifunctional due to the fact that reactants and oxygen are activated on different sites and react with each other at the nanoparticle interfaces.<sup>9</sup> The nature of the reducible oxide combined with the working conditions determines the mechanism of oxygen activation.<sup>8</sup> This is due to the different redox activity of oxides, their oxygen storage capacity, oxygen mobility, and the nature of the catalytically active sites for oxygen activation, which can be formed at the metal-oxide interfaces under specific conditions.<sup>10-12</sup> Supported platinum catalysts promoted with iron oxide present a well-known bifunctional system showing high activity for carbon monoxide oxidation at the temperatures relevant for emission control.<sup>13</sup> Their relatively high selectivity in preferential carbon monoxide oxidation makes them suitable for fuel cell and hydrogen purification applications.<sup>13,14</sup> The choice of these catalysts stems from their activity already at temperatures below the carbon monoxide oxidation light-off (typically below 423 K for metallic platinum catalysts at atmospheric pressure).<sup>15,16</sup> It is assumed that iron promotes oxygen activation, thereby circumventing competitive oxygen and carbon monoxide adsorption on the platinum surface.<sup>13,17</sup>

The performance of Pt-Fe catalysts is intensively studied, and their activity can differ by orders of magnitude depending on the structure of the catalyst, activation procedure, and working conditions.<sup>13,16-22</sup> While the majority of studies agree that iron species have to be in close contact with platinum nanoparticles to aid the activation of oxygen, microscopy could rarely visualize it due to the low iron content in the most active catalysts.<sup>13</sup> Interestingly, platinum nanoparticles directly deposited on iron oxides<sup>19</sup> typically show lower activity than platinum nanoparticles on inert supports promoted by low concentrations of iron species (ca. 0.1-1 wt %).<sup>18,22</sup> Some studies proposed that the formation of a Pt-Fe alloy during the pretreatment of the catalyst in hydrogen is a prerequisite for the formation of active sites.<sup>23-25</sup> Reduction of silica-supported platinum together with the reduction of a minor amount of iron resulted in an increased number of Pt-Fe contacts enhancing catalytic activity.<sup>18,25</sup> In other works, however, only cationic iron and metallic platinum were observed for alumina-supported Pt-FeO<sub>x</sub> catalysts during pretreatment in hydrogen and under operating conditions.<sup>17</sup> Tomita et al. showed that iron in a Pt-FeO<sub>x</sub>/Al<sub>2</sub>O<sub>3</sub> catalyst could exist as both Fe<sup>2+</sup> and Fe<sup>3+</sup> depending on working conditions, suggesting that the Fe<sup>2+</sup>/Fe<sup>3+</sup> redox couple might be involved in the activation of oxygen.<sup>17</sup> Iron hydroxide species were also proposed as active sites for oxygen activation during carbon monoxide oxidation, especially at ambient temperature, in the presence of water and hydrogen in the reacting feed.<sup>26-28</sup>

Various studies have reported different reaction kinetics for carbon monoxide oxidation over Pt-FeO<sub>x</sub> catalysts. While most of these studies agree that the reaction order in carbon monoxide is close to zero,

the reported reaction order in oxygen varies between 0.6 and 1, and the activation energy differs from 10 to 30 kJ·mol<sup>-1</sup> at temperatures below 393 K.<sup>19,22,29</sup> This suggests that carbon monoxide activation takes place on the platinum surface. In contrast, the mechanism of oxygen activation may significantly vary depending on the catalyst structure and working conditions.

To uncover the mechanism of oxygen activation over supported platinum catalysts promoted with iron oxide, we used oxygen cut-off experiments in combination with time-resolved X-ray absorption spectroscopy (XAS) that can quantitatively probe the redox activity of iron and platinum under in situ and operando conditions. A similar approach was successfully applied in the past to clarify the involvement of Ce<sup>4+</sup>/Ce<sup>3+</sup> and Cu<sup>2+</sup>/Cu<sup>+</sup> redox couples in the mechanism of carbon monoxide oxidation over Pt/CeO<sub>2</sub> and Cu/CeO<sub>2</sub>.<sup>30,31</sup> Simultaneous measurement of XAS and catalytic conversion with required time resolution at the scale of seconds enabled us to quantitatively correlate the rate of iron reduction with the rate of carbon dioxide production and propose a catalytic mechanism.

### 3.3 Results and Discussion

#### 3.3.1 Structure of the Catalysts

**Table S1-4** summarizes the elemental composition of the synthesized catalysts and the results of high-angle annular dark-field scanning transmission electron microscopy (HAADF-STEM) and carbon monoxide chemisorption tests for Pt-FeO<sub>x</sub>/Al<sub>2</sub>O<sub>3</sub> (Pt<sub>2.1</sub>Fe<sub>0.7</sub>-Al<sub>2</sub>O<sub>3</sub>-673-5) and the reference samples (Fe<sub>0.6</sub>-Al<sub>2</sub>O<sub>3</sub>-673-5, Pt<sub>2.0</sub>-Al<sub>2</sub>O<sub>3</sub>-673-5). The chlorine and sulfur concentrations were below the detection limit. The sample name here mirrors platinum and iron weight concentrations rounded to one decimal place (Pt<sub>2.1</sub> - 2.09 wt.% Pt, Fe<sub>0.7</sub> - 0.65 wt.%), the temperature of the reduction pretreatment (673 - 673 K), and hydrogen concentration during this pretreatment (5 - 5 vol.% H<sub>2</sub>).

The electron microscopy and carbon monoxide chemisorption experiments were performed after heating under 5 vol.% H<sub>2</sub> up to 673 K. A relatively low platinum loading resulted in the formation of small platinum particles with an average size of 1.1 nm for Pt<sub>2.1</sub>Fe<sub>0.7</sub>-Al<sub>2</sub>O<sub>3</sub>-673-5 (**Figures 3-1a,b** and **S3-6a,b**) and 0.95 nm for Pt<sub>2.0</sub>-Al<sub>2</sub>O<sub>3</sub>-673-5 reference (**Figure S3-6c,d**). The STEM-derived particle size dispersions based on spherical shape approximation are 0.69 for Pt<sub>2.1</sub>Fe<sub>0.7</sub>-Al<sub>2</sub>O<sub>3</sub>-673-5 and 0.82 for Pt<sub>2.0</sub>-Al<sub>2</sub>O<sub>3</sub>-673-5. Dispersions estimated by carbon monoxide chemisorption are slightly smaller, 0.56 for Pt<sub>2.1</sub>Fe<sub>0.7</sub>-Al<sub>2</sub>O<sub>3</sub>-673-5 and 0.58 for Pt<sub>2.0</sub>-Al<sub>2</sub>O<sub>3</sub>-673-5 likely due to the adsorption of one carbon monoxide molecule on multiple platinum surface atoms. These results suggest that iron oxide does not entirely cover the platinum surface, a TEM of Pt<sub>2.1</sub>Fe<sub>0.7</sub>-Al<sub>2</sub>O<sub>3</sub>-673-5 shows no evidence of any crystalline phases, except for metallic platinum. We also did not observe any overlayer of iron oxide on the platinum surface. In situ X-ray diffraction (XRD) of Pt<sub>2.1</sub>Fe<sub>0.7</sub>-Al<sub>2</sub>O<sub>3</sub>-673-5 only demonstrates broad peaks of  $\gamma$ -Al<sub>2</sub>O<sub>3</sub> and none from platinum or iron (**Figure S1-7**).



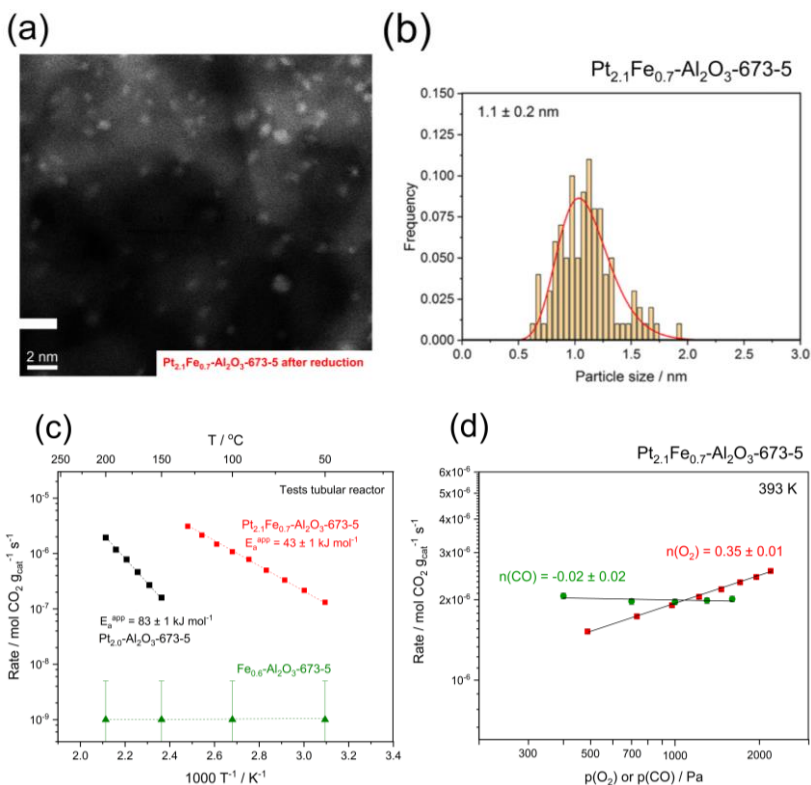


Figure 3-1. (a) HAADF-STEM image of  $\text{Pt}_{2.1}\text{Fe}_{0.7}\text{-Al}_2\text{O}_3\text{-673-5}$  showing Pt particles (elemental contrast, bright spots); (b) size distribution of Pt particles in  $\text{Pt}_{2.1}\text{Fe}_{0.7}\text{-Al}_2\text{O}_3\text{-673-5}$ ; (c) Arrhenius plots of carbon monoxide oxidation over  $\text{Pt}_{2.0}\text{-Al}_2\text{O}_3\text{-673-5}$ ,  $\text{Pt}_{2.1}\text{Fe}_{0.7}\text{-Al}_2\text{O}_3\text{-673-5}$ , and  $\text{Fe}_{0.6}\text{-Al}_2\text{O}_3\text{-673-5}$  measured in a tubular plug flow reactor; (d) double-logarithmic plots of the dependence of the rate of carbon dioxide formation over  $\text{Pt}_{2.1}\text{Fe}_{0.7}\text{-Al}_2\text{O}_3\text{-673-5}$  on varying oxygen and carbon monoxide partial pressures while keeping total pressure and second gas pressure constant. Error bars for (c) and (d) are calculated from two individual experiments.

### 3.3.2 Carbon Monoxide Oxidation Activity and Kinetics

**Figure 3-1c** shows Arrhenius plots of carbon monoxide oxidation over  $\text{Pt}_{2.1}\text{Fe}_{0.7}\text{-Al}_2\text{O}_3\text{-673-5}$ ,  $\text{Pt}_{2.0}\text{-Al}_2\text{O}_3\text{-673-5}$ , and  $\text{Fe}_{0.6}\text{-Al}_2\text{O}_3\text{-673-5}$ , measured in a tubular plug flow reactor after pretreatment in 5 vol.%  $\text{H}_2$ . Only  $\text{Pt}_{2.1}\text{Fe}_{0.7}\text{-Al}_2\text{O}_3\text{-673-5}$  is active for carbon monoxide oxidation below 373 K. Moreover, the apparent activation energy of carbon monoxide oxidation over  $\text{Pt}_{2.1}\text{Fe}_{0.7}\text{-Al}_2\text{O}_3\text{-673-5}$  ( $43 \text{ kJ}\cdot\text{mol}^{-1}$ ) is about half that for  $\text{Pt}_{2.0}\text{-Al}_2\text{O}_3\text{-673-5}$  ( $83 \text{ kJ}\cdot\text{mol}^{-1}$ ).

For Pt<sub>2.1</sub>Fe<sub>0.7</sub>-Al<sub>2</sub>O<sub>3</sub>-673-5, the reaction rate is almost independent of the carbon monoxide pressure, showing a reaction order close to zero, both at 353 and 393 K (**Figures 3-1d** and **S1-8a**), while the reaction order in oxygen is positive: 0.41 at 353 K and 0.35 at 393 K, respectively (**Figures 3-1d** and **S1-8b**). As both reaction orders are positive, oxygen and carbon monoxide activation do not compete. Thus, the catalyst can simultaneously activate both reagents, which suggests a bifunctional mechanism of carbon monoxide oxidation. Variation in carbon dioxide pressure did not affect the rate of reaction (**Figure S1-8c**). Thus, the product desorption equilibrium can be neglected. This agrees with studies by Tomita et al., who found that any bicarbonate species observed by infrared spectroscopy on the surface of Pt<sub>2.1</sub>Fe<sub>0.7</sub>-Al<sub>2</sub>O<sub>3</sub>-673-5 under 1 vol.% CO and 1 vol.% O<sub>2</sub> do not change in concentration and are likely spectators.<sup>17</sup>

Overall, we observe that the presence of the iron oxide promoter significantly increases the carbon monoxide oxidation activity of the platinum catalyst at low temperatures and lowers the activation barrier.

### 3.3.3. Platinum and Iron States During the Pretreatment in Hydrogen

**Figure 3-2** shows the results of the in situ XAS temperature-programmed reduction (TPR) experiments for Pt<sub>2.1</sub>Fe<sub>0.7</sub>-Al<sub>2</sub>O<sub>3</sub>-673-5 performed at the Pt L<sub>3</sub> and Fe K-edges. During these experiments, we heated the catalyst up to 673 K with 10 K·min<sup>-1</sup> in 5 vol.% H<sub>2</sub>. The 10 s averaged Pt L<sub>3</sub> and Fe K-edge XAS spectra are shown in **Figure 3-2a,b**, respectively. The changes in the white line intensities and the shift of the edge positions indicate the reduction of both platinum and iron with increasing temperature.

The multivariate curve resolution-alternating least squares (MCR-ALS) method helped us to obtain the spectra of individual components (**Figure 3-2c,d**) and their evolution with temperature (**Figure 3-2e,f**). Based on the Pt L<sub>3</sub> XAS spectra of the Pt and PtO<sub>2</sub> references (**Figure 3-2c**) and the literature data, we demonstrated that during the TPR experiment, platinum in the catalyst progressively transforms from an oxidized platinum state (close to PtO<sub>2</sub> state) to metallic platinum covered by hydrogen (Pt-H) and finally to bare platinum.<sup>41</sup> The difference between the last two components is expressed as a shift of the white line position to higher energies and an increase in the white line intensity (**Figure S1-9**). These spectral changes are characteristic for hydrogen chemisorption on platinum.<sup>42</sup> The bare platinum component observed at the temperature window of 573-673 K has a lower white line intensity in comparison to the spectrum of metallic platinum foil, in agreement with the literature.<sup>43</sup> For iron, we identified only two spectral components and assigned them to Fe<sup>3+</sup> and Fe<sup>2+</sup> oxidic species based on their resemblance to the spectra of Fe<sub>2</sub>O<sub>3</sub> and FeO references (**Figure 3-2d**). Nevertheless, Fe K-edge XANES shows that the structures of the oxidic Fe<sup>3+</sup> and Fe<sup>2+</sup> species in Pt<sub>2.1</sub>Fe<sub>0.7</sub>-Al<sub>2</sub>O<sub>3</sub>-673-5 are significantly different from the bulk oxide references, which is not surprising considering the low iron content in the catalyst and structural disorder of highly dispersed species.<sup>44,45</sup>

Close examination of the evolution of the platinum and iron spectral components (**Figure 3-2e,f**) during the TPR demonstrates that the oxides of platinum and iron start to reduce at similar temperatures of about 363 K. **Figure S1-10** shows that in the absence of platinum, Fe<sub>0.6</sub>-Al<sub>2</sub>O<sub>3</sub>-673-5 cannot be reduced at such a low temperature. This suggests that hydrogen spillover from platinum to the support is responsible for the low-temperature reduction of iron oxide.<sup>46</sup> In agreement with other work, Fe K- and Pt L<sub>3</sub>-edge XANES do not show the presence of metallic iron and Pt-Fe alloy.<sup>17</sup> The in situ Pt L<sub>3</sub>-edge EXAFS of Pt<sub>2.1</sub>Fe<sub>0.7</sub>-Al<sub>2</sub>O<sub>3</sub>-673-5 measured under 5 vol.% H<sub>2</sub> atmosphere after the TPR at 303 K also shows exclusively a Pt-Pt shell with a coordination number ca. 8.0, characteristic for small platinum nanoparticles (**Figure S1-11** and **Table S1-2**). Disorder parameters are rather large but similar to the ones previously observed for nanometer-sized supported platinum particles.<sup>47</sup> A Pt-Fe shell was observed in the work of Cao et al. for the iron species supported directly on platinum nanoparticles by

the atomic layered deposition (ALD) method.<sup>26</sup> The EXAFS data presented here did not confirm the existence of such a Pt-Fe shell.

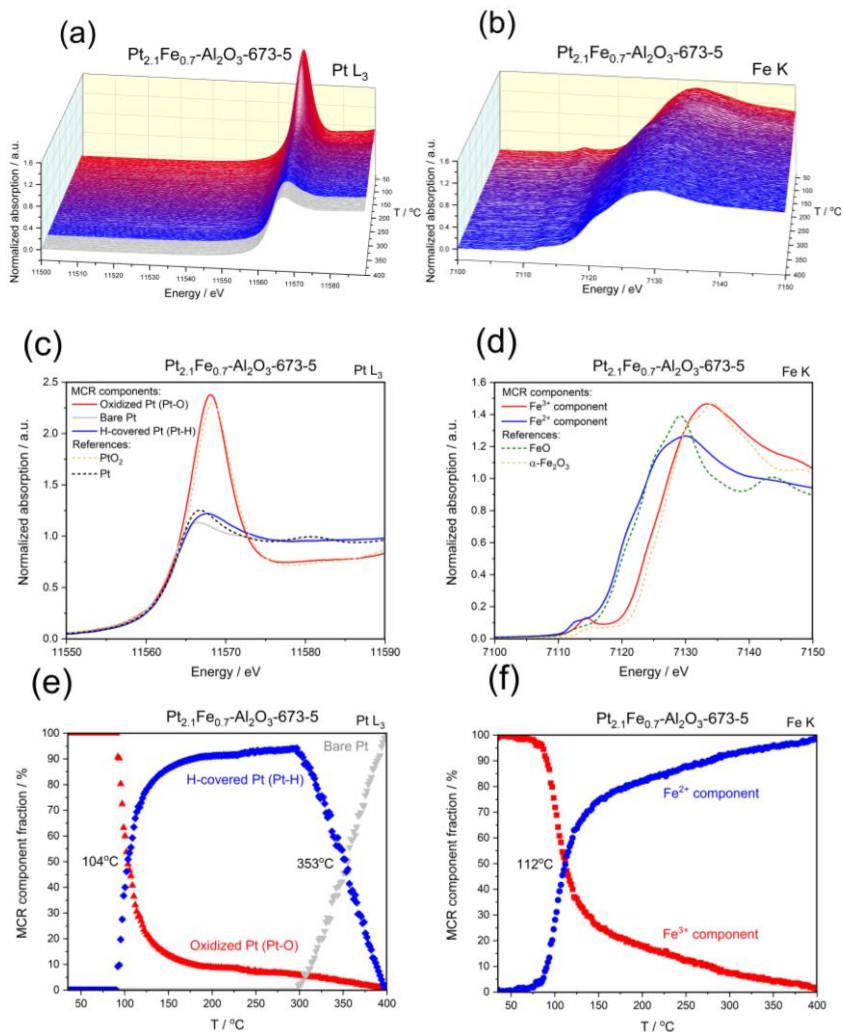


Figure 3-2. Pt  $L_3$ -edge (a) and Fe K-edge (b) XANES spectra of  $\text{Pt}_{2.1}\text{Fe}_{0.7}\text{-Al}_2\text{O}_3\text{-673-5}$  collected during TPR in 5 vol.%  $\text{H}_2$ ; Pt  $L_3$  (c) and Fe K-edge (d) resolved spectral components together with the spectra of references; fractions of platinum (e) and iron (f) species derived from MCR-ALS analysis of the time-resolved TPR-XAS.

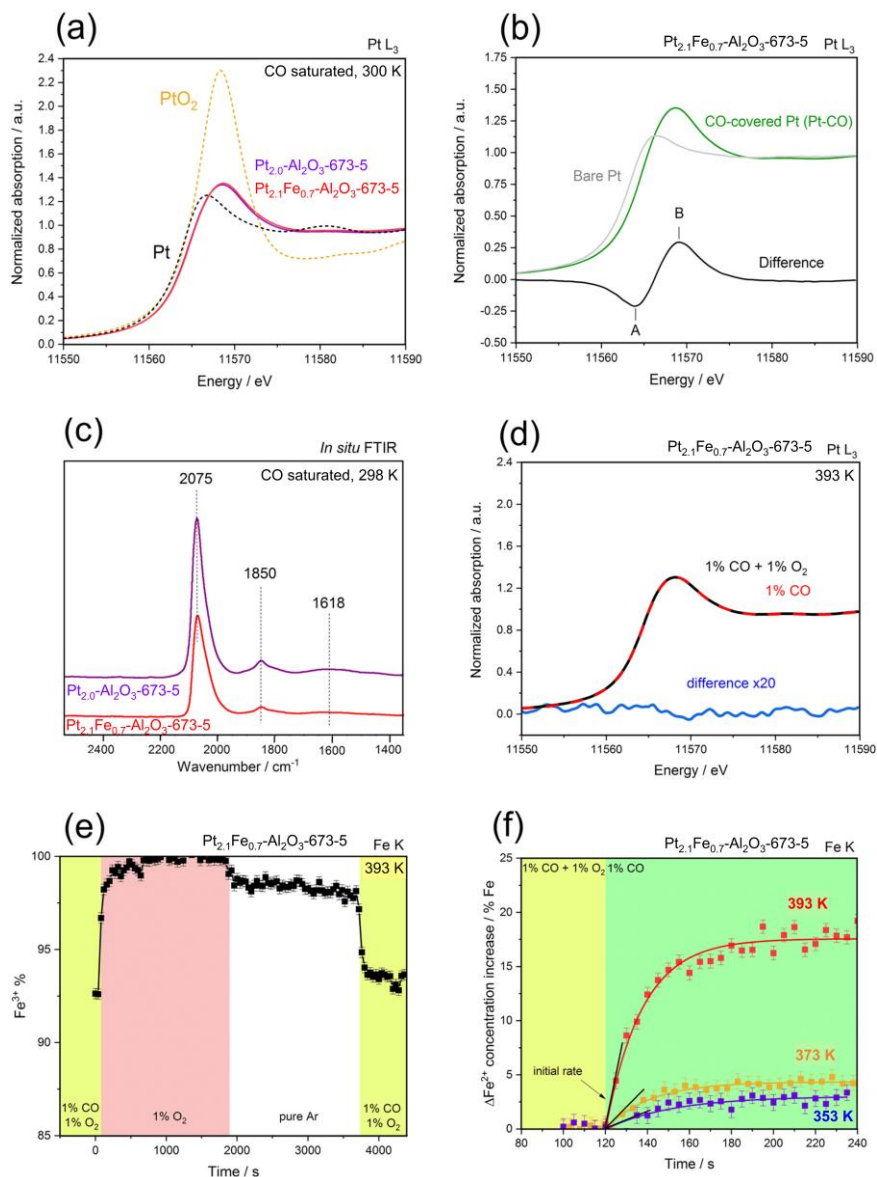


Figure 3-3. (a) In situ Pt  $L_3$ -edge XANES spectra of carbon monoxide-saturated  $Pt_{2.0}\text{-Al}_2\text{O}_3\text{-673-5}$  and  $Pt_{2.1}\text{Fe}_{0.7}\text{-Al}_2\text{O}_3\text{-673-5}$  after reduction in 5 vol.%  $\text{H}_2$ . (b) Difference spectrum between the Pt  $L_3$ -edge XANES spectra of bare and carbon monoxide-covered platinum components for  $Pt_{2.1}\text{Fe}_{0.7}\text{-Al}_2\text{O}_3\text{-673-5}$ . (c) In situ FTIR spectra of carbon monoxide-saturated  $Pt_{2.0}\text{-Al}_2\text{O}_3\text{-673-5}$  and

Pt<sub>2.1</sub>Fe<sub>0.7</sub>-Al<sub>2</sub>O<sub>3</sub>-673-5 after reduction. (d) Comparison of operando Pt L<sub>3</sub>-edge XANES spectra of Pt<sub>2.1</sub>Fe<sub>0.7</sub>-Al<sub>2</sub>O<sub>3</sub>-673-5 under 1 vol.% CO + 1 vol.% O<sub>2</sub> and 1 vol.% CO gas mixtures at 393 K. (e) Iron speciation during in situ/operando Fe K-edge XANES (experiment 1-1, operando experiment with Ar carrier gas) at 393 K under different gas atmospheres. (f) Reversible increase of Fe<sup>2+</sup> concentration in Pt<sub>2.1</sub>Fe<sub>0.7</sub>-Al<sub>2</sub>O<sub>3</sub>-673-5 after switching from 1 vol.% CO + 1 vol.% O<sub>2</sub> to 1 vol.% CO gas mixture at 353-393 K fitted by a delayed exponential-associated decay function; a baseline for each temperature was chosen as the y<sub>0</sub> value of the delayed exponential-associated decay function fit (equation 1).

### 3.3.4 Platinum State under Reaction Conditions

**Figure 3-3a** compares the Pt L<sub>3</sub> XANES spectra of Pt<sub>2.1</sub>Fe<sub>0.7</sub>-Al<sub>2</sub>O<sub>3</sub>-673-5 and Pt<sub>2.0</sub>-Al<sub>2</sub>O<sub>3</sub>-673-5 after exposure to carbon monoxide after the above-mentioned TPR experiments. Carbon monoxide adsorption on the platinum surface causes the 5d valence band to form bonding and antibonding states with the adsorbate.<sup>41</sup> This causes an increase in the intensity of the Pt L<sub>3</sub>-edge white line and an edge shift to higher energies, which is evident in the difference spectrum (**Figure 3-3b**).<sup>48</sup> The Pt L<sub>3</sub> spectra of Pt<sub>2.1</sub>Fe<sub>0.7</sub>-Al<sub>2</sub>O<sub>3</sub>-673-5 and Pt<sub>2.0</sub>-Al<sub>2</sub>O<sub>3</sub>-673-5 are virtually identical, suggesting that the oxidation state of platinum is not affected by the presence of iron.

**Figure 3-3c** shows the in situ FTIR spectra of Pt<sub>2.1</sub>Fe<sub>0.7</sub>-Al<sub>2</sub>O<sub>3</sub>-673-5 and Pt<sub>2.0</sub>-Al<sub>2</sub>O<sub>3</sub>-673-5 after reduction and subsequent saturation with carbon monoxide. We observe only three peaks corresponding to linearly adsorbed 2075 cm<sup>-1</sup>, bridging 1850 cm<sup>-1</sup>, and 3-fold 1618 cm<sup>-1</sup> carbon monoxide adsorbed on metallic platinum.<sup>49,50</sup> The presence of iron does not affect the peak positions and their relative intensity, indicating that the oxidation state of platinum in both samples is similar. **Figure 3d** compares the in situ Pt L<sub>3</sub> XAS of Pt<sub>2.1</sub>Fe<sub>0.7</sub>-Al<sub>2</sub>O<sub>3</sub>-673-5 at 393 K in 1 vol.% CO before and after the addition of 1 vol.% O<sub>2</sub>. In the presence of both carbon monoxide and oxygen, the carbon dioxide yield was below 20% (**Figures S1-12** and **S1-13**), assuring that the catalyst cannot be oxidized by the excess of oxygen. The absence of spectral differences for the whole studied temperature range: 353, 373 K (**Figure S1-14**) and 393 K, as in **Figure 3-3d**, indicates that platinum under catalytic conditions remains metallic and fully covered by carbon monoxide. The average size of platinum nanoparticles did not change during the beamtime measurements (**Figure S1-6**) and, thus, had no influence on the shape of the Pt L<sub>3</sub>-edge XAS either. Therefore, the activation of carbon monoxide is the main function of platinum in Pt<sub>2.1</sub>Fe<sub>0.7</sub>-Al<sub>2</sub>O<sub>3</sub>-673-5, while the activation of oxygen may be aided by iron species.

### 3.3.5 Iron State under Reaction Conditions

Having stabilized the performance of Pt<sub>2.1</sub>Fe<sub>0.7</sub>-Al<sub>2</sub>O<sub>3</sub>-673-5 in the operando reactor after exposure to the 1 vol.% CO and 1 vol.% O<sub>2</sub> gas mixture for 1 h at 383-393 K, we started to investigate the iron oxidation state under reaction conditions by Fe K-edge XANES. **Figure S1-3c** shows that the difference Fe K-edge XAS spectrum of the FeO and Fe<sub>2</sub>O<sub>3</sub> references resembles the corresponding difference spectra of Pt<sub>2.1</sub>Fe<sub>0.7</sub>-Al<sub>2</sub>O<sub>3</sub>-673-5 measured at 393 K in 1 vol.% CO (the most reduced state) and in 5 vol.% O<sub>2</sub> (the most oxidized state). Thus, all intermediate iron states observed in our operando Fe K-edge XAS experiments present partially reduced oxidic iron species with a Fe<sup>2+</sup> concentration in between these two reference states. These two states of Pt<sub>2.1</sub>Fe<sub>0.7</sub>-Al<sub>2</sub>O<sub>3</sub>-673-5 were used as the first (60.2% Fe<sup>2+</sup>) and the second (the most oxidized state, 0% Fe<sup>2+</sup>, 100% Fe<sup>3+</sup>) components to estimate the iron oxidation state in time-resolved operando Fe K-edge XAS experiments (experiment 1-1, **Figure S1-3a,c**). Fe K-edge EXAFS supports the idea that under reaction conditions, the catalyst contains a redox-active Fe<sup>2+</sup>/Fe<sup>3+</sup> pair. The amplitude of the first oxygen shell FT EXAFS progressively increases when changing the gas atmosphere from 1 vol.% CO to 1 vol.% CO + 1 vol.% O<sub>2</sub> and to 5 vol.% O<sub>2</sub> (**Figure S1-15**) in line with the observed changes in Fe K-edge XANES (**Figure S1-15**). The average Fe-O coordination number increases (**Table S1-3**) from 3.5 in the 1 vol.% CO gas mixture to 4.3 for 1 vol.% CO + 1 vol.% O<sub>2</sub> and 4.5 for 5 vol.% O<sub>2</sub> atmosphere, respectively. Thus, Fe<sup>2+</sup> and Fe<sup>3+</sup> cations can be located on the surface of alumina support, most likely in tetrahedral coordination, as it was proposed by Tomita et al. based on Fe K-edge EXAFS.<sup>45</sup> Coordinatively unsaturated Fe<sup>2+</sup> cations can activate molecular oxygen, thereby forming Fe<sup>3+</sup> complexes with charged oxygen species. Once oxygen species react with carbon monoxide, Fe<sup>2+</sup> species regenerate. Neither Fe K-edge nor Pt L<sub>3</sub>-edge EXAFS fits suggest the presence of Pt-Fe or Pt-O-Fe bonds.

To quantify changes in the  $\text{Fe}^{2+}$  concentration from the Fe K-edge XANES data, we used a linear combination fitting (LCF) approach. The exact LCF and further procedures used to extract the  $\text{Fe}^{2+}$  concentration are described in the Experimental Section (XANES analysis, **S1**). An example of such LCF is shown in **Figure S1-3a,c**. **Figure 3-3f** presents reversible changes in the oxidation state of iron in  $\text{Pt}_{2.1}\text{Fe}_{0.7}\text{-Al}_2\text{O}_3\text{-673-5}$  during oxygen cut-off experiments consisting of periodic switching between 1 vol.% CO and 1 vol.%  $\text{O}_2$  gas mixture to the one containing only 1 vol.% CO. We observed similar reversible changes during an additional operando XAS experiment performed at 353 K while using helium carrier gas instead of argon (experiment 4, **Figures S1-3b,d** and **S1-4d**). Spectra of the most reduced (32.3%  $\text{Fe}^{2+}$ ) and most oxidized (0%  $\text{Fe}^{2+}$ , 100%  $\text{Fe}^{3+}$ ) states were used to calculate  $\text{Fe}^{2+}/\text{Fe}^{3+}$  concentrations for this catalyst using the same Fe K-edge XAS LCF approach as for experiment 1-1 (**Figure S1-3b**). In this case, the most reduced state was measured at 393 K under reaction mixture 1 vol.% CO + 1 vol.%  $\text{O}_2$  and, thus, showed a lower degree of reduction (**Figure S1-3a,b**).

Under reaction conditions at 393 K about 6-8% of all iron atoms are in  $\text{Fe}^{2+}$  state as one can see in **Figure 3-3e**, while the catalyst can be further reduced with an additional formation of 18%  $\text{Fe}^{2+}$  (up to 26%  $\text{Fe}^{2+}$  in total) under 1 vol.% CO as shown in **Figure 3f**. Thus, under reaction conditions,  $\text{Pt}_{2.1}\text{Fe}_{0.7}\text{-Al}_2\text{O}_3\text{-673-5}$  contains active iron sites both in  $\text{Fe}^{3+}$  and  $\text{Fe}^{2+}$  states as well as  $\text{Fe}^{3+}$  spectators not reducing in carbon monoxide. These spectator species might consist of scattered coordinatively unsaturated  $\text{Fe}_\text{o}$  species on the alumina surface according to Fe K-edge EXAFS (**Table S1-3** and **Figure S1-15**).<sup>45</sup> As Fe K-edge XANES and EXAFS suggest, the gas atmosphere determines the amount of reduced  $\text{Fe}^{2+}$  oxidic species partially covered by oxygen. Both the Fe-O coordination number (**Figure S1-15b** and **Table S1-3**) and the total oxidation state of iron (**Figures S1-4** and **3-3f**) increase after adding 1 vol.%  $\text{O}_2$  to the 1 vol.% CO gas mixture. This fact corroborates with the intermediate oxygen reaction order of 0.35-0.41 observed for  $\text{Pt}_{2.1}\text{Fe}_{0.7}\text{-Al}_2\text{O}_3\text{-673-5}$ . The platinum-free  $\text{Fe}_{0.6}\text{-Al}_2\text{O}_3\text{-673-5}$ , under the same conditions, showed no changes in the Fe K-edge spectra and, thus, maintained a constant iron oxidation state and contained only  $\text{Fe}^{3+}$  species (**Figure S1-4e**). This means that it is platinum that promotes iron reduction with carbon monoxide at low temperatures.

### 3.3.6 Mechanism of Carbon Monoxide Oxidation over $\text{Pt}_{2.1}\text{Fe}_{0.7}\text{-Al}_2\text{O}_3\text{-673-5}$

Oxygen species involved in a specific catalytic process may exist only under specific reaction conditions; therefore, in situ and operando methods capable of tracking the concentration of active oxygen intermediates and redox-active metal sites involved in oxygen activation are essential to advance the understanding of oxidation catalysis. Raman spectroscopy could not detect any signal of the iron oxide phase or oxygen radicals (**Figure S1-16**). We, therefore, used our ability to quantify an amount of  $\text{Fe}^{2+}$  and  $\text{Fe}^{3+}$  cationic species to propose a model for the type and amount of oxygen anions activating on iron centers.

Detailed analysis of the oxygen cut-off experiments allowed us to extract new information about the mechanism of carbon monoxide oxidation over  $\text{Pt}_{2.1}\text{Fe}_{0.7}\text{-Al}_2\text{O}_3\text{-673-5}$ . During these experiments, we were periodically switching between a 1 vol.% CO and 1 vol.%  $\text{O}_2$  mixture (120 s) and one containing only 1 vol.% CO (120 s) as shown in **Figures S1-2** and **S1-13**. Measured spectra are similar to the ones collected in situ under the steady-state conditions before the oxygen cut-off cycles (**Figures 3-3e** and **S1-17**). The resulting changes in the reaction rates and the oxidation state of iron during operando experiments were reproducible, and we averaged the data over cycling periods to improve the statistics (**Figures S1-18**, **3-4a,b,c**, and **S1-19**). An example of a single cycling period is presented in **Figure S1-2a**. One can observe a decay of the carbon dioxide production rate right after the oxygen cut-off, which reached a saturation value. The minimal value of carbon dioxide formation in 1 vol.% CO was considered as a “background” signal not related to the changes observed during periodic gas switching. This background was always subtracted when we analyzed the oxygen cut-off experiments, for

example, to obtain the results shown in **Figure 3-4d**, and was less than 26% of the steady-state carbon dioxide concentration during experiment 1-1 and less than 36% during experiment 1-4 as shown in **Table S1-5**. The procedure of background subtraction is presented in **Figure S1-2b**. The carbon dioxide production rate in 1 vol.% CO and 1 vol.% O<sub>2</sub> mixture right before the oxygen cut-off, excluding the background conversion, will be referred to as the steady-state reaction rate (**Figure S1-2a**). The amount of carbon dioxide produced after the oxygen cut-off was integrated and will be referred to as the integrated carbon dioxide amount produced in the absence of oxygen (**Figure S1-2b**). The catalytic rates during the cycles were close to the rates obtained during kinetic tests in both tubular reactor and the operando cell (**Figure S1-8d** and **Table S1-5**). Observed differences can be attributed to the catalyst deactivation due to the rapid changes in the gas composition over the course of operando experiments.

**Figure 3-4a,b,c** quantitatively compares the integrated amount of carbon dioxide produced in the absence of oxygen with the amount of reduced iron produced ( $\Delta\text{Fe}^{2+}$  increase). Both values are about the same and increase accordingly with temperature, which indicates the involvement of the redox activity of iron in the mechanism of carbon monoxide oxidation. To prove that the observed  $\text{Fe}^{2+}$  formation is not due to X-ray beam-related effects, we additionally performed an experiment with a lower beam density and found no significant influence on the amplitude of the iron reduction (**Figure S1-5**).

We fitted the  $\Delta\text{Fe}^{2+}$  increase shown in **Figure 3-4a,b,c** (experiment 1) and **Figure S1-18** (experiment 1-4) using a delayed associated exponential decay function (equation 1):

$$(1) y \begin{cases} y_0, & t < t_0 \\ y_0 + A \left[ 1 - e^{-\frac{(t-t_0)}{\tau}} \right], & t \geq t_0 \end{cases}$$

where  $t$  - time (s);  $y_0$  is the concentration of before  $t_0$  (20 s before the cut-off);  $t_0 = 120$  s (moment of switching off oxygen);  $A$  - maximum amplitude of  $\Delta\text{Fe}^{2+}$  at 240 s (120 s in 1 vol.% CO). The initial  $\text{Fe}^{2+}$  formation rate at the moment of cutting off oxygen was calculated as the first derivative of the fitted function at  $t_0 = 120$  s. **Figure 3-4d** (and **Table S1-5**) compare the latter rate measured at 353, 373, and 393 K (from the trends shown in **Figure 3-4a,b,c**) with the steady-state carbon dioxide formation rate just before oxygen cut-off for both experiments 1 and 4 mentioned in **Table S1-1**. The data show a linear correlation suggesting that in the presence of oxygen, the rate of carbon dioxide formation is about 2.3 times higher than the  $\text{Fe}^{2+}$  formation rate in the absence of oxygen. A ratio close to two suggests that oxygen could be activated via a superoxo ( $\text{O}_2^-$ ) intermediate. The whole catalytic process can then be described by equation 2:





At the same time, almost equal amounts of carbon dioxide and  $\Delta\text{Fe}^{2+}$  form after 120 s in 1 vol.% CO (Figure 3-4a,b,c and Table S1-6). This would suggest a one-electron process involving peroxide intermediates according to equations 3 or 4:

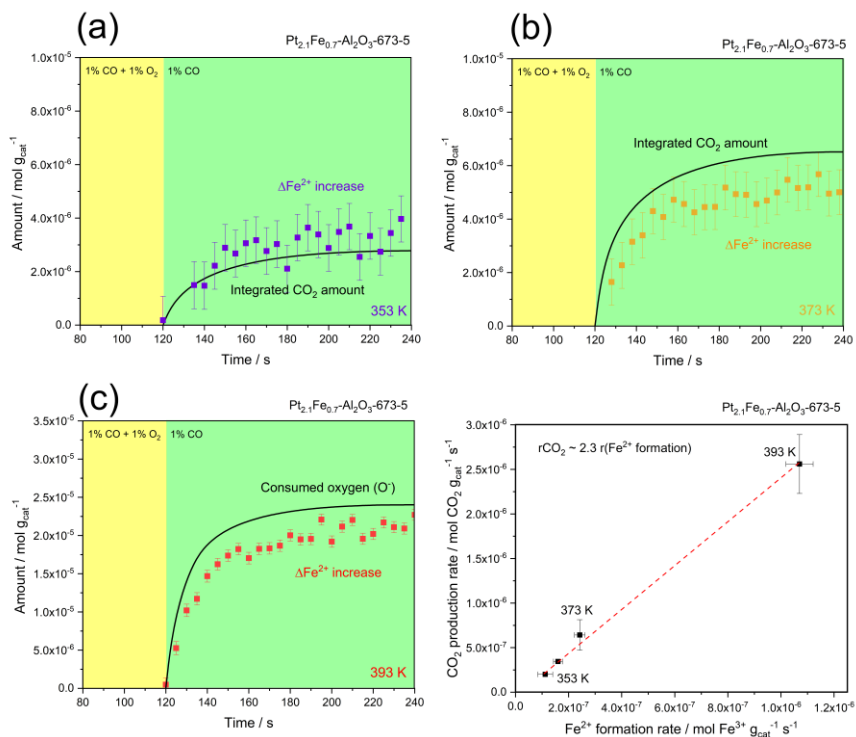


Figure 3-4. (a-c) Amount of carbon dioxide vs. that of produced  $\text{Fe}^{2+}$  after oxygen cut-off obtained from operando Fe K-edge XAS and MS data for  $\text{Pt}_{2.1}\text{Fe}_{0.7}\text{Al}_2\text{O}_3\text{-673-5}$ ; a baseline for each temperature was chosen as the  $y_0$  value of the delayed exponential-associated decay function fit (equation 1). (d) Correlation between the initial rate of  $\text{Fe}^{2+}$  formation after oxygen cut-off and the steady-state rate of carbon dioxide formation before oxygen cut-off after subtraction of a background carbon dioxide conversion (data averaged over all cycles at a given temperature). Gas concentrations are shown as vol.%.

This brings forward the following hypothesis where the surface species remaining in the carbon monoxide atmosphere after oxygen cut-off are reactive radicals presented in equations 3 and 4, but the whole catalytic cycle can only be described by equation 2. From these results, we inferred the reaction model as schematically presented in **Figure 3-5**. The proposed mechanism implies a rapid reaction of electrophilic diatomic oxygen immediately after adsorption with the subsequent formation of  $\text{Fe}^{3+} + \text{O}^{\cdot}$  (step 2). This intermediate is then consumed in a one-electron reduction process (step 3) with the formation of one carbon dioxide molecule per each reduced  $\text{Fe}^{3+}$  cation. Then in step 1, completing the catalytic cycle, gas-phase oxygen activates on the  $\text{Fe}^{2+}$  site formed after step 3. Even though we were able to approximate  $\text{Fe}^{2+}$  formation as a first-order one-electron process using a single exponential decay function, more complex reaction mechanisms involving a combination of different iron-associated reactive oxygen species are still possible. Until now, spectroscopic features of  $\text{Fe}^{3+} - \text{O}^{\cdot}$  species were only discovered for a well-defined Fe-BEA zeolite system using a combination of complex spectroscopic methods and quantum mechanical modeling.<sup>51</sup> In situ Raman spectroscopy was unable to detect any signal of iron oxide or active oxygen species in our catalyst (**Figure S1-16**), probably due to the complex nature of the support, the low concentration of iron, and the presence of metallic platinum. Thus, in the case of complex bimetallic Pt- $\text{FeO}_x$  catalyst on  $\gamma\text{-Al}_2\text{O}_3$  support, operando XAS was the only suitable technique to shed light on the oxygen activation mechanism.

The promotion of iron reduction by carbon monoxide and hydrogen in the presence of platinum suggests that supported  $\text{FeO}_x$  species are in close proximity to platinum nanoparticles. At the same time, we did not observe evidence for the formation of an iron layer over platinum nanoparticles as iron did not alter the platinum oxidation state according to in situ XAS, in situ FTIR (**Figure 3-3a,c**), and carbon monoxide chemisorption experiments. We quantified that one  $\text{Fe}^{2+}/\text{Fe}^{3+}$  redox pair participates in the formation of two carbon dioxide molecules, which we rationalized by the activation of dioxygen and a rapid formation of one carbon dioxide molecule and one  $\text{Fe}^{3+} - \text{O}^{\cdot}$  radical. The sites involved in dioxygen activation likely consist of surface  $\text{Fe}^{2+}$  cations coordinated to 3-4 oxygen atoms (according to Fe K-edge EXAFS fitting, see **Table S1-3**) accepting electrophilic oxygen radicals such as  $\text{O}_2^{\cdot}$  while transforming into  $\text{Fe}^{3+}$ . Cationic iron species are known for their ability to stabilize radical oxygen intermediates such as  $\text{Fe}^{3+} - \text{O}^{\cdot}$  ( $\text{Fe}^{4+} - \text{O}^{2-}$ ) in iron-containing zeolites<sup>51-53</sup> or superoxides ( $\text{O}_2^{\cdot}$ ) and peroxides ( $\text{O}_2^{2-}$ )<sup>54</sup> for iron oxide and iron phosphate systems. It was suggested that oxygen could effectively dissociate on the interface between metallic platinum and iron oxide.<sup>14,55</sup> Previous experiments on a model system FeO/Pt(111) support the idea that molecular oxygen can be activated on the coordinatively-unsaturated  $\text{Fe}^{2+}$  sites.<sup>14,55</sup>

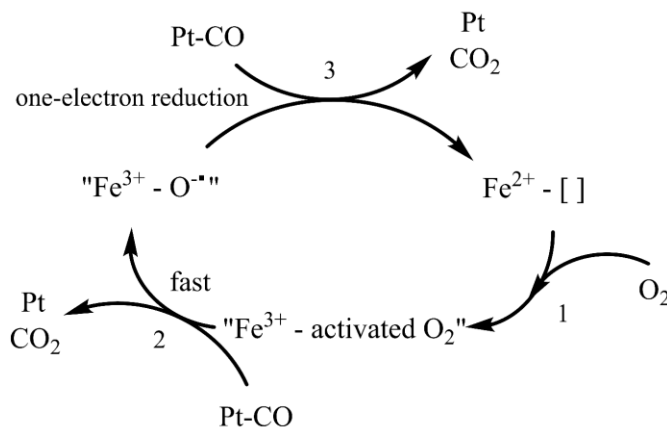


Figure 3-5. Proposed mechanism of carbon monoxide oxidation over  $\text{Pt}_{2.1}\text{Fe}_{0.7}\text{-Al}_2\text{O}_3\text{-673-5}$ . "Activated O<sub>2</sub>" is hypothetical. "[ ]" stands for a surface oxygen vacancy associated with  $\text{Fe}^{2+}$ .

### 3.4 Conclusions

A quantitative comparison of operando structural change, obtained with time-resolved XAS spectroscopy, with catalytic rates revealed that the  $\text{Fe}^{2+}/\text{Fe}^{3+}$  redox pair is directly involved in the catalytic cycle of carbon monoxide oxidation over  $\text{Pt-FeO}_x/\text{Al}_2\text{O}_3$  in the temperature range of 353-393 K. Carbon monoxide chemisorption, HAADF-STEM, in situ XRD, FTIR, and Pt L<sub>3</sub>- and Fe K-edge XAS demonstrated that the presence of iron does not influence the structure of platinum nanoparticles and their carbon monoxide adsorption properties. Activation of carbon monoxide takes place on metallic platinum, which remains fully covered by carbon monoxide during the reaction. Under reaction conditions, molecular oxygen activation proceeds on oxidic  $\text{Fe}^{2+}$  species. After switching off oxygen, approximately one carbon dioxide molecule was formed per each reduced  $\text{Fe}^{3+}$  ion. At the same time, the steady-state carbon dioxide formation rate (before oxygen cut-off) was about twice higher than the initial rate of  $\text{Fe}^{2+}$  formation in the absence of oxygen. This means that abundant oxygen reaction intermediates can be reduced in a one-electron reduction process and are likely presented by oxygen radical species on oxidic  $\text{Fe}^{3+}$  sites. Similar oxygen activation mechanisms might be expected for other catalytic oxidation reactions over cationic iron of both chemical and biological importance.

## 3.5 Methodology of XAS

### 3.5.1 In situ/operando XAS Experiments

We performed the in situ/operando XAS experiments at the Fe K and Pt L<sub>3</sub>-edges using the same operando cell<sup>34</sup> and each time repeated the experiments with a fresh catalyst. A mass spectrometer (MS) was connected to the outlet of the operando cell to measure the composition of the feed and catalyst activity. The same cell and mass spectrometer will be used in Chapters 4 and 5.

The operando cell was filled with 12-20 mg of the catalyst diluted with  $\gamma$ -Al<sub>2</sub>O<sub>3</sub> (the same as the support) in a 1:1 mass ratio and sieved the mixture to obtain a 75-100  $\mu$ m fraction. The front and the back sides of the cell were closed with double 0.25 mm graphite windows partially transparent to X-rays. Two heating cartridges (Türk Hillinger) heating the cell were controlled using a K-type thermocouple inserted inside the cell body and connected to an Eurotherm controller. The temperature readout of this thermocouple was the same as for the thermocouple inserted directly in the catalyst bed for the whole used temperature range. Two sets of the mass flow controllers (Bronkhorst, El Flow) provided two gas mixtures, which could be alternatively supplied to the cell using a dedicated switching valve setup. Fast switching between the two gas feeds was realized using two three-way solenoid switching valves (Parker, Series 9). While one gas mixture was flowing to the cell, the other was directed via a bypass to the exhaust. In all experiments, the pressure drop before the sample was about 110 mbar, and the total flow was 45 ml min<sup>-1</sup>. Using a needle valve on the bypass line, we reduced the back pressure difference between the cell and the bypass line down to 5 mbar. All of this allowed us to perform transient experiments following kinetics at the scale of seconds.

The outlet of the operando cell was connected to the in-line mass spectrometer (OmniStar GSD 320 O1, Pfeiffer). We performed carbon dioxide calibration for each experiment by flowing the corresponding calibration mixtures through a bypass line with the same flow rate and pressure drop as for the operando cell. When using helium/argon as a carrier gas, the rate of carbon dioxide concentration was calculated from the ratio between the mass-to-charge (m/z) signals of 44 (CO<sub>2</sub>) and 4 (He)/40 (Ar), respectively. The residence time of the operando cell was estimated to be 1.9 s by fast switching between 1 vol.% Ar in helium, and helium gas feeds using the same total flows, and similar pressure drops as during the operando experiments (**Fig. S1-1**).<sup>31</sup> In all operando experiments, the carbon monoxide conversion was kept below 20%. This allowed us to estimate reaction rates and avoid the catalyst seeing different gas compositions along the catalyst bed.<sup>35</sup>

The most important in situ/operando XAS experiments are summarized in **Table S1-1**. During the pre-reduction or TPR experiments (experiments 1,2,5 in **Table S1-1**) the catalysts were reduced in situ in 5 vol.% H<sub>2</sub> by heating the cell up to 673 K with a ramp rate of 10 K·min<sup>-1</sup> and dwelling for 20 min. The such pre-reduction procedure was also done prior to all other in situ/operando and kinetic experiments and followed by cooling down to room temperature in 5 vol.% H<sub>2</sub>, exposure to helium or argon for 10 min, 1 vol.% CO for 10 min and, finally, to the reaction mixture containing 1 vol.% CO + 1 vol.% O<sub>2</sub>. Then the catalysts were heated up to 383 K under the reaction mixture and kept at this temperature for 1 h to reach a stable conversion. The following cut-off transient experiments (1,2, 4-6 in **Table S1-1**) consisted of periodic switching between 1 vol.% CO and 1 vol.% O<sub>2</sub> (120 s) gas mixture and the one containing only 1 vol.% CO (120 s). A residual flow of carbon dioxide remaining in the 1 vol.% CO mixture was subtracted from the total flow of carbon dioxide produced under the reaction conditions as shown in **Fig. S1-2**.

### 3.5.2 XANES Analysis

A homemade python-based “ProQEXAFS” v.2.39 software was used for initial XAS data importing, energy calibration, averaging, background subtraction, and normalization to an edge step of one.<sup>36</sup> The multivariate curve resolution with the alternating least squares method (MCR-ALS) allowed us to extract the XANES spectra best representing the species present during the TPR experiments both at the Fe K-edge (7100 - 7150 eV range) and Pt L<sub>3</sub> (11550 - 11590 eV range) edges.<sup>37,38</sup> MCR-ALS minimization was carried out using the MCR-ALS GUI 2.0.<sup>39</sup> The number of spectral components was estimated using the singular value decomposition (SVD) analysis directly in the MCR-ALS GUI 2.0.<sup>39</sup> We also used non-negativity and unimodality constraints, assuming a constant total species concentration and only one concentration maximum for each spectral component, respectively.<sup>39</sup>

Fe K-edge XANES operando experiments aiming to follow the quantity of Fe<sup>2+</sup>/Fe<sup>3+</sup> in time were analyzed using linear combination fitting instead of MCR-ALS. In each operando experiment, after keeping the catalyst under the reaction mixture for 1 h, we measured two reference spectra representing the state of iron under reaction conditions: one of the most oxidized states of iron under 5 vol.% O<sub>2</sub> at 393 K and the other of the most reduced state under 1 vol.% CO at 393 K (**Fig. S1-3a**, experiment 1). We assumed that the most oxidized state contained 100% Fe<sup>3+</sup> in an oxidic state. The same was done for an additional operando Fe K-edge XAS experiment 4 under different carrier gas and the most reduced component measured at 393 K under reaction conditions of 1 vol.% CO + 1 vol.% O<sub>2</sub> instead of 1 vol.% CO (**Fig. S1-3b**). Absolute Fe<sup>2+</sup> and Fe<sup>3+</sup> concentrations in the reduced reference states were determined using a least squares fitting approach (**Fig. S1-3a** for experiment 1 and **Fig. S1-3b** for experiment 4 with different carrier gas and reference states). A standard deviation of this fitting was used to calculate an error in the Fe<sup>2+</sup>/Fe<sup>3+</sup> concentration (mol g<sub>cat</sub><sup>-1</sup>) for each individual spectrum. We then fitted our operando Fe K-edge spectra using spectra of the most oxidized and the most reduced reference states of the catalyst (**Fig. S1-3a** for experiment 1 and **Fig. S1-3b** for experiment 4) with known Fe<sup>2+</sup>, Fe<sup>3+</sup> concentrations to get time-resolved iron concentration profiles. All operando Fe K-edge spectra were averaged to 5 s time resolution, and examples of these spectra are presented in **Fig. S1-4a-c** (experiment 1) and **Fig. S1-4d** (experiment 4). Linear combination fitting of the XANES spectra was performed in the energy range of 7100 - 7130 eV.

In all experiments, the beam size was 200 μm horizontally and 150 μm vertically. Only during the tests of the effects of the intense X-ray beam on the state of the catalyst we increased the size of the beam 10-fold to 200 μm vertically and 1500 μm horizontally, thus decreasing the flux density by a factor of ten. For these experiments, we also used the MCR-ALS approach to extract the relative Fe<sup>3+</sup>/Fe<sup>2+</sup> concentration changes during the oxygen cut-off cycles (**Fig. S1-5a**).<sup>37-39</sup>

### 3.5.3 Pt L<sub>3</sub>-edge EXAFS Analysis

Pt L<sub>3</sub>-edge EXAFS spectra collected under steady state were used for the EXAFS analysis. The Pt L<sub>3</sub>-edge EXAFS analysis of catalysts spectra, initially processed with “ProQEXAFS” v.2.39, was performed using the Demeter software package.<sup>40</sup> Due to the high disorder in the higher coordination shells, only the main peaks in the R range of 1.2 - 3.0 Å were considered in the Fourier transform of the EXAFS. Curve fitting and the fitting parameters are given in **Table S1-2**. The amplitude reduction factor (S<sub>0</sub><sup>2</sup>) was estimated from the fit of the reference Pt foil EXAFS to be 0.84. The fit was performed in R-space in the range of 1.2-3.5 Å, employing the k-range of 3.0-9.0 Å<sup>-1</sup> for the Fourier transform (FT). This dataset was fitted simultaneously with multiple k weightings of 1-3, in order to reduce correlations between the fitting parameters. The amplitude reduction factor S<sub>0</sub><sup>2</sup> was fitted to 0.84.

### 3.5.4 Fe K-edge EXAFS Analysis

An additional experiment was performed to measure the full Fe K-edge EXAFS of  $\text{Pt}_{2.1}\text{Fe}_{0.7}\text{-Al}_2\text{O}_3\text{-673-5}$  in situ. For this experiment, we used the same in situ cell passing  $100 \text{ ml min}^{-1}$  total flow with a helium carrier gas through it. The catalyst was pre-reduced the same way as in all other experiments. Spectra were recorded after cooling down to 303 K. Fe K-edge EXAFS spectra were collected in transmission mode for 30 min under specific gas atmospheres and processed using the same Demeter software package. First, we extracted the amplitude reduction factor from the fitting of the reference iron foil (0.71). Then we performed EXAFS fitting for  $\text{Pt}_{2.1}\text{Fe}_{0.7}\text{-Al}_2\text{O}_3\text{-673-5}$  with the same disorder parameter ( $\sigma^2$ ) for all in situ Fe K-edge spectra measured subsequently under different atmospheres using multiple k weightings of 1-3, a k-range of  $3.0\text{-}10.0 \text{ \AA}^{-1}$  and an R-range of  $1.15\text{-}2.3 \text{ \AA}$ . All fitting parameters are summarized in **Table S1-3**. The EXAFS fitting model for  $\text{Pt}_{2.1}\text{Fe}_{0.7}\text{-Al}_2\text{O}_3\text{-673-5}$  was based on the  $\alpha\text{-Fe}_2\text{O}_3$  crystal structure. The number of independent points was  $N_{\text{ind}} > 8$  when fitting the iron foil and  $N_{\text{ind}} > 14$  for the simultaneous fit of the three spectra for  $\text{Pt}_{2.1}\text{Fe}_{0.7}\text{-Al}_2\text{O}_3\text{-673-5}$ .

### 3.6 References

1. Mejía, E. Catalysis, Oxygen and sustainability ... Quo vadis? In Catalytic aerobic oxidations; Catalysis Series No. 39; Mejía, E., Ed.; Royal Society of Chemistry, **2020**; pp. 1-15.
2. Rousseau, R.; Glezakou, V. A. and Selloni, A. Theoretical insights into the surface physics and chemistry of redox-active oxides. *Nat. Rev. Mater.* **2020**, *5*, 460-475.
3. Mars, P. and van Krevelen, D. W. Oxidations carried out by means of vanadium oxide catalysts. *Chem. Eng. Sci.* **1954**, *3*, 41-59.
4. Grant, J. T.; Venegas, J. M.; McDermott, W. P. and Hermans, I. Aerobic oxidations of light alkanes over solid metal oxide catalysts. *Chem. Rev.* **2018**, *118* (5), 2769-2815.
5. Bielanski, A. and Haber, J. *Oxygen in Catalysis*; Marcel Dekker Inc.: New York, **1990**; pp. 1-466.
6. Vedrine, J. C. The role of redox, acid/base and collective properties and of crystalline state of heterogeneous catalysts in the selective oxidation of hydrocarbons. *Top. Catal.* **2002**, *21*, 97-106.
7. Puigdollers, A. R.; Schlexer, P.; Tosoni, S. and Pacchioni, G. Increasing oxide reducibility: the role of metal/oxide interfaces in the formation of oxygen vacancies. *ACS Catal.* **2017**, *7* (10), 6493-6513.
8. Schlexer, P.; Puigdollers, A.R. and Pacchioni, G. Role of metal/oxide interfaces in enhancing the local oxide reducibility. *Top. Catal.* **2019**, *62*, 1192-1201.
9. Ro, I.; Resasco, J. and Christopher, P. Approaches for understanding and controlling interfacial effects in oxide-supported metal catalysts. *ACS Catal.* **2018**, *8* (8), 7368-7387.
10. Enger, B.C.; Lødeng, R. and Holmen, A. A review of catalytic partial oxidation of methane to synthesis gas with emphasis on reaction mechanisms over transition metal catalysts. *Appl. Catal. A Gen.* **2008**, *346* (1-2), 1-27.
11. An, K. and Somorjai, G. A. Nanocatalysis I: synthesis of metal and bimetallic nanoparticles and porous oxides and their catalytic reaction studies. *Catal. Lett.* **2015**, *145*, 233-248.
12. Cargnello, M.; Fornasiero, P. and Gorte, R.J. Opportunities for tailoring catalytic properties through metal-support interactions. *Catal. Lett.* **2012**, *142*, 1043-1048.
13. Liu, G.; Walsh, A. G. and Zhang, P. Synergism of iron and platinum species for low-temperature CO oxidation: from two-dimensional surface to nanoparticle and single-atom catalysts. *J. Phys. Chem. Lett.* **2020**, *11* (6), 2219-2229.
14. Fu, Q.; Li, W. ; Yao, Y. ; Liu, H. ; Su, H. ; Ma, D. ; Gu, X. ; Chen, L. ; Wang, Z. ; Zhang, H. ; Wang, B. and Bao, X. Interface-confined ferrous centers for catalytic oxidation. *Science* **2010**. *328* (5982), 1141-1144.
15. Tomita, A.; Shimizu, K. and Tai, Y. Effect of metal oxide promoters on low temperature CO oxidation over water-petreated Pt/alumina catalysts. *Catal. Lett.* **2014**, *144*, 1689-1695.
16. Singh, J.; Alayon, E. M. C.; Tromp, M.; Safonova, O.V.; Glatzel, P.; Nachttegaal, M.; Frahm, R. and van Bokhoven, J. A. Generating highly active partially oxidized platinum during oxidation of carbon monoxide over Pt/Al<sub>2</sub>O<sub>3</sub>: in situ, time-resolved, and high-energy-resolution X-ray absorption

spectroscopy.

*Angew. Chemie* **2008**, *120* (48), 9400-9404.

17. Tomita, A.; Shimizu, K. I.; Kato, K.; Akita, T. and Tai, Y. Mechanism of low-temperature CO oxidation on Pt/Fe-containing alumina catalysts pretreated with water. *J. Phys. Chem. C* **2013**, *117* (3), 1268-1277.

18. Ro, I.; Aragao, I. B.; Chada, J. P.; Liu, Y.; Rivera-Dones, K. R.; Ball, M. R.; Zanchet, D.; Dumesic, J. A. and Huber, G. W. The role of Pt-Fe<sub>x</sub>O<sub>y</sub> interfacial sites for CO oxidation. *J. Catal.* **2018**, *358*, 19-26.

19. Qiao, B.; Wang, A.; Yang, X.; Allard, L. F.; Jiang, Z.; Cui, Y.; Liu, J.; Li, J. and Zhang, T. Single-atom catalysis of CO oxidation using Pt<sub>1</sub>/FeO<sub>x</sub>. *Nat. Chem.* **2011**, *3*, 634-641.

20. An, K.; Alayoglu, S.; Musselwhite, N.; Plamthottam, S.; Melae, G.; Lindeman, A. E. and Somorjai, G. A. Enhanced CO oxidation rates at the interface of mesoporous oxides and Pt nanoparticles. *J. Am. Chem. Soc.* **2013**, *135* (44), 16689-16696.

21. Neumann, S.; Doebler, H. H.; Keil, S.; Erdt, A. J.; Gutsche, C.; Borchert, H.; Kolny-Olesiak, J.; Parisi, J.; Bäumer, M. and Kunz, S. Effects of particle size on strong metal-support interactions using colloidal "surfactant-free" Pt nanoparticles supported on Fe<sub>3</sub>O<sub>4</sub>. *ACS Catal.* **2020**, *10* (7), 4136-4150.

22. Liu, L.; Zhou, F.; Wang, L.; Qi, X.; Shi, F. and Deng, Y. Low-temperature CO oxidation over supported Pt, Pd catalysts: Particular role of FeO<sub>x</sub> support for oxygen supply during reactions. *J. Catal.* **2010**, *274* (1), 1-10.

23. Yin, J.; Wang, J.; Zhang, T. and Wang, X. Novel alumina-supported PtFe alloy nanoparticles for preferential oxidation of carbon monoxide in hydrogen. *Catal. Lett.* **2008**, *125*, 76-82.

24. Sakamoto, Y.; Higuchi, N.; Takahashi, N.; Yokota, K.; Doi, H. and Sugiura, M. Effect of the addition of Fe on catalytic activities of Pt/Fe/γ-Al<sub>2</sub>O<sub>3</sub> catalyst. *Appl. Catal. B Environ.* **1999**, *23* (2-3), 159-167.

25. Siani, A.; Alexeev, O. S.; Lafaye, G. and Amiridis, M. D. The effect of Fe on SiO<sub>2</sub>-supported Pt catalysts: Structure, chemisorptive, and catalytic properties. *J. Catal.* **2009**, *266* (1), 26-38.

26. Cao, L.; Liu, W.; Luo, Q.; Yin, R.; Wang, B.; Weissenrieder, J.; Soldemo, M.; Yan, H.; Lin, Y.; Sun, Z.; Ma, C.; Zhang, W.; Chen, S.; Wang, H.; Guan, Q.; Yao, T.; Wei, S.; Yang, J. and Lu, J. Atomically dispersed iron hydroxide anchored on Pt for preferential oxidation of CO in H<sub>2</sub>. *Nature* **2019**, *565*, 631-635.

27. Xu, L.; Ma, Y.; Zhang, Y.; Jiang, Z. and Huang, W. Direct evidence for the interfacial oxidation of CO with hydroxyls catalyzed by Pt/oxide nanocatalysts. *J. Am. Chem. Soc.* **2009**, *131*, 16366-16367.

28. Chen, G.; Zhao, Y.; Fu, G.; Duchesne, P. N.; Gu, L.; Zheng, Y.; Weng, X.; Chen, M.; Zhang, P.; Pao, C.; Lee, J. and Zheng, N. Interfacial effects in iron-nickel hydroxide-platinum nanoparticles enhance catalytic oxidation. *Science* **2014**, *344* (6183), 495-499.

29. Tomita, A.; Shimizu, K. I.; Kato, K. and Tai, Y. Pt/Fe-containing alumina catalysts prepared and treated with water under moderate conditions exhibit low-temperature CO oxidation activity. *Catal. Commun.* **2012**, *17*, 194-199.



30. Safonova, O. V.; Guda, A.; Rusalev, Y.; Kopelent, R.; Smolentsev, G.; Teoh, W. Y.; van Bokhoven, J. A. and Nachttegaal, M. Elucidating the oxygen activation mechanism on ceria-supported copper-oxo species using time-resolved X-ray absorption spectroscopy. *ACS Catal.* **2020**, *10* (8), 4692-4701.
31. Kopelent, R.; van Bokhoven, J. A.; Szlachetko, J.; Edebeli, J.; Paun, C.; Nachttegaal, M. and Safonova, O. V. Catalytically active and spectator Ce<sup>3+</sup> in ceria-supported metal catalysts. *Angew. Chemie - Int. Ed.* **2015**, *127* (30), 8728-8731.
32. Müller, O.; Nachttegaal, M.; Just, J.; Lützenkirchen-Hecht, D. and Frahm, R. Quick-EXAFS setup at the SuperXAS beamline for in situ X-ray absorption spectroscopy with 10 ms time resolution. *J. Synchrotron Radiat.* **2016**, *23*, 260-266.
33. Clark, A. H.; Steiger, P.; Bornmann, B.; Hitz, S.; Frahm, R.; Ferri, D. and Nachttegaal, M. Fluorescence-detected quick-scanning X-ray absorption spectroscopy. *J. Synchrotron Radiat.* **2020**, *27*, 681-688.
34. Chiarello, G. L.; Nachttegaal, M.; Marchionni, V.; Quaroni, L. and Ferri, D. Adding diffuse reflectance infrared Fourier transform spectroscopy capability to extended x-ray-absorption fine structure in a new cell to study solid catalysts in combination with a modulation approach. *Rev. Sci. Instrum.* **2014**, *85*, 074102.
35. Santiago, J. A.; Figueroa, A.; Gibson, D.; Mairs, T.; Pasternak, S.; Newton, M. A.; Michiel, M. D.; Andrieux, J.; Christoforidis, K. C.; Iglesias-Juez, A.; Fernández-García, M. and Prestipino, C. Innovative insights in a plug flow microreactor for operando X-ray studies. *J. Appl. Cryst.* **2013**, *46*, 1523-1527.
36. Clark, A. H.; Imbao, J.; Frahm, R. and Nachttegaal, M. ProQEXAFS: A highly optimized parallelized rapid processing software for QEXAFS data. *J. Synchrotron Radiat.* **2020**, *27*, 551-557.
37. Cassinelli, W. H.; Martins, L.; Passos, A. R.; Pulcinelli, S. H.; Santilli, C. V.; Rochet, A. and Briois, V. Multivariate curve resolution analysis applied to time-resolved synchrotron X-ray Absorption Spectroscopy monitoring of the activation of copper alumina catalyst. *Catal. Today* **2014**, *229*, 114-122.
38. Voronov, A.; Urakawa, A.; van Beek, W.; Tsakoumis, N. E.; Emerich, H. and Rønning, M. Multivariate curve resolution applied to in situ X-ray absorption spectroscopy data: An efficient tool for data processing and analysis. *Anal. Chim. Acta* **2014**, *840*, 20-27.
39. Jaumot, J.; de Juan, A. and Tauler, R. MCR-ALS GUI 2.0: New features and applications. *Chemom. Intell. Lab. Syst.* **2015**, *140*, 1-12.
40. Ravel, B. and Newville, M. ATHENA , ARTEMIS , HEPHAESTUS : data analysis for X-ray absorption spectroscopy using IFEFFIT. *J. Synchrotron Radiat.* **2005**, *12*, 537-541.
41. Glatzel, P.; Singh, J.; Kvashnina, K. O. and van Bokhoven, J. A. In situ characterization of the 5d density of states of Pt nanoparticles upon adsorption of CO. *J. Am. Chem. Soc.* **2010**, *132*, 2555-2557.
42. Bus, E. and van Bokhoven, J. A. Hydrogen chemisorption on supported platinum, gold, and platinum-gold-alloy catalysts. *Phys. Chem. Chem. Phys.* **2007**, *9*, 2894-2902.
43. Lytle, F.W.; Greeger, R.B.; Marques, E.C.; Sandstrom, D.R.; Via, G.H. and Sinfelt, J.H. Structural genesis of Pt on SiO<sub>2</sub>: Determination by X-ray absorption spectroscopy. *J. Catal.* **1985**, *95*, 546-557.

44. Boubnov, A.; Lichtenberg, H.; Mangold, S. and Grunwaldt, J.-D. Structure and reducibility of a Fe/Al<sub>2</sub>O<sub>3</sub> catalyst for selective catalytic reduction studied by Fe K-edge XAFS spectroscopy. *J. Phys.: Conf. Ser.* **2013**, *430*, 012054.
45. Tomita, A.; Miki, T.; Tango, T.; Murakami, T.; Nakagawa, H. and Tai, Y. Fe K-Edge X-ray absorption fine structure determination of  $\gamma$ -Al<sub>2</sub>O<sub>3</sub>-supported iron-oxide species. *ChemPhysChem* **2015**, *16*, 2015-2020.
46. Spreafico, C.; Karim, W.; Ekinici, Y.; van Bokhoven, J. A. and VandeVondele, J. Hydrogen adsorption on nanosized platinum and dynamics of spillover onto alumina and titania. *J. Phys. Chem. C* **2017**, *121* (33), 17862-17872.
47. Avakyan, L. A.; Kolpacheva, N.A.; Paramonova, E.V.; Singh, J.; Hartfelder, U.; van Bokhoven, J.A. and Bugaev, L.A. Evolution of the atomic structure of ceria-supported platinum nanocatalysts: formation of single layer platinum oxide and Pt-O-Ce and Pt-Ce linkages. *J. Phys. Chem. C* **2016**, *120*, 28057-28066.
48. Singh, J.; Nelson, R. C.; Vicente, B. C.; Scott, S. L. and van Bokhoven, J. A. Electronic structure of alumina-supported monometallic Pt and bimetallic PtSn catalysts under hydrogen and carbon monoxide environment. *Phys. Chem. Chem. Phys.* **2010**, *12*, 5668-5677.
49. Hadjiivanov, K.I. and Vayssilov, G. N. Characterization of oxide surfaces and zeolites by carbon monoxide as an IR probe molecule. *Adv. Catal.* **2002**, *307*, 3888-3891.
50. Moscu, A.; Veyre, L.; Thieuleux, C.; Meunier, F. and Schuurman, Y. CO PROX over Pt-Sn/Al<sub>2</sub>O<sub>3</sub>: a combined kinetic and in situ DRIFTS study. *Catal. Today* **2015**, *258*, 241-246.
51. Snyder, B. E. R.; Vanelderen, P.; Bols, M. L.; Hallaert S. D.; Böttger, L. H.; Ungur, L.; Pierloot, K.; Schoonheydt, R. A.; Sels, B. F. and Solomon, E. I. The active site of low-temperature methane hydroxylation in iron-containing zeolites. *Nature* **2016**, *536*, 317-321.
52. Starokon, E. V.; Parfenov, M. V.; Pirutko, L. V.; Abornev, S. I. and Panov, G. I. Room-temperature oxidation of methane by  $\alpha$ -oxygen and extraction of products from the FeZSM-5 surface. *J. Phys. Chem. C* **2011**, *115*, 2155-2161.
53. Malykhin, S.; Zilberberg, I. and Zhidomirov, G. M. Electron structure of oxygen complexes of ferrous ion center. *Chem. Phys. Lett.* **2005**, *414* (4-6), 434-437.
54. Otsuka, K and Wang, Y. Direct conversion of methane into oxygenates. *Appl. Catal. A: General* **2015**, *222* (1-2), 145-161.
55. Kudernatsch, W.; Peng, G.; Zeuthen, H.; Bai, Y.; Merte, L. R.; Lammich, L.; Besenbacher, F.; Mavrikakis, M. and Wendt, S. Direct visualization of catalytically active sites at the FeO-Pt(111) interface. *ACS Nano* **2015**, *9* (8), 7804-7814.

## 4 An Operando XAS Study of Preferential Carbon Monoxide Oxidation over $\gamma$ -Al<sub>2</sub>O<sub>3</sub> and SiO<sub>2</sub>-Supported Pt-Fe Catalysts Active at Ambient Temperature

Chapter 4 is based on the article from Ilia I. Sadykov, Vitaly L. Sushkevich, Frank Krumeich, Rob Jeremiah G. Nuguid, Jeroen A. van Bokhoven, Maarten Nachtegaal and Olga V. Safonova, *Angew. Chem. Int. Ed.*, **2023**, 135, e2022140.

### *Author contributions:*

*Ilia I. Sadykov designed the research, performed most of the experimental work, and analyzed the data. Vitaly L. Sushkevich and Rob Jeremiah G. Nuguid assisted with the in situ Fourier transform infrared spectroscopy measurements. Frank Krumeich executed electron microscopy measurements. Olga V. Safonova, Jeroen A. van Bokhoven, and Maarten Nachtegaal were involved in the research design and helped to connect individual parts of the research.*

## 4.1 Abstract

Operando X-ray absorption spectroscopy identified that the concentration of  $\text{Fe}^{2+}$  species in the operating state-of-the-art Pt- $\text{FeO}_x$  catalysts quantitatively correlates to their preferential carbon monoxide oxidation steady-state reaction rate at ambient temperature. Deactivation of such catalysts with time on stream originates from irreversible oxidation of active  $\text{Fe}^{2+}$  sites. The active  $\text{Fe}^{2+}$  species are presumably  $\text{Fe}^{+2}\text{O}^{-2}$  clusters in contact with platinum nanoparticles; they coexist with spectator trivalent oxidic iron ( $\text{Fe}^{3+}$ ) and metallic iron ( $\text{Fe}^0$ ) partially alloyed with platinum. The concentration of active sites and, therefore, the catalyst activity strongly depend on the pretreatment conditions.  $\text{Fe}^{2+}$  is the resting state of the active sites in the preferential carbon monoxide oxidation cycle.

## 4.2 Introduction

Humanity faces unprecedented challenges related to increasingly growing carbon dioxide emissions and global energy consumption. We rely on hydrocarbon energy and burn more fossil fuels than ever before in human history.<sup>1</sup> Widely used coke, oil, and gas combustion transform chemical energy stored in C-C and C-H bonds into thermal energy with low efficiency. Moreover, this combustion leads to an uncontrollable release of carbon dioxide. Pure green hydrogen is an energy source that can eliminate uncontrolled carbon dioxide emissions and inefficient combustion of hydrocarbons.<sup>2</sup> Energy from renewable sources, natural gas, and hydrocarbons can instead be stored as hydrogen gas. Hydrogen produced in this way could be used to create electricity with much higher control over the entire process using hydrogen fuel cells or to synthesize ammonia and other valuable chemicals.<sup>3-5</sup>

Preferential carbon monoxide oxidation in the presence of hydrogen (PROX) is of great importance for the implementation of fuel cells and other modern hydrogen-based systems. Catalysts required for this reaction must purify hydrogen from the traces of poisonous carbon monoxide, which deactivates the fuel cell anode and is also unwanted in hydrogen gas used for ammonia production.<sup>6</sup> PROX catalysts must oxidize carbon monoxide using molecular oxygen from air close to ambient temperature.<sup>6</sup> PROX requires a redox-active phase or site, which is able to activate molecular oxygen at ambient temperature, and an additional site to activate carbon monoxide.<sup>7</sup>

For this reason, bimetallic catalysts containing noble metal activating carbon monoxide and a redox-active 3d metal oxide show the highest activities in the PROX reaction. Iron, nickel, cerium, or titanium oxides in combination with gold or platinum nanoparticles show one of the highest reported PROX activities in comparison to other bimetallic systems.<sup>7-9</sup> A lack of knowledge of the nature of active sites in these catalysts results in an inability to prevent the rapid deactivation of these catalysts under PROX. Their activity drops significantly during the first several hours of on-stream operation.<sup>9,10</sup> This significantly limits the development of commercially viable PROX catalysts.

Therefore the main goal of this study was to determine the reason for the deactivation of bimetallic PROX catalysts, for which we focused on the Pt-Fe system and the mechanism of this reaction. Despite multiple experimental and theoretical studies on the PROX reaction over Pt-Fe catalysts, the reaction mechanism remains controversially discussed. According to the experimentally observed oxygen reaction order for the state-of-the-art catalysts, which is close to unity, the PROX reaction rate at ambient temperature is limited by oxygen activation.<sup>11</sup> This suggests that the sites activating oxygen under PROX conditions must be mainly reduced (not completely covered with oxygen in the resting state). At the same time, the most recent theoretical models of PROX over Pt-Fe systems propose that the resting state of the sites activating oxygen is rather  $\text{Fe}^{3+}$  in the form of oxides or hydroxide-like species.<sup>11,12</sup> Recent computational models predict activation energies of more than  $50 \text{ kJ mol}^{-1}$ , which contradict experimental apparent activation energies of about  $10 \text{ kJ mol}^{-1}$  over the state-of-the-art Pt- $\text{FeO}_x$  catalysts.<sup>11,12</sup> Also, some works propose platinum subnanometer-sized clusters or Pt-Fe alloys instead of oxides to form active species participating in oxygen activation.<sup>13-17</sup> Because iron in the working catalyst can coexist in multiple states ( $\text{Fe}^0$ ,  $\text{Fe}^{2+}$ , and  $\text{Fe}^{3+}$ ), it is difficult to distinguish active species from spectators. As was demonstrated in Chapter 3, carbon monoxide is activated on platinum, while iron activates oxygen at the same time.<sup>8,11,18</sup>

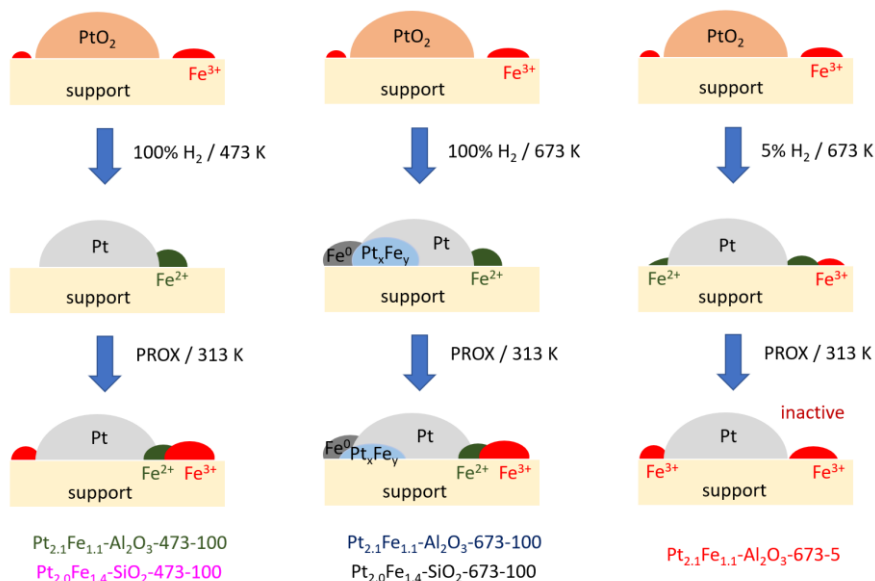
Probing catalytic systems using X-ray absorption spectroscopy (XAS) under operating conditions with constant monitoring of conversion and selectivity allowed us to establish quantitative correlations between the atomic structure of the catalytic sites and the catalytic activity. In Chapter 3, we have shown that operando XAS allows observing various iron species in supported Pt- $\text{FeO}_x$  catalysts and identifying the redox active ones involved in carbon monoxide oxidation at above  $360 \text{ K}$ .<sup>18</sup>

Herein, we prepared a series of supported Pt-FeO<sub>x</sub> catalysts with similar metal loadings on  $\gamma$ -Al<sub>2</sub>O<sub>3</sub> and amorphous SiO<sub>2</sub> and found that their PROX activity strongly depends on the activation procedure in hydrogen, namely concentration of hydrogen and temperature. We applied operando XAS at the Fe K- and Pt L<sub>3</sub>-edges to obtain a correlation between the state of iron in these Pt-FeO<sub>x</sub> catalysts under PROX conditions and the catalytic activity at ambient temperature. For the most active catalysts, the concentration of Fe<sup>2+</sup> linearly correlates with the PROX activity, suggesting that Fe<sup>2+</sup> is the resting state of the PROX-active sites.

## 4.3 Results and Discussion

### 4.3.1 Pretreatment Strategies

Impregnated and calcined 2.1 wt.% Pt-1.1 wt.% Fe/ $\gamma$ -Al<sub>2</sub>O<sub>3</sub> (Pt<sub>2.1</sub>Fe<sub>1.1</sub>-Al<sub>2</sub>O<sub>3</sub>) and 2.0 wt.% Pt-1.4 wt.% Fe/SiO<sub>2</sub> (Pt<sub>2.0</sub>Fe<sub>1.4</sub>-SiO<sub>2</sub>) catalysts were tested in the PROX reaction after different activating pretreatments in a flow of hydrogen. Iron concentrations were increased by a factor of ~2 compared to Chapter 1 to increase platinum-iron interaction, improve activity and boost catalytic rate. Instead of sequential impregnation as in Chapter 1, we did not calcine the samples separately at 473 - 673 K between impregnation with platinum and iron salts. Monometallic reference samples, 2.0 wt.% Pt/ $\gamma$ -Al<sub>2</sub>O<sub>3</sub> (Pt<sub>2.0</sub>-Al<sub>2</sub>O<sub>3</sub>) and 2.0 wt.% Pt/SiO<sub>2</sub> (Pt<sub>2.0</sub>-SiO<sub>2</sub>), were obtained in a similar way as bimetallic compositions, albeit without any added iron (**Table S2-1**; **Scheme 4-1**). Each experiment started with a freshly calcined catalyst, which was then heated to the corresponding reduction temperature in a flow of hydrogen at a rate of 10 K min<sup>-1</sup>, and held for 20 min before cooling down to 313 K under a hydrogen atmosphere. Before the kinetic tests, all as-reduced catalysts were kept for 1 h under a PROX reaction mixture (40 vol.% H<sub>2</sub>, 5 vol.% CO, and 2 vol.% O<sub>2</sub>) to stabilize their activity. **Scheme 4-1** provides a schematic visualization of the state of the catalysts during the different preparation and testing conditions. Samples are designated as in other chapters: Pt<sub>2.1</sub>Fe<sub>1.1</sub>-Al<sub>2</sub>O<sub>3</sub>- (reduction T, K)-(H<sub>2</sub> vol.% during reduction).



Scheme 4-1. Proposed composition of Pt-Fe catalysts formed after reduction under a) 100 vol.% H<sub>2</sub> at 473 K, b) 100 % H<sub>2</sub> at 673 K, c) 5 vol.% H<sub>2</sub> at 673 K during various studied pretreatments and reaction steps.

Monometallic Pt<sub>2.0</sub>-Al<sub>2</sub>O<sub>3</sub>-673-100 and Pt<sub>2.0</sub>-SiO<sub>2</sub>-673-100 catalysts are hardly active in the PROX reaction at ambient temperature (**Figure 4-1a**) and show the apparent activation energies of 61 and 67 kJ mol<sup>-1</sup> (**Figure 4-1a**), respectively. These catalysts also start to oxidize hydrogen above 413 K; the carbon monoxide selectivity drops from 100 % (±2 %) at 413 K to 40 % (±2 %) at 423 K.

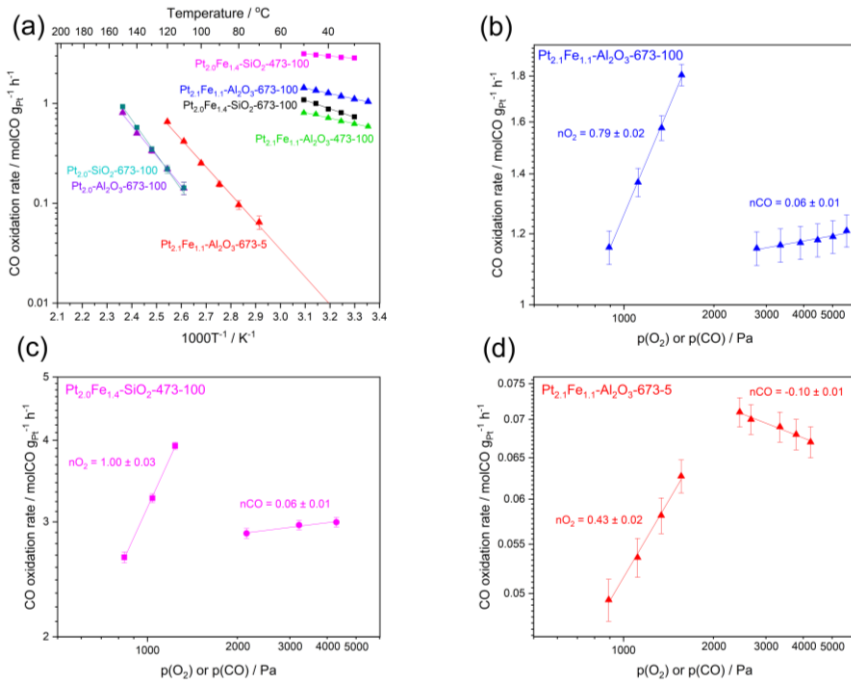


Figure 4-1. a) Arrhenius plots of the PROX activity of different catalysts measured in the operando reactor cell. b-d) Double-logarithmic plots of the PROX activity versus the partial pressures of carbon monoxide and oxygen at 313 K for Pt<sub>2.1</sub>Fe<sub>1.1</sub>-Al<sub>2</sub>O<sub>3</sub>-673-100 (b), Pt<sub>2.0</sub>Fe<sub>1.4</sub>-SiO<sub>2</sub>-473-100 (c), and Pt<sub>2.1</sub>Fe<sub>1.1</sub>-Al<sub>2</sub>O<sub>3</sub>-673-5 catalysts (d). The corresponding reaction orders are given next to the lines.

Bimetallic catalysts have significantly higher PROX activities, which greatly depend on the pretreatment. Reduction temperature (473 or 673 K) and hydrogen concentration (5 vol.% or 100 vol.%) constitute an individual label of each bimetallic Pt-Fe sample. For instance, Pt<sub>2.1</sub>Fe<sub>1.1</sub>-Al<sub>2</sub>O<sub>3</sub>-673-5 catalyst was pretreated under 5 vol.% H<sub>2</sub> (5) at 673 K (673). This particular sample is not active in the PROX reaction at room temperature (**Figure 4-1a**) and shows an apparent activation energy of 56 kJ mol<sup>-1</sup>, which is similar to the reported activation energies for catalysts containing only platinum.

Reduction under 100 vol.% H<sub>2</sub> (at 473-673 K) not only results in a high PROX activity of various Pt<sub>2.1</sub>Fe<sub>1.1</sub>-Al<sub>2</sub>O<sub>3</sub> and Pt<sub>2.0</sub>Fe<sub>1.4</sub>-SiO<sub>2</sub> catalysts at ambient temperature but also significantly decreases



their apparent activation energies (**Figure 4-1a**). The observed reaction rates are similar to those for the state-of-the-art PROX catalysts reported in the literature (**Table S2-2**); the same observation is valid for the apparent activation energies of  $10 \text{ kJ mol}^{-1}$  for  $\text{Pt}_{2.0}\text{Fe}_{1.4}\text{-SiO}_2\text{-473-100}$ ,  $16 \text{ kJ mol}^{-1}$  for  $\text{Pt}_{2.0}\text{Fe}_{1.4}\text{-SiO}_2\text{-673-100}$ ,  $10 \text{ kJ mol}^{-1}$  for  $\text{Pt}_{2.1}\text{Fe}_{1.1}\text{-Al}_2\text{O}_3\text{-673-100}$ , and  $11 \text{ kJ mol}^{-1}$  for  $\text{Pt}_{2.1}\text{Fe}_{1.1}\text{-Al}_2\text{O}_3\text{-473-100}$ .<sup>11-13,19</sup> Silica-supported  $\text{Pt}_{2.0}\text{Fe}_{1.4}\text{-SiO}_2\text{-473-100}$  showed the highest PROX reaction rate of  $3.0 \text{ molCO gPt}^{-1} \text{ h}^{-1}$  at 313 K (**Figure 4-1a**). The reduction temperature had a slightly different effect on alumina-supported catalysts compared to silica-supported ones (**Figure 4-1a**).

For  $\text{Pt}_{2.0}\text{Fe}_{1.4}\text{-SiO}_2$  and  $\text{Pt}_{2.1}\text{Fe}_{1.1}\text{-Al}_2\text{O}_3$  catalysts reduced under 100 %  $\text{H}_2$ , PROX reaction orders and activities (**Figure 4-1b-d**) are close to the state-of-the-art supported Pt- $\text{FeO}_x$  catalysts reported in the literature (**Table S2-2**).<sup>12-14,20,21</sup> Carbon monoxide reaction order is close to zero for all studied bimetallic catalysts, which is consistent with the results in Chapter 3, showing that under reaction conditions, platinum sites are saturated with carbon monoxide (**Figure 4-1b-d**; **Table S2-2**).<sup>11, 18</sup> In contrast,  $\text{Pt}_{2.0}\text{-Al}_2\text{O}_3\text{-673-100}$  and  $\text{Pt}_{2.0}\text{-SiO}_2\text{-673-100}$  catalysts show a typical negative carbon monoxide reaction order of approximately -0.4, which is associated with competitive adsorption of oxygen and carbon monoxide on the metallic platinum surface (**Figure S2-1**).<sup>22</sup>

It is clear that bimetallic catalysts reduced under 100 %  $\text{H}_2$  at 473-673 K demonstrate a different oxygen activation mechanism compared to the bimetallic catalyst reduced under 5 vol.%  $\text{H}_2$  ( $\text{Pt}_{2.1}\text{Fe}_{1.1}\text{-Al}_2\text{O}_3\text{-673-5}$ ) and monometallic platinum catalysts. The reduction temperature and nature of the support are additional factors influencing the PROX activity (**Figure 4-1a**). Sample  $\text{Pt}_{2.1}\text{Fe}_{1.1}\text{-Al}_2\text{O}_3\text{-673-5}$  has a very similar carbon monoxide oxidation activity when compared to the carbon monoxide oxidation activity in the absence of hydrogen for  $\text{Pt}_{2.1}\text{Fe}_{0.7}\text{-Al}_2\text{O}_3\text{-673-5}$  from Chapter 3 (**Figure S2-2**). The activity of  $\text{Pt}_{2.0}\text{-Al}_2\text{O}_3\text{-673-100}$  under PROX at above 373 K is higher than for  $\text{Pt}_{2.0}\text{-Al}_2\text{O}_3\text{-673-5}$  during carbon monoxide oxidation (**Figure S2-2**). This can be explained by the hydrogen-assisted carbon monoxide oxidation and the formation of water due to the drop in selectivity.

Time-on-stream studies at high carbon monoxide conversion in a tubular reactor at 353 K (**Figure S2-3**) were performed at the same conditions as in the original work by Qiao et al.<sup>14</sup> As carbon monoxide concentration drops significantly across the catalyst bed under the realistic operating conditions, carbon monoxide conversion and selectivity are strongly linked under this reaction regime.<sup>14</sup>  $\text{Pt}_{2.0}\text{Fe}_{1.4}\text{-SiO}_2\text{-473-100}$  outperforms atomically dispersed platinum catalyst showing selectivity to carbon monoxide >80 % with 97 % carbon monoxide conversion compared to the selectivity of <50 % with  $\approx 97$  % conversion measured by Qiao et al.<sup>14</sup>  $\text{Pt}_{2.1}\text{Fe}_{1.1}\text{-Al}_2\text{O}_3\text{-673-100}$  catalyst, which also has a high specific rate at low carbon monoxide conversion (**Table S2-3**), loses in its reaction rate at high conversion levels showing 75 % carbon monoxide conversion with just 66 % selectivity.

According to scanning transmission electron microscopy (STEM), all catalysts activated under specific conditions in hydrogen contain platinum nanoparticles. The corresponding size and platinum dispersion ( $D_{\text{TEM}}$ ) values are 1.0 nm ( $D_{\text{TEM}}=0.8$ ) for  $\text{Pt}_{2.0}\text{-Al}_2\text{O}_3\text{-673-100}$ , 1.7 nm (0.4) for  $\text{Pt}_{2.0}\text{-SiO}_2\text{-673-100}$ , 1.1 nm (0.7) for  $\text{Pt}_{2.1}\text{Fe}_{1.1}\text{-Al}_2\text{O}_3\text{-673-5}$ , 1.3 nm (0.4) for  $\text{Pt}_{2.1}\text{Fe}_{1.1}\text{-Al}_2\text{O}_3\text{-673-100}$ , and 2.1 nm (0.3) for  $\text{Pt}_{2.0}\text{Fe}_{1.4}\text{-SiO}_2\text{-473-100}$  (**Figure 4-2**; **Table S2-1**). Carbon monoxide chemisorption experiments gave a similar trend of platinum dispersion ( $D_{\text{CO}}$ ): 0.6 for  $\text{Pt}_{2.0}\text{-Al}_2\text{O}_3\text{-673-100}$ , 0.4 for  $\text{Pt}_{2.0}\text{-SiO}_2\text{-673-100}$ , 0.6 for  $\text{Pt}_{2.1}\text{Fe}_{1.1}\text{-Al}_2\text{O}_3\text{-673-5}$ , 0.3 for  $\text{Pt}_{2.1}\text{Fe}_{1.1}\text{-Al}_2\text{O}_3\text{-673-100}$ , and 0.4 for  $\text{Pt}_{2.0}\text{Fe}_{1.4}\text{-SiO}_2\text{-473-100}$  catalysts (**Table S2-1**). Platinum surface area is overestimated by STEM, especially for  $\text{Pt}_{2.1}\text{Fe}_{1.1}\text{-Al}_2\text{O}_3\text{-673-100}$  (**Table S2-1**). This leads us to believe that iron oxides partially cover the surface of platinum nanoparticles.

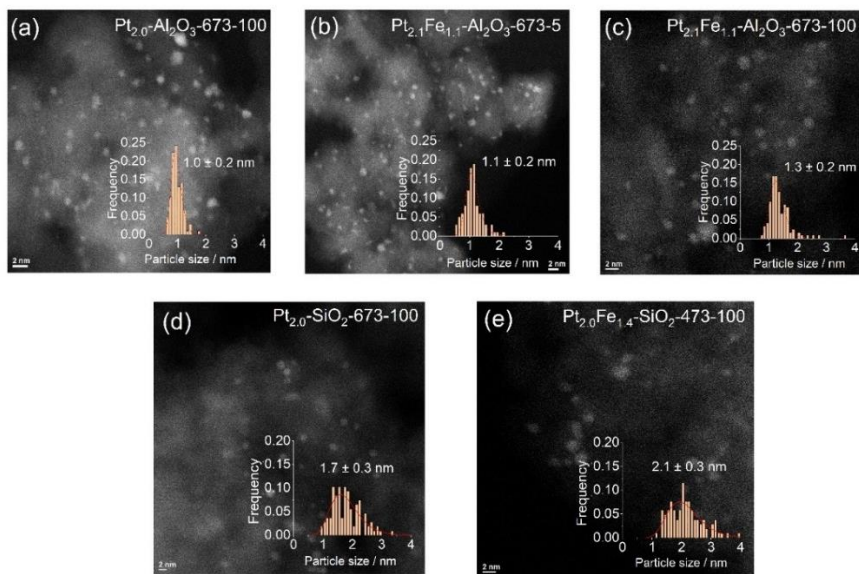


Figure 4-2. STEM images and particle size distributions for a)  $\text{Pt}_{2.0}\text{-Al}_2\text{O}_3\text{-673-100}$ , b)  $\text{Pt}_{2.1}\text{Fe}_{1.1}\text{-Al}_2\text{O}_3\text{-673-5}$ , c)  $\text{Pt}_{2.1}\text{Fe}_{1.1}\text{-Al}_2\text{O}_3\text{-673-100}$ , d)  $\text{Pt}_{2.0}\text{-SiO}_2\text{-673-100}$ , and e)  $\text{Pt}_{2.0}\text{Fe}_{1.4}\text{-SiO}_2\text{-473-100}$  catalysts.

#### 4.3.2 In situ FTIR

Complimentary in situ Fourier transform infrared spectroscopy (FTIR) of adsorbed carbon monoxide evidenced the main FTIR peak associated with linearly adsorbed carbon monoxide at  $2074\text{ cm}^{-1}$  for  $\text{Pt}_{2.0}\text{-Al}_2\text{O}_3\text{-673-100}$  (Figure 3a) and  $2072\text{ cm}^{-1}$  for  $\text{Pt}_{2.1}\text{Fe}_{1.1}\text{-Al}_2\text{O}_3\text{-673-5}$  (Figure 4-3b), which are typical for carbon monoxide adsorption on nano-sized metallic platinum nanoparticles supported on alumina or iron oxide.<sup>23-25</sup> A redshift of the linearly adsorbed carbon monoxide maximum to  $2063\text{ cm}^{-1}$  is observed for  $\text{Pt}_{2.1}\text{Fe}_{1.1}\text{-Al}_2\text{O}_3\text{-673-100}$  (Figure 4-3c), due to a more electron-rich state of platinum.<sup>15,17,25</sup> Detailed fit of the linearly adsorbed carbon monoxide peak using pseudo-Voigt functions for  $\text{Pt}_{2.1}\text{Fe}_{1.1}\text{-Al}_2\text{O}_3\text{-673-100}$  reveals that observed redshift can, in fact, manifest as an additional peak at  $2049\text{ cm}^{-1}$  having a full-width at half maximum (FWHM) of  $46\text{ cm}^{-1}$  with the other peak at  $2073\text{ cm}^{-1}$  having FWHM of  $28\text{ cm}^{-1}$  (Figure 4-3c; Figure S2-4; Table S2-4). Treatment of this catalyst at 673 K in hydrogen results in the formation of the Pt-FeO interface with  $\text{Fe}^0$  partially alloyed with platinum. The presence of this interface affects the carbon monoxide bonding energy as iron, a less electronegative element, donates electron density to platinum. This is consistent with the literature; alloyed platinum particles incorporate iron, grow larger, and, thus, have a more electron-rich state.<sup>15,17,25</sup> It is worth noticing that both  $\text{Pt}_{2.0}\text{-Al}_2\text{O}_3\text{-673-100}$  and  $\text{Pt}_{2.1}\text{Fe}_{1.1}\text{-Al}_2\text{O}_3\text{-673-5}$  catalysts show broad peaks due to the small size of platinum nanoparticles with broad size distributions, and, thus, cannot be adequately fitted using just 3 peaks, as in the model (Figure 4-3c; Figure S2-3; Table S2-4).

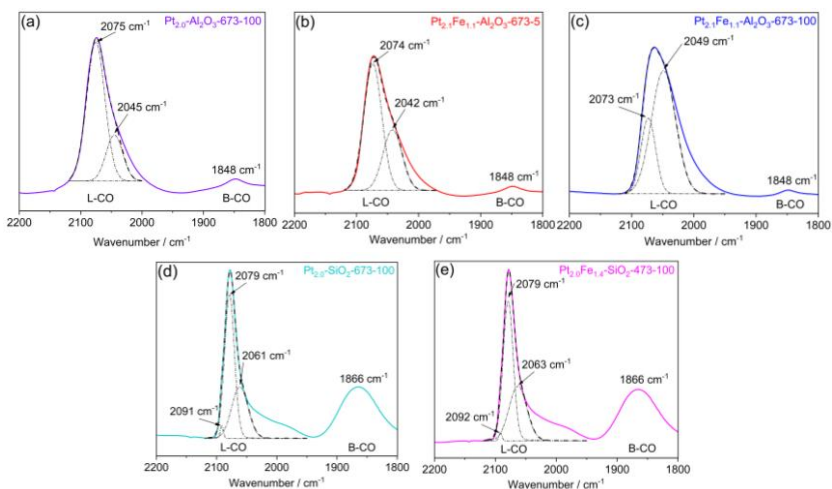


Figure 4-3. Fitted in situ FTIR spectra of carbon monoxide adsorption at 300 K on a)  $\text{Pt}_{2.0}\text{-Al}_2\text{O}_3\text{-673-100}$ , b)  $\text{Pt}_{2.1}\text{Fe}_{1.1}\text{-Al}_2\text{O}_3\text{-673-5}$ , c)  $\text{Pt}_{2.1}\text{Fe}_{1.1}\text{-Al}_2\text{O}_3\text{-673-100}$ , d)  $\text{Pt}_{2.0}\text{-SiO}_2\text{-673-100}$ , and e)  $\text{Pt}_{2.0}\text{Fe}_{1.4}\text{-SiO}_2\text{-473-100}$  catalysts. Key: experiment: experimental data (solid line), fit (dashed line), separate fit components (dashed-dotted line).

$\text{Pt}_{2.0}\text{-SiO}_2\text{-673-100}$  (Figure 4-3d; Figure S2-4; Table S2-4) and  $\text{Pt}_{2.0}\text{Fe}_{1.4}\text{-SiO}_2\text{-473-100}$  (Figure 4-3e; Figure S2-4; Table S2-4) contain two main sites for linear adsorption of carbon monoxide: electro deficient platinum attributed to the peak at  $2079\text{ cm}^{-1}$  (peak FWHM  $\approx 19\text{ cm}^{-1}$ ), and purely metallic platinum corresponding to the peak at  $2061\text{-}2063\text{ cm}^{-1}$  (peak width ca.  $32\text{-}34\text{ cm}^{-1}$ ). At first glance, the presence of these sharp ( $<25\text{ cm}^{-1}$ ) features of  $\text{Pt}^{\delta+}$  sites at  $2074\text{-}2079\text{ cm}^{-1}$  for alumina- and silica-supported catalysts can suggest that these are all atomically dispersed as similar peaks were obtained by Qiao et al. for the single atom platinum on iron oxide.<sup>14</sup> The main difference lies, however, in the presence of bridging carbon monoxide adsorption peaks only existing for platinum nanoparticles. These bands are visible for both alumina- ( $1848\text{ cm}^{-1}$ ) and silica-supported catalysts ( $1866\text{ cm}^{-1}$ ), as shown in Figure 4-3 and Figure S2-4.<sup>17,23</sup> Detailed comparison with the literature shows that the  $\approx 2079\text{ cm}^{-1}$  peak is typical for platinum nanoparticles of about 1-3 nm on silica support with narrow size distribution.<sup>12,26</sup> As will be confirmed later by in situ Pt  $L_3$ -edge XAS data, platinum indeed exists in a fully metallic state for all catalysts. Nonetheless, a narrow peak at  $2091\text{-}2092\text{ cm}^{-1}$  observed only for silica-supported catalysts (peak FWHM  $\approx 6\text{ cm}^{-1}$ ) is a clear manifestation of a small fraction (1 % of the total peak area (Figure 4-3d,e; Figure S2-4; Table S2-4)) of atomically dispersed platinum or platinum clusters with  $<10$  atoms.<sup>23, 27</sup> However, the atomically dispersed platinum sites are not likely responsible for the primary PROX mechanism for  $\text{Pt}_{2.0}\text{Fe}_{1.4}\text{-SiO}_2\text{-473-100}$ , as the specific reaction rate of platinum in this catalyst is at least an order of magnitude higher than that of the atomically dispersed platinum (Figure 4-3; Figure S2-4; Table S2-3), while the majority of platinum atoms in  $\text{Pt}_{2.0}\text{Fe}_{1.4}\text{-SiO}_2\text{-473-100}$  catalyst are metallic.<sup>14</sup>

### 4.3.3 In situ XAS after Reduction

Partial alloying in active  $\text{Pt}_{2.1}\text{Fe}_{1.1}\text{-Al}_2\text{O}_3\text{-673-100}$  was confirmed by in situ Fe K-edge extended X-ray absorption fine structure (EXAFS) spectroscopy measured at 313 K in hydrogen after reduction in the operando reactor cell. **Figure 4-4** shows the Fe K-edge EXAFS spectra for two iron-containing catalysts on alumina reduced at 673 K at different hydrogen concentrations in comparison with the Pt-Fe/C alloy reference. The distinction between the Fe K-edge EXAFS of active  $\text{Pt}_{2.1}\text{Fe}_{1.1}\text{-Al}_2\text{O}_3\text{-673-100}$  and inactive  $\text{Pt}_{2.1}\text{Fe}_{1.1}\text{-Al}_2\text{O}_3\text{-673-5}$  lies in the completely different structure of the first coordination shell of iron. Reduction under 5 vol.%  $\text{H}_2$  for inactive  $\text{Pt}_{2.1}\text{Fe}_{1.1}\text{-Al}_2\text{O}_3\text{-673-5}$  results in a first coordination shell peak at 1.5 Å similar to the Fe-O shell, whereas the use of 100 %  $\text{H}_2$  for active  $\text{Pt}_{2.1}\text{Fe}_{1.1}\text{-Al}_2\text{O}_3\text{-673-100}$  gives rise to the metallic iron shell at 2.2 Å, close to the position of the corresponding Fe-Fe shell for the Pt-Fe/C alloy reference (**Figure 4-4**).<sup>28,29</sup> Oscillations of the imaginary part of the Fourier-transformed Fe K-edge EXAFS of  $\text{Pt}_{2.1}\text{Fe}_{1.1}\text{-Al}_2\text{O}_3\text{-673-100}$  align with that of the reference alloy and not pure  $\text{Fe}^0$  (**Figure 4-4b**).

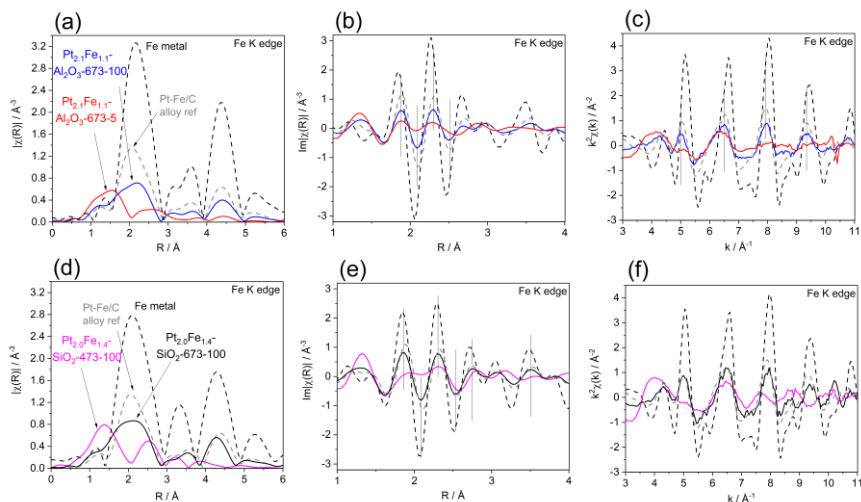


Figure 4-4. a,d) Modulus and b,e) imaginary parts of the Fourier-transformed Fe K-edge EXAFS of  $\text{Pt}_{2.1}\text{Fe}_{1.1}\text{-Al}_2\text{O}_3\text{-673-100}$ ,  $\text{Pt}_{2.1}\text{Fe}_{1.1}\text{-Al}_2\text{O}_3\text{-673-5}$ ,  $\text{Pt}_{2.0}\text{Fe}_{1.4}\text{-SiO}_2\text{-673-100}$ , and  $\text{Pt}_{2.0}\text{Fe}_{1.4}\text{-SiO}_2\text{-473-100}$  (solid lines), as well as references: Pt-Fe/C and Fe (dashed lines). c,f) Fe K-edge EXAFS in  $k$ -space of  $\text{Pt}_{2.1}\text{Fe}_{1.1}\text{-Al}_2\text{O}_3\text{-673-100}$ ,  $\text{Pt}_{2.1}\text{Fe}_{1.1}\text{-Al}_2\text{O}_3\text{-673-5}$ ,  $\text{Pt}_{2.0}\text{Fe}_{1.4}\text{-SiO}_2\text{-673-100}$ , and  $\text{Pt}_{2.0}\text{Fe}_{1.4}\text{-SiO}_2\text{-473-100}$  (solid lines), as well as references: Pt-Fe/C and Fe (dashed lines). All spectra were measured at 313 K under hydrogen after reduction. All spectra are  $k^2$ -weighted. Black vertical lines are intended to guide the eye.

In situ Pt  $L_3$ -edge EXAFS corroborates the formation of a partially alloyed  $\text{Fe}^0$ . Both  $\text{Pt}_{2.0}\text{-Al}_2\text{O}_3\text{-673-100}$  and inactive  $\text{Pt}_{2.1}\text{Fe}_{1.1}\text{-Al}_2\text{O}_3\text{-673-5}$  demonstrate only a Pt-Pt shell specific for metallic platinum nanoparticles with a characteristic profile of the Fourier-transformed Pt  $L_3$ -edge EXAFS (**Figure 4-5a-**

c). Pt L<sub>3</sub>-edge EXAFS fit yields the nearest Pt-Pt coordination numbers of ca. 10, which, according to a simple spherical model proposed by Calvin et al., correspond to nanoparticles of 2.46 nm in size.<sup>30</sup> The model of Frenkel et al. used to estimate the Pt-Pt coordination number from a particle size distribution yields coordination numbers of 7.89 for Pt<sub>2.1</sub>Fe<sub>1.1</sub>-Al<sub>2</sub>O<sub>3</sub>-673-5, 8.38 for Pt<sub>2.1</sub>Fe<sub>1.1</sub>-Al<sub>2</sub>O<sub>3</sub>-673-100, and 9.56 for Pt<sub>2.0</sub>Fe<sub>1.4</sub>-SiO<sub>2</sub>-473-100.<sup>31</sup> Platinum particle sizes for alumina-supported catalysts derived from Pt L<sub>3</sub>-edge EXAFS significantly deviate from those measured by STEM. As evident from the literature, such particles with 1.1-1.3 nm mean diameter cannot be described by cubooctahedral or spherical models used here. It is known, however, that EXAFS analysis can overestimate particle size for platinum nanoparticles of such size.<sup>31,32</sup>

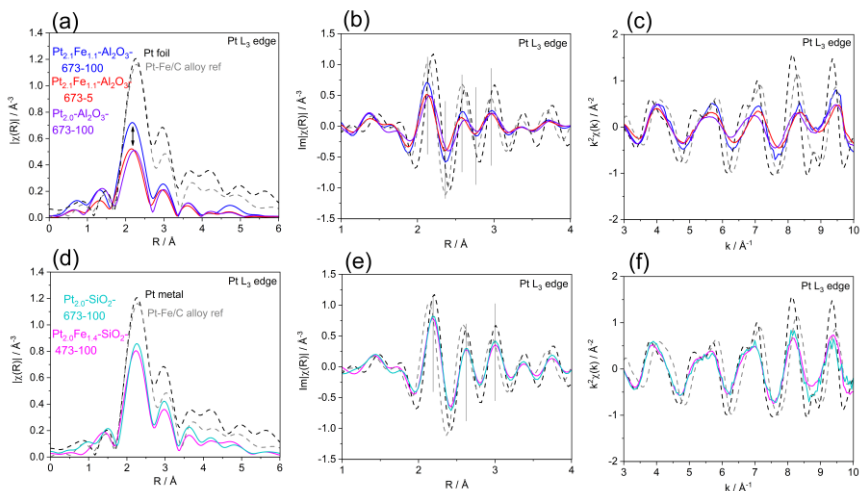


Figure 4-5. a,d) Modulus and b,e) imaginary parts of the Fourier-transformed Pt L<sub>3</sub>-edge EXAFS of Pt<sub>2.1</sub>Fe<sub>1.1</sub>-Al<sub>2</sub>O<sub>3</sub>-673-100, Pt<sub>2.1</sub>Fe<sub>1.1</sub>-Al<sub>2</sub>O<sub>3</sub>-673-5, Pt<sub>2.0</sub>-Al<sub>2</sub>O<sub>3</sub>-673-100, Pt<sub>2.0</sub>Fe<sub>1.4</sub>-SiO<sub>2</sub>-473-100, and Pt<sub>2.0</sub>-SiO<sub>2</sub>-673-100 (solid lines), as well as references: Pt-Fe/C and Pt (dashed lines). c,f) Fe K-edge EXAFS in k-space of Pt<sub>2.1</sub>Fe<sub>1.1</sub>-Al<sub>2</sub>O<sub>3</sub>-673-100, Pt<sub>2.1</sub>Fe<sub>1.1</sub>-Al<sub>2</sub>O<sub>3</sub>-673-5, Pt<sub>2.0</sub>Fe<sub>1.4</sub>-SiO<sub>2</sub>-673-100, and Pt<sub>2.0</sub>Fe<sub>1.4</sub>-SiO<sub>2</sub>-473-100 (solid lines), as well as references: Pt-Fe/C and Fe (dashed lines). All spectra were measured at 313 K under hydrogen after reduction. All spectra are k<sup>2</sup>-weighted. Black vertical lines are intended to guide the eye.

Fourier-transformed Pt L<sub>3</sub>-edge EXAFS profile becomes asymmetric for the active Pt<sub>2.1</sub>Fe<sub>1.1</sub>-Al<sub>2</sub>O<sub>3</sub>-673-100, which is confirmed to be associated with the formation of the Pt-Fe bond through the Pt L<sub>3</sub>-edge EXAFS fitting (**Figure 4-5a,b**; **Figure S2-5**; **Table S2-5**).<sup>12,28,29</sup> Imaginary part of the Fourier-transformed Pt L<sub>3</sub>-edge EXAFS for Pt<sub>2.1</sub>Fe<sub>1.1</sub>-Al<sub>2</sub>O<sub>3</sub>-673-100 is similar to the one from alloyed reference Pt-Fe nanoparticles, not pure Fe<sup>0</sup> (**Figure 4-5b**). An attempt to fit Pt<sub>2.1</sub>Fe<sub>1.1</sub>-Al<sub>2</sub>O<sub>3</sub>-673-100 Pt L<sub>3</sub>-edge EXAFS without the Pt-Fe shell was not successful (**Figure S2-4 d-f**; **Table S2-5**). Thus, the reduction of the bimetallic catalyst supported on alumina with higher hydrogen concentration facilitates iron and platinum aggregation and results in a partially alloyed state at 673 K. All observed trends are depicted in **Scheme 4-1**, showing a strong influence of the pretreatment conditions on the catalytic activity.

In situ Fe K-edge X-ray absorption near edge structure (XANES) confirms that iron in active  $\text{Pt}_{2.1}\text{Fe}_{1.1}\text{-Al}_2\text{O}_3\text{-673-100}$  catalyst is more reduced than in inactive  $\text{Pt}_{2.1}\text{Fe}_{1.1}\text{-Al}_2\text{O}_3\text{-673-5}$ . Active  $\text{Pt}_{2.1}\text{Fe}_{1.1}\text{-Al}_2\text{O}_3\text{-673-100}$  shows a distinct pre-edge feature typical for  $\text{Fe}^0$  at 7115 eV (**Figure S2-6a**). Comparison with the Fe K-edge XANES of  $\text{Fe}_2\text{O}_3$  and FeO references shows that both catalysts may as well contain a significant fraction of iron in oxidized form (Figure S5a,b). At the same time, Pt  $L_{3\text{-edge}}$  XAS (**Figure 4-5 a-c**; **Figure S2-6c**) confirms that platinum on all alumina-supported catalysts is in a metallic state. This is also true for the silica-supported catalysts, as can be seen from **Figure 4-5 d-f** and **Figure S2-6d**. Nevertheless, Fe K-edge and Pt  $L_{3\text{-edge}}$  EXAFS data (**Figures 4-4 d-f** and **4-5 d-f**; **Tables S2-5** and **S2-6**) show that the most active  $\text{Pt}_{2.0}\text{Fe}_{1.4}\text{-SiO}_2\text{-473-100}$  catalyst does not contain metallic iron or alloy with platinum after reduction.  $\text{Pt}_{2.0}\text{-SiO}_2\text{-673-100}$  and  $\text{Pt}_{2.0}\text{Fe}_{1.4}\text{-SiO}_2\text{-473-100}$  Pt  $L_{3\text{-edge}}$  spectra are also similar (**Figure 4-5 d-f**).

The linear combination fitting of Fe K-edge XANES spectra confirms the EXAFS observations and does not find any Pt-Fe alloyed components in the most active  $\text{Pt}_{2.0}\text{Fe}_{1.4}\text{-SiO}_2\text{-473-100}$ ; the main component is  $\text{Fe}^{2+}$  with a XANES signature similar to oxidic  $\text{Fe}^{2+}$  as in a crystalline FeO (**Figure S2-7c**). However, the catalyst reduced at higher temperature ( $\text{Pt}_{2.0}\text{Fe}_{1.4}\text{-SiO}_2\text{-673-100}$ ) shows a 71 % fraction of the  $\text{Fe}^0$  in the partially alloyed state and just 3 % of the  $\text{Fe}^{2+}$  (FeO) component (**Figure S2-7f**). The partially alloyed Fe-Pt shell is also pronounced in Fe K-edge EXAFS of  $\text{Pt}_{2.0}\text{Fe}_{1.4}\text{-SiO}_2\text{-673-100}$  as shown in **Figure 4-4 d-f**, while  $\text{Pt}_{2.0}\text{Fe}_{1.4}\text{-SiO}_2\text{-473-100}$  shows only a Fe-O shell at 1.4 Å. This highlights the strong influence of pre-reduction conditions on the catalyst state.

#### 4.3.4 Operando XAS under Preferential Carbon Monoxide Oxidation Conditions

To fully understand how the partially alloyed  $\text{Fe}^0$  and other iron structural components behave under PROX conditions, we used operando Fe K-edge and Pt  $L_{3\text{-edge}}$  XAS for probing the electronic state of iron and platinum and simultaneously monitored the PROX activity using an in-line mass spectrometer. We performed this study for the most active  $\text{Pt}_{2.1}\text{Fe}_{1.1}\text{-Al}_2\text{O}_3\text{-673-100}$  and  $\text{Pt}_{2.0}\text{Fe}_{1.4}\text{-SiO}_2\text{-473-100}$  and compared them to the inactive  $\text{Pt}_{2.1}\text{Fe}_{1.1}\text{-Al}_2\text{O}_3\text{-673-5}$ .  $\text{Pt}_{2.1}\text{Fe}_{1.1}\text{-Al}_2\text{O}_3\text{-673-100}$  catalyst was measured three times in a series of separate experiments (1-3). A fresh portion of the catalyst in each experiment was firstly reduced, then cooled to 313 K under 100 vol.%  $\text{H}_2$ , and exposed to the reaction gases afterward. In experiment 1  $\text{Pt}_{2.1}\text{Fe}_{1.1}\text{-Al}_2\text{O}_3\text{-673-100}$  was additionally exposed to 40 vol.%  $\text{H}_2$  and 5 vol.% CO gas mixture. Fe K-edge EXAFS did not show any significant changes under 40 vol.%  $\text{H}_2$  and 5 vol.% CO for different catalysts under study for both imaginary and modulus parts of the Fourier-transformed Fe K-edge EXAFS. (**Figure S2-8**). Pt  $L_{3\text{-edge}}$  XANES demonstrated a characteristic shift to higher energy in platinum 5d electronic structure, associated with the carbon monoxide chemisorption on platinum nanoparticles for alumina-supported catalysts (**Figure S2-9**).<sup>33,34</sup>

Then the catalysts were exposed to the PROX reaction mixture of 40 vol.%  $\text{H}_2$ , 5 vol.% CO, and 2 vol.%  $\text{O}_2$  at the same temperature of 313 K. While the electronic structure of platinum is altered by the carbon monoxide chemisorption, it is not affected by the addition of oxygen to the reaction mixture (**Figure S2-10**). This is consistent with the platinum surface being fully saturated by carbon monoxide (Chapter 3), even in the partially alloyed  $\text{Pt}_{2.1}\text{Fe}_{1.1}\text{-Al}_2\text{O}_3\text{-673-100}$ .<sup>18</sup> Clearly, partial alloying does not allow competitive adsorption of oxygen and carbon monoxide and has no effect on the reaction mechanism. The selectivity towards carbon monoxide oxidation monitored by mass spectrometer was 100 % ( $\pm 2$  %) for all three catalysts under study. According to independent kinetic tests, the hydrogen concentration has no impact on the reaction rate, which suggests that the platinum surface is covered by carbon monoxide and no hydrogen adsorption occurs within the studied temperature range (**Figure S2-11**).

Unlike Pt  $L_{3}$ -edge XAS, the Fe K-edge XAS spectra of the catalysts strongly evolved during PROX. We fitted Fe K-edge XANES using three components: Pt-Fe/C alloy ( $\text{Fe}^0$ ), FeO ( $\text{Fe}^{2+}$ ), and fully oxidized iron ( $\text{Fe}^{3+}$ ; **Figures S2-7 and S2-12; Table S2-7**). Fully oxidized  $\text{Fe}^{3+}$  components were slightly different for silica- and alumina-supported catalysts; they were obtained after the ex situ oxidation of active  $\text{Pt}_{2.0}\text{Fe}_{1.4}\text{-SiO}_2\text{-473-100}$  and  $\text{Pt}_{2.1}\text{Fe}_{1.1}\text{-Al}_2\text{O}_3\text{-673-100}$  under air at 473 K. (**Figure S2-12**).

Platinum promotes the reduction of surface iron oxidic species that are located sufficiently close, as shown in Chapter 3.<sup>18,35</sup> Directly after reduction under hydrogen atmosphere for the active  $\text{Pt}_{2.1}\text{Fe}_{1.1}\text{-Al}_2\text{O}_3\text{-673-100}$ , we observed: 29 %  $\text{Fe}^{2+}$ /61 %  $\text{Fe}^0$ /10 %  $\text{Fe}^{3+}$  in experiment 1, 42 %  $\text{Fe}^{2+}$ /49 %  $\text{Fe}^0$ /9 %  $\text{Fe}^{3+}$  in experiment 2, and 36 %  $\text{Fe}^{2+}$ /41 %  $\text{Fe}^0$ /23 %  $\text{Fe}^{3+}$  in experiment 3 (**Figure 4-6a; Figure S2-7a,c; Table S2-7**), performed with the new portion of the catalyst in each experiment. In experiments 2 and 3,  $\text{Pt}_{2.1}\text{Fe}_{1.1}\text{-Al}_2\text{O}_3\text{-673-100}$  was additionally exposed to inert gas that contained oxygen impurities, which resulted in a lower alloy concentration due to its oxidation. Reduction of active  $\text{Pt}_{2.0}\text{Fe}_{1.4}\text{-SiO}_2\text{-473-100}$  performed at 473 K did not yield  $\text{Fe}^0$  and resulted in just 27 %  $\text{Fe}^{2+}$  (**Figure 4-6b; Figure S2-7c,d; Table S2-7**).

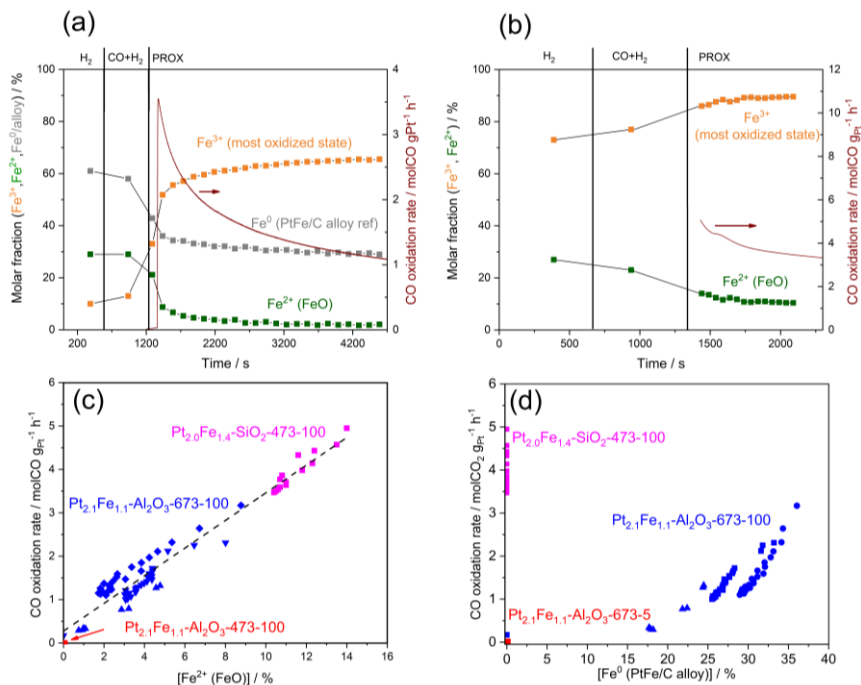


Figure 4-6. a,b) Concentration of  $\text{Fe}^{3+}$ ,  $\text{Fe}^{2+}$ , and  $\text{Fe}^0$  species (determined by XAS) and PROX activity (313 K) measured operando during the deactivation of  $\text{Pt}_{2.1}\text{Fe}_{1.1}\text{-Al}_2\text{O}_3\text{-673-100}$  catalyst (experiment 1) (a) and  $\text{Pt}_{2.0}\text{Fe}_{1.4}\text{-SiO}_2\text{-473-100}$  catalyst (b). c,d) Correlation between the concentrations of  $\text{Fe}^{2+}$  (c) and  $\text{Fe}^0$  (d) and PROX activity at 313 K for  $\text{Pt}_{2.1}\text{Fe}_{1.1}\text{-Al}_2\text{O}_3\text{-673-100}$  (different shapes of blue symbols correspond to three independent experiments),  $\text{Pt}_{2.0}\text{Fe}_{1.4}\text{-SiO}_2\text{-473-100}$  (pink), and  $\text{Pt}_{2.1}\text{Fe}_{1.1}\text{-Al}_2\text{O}_3\text{-673-5}$  (red); least squares fit (dashed line). Gas concentrations are shown as vol.%.



Operando Fe K-edge XANES and EXAFS measured for active Pt<sub>2.1</sub>Fe<sub>1.1</sub>-Al<sub>2</sub>O<sub>3</sub>-673-100 at least 30 min after an introduction of PROX mixture show partial alloy decomposition and significant oxidation of iron (**Figure S2-7b**; **Figure S2-13**); for the inactive Pt<sub>2.1</sub>Fe<sub>1.1</sub>-Al<sub>2</sub>O<sub>3</sub>-673-5 all iron is completely oxidized into Fe<sup>3+</sup> under PROX conditions (**Figures S2-7e** and **S2-13 a-c**, experiment 1). Pt<sub>2.1</sub>Fe<sub>1.1</sub>-Al<sub>2</sub>O<sub>3</sub>-673-100 still retains some fraction of Fe-Pt bonds, but due to the presence of, likely, Fe-Fe bonds, EXAFS fit has high error values (**Figure S2-14 a-c**; **Table S2-6**). An attempt to fit Fe K-edge EXAFS of Pt<sub>2.1</sub>Fe<sub>1.1</sub>-Al<sub>2</sub>O<sub>3</sub>-673-100 using Fe-O and Fe-O-Fe shells exclusively was not successful, as shown in **Figure S2-14 d-f** and **Table S2-6**. For the highly active Pt<sub>2.0</sub>Fe<sub>1.4</sub>-SiO<sub>2</sub>-473-100, the majority of Fe<sup>3+</sup> species is oxidized under PROX. However, 10 % of initial Fe<sup>2+</sup> is retained (**Figures S2-7d** and **S2-13 d-f**; **Table S2-7**).

To compare the localization of iron in active and inactive catalysts, we fitted Fe K-edge EXAFS spectra for all three catalysts after 30 min under PROX conditions at 313 K. Combination of EXAFS and XANES suggests that inactive Pt<sub>2.1</sub>Fe<sub>1.1</sub>-Al<sub>2</sub>O<sub>3</sub>-673-5 contains exclusively fully oxidized Fe<sup>3+</sup> species in tetrahedral oxygen coordination with only a low degree of oligomerization (1±0.4 iron neighbors in the second Fe-O-Fe shell; **Figures S2-7e** and **S2-14 g-i**; **Table S2-6**) resembling isolated Fe<sup>3+</sup> oxide species on  $\gamma$ -Al<sub>2</sub>O<sub>3</sub>.<sup>36</sup> Fe K-edge EXAFS fitting of Pt<sub>2.1</sub>Fe<sub>1.1</sub>-Al<sub>2</sub>O<sub>3</sub>-673-100 shows the coexistence of Fe-O and Fe-Pt bonds after 30 min of PROX at 313 K (**Figure S2-14 a-c**; **Table S2-6**), Pt-Fe bond is pronounced in Pt L<sub>3</sub>-edge EXAFS measured under hydrogen as well (**Figure S2-5a-c**; **Table S2-5**). The fitting of the most active Pt<sub>2.0</sub>Fe<sub>1.4</sub>-SiO<sub>2</sub>-473-100 shows only the Fe-O first coordination shell. Despite being partially reduced under PROX conditions, both active Pt<sub>2.0</sub>Fe<sub>1.4</sub>-SiO<sub>2</sub>-473-100 and Pt<sub>2.1</sub>Fe<sub>1.1</sub>-Al<sub>2</sub>O<sub>3</sub>-673-100 contain more oxygen neighbors (5) in comparison to inactive Pt<sub>2.1</sub>Fe<sub>1.1</sub>-Al<sub>2</sub>O<sub>3</sub>-673-5 catalyst containing only oxidized Fe<sup>3+</sup> species in tetrahedral coordination (Fe-O coordination number of 4; **Table S2-6**). This is consistent with an agglomeration of FeO<sub>x</sub> clusters next to platinum nanoparticles in active catalysts. The fits of the second coordination shell of iron also confirm FeO<sub>x</sub> agglomeration for active catalysts: the Fe-O-Fe coordination number is 2-3 for active catalysts versus 1 for the inactive Pt<sub>2.1</sub>Fe<sub>1.1</sub>-Al<sub>2</sub>O<sub>3</sub>-673-5. (**Table S2-6**; **Figures S2-13** and **S2-14**). Complete oxidation of active catalysts in air results in a further increase of Fe-O coordination up to 6 for Pt<sub>2.0</sub>Fe<sub>1.4</sub>-SiO<sub>2</sub>-473-100 (**Table S2-6**; **Figures S2-13** and **S2-14**). As the bulk FeO and Fe<sub>2</sub>O<sub>3</sub> phases typically contain iron sites in octahedral coordination, the results suggest that FeO<sub>x</sub> species in active Pt-FeO<sub>x</sub> catalysts under PROX conditions are coordinately unsaturated in comparison to the completely oxidized FeO<sub>x</sub> species in deactivated catalysts. The fact that the FeO<sub>x</sub> phase is stronger agglomerated for active catalysts and is partially reduced under PROX conditions supports the model of activation of oxygen at the coordinatively unsaturated FeO islands in contact with metallic platinum, observed for model surfaces in vacuum.<sup>37</sup> Energy dispersive X-ray fluorescence (EDX) and STEM confirm that iron is localized on platinum nanoparticles for Pt<sub>2.1</sub>Fe<sub>1.1</sub>-Al<sub>2</sub>O<sub>3</sub>-673-100 and Pt<sub>2.0</sub>Fe<sub>1.4</sub>-SiO<sub>2</sub>-473-100 (**Figure S2-15**).

**Figure 4-6a,b** and **Figure S2-16** show the evolution of the fractions of Fe<sup>0</sup>, Fe<sup>2+</sup> and Fe<sup>3+</sup> species (and PROX activity) over time for the active Pt<sub>2.1</sub>Fe<sub>1.1</sub>-Al<sub>2</sub>O<sub>3</sub>-673-100 and active Pt<sub>2.0</sub>Fe<sub>1.4</sub>-SiO<sub>2</sub>-473-100 under PROX conditions at 313 K. Iron in both catalysts progressively oxidizes and, thus, their activity drops. In contrast, iron in inactive Pt<sub>2.1</sub>Fe<sub>1.1</sub>-Al<sub>2</sub>O<sub>3</sub>-673-5 remains as Fe<sup>3+</sup> (**Figure S2-7e**). During the first hour of PROX, Pt<sub>2.1</sub>Fe<sub>1.1</sub>-Al<sub>2</sub>O<sub>3</sub>-673-100 activity decreases from about 3.5 molCO gPt<sup>-1</sup> h<sup>-1</sup> to 1.1 molCO gPt<sup>-1</sup> h<sup>-1</sup>, which is mirrored by a decrease in the fractions of reduced Fe<sup>2+</sup> and Fe<sup>0</sup> (**Figure 4-6a**). The data are reproducible (**Figure 4-6a**; **Figure S2-16**) for three separate experiments 1-3 performed using each time three fresh portions of Pt<sub>2.1</sub>Fe<sub>1.1</sub>-Al<sub>2</sub>O<sub>3</sub>-673-100, as it was described earlier. After 1 h of PROX Pt<sub>2.1</sub>Fe<sub>1.1</sub>-Al<sub>2</sub>O<sub>3</sub>-673-100 keeps less than 2 % of oxidic Fe<sup>2+</sup> sites, while in Pt<sub>2.0</sub>Fe<sub>1.4</sub>-SiO<sub>2</sub>-473-100 it retains about 10 %.



Pt<sub>2.1</sub>Fe<sub>1.1</sub>-Al<sub>2</sub>O<sub>3</sub>-673-100 in experiment 3 was subsequently exposed to 5 vol.% O<sub>2</sub> for 40 min at the same temperature of 313 K. This resulted in fast oxidation of Fe<sup>0</sup> and Fe<sup>2+</sup> species coincidentally with a significant activity drop (**Figure S2-16b**). A separate operando Pt L<sub>3</sub>-edge XANES experiment with the fresh portion of Pt<sub>2.1</sub>Fe<sub>1.1</sub>-Al<sub>2</sub>O<sub>3</sub>-673-100 clarifies that this deactivation does not affect the state of platinum (**Figure S2-17**).

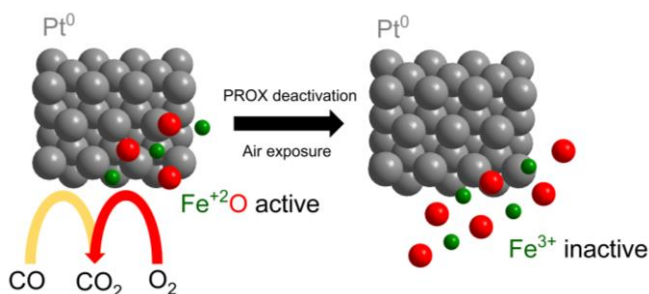
In **Figure 6c**, we correlate the fraction of Fe<sup>2+</sup> obtained from all operando Fe K-edge XAS experiments (**Figure 4-6a,b**; **Figure S2-16**) for active Pt<sub>2.1</sub>Fe<sub>1.1</sub>-Al<sub>2</sub>O<sub>3</sub>-673-100 and Pt<sub>2.0</sub>Fe<sub>1.4</sub>-SiO<sub>2</sub>-473-100 to their PROX activity. We also added the data for Pt<sub>2.1</sub>Fe<sub>1.1</sub>-Al<sub>2</sub>O<sub>3</sub>-673-100 after the oxygen deactivation in experiment 3 and for the inactive Pt<sub>2.1</sub>Fe<sub>1.1</sub>-Al<sub>2</sub>O<sub>3</sub>-673-5 (red dot). The plot (**Figure 4-6c**; **Figure S2-18**) gives a positive linear correlation between the number of oxidic Fe<sup>2+</sup> sites and the PROX reaction activity. Fe<sup>0</sup> fraction does not correlate with PROX activity when considering all the samples together in **Figure 4-6d**. Partially alloyed Fe<sup>0</sup> is slowly and irreversibly oxidized into Fe<sup>3+</sup>, as shown in **Figure 4-6a**. The slope of the steady-state PROX activity—[Fe<sup>2+</sup>] plot equals to 0.71±0.02 molCO (molFe<sup>2+</sup> s)<sup>-1</sup> (**Figure 4-6c**). Fe<sup>3+</sup> concentration is inversely proportional to the PROX activity (**Figure S2-19**).

After keeping Pt<sub>2.1</sub>Fe<sub>1.1</sub>-Al<sub>2</sub>O<sub>3</sub>-673-100 under the PROX mixture for 1 h, we performed five repetitive oxygen cut-off cycles and, subsequently, five hydrogen cut-off cycles at 313 K, similar to those in Chapter 3 (**Figure S2-20**).<sup>18</sup> During each cycle, we kept the catalyst under the PROX mixture for 120 s and then cut-off oxygen or hydrogen for 120 s, compensating the total flow with helium gas. We averaged the XAS data for each five oxygen and hydrogen cut-off cycles and performed the linear combination fitting to quantify the fractions of iron species using the same references (**Figure S2-7**). The results for oxygen and hydrogen cut-off cycles are shown in **Figures S2-20** and **S2-21**. The concentration of Fe<sup>2+</sup> species is not affected by the presence of hydrogen in the feed, as we can see in hydrogen cut-off cycles for both Pt<sub>2.1</sub>Fe<sub>1.1</sub>-Al<sub>2</sub>O<sub>3</sub>-673-100 (**Figure S2-20b,d**) and Pt<sub>2.0</sub>Fe<sub>1.4</sub>-SiO<sub>2</sub>-473-100 (**Figure S2-21b**). At the same time, in the oxygen cut-off cycles for Pt<sub>2.1</sub>Fe<sub>1.1</sub>-Al<sub>2</sub>O<sub>3</sub>-673-100, approximately 1 % of Fe<sup>3+</sup> is converted to Fe<sup>2+</sup> after the oxygen cut-off (**Figure S2-20a,c**). This reduction happens reversibly over the period of all cycles. The fact that catalyst activity is sensitive to the oxygen partial pressure indicates that active sites are partially covered with oxygen under PROX conditions. That is why we observe only a slight reduction of Fe<sup>3+</sup>, as the majority of Fe<sup>2+</sup> sites activating oxygen remain vacant in the resting state, which is additionally confirmed by an oxygen reaction order of 0.79, which is close to, but not equal to unity. Interestingly, Pt<sub>2.0</sub>Fe<sub>1.4</sub>-SiO<sub>2</sub>-473-100, while having an oxygen reaction order equal unity, shows no significant reduction of iron after the oxygen cut-off (**Figure S2-21a**). This proves that oxygen reaction order can serve as an indication of a number of Fe<sup>+2</sup>O sites capable of dissociative adsorption of molecular oxygen from the reaction stream.

#### 4.3.5 Mechanism of Preferential Carbon Monoxide Oxidation

Combining all information, we propose a schematic model of the PROX active sites, consisting of the surface of the metallic platinum particle in contact with Fe<sup>2+</sup>O species, which activate oxygen during the PROX reaction (**Scheme 4-2**). These species can bind oxygen and reversibly oxidize into the Fe<sup>3+</sup> state. This process, however, is slower than carbon monoxide oxidation. Because of that, PROX activity correlates with the concentration of Fe<sup>2+</sup>, the resting state of iron species activating oxygen. Carbon monoxide is activated separately on a metallic platinum surface next to Fe<sup>2+</sup>O<sup>2-</sup> species, which allows circumventing the carbon monoxide poisoning effect.<sup>22</sup> The **Scheme 4-2** model is based on the studies of the FeO/Pt(111) surface and correlates well with our Fe K-edge EXAFS observations of FeO<sub>x</sub> clustering in PROX-active Pt-FeO<sub>x</sub> catalysts (**Table S2-6**).<sup>37-39</sup> Fe K-edge EXAFS of active Pt-FeO<sub>x</sub> catalysts also suggests that oxygen activation can proceed on the highly-dispersed FeO sites, undercoordinated under PROX conditions (**Table S2-6**). These sites can also bind hydroxyl groups,

which will be discussed in detail in Chapter 5. The amount of metallic partially alloyed iron and  $\text{Fe}^{3+}$  species do not correlate well with the PROX activity because these species mainly serve as spectators. The observed fraction of metallic iron is probably hidden in the core of platinum nanoparticles as its amount does not correlate with the activity (**Scheme 4-2**). Exposure to an oxygen atmosphere destroys the active FeO/Pt interface through the irreversible oxidation of  $\text{Fe}^{2+}$  at ambient temperatures. Similarly, a small fraction of an atomically dispersed platinum or small oxidized platinum clusters exists not only in active  $\text{Pt}_{2.0}\text{Fe}_{1.4}\text{-SiO}_2\text{-473-100}$  but also in an inactive  $\text{Pt}_{2.0}\text{-SiO}_2\text{-473-100}$  catalyst.<sup>14</sup> It further confirms that atomically dispersed platinum does not significantly contribute to the PROX activity of  $\text{Pt}_{2.0}\text{Fe}_{1.4}\text{-SiO}_2\text{-473-100}$ , as it was described earlier. We conclude that silica- and alumina-supported platinum nanoparticles decorated by a highly dispersed FeO constitute active sites for ambient temperature PROX over studied catalysts as depicted in **Scheme 4-2**.



Scheme 4-2. Model showing irreversible deactivation via the oxidation of the active platinum-iron oxide interface.

## 4.4 Conclusions

We synthesized alumina- and silica-supported Pt-FeO<sub>x</sub> catalysts that are active in ambient temperature preferential carbon monoxide oxidation. Operando XAS allowed us to determine that Fe<sup>2+</sup> active sites are formed during reduction pretreatment under a flow pure hydrogen. We discovered that the catalyst activity is directly proportional to the Fe<sup>2+</sup> concentration, which is the resting state of active sites activating oxygen. Fe<sup>2+</sup> irreversibly oxidizes over time, which is the leading cause of Pt-Fe catalysts deactivation. Supported metallic platinum nanoparticles decorated by a highly dispersed FeO constitute active sites. Adsorption of carbon monoxide on metallic platinum and oxygen activation mostly on reduced oxidic Fe<sup>2+</sup> sites constitute the mechanism of preferential carbon monoxide oxidation over Pt-Fe catalysts at ambient temperature.

## 4.5 References

1. Peters, G. P.; Andrew, R. M.; Canadell, J. G.; Friedlingstein, P.; Jackson, R. B.; Korsbakken, J. I.; Le Quéré, C. and Peregón, A. Carbon dioxide emissions continue to grow amidst slowly emerging climate policies. *Nat. Clim. Chang.* **2020**, *10*, 3-6.
2. Ueckerdt, F.; Bauer, C.; Dirmaichner, A.; Everall, J.; Sacchi, R. and Luderer, G. Potential and risks of hydrogen-based e-fuels in climate change mitigation. *Nat. Clim. Chang.* **2021**, *11*, 384-393.
3. Ausfelder, F. and Bazzanella, A. in *Hydrogen Science and Engineering: Materials, Processes, Systems and Technology*, Vol. 1 (Eds: D. Stolten, B. Emonts), Wiley-VCH, Weinheim, Germany **2016**, Ch. 2.
4. Pei, P.; Wang, M.; Chen, D.; Ren, P. and Zhang, L. Key technologies for polymer electrolyte membrane fuel cell systems fueled impure hydrogen. *Progr. In Nat. Sci.: Materials Int.* **2020**, *30*, 751-763.
5. Neef, H. J. International overview of hydrogen and fuel cell research. *Energy.* **2009**, *34*, 327-333.
6. Valdés-López, V. F., Mason, T.; Shearing, P. R. and Brett, D. J. L. Carbon monoxide poisoning and mitigation strategies for polymer electrolyte membrane fuel cells-A review. *Progr. in Energ. and Comb. Sci.* **2020**, *79*, 100842.
7. Jing, P.; Gong, X.; Liu, B. and Zhang, Recent advances in synergistic effect promoted catalysts for preferential oxidation of carbon monoxide. *J. Catal. Sci. Technol.* **2020**, *10*, 919-934.
8. Liu, G.; Walsh, A. G. and Zhang, P. Synergism of iron and platinum species for low-temperature CO oxidation: From two-dimensional surface to nanoparticle and single-atom catalysts. *J. Phys. Chem. Lett.* **2020**, *11*, 2219-2229.
9. Saavedra, J.; Whittaker, T.; Chen, Z.; Pursell, C. J.; Rioux, R. M. and Chandler, B. D. Controlling activity and selectivity using water in the Au-catalysed preferential oxidation of CO in H<sub>2</sub>. *Nature Chem.* **2016**, *8*, 584-589.
10. Sirijaruphan, A.; Goodwin, J. G. and Rice, R. W. Effect of Fe promotion on the surface reaction parameters of Pt/ $\gamma$ -Al<sub>2</sub>O<sub>3</sub> for the selective oxidation of CO. *J. Catal.* **2004**, *224*, 304-313.
11. Chen, G.; Zhao, Y.; Fu, G.; Duchesne, P. N.; Gu, L.; Zheng, Y.; Weng, X.; Chen, M.; Zhang, P.; Pao, C.; Lee, J. and Zheng, N. Interfacial effects in iron-nickel hydroxide-platinum nanoparticles enhance catalytic oxidation. *Science* **2014**, *344*, 495-499.
12. Cao, L.; Liu, W.; Luo, Q.; Yin, R.; Wang, B.; Weissenrieder, J.; Soldemo, M.; Yan, H.; Lin, Y.; Sun, Z.; Ma, C.; Zhang, W.; Chen, S.; Wang, H.; Guan, Q.; Yao, T.; Wei, S.; Yang, J. and Lu, J. Atomically dispersed iron hydroxide anchored on Pt for preferential oxidation of CO in H<sub>2</sub>. *Nature* **2019**, *565*, 631-635.
13. Qiao, B.; Wang, A.; Li, L.; Lin, Q.; Wei, H.; Liu, J. and Zhang, T. Ferric oxide-supported pt subnano clusters for preferential oxidation of CO in H<sub>2</sub>-rich gas at room temperature. *ACS Catal.* **2014**, *4*, 2113-2117.
14. Qiao, B.; Wang, A.; Yang, X.; Allard, L. F.; Jiang, Z.; Cui, Y.; Liu, J.; Li, J. and Zhang, T. Single-atom catalysis of CO oxidation using Pt<sub>1</sub>/FeO<sub>x</sub>. *Nature Chem.* **2011**, *3*, 634-641.

15. Zhang, H.; Liu, X.; Zhang, N.; Zheng, J.; Zheng, Y.; Li, Y.; Zhong, C. and Chen, B. H. Construction of ultrafine and stable PtFe nano-alloy with ultra-low Pt loading for complete removal of CO in PROX at room temperature. *Appl. Catal. B: Environ.* **2016**, *180*, 237-245.
16. Yin, J.; Wang, J.; Zhang, T. and Wang, X. Novel alumina-supported PtFe alloy nanoparticles for preferential oxidation of carbon monoxide in hydrogen. *Catal. Lett.* **2008**, *125*, 76-82.
17. Siani, A.; Alexeev, O. S.; Lafaye, G. and Amiridis, M. D. The effect of Fe on SiO<sub>2</sub>-supported Pt catalysts: Structure, chemisorptive, and catalytic properties. *J. Catal.* **2009**, *266*, 26-38.
18. Sadykov, I. I.; Zabilskiy, M.; Clark, A. H.; Krumeich, F.; Sushkevich, V.; van Bokhoven, J. A.; Nachttegaal, M. and Safonova, O. V. Time-resolved XAS provides direct evidence for oxygen activation on cationic iron in a bimetallic Pt-FeO<sub>x</sub>/Al<sub>2</sub>O<sub>3</sub> catalyst. *ACS Catal.* **2021**, *11*, 11793-11805.
19. Liu, K. Wang, A. and Zhang, T. Recent advances in preferential oxidation of CO reaction over platinum group metal catalysts. *ACS Catal.* **2012**, *2*, 1165-1178.
20. Lou, Y. and Liu, J. A highly active Pt-Fe/γ-Al<sub>2</sub>O<sub>3</sub> catalyst for preferential oxidation of CO in excess of H<sub>2</sub> with a wide operation temperature window. *Chem. Commun.* **2017**, *53*, 9020-9023.
21. Fu, Q.; Li, W.; Yao, Y.; Liu, H.; Su, H.; Ma, D.; Gu, X.; Chen, L.; Wang, Z.; Zhang, H.; Wang, B. and Bao, X. Interface-confined ferrous centers for catalytic oxidation. *Science* **2010**, *328*, 1141-1144.
22. Allian, A. D.; Takanabe, K.; Fujidala, K. L.; Hao, X.; Truex, T. J.; Cai, J.; Buda, C.; Neurock, M. and Iglesia, E. Chemisorption of CO and mechanism of CO oxidation on supported platinum nanoclusters. *J. Am. Chem. Soc.* **2011**, *133*, 4498-4517.
23. Hadjiivanov, K. I. and Vayssilov, G. N. Characterization of oxide surfaces and zeolites by carbon monoxide as an IR probe molecule. *Adv. Catal.* **2002**, *307*, 3888-3891.
24. Li, S.; Jia, M.; Gao, J.; Wu, P.; Yang, M.; Huang, S.; Dou, X.; Yang, Y. and Zhang, W. Infrared studies of the promoting role of water on the reactivity of Pt/FeO<sub>x</sub> catalyst in low-temperature oxidation of carbon monoxide. *J. Phys. Chem. C* **2015**, *119*, 2483-2490.
25. Liu, X.; Korotkikh, O. and Farrauto, R. Selective catalytic oxidation of CO in H<sub>2</sub>: structural study of Fe oxide-promoted Pt/alumina catalyst. *Appl. Catal. A: General* **2002**, *226*, 293-303.
26. Lentz, C.; Jand, S. P.; Melke, J.; Roth, C. and Kaghazchi, P. DRIFTS study of CO adsorption on Pt nanoparticles supported by DFT calculations. *J. Mol. Catal. A: Chem.* **2017**, *426*, part A, 1-9.
27. Chen, Y.; Sun, H. and Gates, B. C. Prototype atomically dispersed supported metal catalysts: iridium and platinum. *Small* **2020**, 2004665.
28. Li, Q.; Zhu, H.; Zheng, L.; Liu, H.; Ren, Y.; Wang, N.; Chen, J.; Deng, J. and Xing, X. Local chemical strain in PtFe alloy nanoparticles. *Inorg. Chem.* **2018**, *57*, 10494-10497.
29. Kousa, M.; Iwasaki, S.; Ishimatsu, N.; Kawamura, N.; Nomura, R.; Kakizawa, S.; Mizumaki, M.; Sumiya, H. and Irifune, T. Element-selective elastic properties of Fe<sub>65</sub>Ni<sub>35</sub> Invar alloy and Fe<sub>72</sub>Pt<sub>28</sub> alloy studied by extended X-ray absorption fine structure. *High Pressure Res.* **2020**, *40*, 130-139.

30. Calvin, S.; Miller, M. M.; Goswami, R.; Cheng, S. F.; Mulvaney, S. P.; Whitman, L. J.; and Harris, V. G. Determination of crystallite size in a magnetic nanocomposite using extended x-ray absorption fine structure. *J. Appl. Phys.* **2003**, *94*, 778-783.
31. Frenkel, A. I.; Yevick, A.; Cooper, C. and Vasic, R. Modeling the structure and composition of nanoparticles by extended X-ray absorption fine-structure spectroscopy. *Annu. Rev. Anal. Chem.* **2011**, *4*, 23-39.
32. Chepulskii, R. V. and Curtarolo, S. Ab Initio Insights on the Shapes of Platinum Nanocatalysts. *ACS Nano* **2011**, *5*, 247-254.
33. Singh, J.; Nelson, R. C.; Vicente, B. C.; Scott, S. L. and van Bokhoven, J. A. Electronic structure of alumina-supported monometallic Pt and bimetallic PtSn catalysts under hydrogen and carbon monoxide environment. *Phys. Chem. Chem. Phys.* **2010**, *12*, 5668-5677.
34. Glatzel, P.; Singh, J.; Kvashnina, K. O. and van Bokhoven, J. A. In situ characterization of the 5d density of states of Pt nanoparticles upon adsorption of CO. *J. Am. Chem. Soc.* **2010**, *132*, 2555-2557.
35. Karim, W.; Spreafico, C.; Kleibert, A.; Gobrecht, J.; Vondele, J. V.; Ekinici, Y. and van Bokhoven, J. A. Catalyst support effects on hydrogen spillover. *Nature* **2017**, *541*, 68-71.
36. Tomita, A.; Miki, T.; Tango, T.; Murakami, T.; Nakagawa, H. and Tai, Y. Fe K-Edge X-ray absorption fine structure determination of  $\gamma$ -Al<sub>2</sub>O<sub>3</sub>-supported iron - oxide species. *ChemPhysChem* **2015**, *16*, 2015-2020.
37. Kudernatsch, W.; Peng, G.; Zeuthen, H.; Bai, Y.; Merte, L. R.; Lammich, L.; Besenbacher, F.; Mavrikakis, M. and Wendt, S. Direct visualization of catalytically active sites at the FeO-Pt (111) interface. *ACS Nano* **2015**, *9*, 7804-7814.
38. Wang, Y.; Zhang, H.; Yao, X. and Zhao, X. Edges of FeO/Pt(111) interface: a first-principle theoretical study. *Phys. Chem. C.* **2013**, *117*, 1672-1676.
39. Chen, H.; Liu, Y.; Yang, F.; Wei, M.; Zhao, X.; Ning, Y.; Liu, Q.; Zhang, Y.; Fu, Q. and Bao, X. Active phase of FeO<sub>x</sub>/Pt catalysts in low-temperature CO oxidation and preferential oxidation of CO reaction. *J. Phys. Chem. C.* **2017**, *121*, 10398-10405.

---

## 5 Role of Water in the Promotion of Preferential Carbon Monoxide Oxidation over $\gamma$ -Al<sub>2</sub>O<sub>3</sub>- and SiO<sub>2</sub>-Supported Platinum-Iron Catalysts

Chapter 5 contains scientific contributions from Ilia I. Sadykov, Frank Krumeich, Dennis Palagin, Davide Ferri, Igor V. Plokhikh, Jeroen A. van Bokhoven, Maarten Nachtegaal, and Olga V. Safonova.

### *Author contributions:*

*Ilia I. Sadykov designed the research, performed most of the experimental work, analyzed the data, and modeled the structure of the catalyst. Frank Krumeich executed electron microscopy measurements. Dennis Palagin performed density functional theory calculations. Igor V. Plokhikh assisted with the operando X-ray absorption measurements. Olga V. Safonova, Davide Ferri, Jeroen A. van Bokhoven, and Maarten Nachtegaal were involved in the research design and helped to connect individual parts of the research.*

## 5.1 Abstract

A systematic study of water influence on the preferential carbon monoxide oxidation (PROX) activity of supported platinum-iron catalysts showed that the addition of water both during the reduction pretreatment at high temperatures and during catalysis is beneficial for PROX and can lead to a significant increase in carbon monoxide conversion whilst preserving high selectivity. The reduction of

Pt-Fe/ $\gamma$ -Al<sub>2</sub>O<sub>3</sub> under a 98 vol.% H<sub>2</sub> - 2 vol.% H<sub>2</sub>O mixture up to 473 K allows obtaining one of the highest catalytic activities among all bimetallic Pt-Fe catalysts known to this date. The kinetic experiments, including those with <sup>18</sup>O-labeled water, in combination with operando infrared spectroscopy, show that water hydroxylates the redox-active iron phases during high-temperature pretreatment in the hydrogen-steam mixture. This pretreatment creates active iron-associated hydroxyl groups with enhanced reactivity towards carbon monoxide chemisorbed on platinum nanoparticles. A quantitative correlation between the catalytic activity of Pt-Fe/ $\gamma$ -Al<sub>2</sub>O<sub>3</sub> catalysts and the Fe<sup>2+</sup> concentration, obtained using operando X-ray absorption spectroscopy, shows that the number of carbon monoxide molecules converted per each individual active Fe<sup>2+</sup> site increases after the reduction pretreatment in the hydrogen-water mixture. Density functional theory provides a model demonstrating that hydroxylation of oxidic iron species stabilizes the FeO<sub>x</sub>(OH)<sub>y</sub>/Pt interface, which can be the reason for the enhanced catalytic activity of water-treated catalysts.



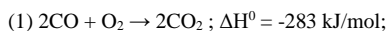
## 5.2 Introduction

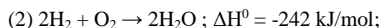
Hydrogen production scaling to more than 50 million tons a year is the backbone of the modern chemical industry.<sup>1</sup> Pure hydrogen is crucial for ammonia and methanol production, petroleum hydrogenation, and refining processes.<sup>2</sup> The widely used combination of methane steam reforming and water-gas shift reactions is enough to obtain hydrogen with about 0.5% of carbon monoxide on top of other impurities, such as, water, and carbon dioxide.<sup>2</sup> Nonetheless, even this relatively small carbon monoxide content is unacceptable for ammonia production and conventional proton-exchange membrane fuel cells, which only accept hydrogen with carbon monoxide impurities at ppm level.<sup>3</sup> Pressure swing adsorption can be considered a robust hydrogen purification method but requires vast energy input and significant capital investments for constant pressure cycling. Furthermore, it can only recover 70-90% of hydrogen. Similar problems occur during carbon monoxide methanation, which is able to recover only 85-90% of hydrogen.<sup>2</sup> Both processes also require elevated pressure and temperature.<sup>2</sup>

A valid alternative to these two processes is preferential carbon monoxide oxidation, which can operate without any additional energy supply and only requires a specific catalyst able to selectively oxidize traces of carbon monoxide and leave hydrogen intact.<sup>2</sup> Commercially, this process is known as the Selectoxo process (**S**elective **C**atalytic **O**xidation) developed by the Engelhard Corporation in the early 1960s.<sup>2</sup> The family of Selectoxo catalysts typically consists of platinum supported on  $\gamma$ -Al<sub>2</sub>O<sub>3</sub> potentially promoted with d-metal oxides.<sup>2</sup> One of the most active catalysts in this family is Pt-FeO<sub>x</sub>/γ-Al<sub>2</sub>O<sub>3</sub> where, as we have shown in our previous works and discussed here in Chapters 3 and 4, the redox activity of oxidic iron species is responsible for oxygen activation. At the same time, metallic platinum nanoparticles activate carbon monoxide, enabling preferential carbon monoxide oxidation at ambient temperature.<sup>4,5,6</sup> Depending on the catalyst structure and the operating temperature range, at least two mechanisms of carbon monoxide oxidation can be detected, as discussed in Chapters 3 and 4. As shown in Chapter 4, active Fe<sup>2+</sup> species responsible for ambient temperature preferential carbon monoxide oxidation are formed in close proximity to platinum nanoparticles and deactivate on stream due to their irreversible oxidation into a Fe<sub>2</sub>O<sub>3</sub>-like phase. This observation renders it impossible to run preferential carbon monoxide oxidation over Pt-FeO<sub>x</sub>/γ-Al<sub>2</sub>O<sub>3</sub> catalysts without a significant loss of activity.

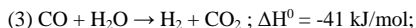
Several recent works have paved the way to increase the activity of Pt-FeO<sub>x</sub> catalysts by introducing iron hydroxides or oxyhydroxides instead of oxidic iron species. Water vapor present in reformat gas can stabilize iron hydroxides.<sup>2,3</sup> Traces of water can also be formed by undesired oxidation of hydrogen in small amounts when the selectivity drops below 100%. Amorphous porous alumina and silica supports per se contain ca. 6 and 2 H<sub>2</sub>O molecules per nm<sup>2</sup> of the surface at ambient conditions, respectively.<sup>7</sup> Relative humidity of hydrogen-containing feed gas determines the structure of adsorbed water and the concentration of hydroxyl groups on the support surface.<sup>8</sup> Relative humidity above 70% can lead to the formation of several layers of water adsorbed on the surface together with the complex network of hydroxyl groups existing even at a relative humidity below 10%.<sup>8,9</sup>

Even in the absence of water in the reaction stream, residual hydroxyl groups and adsorbed water can facilitate preferential carbon monoxide oxidation on pure platinum above 373 K.<sup>10</sup> In this case hydroxyl groups can actively produce formate (HCOO) intermediates through the reaction with carbon monoxide adsorbed on platinum nanoparticles.<sup>11</sup> In addition to carbon monoxide and unwanted hydrogen oxidation:

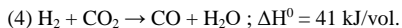




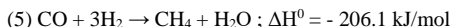
water and hydroxyl groups next to platinum can induce a complex set of interdependent reactions, such as water-gas shift reaction:



reverse water-gas shift reaction:



Carbon monoxide methanation:



can also occur at higher temperatures, as discussed in Chapter 1.<sup>2</sup>

Promoting platinum with iron can increase the catalytic activity by several orders of magnitude, enabling preferential carbon monoxide oxidation close to ambient temperature.<sup>4,5,6</sup> Fundamental studies performed with model FeO(111) and Fe<sub>3</sub>O<sub>4</sub>(111) islands on the Pt(111) surface showed that water readily adsorbs on iron sites located at the FeO<sub>x</sub>/Pt(111) interface and spontaneously dissociates to form iron-bound hydroxyl groups, which can migrate across FeO<sub>x</sub>.<sup>12-14</sup> Hydrogen can also hydroxylate surface FeO<sub>x</sub> on Pt(111) through hydrogen spillover.<sup>15</sup> The obtained FeO<sub>x</sub>(OH)<sub>y</sub> model layers are able to react with carbon monoxide adsorbed on Pt(111) already at 300 K.<sup>16</sup>

As water does not evaporate below 373 K, it accumulates on the surface of Pt-FeO<sub>x</sub> catalysts and can decrease or increase carbon monoxide selectivity and conversion.<sup>17,18</sup> There is no distinct way of predicting when water is beneficial for supported Pt-FeO<sub>x</sub> catalysts, as it can potentially affect both platinum and iron sites, and there is no clear consensus on its mechanism of action. Previous studies on the influence of water on PROX showed that Pt/FeO<sub>x</sub> had higher activity in carbon monoxide oxidation reaction when treated with water;<sup>18-20</sup> at the same time, added water poisoned Pt-Fe/mordenite and Pt-Fe/CNT catalysts.<sup>21,22</sup> Everything was complicated by the fact that these studies did not demonstrate how water impacted the Fe<sup>2+</sup>/Fe<sup>3+</sup> redox cycle. Under preferential carbon monoxide oxidation conditions surface iron hydroxides appear to be completely oxidized in the presence of water, which contradicts an observed oxygen reaction order close to unity suggesting that surface sites activating oxygen are empty.<sup>20,23</sup> Infrared and X-ray absorption spectroscopy studies presented so far only demonstrated how water affects the majority of iron species and did not reveal the structure of the actual active sites constituting only a tiny percentage of all surface iron oxides/hydroxides/oxyhydroxides.<sup>18,19</sup>

Given the complex role of water in preferential carbon monoxide oxidation, we ventured to study how water affects not the entirety of supported Pt-FeO<sub>x</sub> catalysts but the actual active sites. This was made possible via operando X-ray absorption spectroscopy (XAS) complemented by operando diffuse reflectance infrared Fourier transform spectroscopy (DRIFTS), both following conversion, selectivity, and the state of the active species in real-time. These methods, together with scanning transmission electron microscopy (STEM), kinetic characterization, and isotope-labeling experiments, showed that water treatment of supported Pt-Fe/γ-Al<sub>2</sub>O<sub>3</sub> catalysts during the initial reduction step enables to create one of the most active platinum iron catalysts on inert support known to date. The presence of adsorbed water and active hydroxyl groups was demonstrated to influence the reactivity of catalytically active Fe<sup>2+</sup> sites at the FeO<sub>x</sub>(OH)<sub>y</sub>/Pt interface. Hydroxyl groups on active FeO<sub>x</sub>(OH)<sub>y</sub> sites can directly react

with carbon monoxide chemisorbed on metallic platinum nanoparticles, which explains the observed promotional role of water in preferential carbon monoxide oxidation over supported Pt-Fe catalysts.

## 5.3 Results and Discussion

### 5.3.1 Water Pretreatment Strategies

Synthesis of supported bimetallic catalysts and monometallic reference samples was carried out by incipient wetness impregnation of corresponding  $\gamma$ -Al<sub>2</sub>O<sub>3</sub> and SiO<sub>2</sub> supports, just as in Chapter 4. The impregnated supports were dried and then sequentially calcined in air for 2 h at 473 K and 2 h at 673 K. The samples obtained in this way were used in all subsequent experiments. Inductively coupled plasma-optical emission spectrometry (ICP-OES) determined the composition of the bimetallic samples to be 2.1 wt.% Pt - 3.6 wt.% Fe /  $\gamma$ -Al<sub>2</sub>O<sub>3</sub> and 2.0 wt.% Pt - 1.4 wt.% Fe / SiO<sub>2</sub>. Compositions of monometallic references were determined to be 2.0 wt.% Pt / SiO<sub>2</sub>, 2.0 wt.% Pt /  $\gamma$ -Al<sub>2</sub>O<sub>3</sub>, and 3.4 wt.% Fe /  $\gamma$ -Al<sub>2</sub>O<sub>3</sub>. Higher iron concentrations compared to the catalysts in Chapters 3 and 4 helped increase the sensitivity of X-ray absorption spectroscopy to iron species and achieve higher catalytic activities.

Reduction of such calcined samples under a hydrogen atmosphere is necessary to create active preferential carbon monoxide oxidation catalysts containing metallic platinum nanoparticles decorated by active oxidic Fe<sup>2+</sup> species. As we found in our previous work (Chapter 4), hydrogen pressure during reduction, as well as reduction temperature affect the degree of iron reduction. A high concentration of reduced Fe<sup>2+</sup> is vital to achieve high catalytic activity. At the same time, reduction at 673 K results in a high concentration of inactive metallic iron partially alloyed with platinum on both  $\gamma$ -Al<sub>2</sub>O<sub>3</sub> and SiO<sub>2</sub> supports. To reproduce high activities on both supports as in our previous work and to avoid metallic iron formation, here we have chosen to reduce all samples at 373 or 473 K under pure hydrogen. As-reduced samples are labeled in accordance with their composition and the pretreatment protocols (**Figure 5-1**, **Table S3-1**).

Four different pretreatment strategies were chosen to study the effect of water on the activity and the structure of the catalysts, as shown in **Figure 5-1** and **Table S3-1**. The first set of samples was reduced under pure hydrogen without added water. These materials are labelled as, for instance, Pt<sub>2.1</sub>Fe<sub>3.6</sub>-Al<sub>2</sub>O<sub>3</sub>-373-100 and Pt<sub>2.0</sub>Fe<sub>1.4</sub>-SiO<sub>2</sub>-473-100, where 'Al<sub>2</sub>O<sub>3</sub>' and 'SiO<sub>2</sub>' indicate the support, '373' and '473' reflect the reduction temperature in K, '100' means that 100 % hydrogen mixture was used during reduction. Subscript numbers indicate the weight percentage of each element. Temperature-programmed desorption of water from  $\gamma$ -Al<sub>2</sub>O<sub>3</sub> and SiO<sub>2</sub> supports showed that they contain 4 and 3 H<sub>2</sub>O molecules per nm<sup>2</sup>, respectively (**Figure S3-1**, **Table S3-2**); pretreatment at 473 K leaves only 1-2 H<sub>2</sub>O molecules per nm<sup>2</sup>. As dehydration of SiO<sub>2</sub> at 673 K under inert gas leaves only about 0.3 H<sub>2</sub>O molecules per nm<sup>2</sup>, we decided to additionally test how this dehydration procedure performed right after the reduction impacts the catalytic activity. The corresponding second set of samples dehydrated at 673 K are designated as Pt<sub>2.0</sub>Fe<sub>1.4</sub>-SiO<sub>2</sub>-473-100-deh and Pt<sub>2.1</sub>Fe<sub>3.6</sub>-Al<sub>2</sub>O<sub>3</sub>-473-100-deh.

The third and fourth sets of samples were prepared by adding water before or during the reduction pretreatment, respectively. Pt<sub>2.1</sub>Fe<sub>3.6</sub>-Al<sub>2</sub>O<sub>3</sub>-wet-473-100 and Pt<sub>2.1</sub>Fe<sub>3.6</sub>-Al<sub>2</sub>O<sub>3</sub>-wet-373-100 were impregnated with deionized water before the reduction (**Table 1-1**, Chapter 1). The water volume was kept equal to the pore volume of the support. By dividing the volume of liquid water by the surface area of the support, we estimate that about 3400 H<sub>2</sub>O molecules can be present for each nm<sup>2</sup> of the

support surface, which clearly points to the existence of liquid water in the pores before reduction. To test how only adsorbed water affects the activity, Pt<sub>2.1</sub>Fe<sub>3.6</sub>-Al<sub>2</sub>O<sub>3</sub>-473-98-steam and Pt<sub>2.0</sub>-Al<sub>2</sub>O<sub>3</sub>-473-98-steam were reduced under the gas mixture of 98 vol.% H<sub>2</sub> and 2 vol.% H<sub>2</sub>O (Figure S3-2). The total amount of water added by the aforementioned steam treatment was estimated to be around 4 H<sub>2</sub>O molecules per nm<sup>2</sup> for the pure  $\gamma$ -Al<sub>2</sub>O<sub>3</sub> support, in addition to 1.2 H<sub>2</sub>O molecules per nm<sup>2</sup> already present on the support surface (Figure S3-1, Table S3-1).

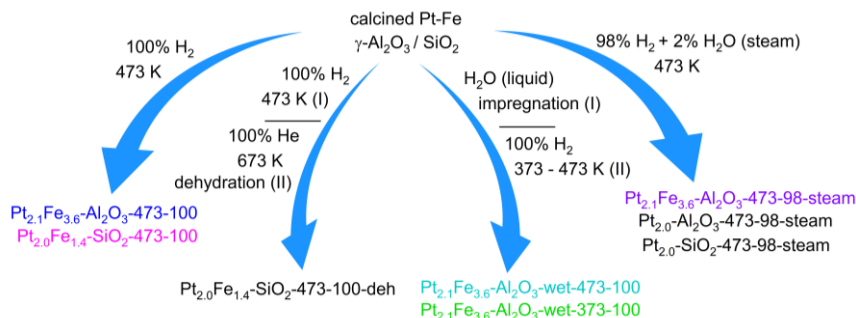


Figure 5-1. Schematic representation of the preparation of specific catalysts explaining different pretreatment protocols. Gas concentrations are shown in vol. %.

For all measurements, a portion of a pre-made calcined catalyst from the same batch was placed in an operando reactor cell dedicated either to XAS or DRIFTS experiment. XAS experiments made use of the same cell as reported in Chapters 3 and 4 built into our setup for preferential carbon monoxide oxidation shown in Figure S3-2.<sup>5,6,24</sup> The same setup was used for operando DRIFTS measurements with the dedicated DRIFTS cell instead.<sup>25</sup> Each separate experiment started with the water-assisted or dry reduction, after which the catalyst was cooled to 313 K under helium or argon atmosphere and exposed to 40 vol.% H<sub>2</sub> + 5 vol.% CO for 10 min. Significant catalytic activity appeared only after the addition of 2 vol.% O<sub>2</sub> into the reaction mixture, as shown in Figure 5-2. During these experiments, selectivity to carbon monoxide oxidation for all catalysts at 313 K was above 99%, for Pt<sub>2.1</sub>Fe<sub>3.6</sub>-Al<sub>2</sub>O<sub>3</sub>-473-98-steam, it was above 97%. During all operando experiments, carbon monoxide conversion was kept below 20% to preserve a kinetically controlled regime of carbon monoxide oxidation.

As evident from Figure 5-2, Pt<sub>2.1</sub>Fe<sub>3.6</sub>-Al<sub>2</sub>O<sub>3</sub>-473-98-steam outperforms all other catalysts in this study. In fact, it shows one of the highest reported preferential carbon monoxide oxidation activities among Pt-Fe catalysts on inert supports reported in the literature (Table 1-1, Chapter 1). Pt<sub>2.1</sub>Fe<sub>3.6</sub>-Al<sub>2</sub>O<sub>3</sub>-473-98-steam activity after 20 min on stream (6.93 molCO gPt<sup>-1</sup> h<sup>-1</sup>, Figure 5-2) is slightly higher than that of the state-of-the-art catalysts comprised of iron hydroxides supported on platinum nanoparticles by atomic layer deposition (5.61 molCO gPt<sup>-1</sup> h<sup>-1</sup>, Figure 5-2). Notably, more complex compositions such as Pt/FeNi(OH)<sub>x</sub>/TiO<sub>2</sub> and gold-based catalysts treated with water can have higher activities per mass of noble metal (Table 1-1, Chapter 1). An additional stability test performed under a simulated reformate feed: 5 vol.% CO + 40 vol.% H<sub>2</sub> + 10 vol.% O<sub>2</sub> + 2 vol.% H<sub>2</sub>O / He confirms that Pt<sub>2.1</sub>Fe<sub>3.6</sub>-Al<sub>2</sub>O<sub>3</sub>-473-98-steam outperforms the most active bimetallic Pt-Fe catalyst known to this date obtained by Lou et al. with a solution deposition method (Table 1-1, Chapter 1).<sup>4</sup>

Pt<sub>2.1</sub>Fe<sub>3.6</sub>-Al<sub>2</sub>O<sub>3</sub>-473-98-steam achieves an estimated average carbon monoxide consumption rate of 15.5 molCO g<sub>Pt</sub><sup>-1</sup> h<sup>-1</sup> as shown in **Figure S3-3**.<sup>4</sup> Selectivity to carbon monoxide oxidation is about 60% and can be improved by decreasing oxygen concentration, as discussed in Chapter 1. Pt<sub>2.1</sub>Fe<sub>3.6</sub>-Al<sub>2</sub>O<sub>3</sub>-473-100 and Pt<sub>2.1</sub>Fe<sub>1.1</sub>-Al<sub>2</sub>O<sub>3</sub>-473-100 (Chapter 4) have similar activities after 200 min under PROX mixture as shown in **Table S3-3**.

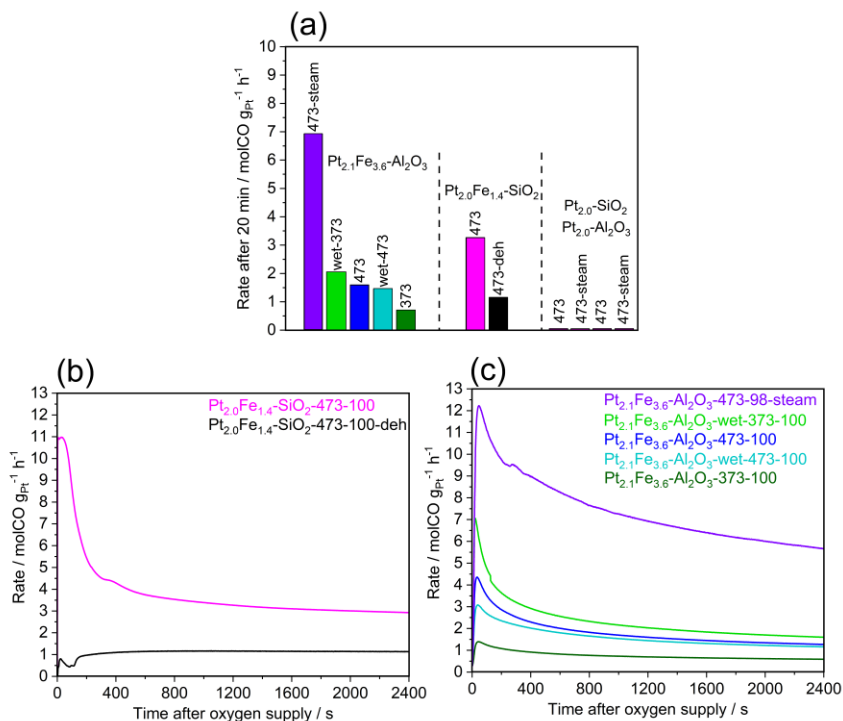


Figure 5-2. (a) PROX activities of the catalysts under study after 20 min under PROX mixture. Time-on-stream PROX activities of SiO<sub>2</sub>- (b) and γ-Al<sub>2</sub>O<sub>3</sub>-supported (c) catalysts under study. Reaction feed: 40 vol.% H<sub>2</sub>, 5 vol.% CO, 2 vol.% O<sub>2</sub>, and helium balance. Reaction temperature 313 K. Sample names specify the samples compositions and the pre-treatment conditions typically involving reduction in concentrated hydrogen and several optional conditions, such as the impregnation of the samples with water (wet), the addition of water (2 vol.%) into hydrogen flow during the reduction (steam) or an additional dehydration step in an inert gas at 673 K (deh).

Impregnation of bimetallic catalysts with water before the reduction step also has a significant promotion effect on the catalytic activity, but only if the reduction step is carried out at 373 K (**Figure 5-2a**). The PROX reaction rate of Pt<sub>2.1</sub>Fe<sub>3.6</sub>-Al<sub>2</sub>O<sub>3</sub>-wet-373-100 after 20 min under PROX is 2.03 molCO g<sub>Pt</sub><sup>-1</sup> h<sup>-1</sup>, which is higher than for Pt<sub>2.1</sub>Fe<sub>3.6</sub>-Al<sub>2</sub>O<sub>3</sub>-473-100 (1.60 molCO g<sub>Pt</sub><sup>-1</sup> h<sup>-1</sup>) and Pt<sub>2.1</sub>Fe<sub>3.6</sub>-Al<sub>2</sub>O<sub>3</sub>-wet-473-100 (1.45 molCO g<sub>Pt</sub><sup>-1</sup> h<sup>-1</sup>). Interestingly, the reduction at 373 K without

added water results in Pt<sub>2.1</sub>Fe<sub>3.6</sub>-Al<sub>2</sub>O<sub>3</sub>-373-100 with a significantly smaller PROX reaction rate of 0.7 molCO gPt<sup>-1</sup> h<sup>-1</sup> (**Figure 5-2**). Addition of water during the reduction step evidently improves PROX activity without compromising the carbon monoxide selectivity under the kinetic reaction regime. Catalyst dehydration significantly decreases the catalytic activity. Pt<sub>2.0</sub>Fe<sub>1.4</sub>-SiO<sub>2</sub>-473-100 loses its activity after dehydration at 673 K under an inert atmosphere, as shown in **Figure 5-2**. After 20 min of the reaction, Pt<sub>2.0</sub>Fe<sub>1.4</sub>-SiO<sub>2</sub>-473-100 shows a PROX reaction rate of 3.3 molCO gPt<sup>-1</sup> h<sup>-1</sup>; the dehydration at 673 K decreases this value to 1.16 molCO gPt<sup>-1</sup> h<sup>-1</sup> for Pt<sub>2.0</sub>Fe<sub>1.4</sub>-SiO<sub>2</sub>-473-100-deh (**Figure 5-2a**). Reaction rates drop significantly over 20 min on stream for all catalysts except for deactivated Pt<sub>2.0</sub>Fe<sub>1.4</sub>-SiO<sub>2</sub>-473-100-deh. Likely, deactivation can be explained by dehydroxylation of active FeO<sub>x</sub>(OH)<sub>y</sub> sites, which is irreversible under preferential carbon monoxide oxidation conditions. The activity of unpromoted platinum catalysts: Pt<sub>2.0</sub>-Al<sub>2</sub>O<sub>3</sub>-473-100 and Pt<sub>2.0</sub>-SiO<sub>2</sub>-473-100 lies below the detection limit of the mass spectrometer at 313 K (**Figure 5-2a**). **Figure 5-2a** also demonstrates that steam treatment is incapable of improving the catalytic activity of unpromoted platinum catalysts.

As evident from electron microscopy images, the addition of water does not significantly affect particle size distribution of the reduced catalysts. Ex situ scanning transmission electron microscopy (STEM) coupled with energy dispersive X-ray emission analysis showed that the nanoparticles formed after reduction contain both iron and platinum (**Figure S3-4**). The size of nanoparticles (**Figure S3-5**) on silica in Pt<sub>2.0</sub>-SiO<sub>2</sub>-473-100 (1.7 ± 0.3 nm) slightly increases upon the addition of iron (Pt<sub>2.0</sub>Fe<sub>1.4</sub>-SiO<sub>2</sub>-473-100: 2.1 ± 0.3 nm). Dehydration also does not strongly impact platinum particle size distribution for Pt<sub>2.0</sub>Fe<sub>1.4</sub>-SiO<sub>2</sub>-473-100-deh (1.7 ± 0.2 nm). The average particle diameter in alumina-supported Pt<sub>2.0</sub>-Al<sub>2</sub>O<sub>3</sub>-473-100 (1.0 ± 0.2 nm) also slightly increases upon the addition of iron for Pt<sub>2.1</sub>Fe<sub>3.6</sub>-Al<sub>2</sub>O<sub>3</sub>-473-100 (1.5 ± 0.3 nm) and Pt<sub>2.1</sub>Fe<sub>3.6</sub>-Al<sub>2</sub>O<sub>3</sub>-wet-473-100 (1.3 ± 0.3 nm). Reduction in the presence of water vapor for Pt<sub>2.1</sub>Fe<sub>3.6</sub>-Al<sub>2</sub>O<sub>3</sub>-473-98-steam yields a particle size distribution 0.9 ± 0.3 nm, similar to that of Pt<sub>2.0</sub>-Al<sub>2</sub>O<sub>3</sub>-473-100 (**Figure S3-5**).

### 5.3.2 Water Influence on Reaction Kinetics

Thus, water likely assists the formation of a certain active FeO<sub>x</sub>OH<sub>y</sub>/Pt interface, and, at the same time, does not significantly influence the nanoparticles size distribution. To understand whether addition of water to the PROX mixture can affect carbon monoxide oxidation we performed independent kinetic tests. These tests revealed that water vapor increases the reaction rate. Water exposure time was controlled using a mechanical 3-way valve (**Figure S3-2**). Water content added to the flow was varied between 0.8 vol.% and 4 vol.% H<sub>2</sub>O. Water content after the reactor was additionally monitored using a mass spectrometer as indicated in **Figure 5-3**, its signal was delayed because of the water absorption by the sample. The carbon monoxide oxidation rate increased with the water vapor addition and decreased upon its removal. This was tested repeatedly for various catalysts and yielded a water reaction order of 0.09-0.17 (**Figure 5-3d**). The addition of water to the reaction stream for Pt<sub>2.1</sub>Fe<sub>3.6</sub>-Al<sub>2</sub>O<sub>3</sub>-473-100 and Pt<sub>2.1</sub>Fe<sub>3.6</sub>-Al<sub>2</sub>O<sub>3</sub>-wet-473-100 was realized after the main kinetic measurements (**Figure 5-3a,c**), while a separate experiment was done for Pt<sub>2.1</sub>Fe<sub>3.6</sub>-Al<sub>2</sub>O<sub>3</sub>-473-98-steam to test the reproducibility (**Figure 5-3b**). The water-gas shift reaction with the mixture of 5 vol.% CO + 2 vol.% H<sub>2</sub>O showed the estimated rate of under 0.008 molCO gPt<sup>-1</sup> h<sup>-1</sup> for alumina-supported catalysts and also for Pt<sub>2.0</sub>Fe<sub>1.4</sub>-SiO<sub>2</sub>-473-100 (**Figure S3-6**), which is two orders of magnitude smaller than the actual PROX rate. The methanation did not take place as no methane (m/z = 15) was detected in the mass spectrometer for all kinetic tests. Clearly, water affected either the PROX catalytic cycle or the number of active sites. Previously, we reported that the PROX activity of Pt-Fe-FeO<sub>x</sub>/γ-Al<sub>2</sub>O<sub>3</sub> reduced in pure hydrogen at 673 K was not affected by the addition of water. Counting all the evidence, we conclude that the effect of water vapor on catalytic activity depends on the catalyst history. Moreover, the reduction in hydrogen atmosphere containing steam at 473 K (**Figure 5-2a,c**) increases the catalytic activity much more than a simple addition of water vapor to the PROX mixture at 313 K (**Figure 5-3**).

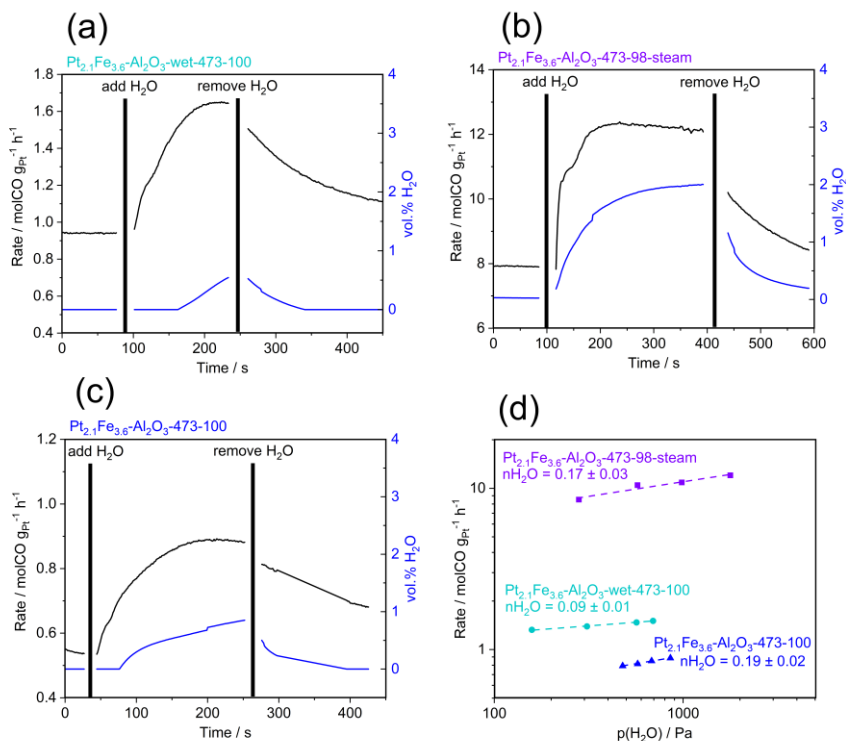


Figure 5-3. The effect of water addition on PROX rate at 313 K under 2 vol.%  $\text{O}_2$  + 40 vol.%  $\text{H}_2$  + 5 vol.%  $\text{CO}$  at 313 K over  $\text{Pt}_{2.1}\text{Fe}_{3.6}\text{-Al}_2\text{O}_3\text{-wet-473-100}$  (a),  $\text{Pt}_{2.1}\text{Fe}_{3.6}\text{-Al}_2\text{O}_3\text{-473-98-steam}$  (b), and  $\text{Pt}_{2.1}\text{Fe}_{3.6}\text{-Al}_2\text{O}_3\text{-473-100}$  (c); (d) correlations between the estimated partial pressure of added water and the PROX rate.

### 5.3.3 $^{18}\text{O}$ -labeling Experiments

With the aim of understanding the mechanism of water action, we performed targeted experiments with  $^{18}\text{O}$ -labeled water. In these experiments, initial calcined samples were impregnated with  $\text{H}_2^{18}\text{O}$  instead of standard water and then exposed to the same reduction and reaction procedures as the original  $\text{Pt}_{2.1}\text{Fe}_{3.6}\text{-Al}_2\text{O}_3\text{-wet-473-100}$  and  $\text{Pt}_{2.1}\text{Fe}_{3.6}\text{-Al}_2\text{O}_3\text{-wet-373-100}$  catalysts. Under the catalytic conditions, **Figure S3-7a** shows no evidence of  $^{18}\text{O}$ -labeled oxygen, carbon monoxide, carbon dioxide, or even water present over reduced  $\text{Pt}_{2.1}\text{Fe}_{3.6}\text{-Al}_2\text{O}_3\text{-wet}(\text{H}_2^{18}\text{O})\text{-473-100}$ . This behavior explains why  $\text{Pt}_{2.1}\text{Fe}_{3.6}\text{-Al}_2\text{O}_3\text{-473-100}$  and  $\text{Pt}_{2.1}\text{Fe}_{3.6}\text{-Al}_2\text{O}_3\text{-wet-473-100}$  have similar activities. During the reduction at 473 K, adsorbed water species evaporate and have no influence on the catalytic activity of  $\text{Pt}_{2.1}\text{Fe}_{3.6}\text{-Al}_2\text{O}_3\text{-wet-473-100}$ .

On the contrary,  $\text{Pt}_{2.1}\text{Fe}_{3.6}\text{-Al}_2\text{O}_3\text{-wet}(\text{H}_2^{18}\text{O})\text{-373-100}$  retains some  $\text{H}_2^{18}\text{O}$  on the surface, which indicates that reduction at 373 K is unable to completely remove adsorbed water. Most importantly, right after the addition of oxygen to the hydrogen and carbon monoxide mixture, this catalyst exhibits a prominent peak of  $\text{C}^{16}\text{O}^{18}\text{O}$  (**Figure 5-4a**), which does not appear during the blank experiment with the unlabeled water (**Figure 5-4b**). It is essential that the  $\text{C}^{16}\text{O}^{18}\text{O}$  signals appear only after the addition of oxygen to the feed, and the rate of isotopic exchange between  $\text{H}_2^{18}\text{O}$  and  $\text{CO}_2$  is 10 times lower (**Figure S3-7c**). Notably, the signal of  $^{18}\text{O}$ -labeled water and carbon dioxide gradually disappear, however,  $\text{Pt}_{2.1}\text{Fe}_{3.6}\text{-Al}_2\text{O}_3\text{-wet-373-100}$  still stays more active than  $\text{Pt}_{2.1}\text{Fe}_{3.6}\text{-Al}_2\text{O}_3\text{-473-100}$  and  $\text{Pt}_{2.1}\text{Fe}_{3.6}\text{-Al}_2\text{O}_3\text{-473-100}$ , which suggests that for this catalyst active water or hydroxyl species are always present on the surface. This is confirmed by another experiment during which the pulse of oxygen is added directly into the PROX mixture over  $\text{Pt}_{2.1}\text{Fe}_{3.6}\text{-Al}_2\text{O}_3\text{-473-100}$  treated with  $\text{H}_2^{18}\text{O}$  vapor, and the catalyst immediately produces  $\text{C}^{16}\text{O}^{18}\text{O}$  (**Figure 5-4c**). The observed production of  $\text{C}^{16}\text{O}^{18}\text{O}$  cannot be explained by an isotopic exchange between water and reaction gases, as confirmed by blank experiments shown in **Figures S3-7 and 5-4d**. These results confirm that water or active hydroxyls adsorbed next to active  $\text{Fe}^{2+}$  sites can be directly involved in the PROX catalytic cycle.

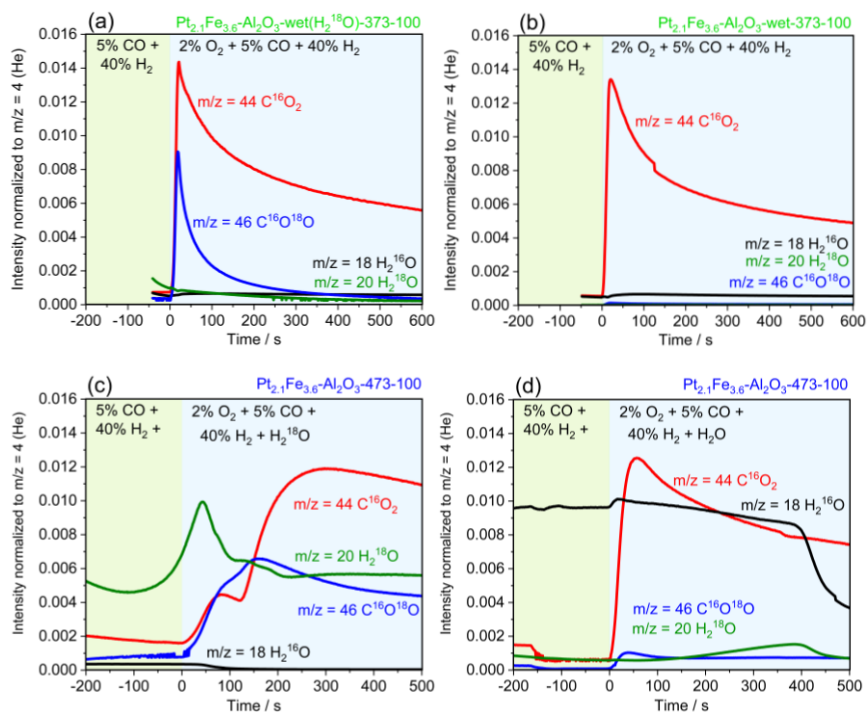


Figure 5-4. Helium-normalized MS signals of reaction gases at 313 K during (a,b) oxygen addition into PROX mixture over  $\text{Pt}_{2.1}\text{Fe}_{3.6}\text{-Al}_2\text{O}_3\text{-wet-373-100}$  catalyst soaked with  $\text{H}_2^{18}\text{O}$  before reduction (a) and soaked with standard water before reduction (b); helium-normalized MS signals of reaction gases at 313 K during direct addition of oxygen together with  $\text{H}_2^{18}\text{O}$  (c) and standard  $\text{H}_2\text{O}$  (d) pulses over  $\text{Pt}_{2.1}\text{Fe}_{3.6}\text{-Al}_2\text{O}_3\text{-473-100}$ . Gas concentrations are shown in vol. %.



### 5.3.4 Operando Fe K-edge XAS Experiments

As it was shown in Chapter 4, the ambient temperature PROX activity of supported Pt-Fe catalysts is directly proportional to the number of oxidic  $\text{Fe}^{2+}$  species. It is essential to verify how water affects the structure or the amount of these species. Operando XAS allowed us to extract this information by measuring Fe K-edge XAS during all kinetic measurements and temperature-programmed reduction experiments. The spectra measured during temperature-programmed reduction are shown in **Figure S3-8**. We performed a linear combination fit using  $\text{Fe}^{2+}$  and  $\text{Fe}^{3+}$  references to determine the concentration of different iron oxidic species in the same manner as in Chapter 4. Fe K-edge XAS of FeO was used as a general  $\text{Fe}^{2+}$  reference for all catalysts.  $\text{Fe}^{3+}$  references were slightly different for each catalyst; they were measured on each individual catalyst after PROX tests followed by temperature-programmed oxidation up to 473 K, assuring complete oxidation of all  $\text{Fe}^{2+}$ .

Using these references, a linear combination fit of Fe K-edge XANES spectra in the 7100 - 7160 eV range made it possible to extract the concentration of  $\text{Fe}^{2+}$  sites during temperature-programmed reduction, as shown in **Figure 5-5a**. No metallic iron was detected in any of the samples. About 44-46%  $\text{Fe}^{2+}$  was formed after the reduction of  $\text{Pt}_{2.1}\text{Fe}_{3.6}\text{-Al}_2\text{O}_3\text{-473-100}$  and  $\text{Pt}_{2.1}\text{Fe}_{3.6}\text{-Al}_2\text{O}_3\text{-wet-473-100}$ . As was expected from the catalytic tests and experiments with  $\text{H}_2^{18}\text{O}$ , water desorbed below 473 K and, thus, had no effect on the amount of produced  $\text{Fe}^{2+}$  after the reduction at this temperature. Water started to influence the reduction of oxidic iron sites only below 430 K. In  $\text{Pt}_{2.1}\text{Fe}_{3.6}\text{-Al}_2\text{O}_3\text{-473-98}$ -steam catalyst water vapor was constantly present in small amounts during the reduction step, which promoted the formation of  $\text{Fe}^{2+}$ , resulting in ca. 54%  $\text{Fe}^{2+}$  at 473 K.  $\text{Pt}_{2.1}\text{Fe}_{3.6}\text{-Al}_2\text{O}_3\text{-wet-373-100}$  catalyst almost reproduced the iron reduction curve of  $\text{Pt}_{2.1}\text{Fe}_{3.6}\text{-Al}_2\text{O}_3\text{-wet-473-100}$  below 373 K. The formation of iron hydroxides can facilitate  $\text{Fe}^{3+}$  reduction, as certain iron hydroxides are less thermodynamically stable towards reduction than iron oxides (**Table S3-4**). Fe K-edge XANES and EXAFS spectra of  $\text{Pt}_{2.0}\text{Fe}_{1.4}\text{-SiO}_2\text{-473-100}$  and  $\text{Pt}_{2.0}\text{Fe}_{1.4}\text{-SiO}_2\text{-473-100-deh}$  recorded after reduction are almost identical (**Figure 5-5b**), which confirms that dehydration at 673 K does not change the local structure of the majority of iron species. Interestingly, iron sites in  $\text{Pt}_{2.1}\text{Fe}_{3.6}\text{-Al}_2\text{O}_3\text{-473-100-deh}$  sample undergo auto-reduction under helium at 673 K, similarly to FeZSM-5, which, however, does not affect the catalytic activity significantly (**Figure S3-9**).<sup>26</sup> The negative effect of dehydration of  $\text{Pt}_{2.1}\text{Fe}_{3.6}\text{-Al}_2\text{O}_3\text{-473-100-deh}$  is compensated by a higher amount of  $\text{Fe}^{2+}$ , in comparison to  $\text{Pt}_{2.1}\text{Fe}_{3.6}\text{-Al}_2\text{O}_3\text{-473-100}$ .

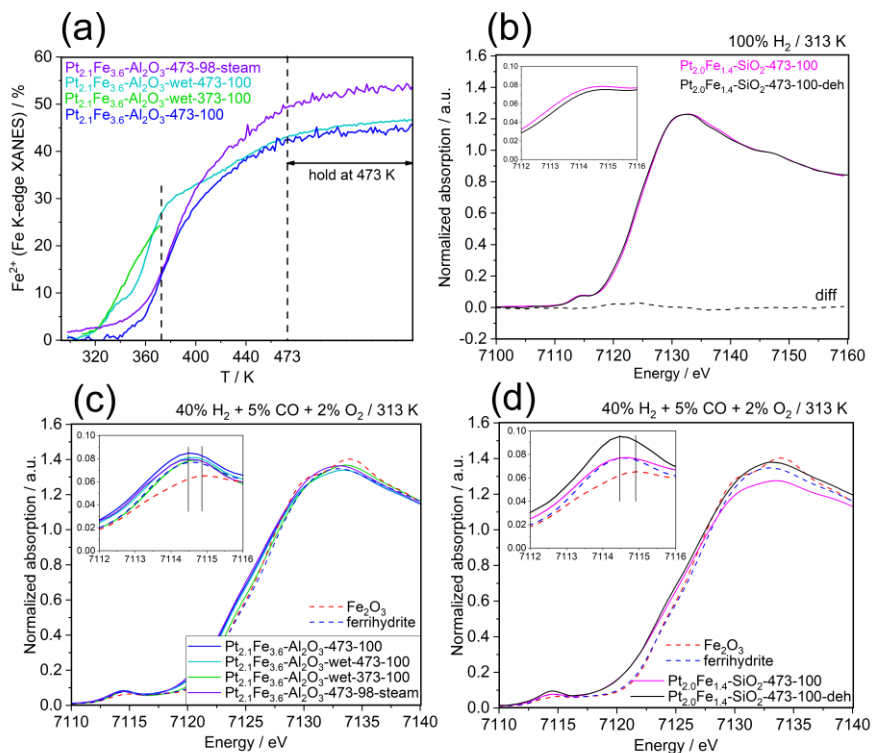


Figure 5-5. (a) Concentration of  $\text{Fe}^{2+}$  during the temperature-programmed reduction obtained using linear combination fitting of in situ Fe K-edge XANES; (b) in situ Fe K-edge XANES of  $\text{SiO}_2$ -supported catalysts after reduction under 100%  $\text{H}_2$  and optional dehydration at 673 K under helium; (c) operando Fe K-edge XANES of  $\gamma\text{-Al}_2\text{O}_3$ - and (d)  $\text{SiO}_2$ -supported catalysts (solid lines) under PROX conditions at 313 K;  $\text{Fe}_2\text{O}_3$ , ferrihydrate references (dashed) are shown for comparison. Gas concentrations are shown in vol. %.

Fe K-edge XANES data measured during 200 - 500 s of preferential carbon monoxide oxidation kinetic tests were averaged and shown in **Figure 5-5c,d**. As we reported before, iron sites unable to be reduced by carbon monoxide adsorbed on platinum are irreversibly oxidized during the first 100 s after the addition of oxygen, while only the minority of sites remain in a reduced state, and these are precisely the sites that are catalytically active. This explains why Fe K-edge XANES spectra of all catalysts under PROX look similar to fully oxidized ferrihydrate or  $\alpha\text{-Fe}_2\text{O}_3$  with only a tiny percentage of active oxidic  $\text{Fe}^{2+}$  sites. The Fe K-edge pre-edge position is sensitive to the oxidation state, while its intensity correlates with the oxygen coordination number. Fe K-edge spectra of the catalysts look similar to that of an amorphous ferrihydrate reference, in which a high fraction of  $\text{Fe}^{3+}$  sites are coordinated by four oxygen ligands (**Figure S3-10**). This is particularly noticeable in the pre-edge region due to the low-

coordinated nature of oligomeric oxidic surface iron species coordinating oxygen and water molecules in the catalyst.<sup>27</sup> Fourier-transformed Fe K-edge EXAFS (**Figure S3-10**) shows that the amplitude of the first Fe-O coordination sphere peak of Fe K-edge EXAFS at ca. 1.38 Å is the highest for Pt<sub>2.1</sub>Fe<sub>3.6</sub>-Al<sub>2</sub>O<sub>3</sub>-wet-373-100 and Pt<sub>2.0</sub>Fe<sub>1.4</sub>-SiO<sub>2</sub>-473-100-deh.

The number of Fe-O-Fe bonds in the second coordination sphere indicates the level of aggregation and disorder of the iron oxide phase. As one can see in **Figure S3-10**, the second coordination shell peak at ca. 2.5 Å has an intermediate intensity between amorphous ferrihydrite (first Fe-O-Fe neighbor) and Fe<sub>2</sub>O<sub>3</sub> for all catalysts. To estimate the coordination numbers and bond lengths, we performed Fe K-edge EXAFS fitting. The results are shown in **Table S3-5** and **Figures S3-11-1 and S3-11-2**. For all catalysts, the number of Fe-O-Fe bonds in the second coordination sphere corresponds to 1-2 iron neighbors at a distance of about 2.94-2.96 Å (**Table S3-5**). Fe-O coordination for most samples is close to 4-5, which is typical for surface FeO<sub>x</sub>OH<sub>y</sub> oligomers on  $\gamma$ -Al<sub>2</sub>O<sub>3</sub> supports in a partially reduced state.<sup>5,6</sup> Smaller number of Fe-O-Fe bonds in Pt<sub>2.1</sub>Fe<sub>3.6</sub>-Al<sub>2</sub>O<sub>3</sub>-473-98-steam (**Table S3-5**) might indicate that water hinders the aggregation of oxidic iron clusters, which could stabilize an active interface with platinum, as was shown in Chapter 4. A linear combination fitting of Fe K-edge XANES allowed us to extract the average oxidation state of surface FeO<sub>x</sub>(OH)<sub>y</sub> species using the same references as for the in situ temperature-programmed reduction. The results of these fits for the catalysts under PROX conditions in the time period of 200 - 500 s are presented in **Figure S3-12**; Fe K-edge XANES spectra were averaged every 100 s as shown in **Figure 5-6a**. 54% Fe<sup>2+</sup> sites reduced by hydrogen in Pt<sub>2.1</sub>Fe<sub>3.6</sub>-Al<sub>2</sub>O<sub>3</sub>-473-98-steam catalysts are rapidly oxidized under PROX conditions to 14-17% Fe<sup>2+</sup>; the same occurs for all alumina-supported catalysts, Pt<sub>2.1</sub>Fe<sub>3.6</sub>-Al<sub>2</sub>O<sub>3</sub>-473-100 and Pt<sub>2.1</sub>Fe<sub>3.6</sub>-Al<sub>2</sub>O<sub>3</sub>-wet-473-100 show similar amounts of active Fe<sup>2+</sup> sites (8-16% Fe<sup>2+</sup> under PROX conditions). Fe<sup>2+</sup> concentration in Pt<sub>2.1</sub>Fe<sub>3.6</sub>-Al<sub>2</sub>O<sub>3</sub>-wet-373-100 decreased to less than 2% under PROX conditions.

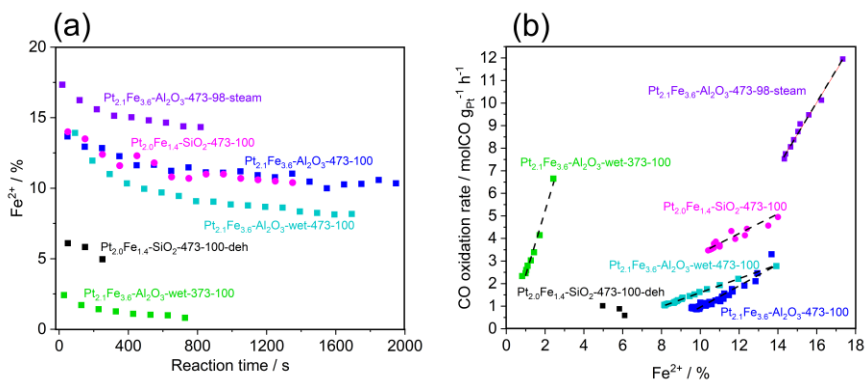


Figure 5-6. Evolution of the Fe<sup>2+</sup> concentration under PROX conditions for different catalysts monitored by operando Fe K-edge XANES (a). Correlation between the concentration of Fe<sup>2+</sup> and the PROX activity (b). At time zero, we added 2 vol.% O<sub>2</sub> into the 40 vol.% H<sub>2</sub> + 5 vol.% CO mixture; the reaction temperature was 313 K; data points were averaged every 100 s.

To visualize the structure-activity relationship, we correlated the PROX activity and  $\text{Fe}^{2+}$  concentrations measured during the deactivation of the catalysts under PROX conditions (**Figure 5-6b**). As we have shown in Chapter 4, the concentration of surface  $\text{Fe}^{2+}$  species linearly correlates with the PROX activity. The slope between the PROX rate and  $\text{Fe}^{2+}$  concentration indicates how much carbon monoxide can be oxidized per single active  $\text{Fe}^{2+}$  cation. Water treatment of  $\text{Pt}_{2.1}\text{Fe}_{3.6}\text{-Al}_2\text{O}_3\text{-473-98-steam}$  and  $\text{Pt}_{2.1}\text{Fe}_{3.6}\text{-Al}_2\text{O}_3\text{-wet-373-100}$  results in a steeper activity -  $\text{Fe}^{2+}$  concentration slope. This slope expressed in  $\text{molCO} (\text{molFe}^{2+} \text{ s})^{-1}$  units can be assigned to the apparent turnover frequency for each active  $\text{Fe}^{2+}$  site. For  $\text{Pt}_{2.1}\text{Fe}_{3.6}\text{-Al}_2\text{O}_3\text{-wet-373-100}$ , the slope is  $2.5 \text{ molCO} (\text{molFe}^{2+} \text{ s})^{-1}$ ; for  $\text{Pt}_{2.1}\text{Fe}_{3.6}\text{-Al}_2\text{O}_3\text{-473-98-steam}$ , it is  $1.3 \text{ molCO} (\text{molFe}^{2+} \text{ s})^{-1}$ . As shown previously,  $\text{Pt}_{2.1}\text{Fe}_{3.6}\text{-Al}_2\text{O}_3\text{-wet-473-100}$  does not retain any initially adsorbed water after the pretreatment step, thus, its slope is only  $0.3 \text{ molCO} (\text{molFe}^{2+} \text{ s})^{-1}$ , which is close to  $0.4 \text{ molCO} (\text{molFe}^{2+} \text{ s})^{-1}$  observed for  $\text{Pt}_{2.1}\text{Fe}_{3.6}\text{-Al}_2\text{O}_3\text{-473-100}$ .  $\text{Pt}_{2.0}\text{Fe}_{1.4}\text{-SiO}_2\text{-473-100}$  exhibits a slope of  $0.8 \text{ molCO} (\text{molFe}^{2+} \text{ s})^{-1}$ . Further dehydration at 673 K under an inert atmosphere for  $\text{Pt}_{2.0}\text{Fe}_{1.4}\text{-SiO}_2\text{-473-100-deh}$  results in a lower number of active  $\text{Fe}^{2+}$  sites under PROX conditions due to the removal of adsorbed water. As the linear curve of activity -  $\text{Fe}^{2+}$  trend of  $\text{Pt}_{2.1}\text{Fe}_{3.6}\text{-Al}_2\text{O}_3\text{-473-98-steam}$  does not tend to zero, it seems that along with the active  $\text{Fe}^{2+}$  sites, this catalyst contains a significant concentration of inactive (spectator)  $\text{Fe}^{2+}$ . The same is true for  $\text{Pt}_{2.1}\text{Fe}_{3.6}\text{-Al}_2\text{O}_3\text{-473-100}$  and  $\text{Pt}_{2.1}\text{Fe}_{3.6}\text{-Al}_2\text{O}_3\text{-wet-473-100}$ . These spectator species most likely represent trapped  $\text{Fe}^{2+}$  sites not accessible for direct oxidation and not participating in catalysis.

Oxygen reaction orders (**Figure S3-13**) during PROX are almost the same for all alumina-supported catalysts and lie within 0.7-0.8, which means that the presence of hydroxyl groups or adsorbed water on  $\text{Fe}^{2+}\text{O}_x\text{OH}_y$  sites does not significantly influence the mechanism of oxygen activation over alumina-supported catalysts. At the same time,  $\text{Pt}_{2.0}\text{Fe}_{1.4}\text{-SiO}_2\text{-473-100-deh}$  has a lower oxygen reaction order (0.5), while it is much higher for  $\text{Pt}_{2.0}\text{Fe}_{1.4}\text{-SiO}_2\text{-473-100}$  (1.0). Thus, we conclude that in the absence of water, oxygen activation takes a different path for the dehydrated  $\text{Pt}_{2.0}\text{Fe}_{1.4}\text{-SiO}_2\text{-473-100-deh}$ , likely similar to the one described in Chapter 3. At the same time, there is no clear correlation between water treatment and carbon monoxide reaction order (**Figure S3-13**), suggesting the mechanism of carbon monoxide activation remains similar.

### 5.3.5 Operando DRIFTS Experiments

In situ DRIFTS spectroscopy was subsequently employed to clarify the nature of adsorbed water species. For operando DRIFTS, we employed the same experimental protocols as for operando Fe K-edge XAS. **Figure S3-14** shows averaged DRIFTS spectra of  $\text{Pt}_{2.1}\text{Fe}_{3.6}\text{-Al}_2\text{O}_3\text{-473-100}$ ,  $\text{Pt}_{2.0}\text{-Al}_2\text{O}_3\text{-473-98-steam}$ , and  $\text{Pt}_{2.1}\text{Fe}_{3.6}\text{-Al}_2\text{O}_3\text{-473-98-steam}$  catalysts during 200-500 s of exposure to PROX conditions. Adsorbed water forms surface hydroxyl groups with the O-H stretching peaks centred at  $3681 \text{ cm}^{-1}$  for  $\text{Pt}_{2.1}\text{Fe}_{3.6}\text{-Al}_2\text{O}_3\text{-473-98-steam}$  and  $3735 \text{ cm}^{-1}$  for  $\text{Pt}_{2.0}\text{-Al}_2\text{O}_3\text{-473-98-steam}$  catalysts, respectively.<sup>18,19</sup> The C-O stretching peak, corresponding to carbon monoxide linearly adsorbed on metallic platinum, shifts for water-treated samples. Namely,  $\text{Pt}_{2.1}\text{Fe}_{3.6}\text{-Al}_2\text{O}_3\text{-473-98-steam}$  and  $\text{Pt}_{2.0}\text{-Al}_2\text{O}_3\text{-473-98-steam}$  exhibit these peaks at  $2041\text{-}2042 \text{ cm}^{-1}$ , while for  $\text{Pt}_{2.1}\text{Fe}_{3.6}\text{-Al}_2\text{O}_3\text{-473-100}$ , this peak is at  $2052\text{-}2054 \text{ cm}^{-1}$ . This shift indicates that water adsorbs on the support close to metallic platinum and influences its electronic structure<sup>18,19</sup>, even without iron. The shoulder at  $2075 \text{ cm}^{-1}$  is assigned to carbon monoxide adsorbed on  $\text{Pt}^{\delta+}$  species; the band at  $1820 \text{ cm}^{-1}$  is typical for platinum nanoparticles of 1-2 nm in size, as discussed in Chapter 4.<sup>27</sup> Additional peaks at  $1578$  and  $1457 \text{ cm}^{-1}$  correspond to O-C-O stretching vibrations in carbonates and formates, which exist even in the absence of iron.<sup>18,28,29</sup> A broad band above  $3650 \text{ cm}^{-1}$  is present only for iron-containing samples and was previously observed for Pt- $\text{FeO}_x$  catalysts exposed to carbon monoxide.<sup>19</sup> This band was found to be sensitive to the redox state of iron oxidic species and is likely associated with a general change in reflectivity and a certain optical band gap of a reduced iron oxide/hydroxide lattice.<sup>19</sup>

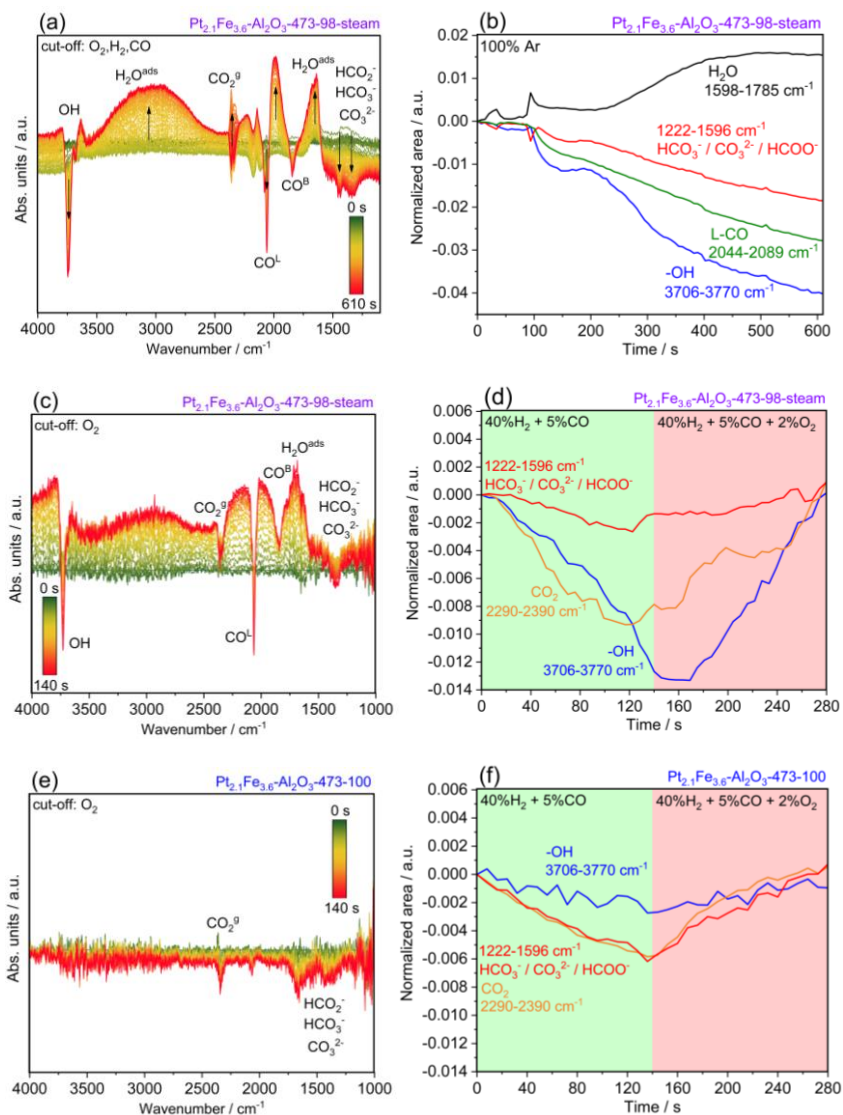


Figure 5-7. In situ DRIFTS spectra measured during selected cut-offs: (a) of all reaction gases over Pt<sub>2.1</sub>Fe<sub>3.6</sub>-Al<sub>2</sub>O<sub>3</sub>-473-98-steam, of oxygen over Pt<sub>2.1</sub>Fe<sub>3.6</sub>-Al<sub>2</sub>O<sub>3</sub>-473-98-steam (c) and Pt<sub>2.1</sub>Fe<sub>3.6</sub>-Al<sub>2</sub>O<sub>3</sub>-473-100 (e); corresponding changes in the normalized area of DRIFTS peaks in the consecutive oxygen cut-offs during 0-140 s and oxygen addition after 140 s (d,f), and these changes after the cut-off of all reaction gases from the reaction mixture (b). All spectra were measured at 313 K; gas concentrations were 40 vol.% H<sub>2</sub>, 5 vol.% CO, 2 vol.% O<sub>2</sub>.

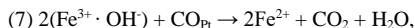
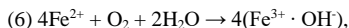
Fast gas switching (cut-off) experiments allowed us to extract the evolution of DRIFTS signals related to surface species. First, after 500 s exposure of Pt<sub>2.1</sub>Fe<sub>3.6</sub>-Al<sub>2</sub>O<sub>3</sub>-473-98-steam to PROX mixture, we cut all reaction gases using fast solenoid valves installed in our experimental setup (**Figure S3-2**) and replaced them with the same flow of argon. As evident from **Figure 5-7a**, after the catalyst was left without any reactive gases, the intensity of bands associated with surface -OH groups (3745 cm<sup>-1</sup>) and adsorbed carbon monoxide (2058 cm<sup>-1</sup>, 1842 cm<sup>-1</sup>) decreased, and at the same time, the amount of adsorbed water increased as it is evident from the appearance of 2800-3300, 1637 and 1984 cm<sup>-1</sup> bands.<sup>18,19</sup> A raise of DRIFTS intensity at 1980 cm<sup>-1</sup> indicates the change of surface carbon monoxide coverage.<sup>18,19</sup> The amount of produced gas phase carbon dioxide (2290-2390 cm<sup>-1</sup>) initially increased and then gradually decreased.<sup>18,19</sup> This carbon dioxide should be produced from adsorbed carbon monoxide remaining on the platinum surface. For each peak, the integrated areas were normalized to the energy window ( $\Delta E$ , cm<sup>-1</sup>) and are presented in **Figure 5-7b**. Consumption of carbon monoxide and hydroxyl groups happen simultaneously, water-associated bands at 1598-1785 and around 3000 cm<sup>-1</sup> start appearing at the same time. The bands in the 1222-1596 cm<sup>-1</sup> region corresponding to surface bicarbonates, carbonates, and formates cannot be separated from each other and are likely related to the shift in DRIFTS background due to the change in surface reflectivity.<sup>18,29,30</sup>

The results of oxygen cut-off experiments shown in **Figure 5-7c,d** confirm that surface hydroxyl groups participate in the oxidation of carbon monoxide under reaction conditions over Pt<sub>2.1</sub>Fe<sub>3.6</sub>-Al<sub>2</sub>O<sub>3</sub>-473-98-steam. Hydroxyl groups (3730 cm<sup>-1</sup>) are removed together with the gas phase carbon dioxide (2290 - 2390 cm<sup>-1</sup>) immediately after the oxygen cut-off (**Figure 5-7c**). These hydroxyl groups are absent for the Pt<sub>2.1</sub>Fe<sub>3.6</sub>-Al<sub>2</sub>O<sub>3</sub>-473-100 catalyst (**Figure 5-7e**), which shows only a slight decrease in the carbon dioxide band due to lower PROX activity. Surface bicarbonate, carbonate, and formate species do not play a significant role in PROX over Pt<sub>2.1</sub>Fe<sub>3.6</sub>-Al<sub>2</sub>O<sub>3</sub>-473-98-steam as evident from **Figure 5-7d**, in contradiction to the previously proposed water-assisted mechanism involving surface formates (HCOO).<sup>29</sup> As was shown previously for Pt-FeO<sub>x</sub>/ $\gamma$ -Al<sub>2</sub>O<sub>3</sub>, these species are always present on the surface of  $\gamma$ -Al<sub>2</sub>O<sub>3</sub> support, and their formation does not limit the desorption of carbon dioxide as the reaction product.<sup>26</sup> The observed reaction of hydroxyl groups with adsorbed carbon monoxide is reversible (**Figure 5-7d**), which indicates that active hydroxyl groups are formed during oxygen exposure of Pt<sub>2.1</sub>Fe<sub>3.6</sub>-Al<sub>2</sub>O<sub>3</sub>-473-98-steam and are quickly consumed upon oxygen removal. Changes in the concentration of hydroxyl groups do not appear during oxygen cut-off over Pt<sub>2.0</sub>-Al<sub>2</sub>O<sub>3</sub>-473-98-steam (**Figure S3-15**), which suggests that the reactive hydroxyl groups are linked exclusively to surface iron sites and the formation of hydroxylated surface FeO<sub>x</sub>(OH)<sub>y</sub> species is responsible for the enhanced PROX activity.

### 5.3.6 Water Influence on Reaction Mechanism

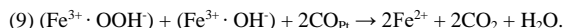
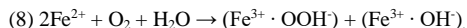
Performed experiments clarify that the presence of iron-associated hydroxyl groups is critical to ensure high activity in preferential carbon monoxide oxidation at ambient temperature. Complex synthetic methods reported before are not always necessary to create active FeO<sub>x</sub>(OH)<sub>y</sub> sites. A simple treatment of supported Pt-FeO<sub>x</sub>(OH)<sub>y</sub> catalysts with water during the reduction in hydrogen at 473 K makes it possible to achieve high activities.<sup>4,20,23</sup> Moreover, the dehydration of platinum-iron catalysts at 673 K (as in the case of Pt<sub>2.0</sub>Fe<sub>1.4</sub>-SiO<sub>2</sub>-473-100-deh) reduces the activity of each individual Fe<sup>2+</sup> oxidic site. Importantly, the use of water during the reduction step below 473 K increases the apparent PROX turnover rate of active Fe<sup>2+</sup> sites (**Figure 5-6b**). Since the oxygen reaction order is close to unity (0.7 - 1.0) and catalytic activity is proportional to the concentration of unsaturated Fe<sup>2+</sup> sites, we propose that the main rate-limiting step of ambient temperature PROX for the water-pretreated catalysts is the activation of oxygen (**Scheme 5-1**). As suggested by Fe K-edge EXAFS, iron forms FeO<sub>x</sub>(OH)<sub>y</sub> oligomers in close proximity to platinum nanoparticles with about 1-2 nearest iron neighbors. Since iron-associated hydroxyl groups distinguish the most active Pt-Fe catalysts, we could

suggest two various reaction mechanisms involving either dissociative or non-dissociative oxygen adsorption on unsaturated  $\text{Fe}^{2+}$  sites. Dissociative oxygen adsorption would result in the following reaction pathway:

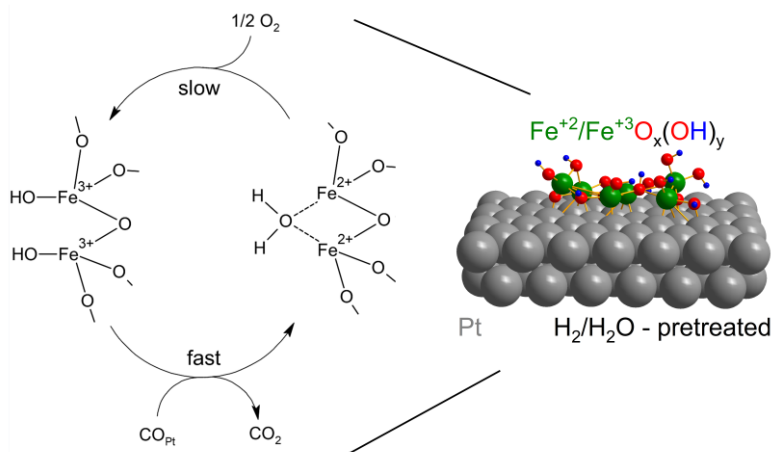


where  $\text{CO}_{\text{Pt}}$  represents the carbon monoxide molecule adsorbed on platinum.

As suggested in the literature, the presence of  $\text{FeO}_x(\text{OH})_y$  species enables to retain and rapidly exchange hydroxyl groups and water.<sup>20</sup> The presence of catalytically active hydroxyl groups is confirmed by DRIFTS (**Figure 5-7**). However, as equation 6 suggests, the dissociative water-assisted adsorption of oxygen requires up to four iron atoms. Catalysts under investigation have oxygen reaction orders of 0.7-1.0, which suggests a non-dissociative mechanism of oxygen adsorption. The non-dissociative water-assisted adsorption of oxygen can be realized through  $\text{OOH}^-$  intermediates, as discovered previously for gold-based catalysts.<sup>31</sup> In this case, another reaction pathway could take place:



In both cases, oxygen activation is the limiting step, and hydroxyl groups are directly involved. Previous theoretical studies confirm that hydroxylation of oxidic iron species at the Pt -  $\text{FeO}_x$  interface can, indeed, decrease the reaction barrier of carbon monoxide oxidation.<sup>32,33</sup> Based on these findings, we propose the following generalized mechanism scheme drawn in **Scheme 5-1**. It is worth noting that individual protons are not spent in the catalytic cycle and must be already present on the surface in adsorbed water or hydroxyl groups.



Scheme 5-1. Schematic representation of the proposed mechanism of preferential carbon monoxide oxidation over catalytically active  $\text{FeO}_x(\text{OH})_y/\text{Pt}$  sites. The model of the  $\text{FeO}_x(\text{OH})_y/\text{Pt}$  interface optimized by DFT is presented on the right.

An additional experiment with Pt<sub>2.1</sub>Fe<sub>3.6</sub>-Al<sub>2</sub>O<sub>3</sub>-wet-473-100 monitoring the concentration of Fe<sup>2+</sup> using operando Fe K-edge XAS during the addition of water directly into the PROX mixture (**Figure S3-16**) shows that while added water increases the carbon monoxide oxidation rate, it does not affect the average oxidation state of iron. From this experiment, it is clear that water can influence the structure of active sites only at higher temperatures (e.g. 473 K). Fe K-edge EXAFS shows that Pt<sub>2.1</sub>Fe<sub>3.6</sub>-Al<sub>2</sub>O<sub>3</sub>-473-98-steam contains FeO<sub>x</sub>(OH)<sub>y</sub> species in the least aggregated state (~0.7 Fe-O-Fe neighbors, **Table S3-5**) in comparison to other samples. Therefore, water treatment might stabilize active FeO<sub>x</sub>(OH)<sub>y</sub> species at the platinum interface by driving strong metal-support interaction between platinum and iron and preventing their aggregation in a Fe<sub>2</sub>O<sub>3</sub>-like phase described in Chapter 4. At the same time, an additional iron neighbor would be required to retain hydroxyls groups and water as shown in **Scheme 5-1**. To prove that water treatment at high temperatures can stabilize FeO<sub>x</sub>(OH)<sub>y</sub> oligomers on the surface of metallic platinum, we employed density functional theory calculations of an optimized cluster model of Fe<sub>6</sub>O<sub>14</sub>H<sub>11</sub>/Pt(111) depicted in Scheme 5-1. The calculations (**Figure S3-17**) showed that dehydration of this cluster results in its destabilization with dE = +0.38 eV after the removal of three structural water molecules and dE = +0.94 after the removal of five water molecules. Thus, the insertion of water in the cluster has a definitive stabilization effect and prevents oligomeric FeO<sub>x</sub>(OH)<sub>y</sub> species from aggregation and irreversible oxidation discussed in Chapter 4, leading to higher PROX activities. Catalyst deactivation can also be associated with water desorption and can be mitigated by feeding water vapor into the PROX mixture.



## 5.4 Conclusions

By means of a simple incipient wetness impregnation method, we prepared supported platinum-iron catalysts active in preferential carbon monoxide oxidation at ambient temperature. The reduction of alumina-supported platinum-iron catalysts under hydrogen mixed with water vapor allowed us to create one of the most active bimetallic platinum-iron catalysts on inert supports known to date. Operando XAS experiments demonstrated that water-treated platinum-iron catalysts supported on alumina exhibit PROX turnover frequencies of 1.3-2.5 molCO (molFe<sup>2+</sup> s)<sup>-1</sup> for active Fe<sup>2+</sup> sites, which is higher than for non-water treated catalysts exhibiting lower corresponding values of 0.3-0.4 molCO (molFe<sup>2+</sup> s)<sup>-1</sup>. We established that the addition of liquid water before the reduction pretreatment in pure hydrogen or the addition of steam during the pretreatment facilitates the reduction of surface iron oxidic oligomers and creates iron-associated hydroxyl groups that increase the PROX catalytic reaction rate. Direct addition of water into the PROX mixture can also increase the catalytic activity by hydroxylating FeO<sub>x</sub>(OH)<sub>y</sub> species but is unable to change the concentration of active Fe<sup>2+</sup>. On the contrary, dehydration of platinum-iron catalysts decreases the number of active Fe<sup>2+</sup> sites and leads to lower activity. Density functional theory calculations suggest that the addition of water during the pretreatment at 473 K can create active FeO<sub>x</sub>(OH)<sub>y</sub>/Pt interface.

## 5.5 References

1. International Renewable Energy Agency. Hydrogen overview. <https://www.irena.org/Energy-Transition/Technology/Hydrogen> (accessed January 2023).
2. Liu, K; Song, C. and Subramani, V., Ed. Hydrogen and syngas production and purification technologies.; John Wiley & Sons, Inc., 2010; pp. 127-155.
3. Pei, P.; Wang, M.; Chen, D.; Ren, P. and Zhang, L. Key technologies for polymer electrolyte membrane fuel cell systems fueled impure hydrogen. *Prog. Nat. Sci.* **2020**, *30*, 751-763.
4. Lou, Y. and Liu, J. A highly active Pt-Fe/ $\gamma$ -Al<sub>2</sub>O<sub>3</sub> catalyst for preferential oxidation of CO in excess of H<sub>2</sub> with a wide operation temperature window. *Chem. Comm.* **2017**, *53*, 9020-9023.
5. Sadykov, I.I.; Zabilskiy, M.; Clark, A.H.; Krumeich, F.; Sushkevich, V.L.; van Bokhoven, J.A.; Nachttegaal, M. and Safonova, O.V. Time-resolved XAS provides direct evidence for oxygen activation on cationic iron in a bimetallic Pt-FeO<sub>x</sub>/Al<sub>2</sub>O<sub>3</sub> catalyst. *ACS Catal.*, **2021**, *11*, 11793-11805.
6. Sadykov, I.I.; Sushkevich, V.L.; Krumeich, F.; Nuguid, R.J.G.; van Bokhoven, J.A.; Nachttegaal, M. and Safonova, O.V. Platinum-Iron(II) oxide sites directly responsible for preferential carbon monoxide oxidation at ambient temperature: an operando X-ray absorption spectroscopy study. *Angew. Chem. Int. Ed.*, **2023**, *135*, e2022140.
7. Morimoto, T.; Nagao, M. and Imai, J. The adsorption of water on SiO<sub>2</sub>, Al<sub>2</sub>O<sub>3</sub>, and SiO<sub>2</sub>:Al<sub>2</sub>O<sub>3</sub>. The relation between the amounts of physisorbed and chemisorbed water. *Bull. Chem. Soc. Japan* **1971**, *44*, 1282-1288.
8. Al-Abadleh, H.A. and Grassian, V.H. FT-IR study of water adsorption on aluminum oxide surfaces. *Langmuir* **2003**, *19*, 341-347.
9. Merle, N.; Tabassum, T.; Scott, S.; Motta, A.; Szeto, K.; Taoufik, M.; Gauvin, R. and Delevoye, L. High-field NMR, reactivity, and DFT modeling reveal the gamma-Al<sub>2</sub>O<sub>3</sub> surface hydroxyl network. *ChemRxiv* **2022**.
10. Son, I.H.; Lane, A.M. and Johnson, D.T. The study of the deactivation of water-pretreated Pt/ $\gamma$ -Al<sub>2</sub>O<sub>3</sub> for low-temperature selective CO oxidation in hydrogen. *J. Power Sources* **2003**, *124*, 415-419.
11. Maeda, N.; Meemken, F. and Baiker, A. Insight into the mechanism of the preferential oxidation of carbon monoxide by using isotope-modulated excitation IR spectroscopy. *ChemCatChem* **2013**, *5*, 2199-2202.
12. Wang, W.; Zhang, H.; Wang, W.; Zhao, A.; Wang, B. and Hou, J.G. Observation of water dissociation on nanometer-sized FeO islands grown on Pt (111). *Chem. Phys. Lett.* **2010**, *500*, 76-81.
13. Ringleb, F.; Fujimori, Y.; Wang, H.F.; Ariga, H.; Carrasco, E.; Sterrer, M.; Freund, H.J.; Giordano, L.; Pacchioni, G. and Goniakowski, J. Interaction of water with FeO (111)/Pt (111): environmental effects and influence of oxygen. *J. Phys. Chem. C* **2011**, *115*, 19328-19335.
14. Xu, L.; Wu, Z.; Zhang, W.; Jin, Y.; Yuan, Q.; Ma, Y. and Huang, W. Oxygen vacancy-induced novel low-temperature water splitting reactions on FeO (111) monolayer-thick film. *J. Phys. Chem. C* **2012**, *116*, 22921-22929.

15. Knudsen, J.; Merte, L.R.; Grabow, L.C.; Eichhorn, F.M.; Porsgaard, S.; Zeuthen, H.; Vang, R.T.; Lægsgaard, E.; Mavrikakis, M. and Besenbacher, F. Reduction of FeO/Pt (111) thin films by exposure to atomic hydrogen. *Surf. Sci.* **2010**, *604*, 11-20.
16. Muraki, H.; Matunaga, S.I.; Shinjoh, H.; Wainwright, M.S. and Trimm, D.L. The effect of steam and hydrogen in promoting the oxidation of carbon monoxide over a platinum on alumina catalyst. *J. Chem. Tech. & Biotech.* **1991**, *52*, 415-424.
17. Schubert M. M. Mechanistic Insights into the Preferential CO Oxidation in H<sub>2</sub>-rich Gas (PROX) over Supported Noble Metal Catalysts. PhD Thesis. University of Ulm, **2000**.
18. Li, S.; Jia, M.; Gao, J.; Wu, P.; Yang, M.; Huang, S.; Dou, X.; Yang, Y. and Zhang, W. Infrared studies of the promoting role of water on the reactivity of Pt/FeO<sub>x</sub> catalyst in low-temperature oxidation of carbon monoxide. *J. Phys. Chem. C* **2015**, *119*, 2483-2490.
19. Zheng, B.; Liu, G.; Geng, L.; Cui, J.; Wu, S.; Wu, P.; Jia, M.; Yan, W. and Zhang, W. Role of the FeO<sub>x</sub> support in constructing high-performance Pt/FeO<sub>x</sub> catalysts for low-temperature CO oxidation. *Catal. Sci. & Tech.* **2016**, *6*, 1546-1554.
20. Chen, G.; Zhao, Y.; Fu, G.; Duchesne, P.N.; Gu, L.; Zheng, Y.; Weng, X.; Chen, M.; Zhang, P.; Pao, C.W. and Lee, J.F. Interfacial effects in iron-nickel hydroxide-platinum nanoparticles enhance catalytic oxidation. *Science* **2014**, *344*, 495-499.
21. Kotobuki, M.; Watanabe, A.; Uchida, H.; Yamashita, H. and Watanabe, M. High catalytic performance of Pt-Fe alloy nanoparticles supported in mordenite pores for preferential CO oxidation in H<sub>2</sub>-rich gas. *Appl. Catal. A: General* **2006**, *307*, 275-283.
22. Hu, X.; Gao, Y.; Wang, W. and Chen, C. Structural features and catalytic performance in CO preferential oxidation of MWCNT-supported Pt-Fe catalysts. *Intern. J. Hydrogen Energy* **2016**, *41*, 14079-14087.
23. Cao, L.; Liu, W.; Luo, Q.; Yin, R.; Wang, B.; Weissenrieder, J.; Soldemo, M.; Yan, H.; Lin, Y.; Sun, Z. and Ma, C. Atomically dispersed iron hydroxide anchored on Pt for preferential oxidation of CO in H<sub>2</sub>. *Nature* **2019**, *565*, 631-635.
24. Chiarello, G. L.; Nachttegaal, M.; Marchionni, V.; Quaroni, L. and Ferri, D. Adding diffuse reflectance infrared Fourier transform spectroscopy capability to extended x-ray-absorption fine structure in a new cell to study solid catalysts in combination with a modulation approach. *Rev. Sci. Instrum.* **2014**, *85*, 074102.
25. Nuguid, R. J. G.; Ferri, D. and Kröcher, O. Design of a reactor cell for modulated excitation Raman and diffuse reflectance studies of selective catalytic reduction catalysts. *Emission Control Sci. Tech.* **2019**, *5*, 307-316.
26. Pérez-Ramírez, J.; Mul, G.; Kapteijn, F.; Moulijn, J. A.; Overweg, A. R.; Doménech, A.; Ribera, A. and Arends, I. W. C. E. Physicochemical characterization of isomorphously substituted FeZSM-5 during activation. *J. Catal.* **2002**, *207*, 113-126.
27. Hiemstra, T. Surface and mineral structure of ferrihydrite. *Geochimica et Cosmochimica Acta* **2013**, *105*, 316-325.

28. Tomita, A.; Miki, T.; Tango, T.; Murakami, T.; Nakagawa, H. and Tai, Y. Fe K-Edge X-ray absorption fine structure determination of  $\gamma$ -Al<sub>2</sub>O<sub>3</sub>-Supported Iron-Oxide Species. *ChemPhysChem* **2015**, *16*, 2015-2020.
29. Tomita, A.; Shimizu, K.I.; Kato, K.; Akita, T. and Tai, Y. Mechanism of low-temperature CO oxidation on Pt/Fe-containing alumina catalysts pretreated with water. *J. Phys. Chem. C* **2013**, *117*, 1268-1277.
30. Tanaka, K.I.; He, H.; Shou, M. and Shi, X. Mechanism of highly selective low temperature PROX reaction of CO in H<sub>2</sub>: oxidation of CO via HCOO with OH. *Catal. Today* **2011**, *175*, 467-470.
31. Saavedra, J.; Pursell, C.J. and Chandler, B.D. CO oxidation kinetics over Au/TiO<sub>2</sub> and Au/Al<sub>2</sub>O<sub>3</sub> catalysts: evidence for a common water-assisted mechanism. *JACS* **2018**, *140*, 3712-3723.
32. Zhao, Y.; Chen, G.; Zheng, N. and Fu, G. Mechanisms for CO oxidation on Fe(III)-OH-Pt interface: a DFT study. *Faraday Discuss.* **2014**, *176*, 381-392.
33. Gu, X.; Ouyang, R.; Sun, D.; Su, H. and Li, W. CO oxidation at the perimeters of an FeO/Pt(111) interface and how water promotes the activity: a first-principles study. *ChemSusChem* **2012**, *5*, 871-878.

## 6 Conclusions and Outlook

The goal of this thesis was to understand the crucial role of iron in the promotion of preferential carbon monoxide oxidation over supported platinum-based catalysts. Operando X-ray absorption spectroscopy, in combination with other methods, made it possible to determine active iron and platinum sites responsible for carbon monoxide oxidation and to understand how pretreatment conditions change the structure of the active sites.

Catalysts for preferential carbon monoxide oxidation based on Pt/ $\gamma$ -Al<sub>2</sub>O<sub>3</sub> or Pt/SiO<sub>2</sub> were successfully promoted with iron through the sequential incipient wetness impregnation with the subsequent calcination. The reduction of the calcined materials is a key step to create the active interface between platinum nanoparticles and oxidic iron species, responsible for the promotional effect of iron. The oxidation state and the degree of hydroxylation of oxidic iron species, as well as their proximity to platinum nanoparticles, are the key structural parameters determining the final activity of Pt-Fe catalysts. These parameters depend on the partial pressure of hydrogen and water, as well as the temperature during the reduction step. As shown in Chapter 4, neither atomically dispersed platinum nor Pt-Fe alloy per se is responsible for the high catalytic activities of the state-of-the-art Pt-Fe PROX catalysts. Instead, the interface between FeO<sub>x</sub>(OH)<sub>y</sub> species (activating oxygen) and metallic platinum (covered with carbon monoxide) is essential for efficient preferential oxidation of carbon monoxide. Moreover, the high degree of hydroxylation of redox-active FeO<sub>x</sub>(OH)<sub>y</sub> species can further enhance their PROX activity.

Chapter 3 showed that doping of a Pt/ $\gamma$ -Al<sub>2</sub>O<sub>3</sub> catalyst with 0.65wt.% Fe followed by reduction under 5 vol.% H<sub>2</sub> creates redox active oxidic Fe<sup>2+</sup>/Fe<sup>3+</sup> species in close proximity to metallic platinum nanoparticles of about 1 nm in size. X-ray absorption spectroscopy coupled with quantitative mass-spectrometry provided insight into the formation of these sites and their behavior under carbon monoxide oxidation conditions. Low concentration of iron, relatively low hydrogen pressure, and dry conditions yield catalysts with the carbon monoxide oxidation rate of 0.02 mol<sub>CO</sub> g<sub>Pt</sub><sup>-1</sup> h<sup>-1</sup> at 323 K, far superior to that of Pt/ $\gamma$ -Al<sub>2</sub>O<sub>3</sub>, but still not enough for ambient temperature preferential carbon monoxide oxidation. As it was clearly demonstrated by in situ/operando X-ray absorption and Fourier transform infrared spectroscopies, under reaction conditions platinum surface is completely covered by carbon monoxide, which can be replenished from the gas phase. A quantitative comparison between the oxidation state of Fe<sup>2+</sup>/Fe<sup>3+</sup>O<sub>x</sub> species determined by XAS and the catalytic conversion measured simultaneously provided us with a deep understanding of the oxygen activation mechanism. As oxygen cannot be activated on platinum, which is covered by carbon monoxide at around 373 K, redox-active oxidic iron species take over the oxygen chemisorption step. This allows circumventing the classical mechanism of carbon monoxide oxidation on platinum, involving competitive adsorption of reactants taking place above 373 K.<sup>1</sup> The results of the transient operando X-ray absorption spectroscopy experiments prove that redox-active oxidic iron is partially oxidized (Fe<sup>2+</sup>/Fe<sup>3+</sup> state) under carbon monoxide oxidation conditions. During the carbon monoxide oxidation reaction, active Fe<sup>2+</sup>/Fe<sup>3+</sup> cations are present in dynamic equilibrium; being reversibly oxidized by oxygen to the Fe<sup>3+</sup> state and then reduced back to Fe<sup>2+</sup> by carbon monoxide chemisorbed on platinum. An increase in oxygen partial pressure increases the coverage of active iron by oxygen, reflected by the positive oxygen reaction order of 0.35.

Chapter 4 demonstrates that high-temperature reduction of supported Pt-Fe catalysts with approximately two times higher iron concentration (1.1-1.4wt.% Fe) under higher hydrogen partial

pressure (100% H<sub>2</sub>) can drastically modify the catalytic interface, creating much more catalytically active oxidic iron sites in comparison to the ones reported in Chapter 3, also demonstrating a significantly higher oxygen reaction orders of 0.7-1. This helps to achieve much higher carbon monoxide oxidation or PROX activities at ambient temperature, up to 3 mol<sub>CO</sub> g<sub>Pt</sub><sup>-1</sup> h<sup>-1</sup> at 313 K, which is approximately two orders of magnitude higher than for the same catalysts reduced under 5 vol.% H<sub>2</sub> at the same temperature (Chapter 4). The hydrogen pressure and the temperature of the reduction step are the main parameters controlling the changes in the structure of FeO<sub>x</sub> oligomers and the FeO<sub>x</sub> - Pt interface. Operando X-ray absorption spectroscopy demonstrated a direct correlation between the catalytic activity and concentration of active Fe<sup>2+</sup> species, explaining the increased oxygen reaction order, since, in the resting state, these active sites remain unsaturated by oxygen. Apart from the active oxidic Fe<sup>2+</sup> species on metallic platinum nanoparticles of about 1-2 nm in size, the catalysts reduced at 673 K in 100 vol.% H<sub>2</sub> contain inactive Fe<sup>0</sup> (partially alloyed with platinum) and inactive Fe<sup>3+</sup> species (forming Fe<sub>2</sub>O<sub>3</sub> clusters). The catalysts deactivation on stream or upon exposure to air is linked to the decomposition of FeO oligomers, which presumably migrate away from the platinum surface and aggregate to form Fe<sub>2</sub>O<sub>3</sub> oligomers on SiO<sub>2</sub> or γ-Al<sub>2</sub>O<sub>3</sub> supports.

Finally, in Chapter 5, we show that an introduction of water both during the reduction pretreatment step and during the PROX reaction can highly benefit the rate of preferential carbon monoxide oxidation. The introduction of water allows obtaining one of the most active supported bimetallic Pt-Fe catalysts (3.6wt.% Fe) for preferential carbon monoxide oxidation reported to date with the PROX reaction rate of 6.93 mol<sub>CO</sub> g<sub>Pt</sub><sup>-1</sup> h<sup>-1</sup>. The addition of water during the reduction of Pt-Fe/γ-Al<sub>2</sub>O<sub>3</sub> under 100% H<sub>2</sub> at 373 K (liquid water or steam) and 473 K (steam) can stabilize the platinum-iron interface by hydroxylating highly active FeO producing even more active oligomeric FeO<sub>x</sub>(OH)<sub>y</sub> species. The addition of water vapor into the PROX stream at 313 K does not change the structure of the iron-containing oligomers but helps to boost their catalytic activity. The presence of active iron-associated hydroxyl groups is revealed by operando diffuse reflectance Fourier transform infrared spectroscopy. The active hydroxyl groups form only over the catalyst treated with water. The treatment of Pt-Fe/SiO<sub>2</sub> catalyst at 673 K deprives the surface of these active hydroxyls and results in reduced catalytic rates, correlated to lower reaction order in oxygen. Therefore, leading causes of the deactivation of the most active Pt-Fe catalysts are dehydration and irreversible oxidation of active oxidic Fe<sup>2+</sup> species.

By comparing different pretreatment strategies, we proposed several possible reaction mechanisms of carbon monoxide oxidation over supported Pt-Fe catalysts. Dry reduction of supported platinum nanoparticles can lead to the overall mechanism of carbon monoxide oxidation proposed in Chapter 3:

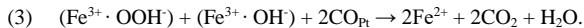


where CO<sub>Pt</sub> indicates a carbon monoxide molecule adsorbed on platinum.

In this reaction, molecular oxygen reacts with surface FeO creating electrophilic species via non-dissociative adsorption, while carbon monoxide is oxidized over metallic platinum nanoparticles. Reduction under 100% H<sub>2</sub> or the hydrogen-steam mixture can promote the formation of the active FeO<sub>x</sub>(OH)<sub>y</sub>/Pt interface (Chapter 4). While carbon monoxide still activates on platinum, oxygen undergoes either a dissociative or non-dissociative water-assisted adsorption on unsaturated Fe<sup>2+</sup>, forming reactive hydroxyl groups and, possibly, electrophilic OOH<sup>-</sup> species. This mechanism can be similar to that reported for gold-based PROX catalysts<sup>2,3</sup> However, due to the much stronger adsorption of carbon monoxide on platinum, reactive oxygen species are bound to Fe<sup>3+</sup> instead of the noble metal surface, as reported for gold-based catalysts. The catalytic mechanism can then be described as:



or



Clearly,  $\text{FeO}_x(\text{OH})_y/\text{Pt}$  catalytic interface helps to achieve high PROX activities; however, it lacks stability. This problem needs to be solved in the future by further optimizing catalysts composition and activation procedures. There are several ways to increase the stability of active hydroxides at the platinum interface. For instance, mixed iron-nickel hydroxides are more stable than pure iron hydroxides. Iron-nickel or iron-cobalt hydroxides can be obtained through a micellar synthesis of respective PtFeNi, PtFeCo alloys using the hot injection method with the subsequent oxidation in a humid atmosphere allowing to create interwoven  $\text{FeNiO}_x(\text{OH})_y$  or  $\text{FeCoO}_x(\text{OH})_y$  hydroxides/oxyhydroxides in contact with metallic platinum.<sup>4</sup> Another possibility would include a deposition of platinum nanoparticles inside hierarchical layered porous hydroxides of iron and nickel.<sup>5</sup> Rational design of these catalysts with operando methods can bring about a more deep understanding of their catalytically active sites.

The increased activity towards hydrogen oxidation at high conversion levels is another negative effect hindering the potential commercial development of Pt-Fe PROX catalysts. As described in Chapter 1, gold has the smallest hydrogen adsorption energy among other noble metals, which is beneficial for high selectivity towards carbon monoxide oxidation. A combination of highly active supported Pt- $\text{FeO}_x(\text{OH})_y$  catalyst at the beginning of the catalyst bed with the gold-based one at the reactor end would benefit from both the high activity of Pt-Fe catalysts and the high selectivity of gold-based ones.<sup>2,4</sup> Thus, at the beginning of the catalyst bed, platinum surface would be saturated with carbon monoxide ensuring no parallel oxidation of hydrogen taking place. Adaptive control of oxygen intake linked to the initial carbon monoxide concentration might also minimize unwanted hydrogen oxidation.

The minimization of free metallic platinum surface able to adsorb hydrogen and an increase in the number of  $\text{FeO}_x(\text{OH})_y$ -Pt contacts would significantly enhance both PROX activity and selectivity. Since atomically-dispersed platinum cannot reach high activities, as discussed in Chapter 4, metallic platinum would still have to stay in a metallic cluster form. To realize this, we can propose a bottom-up approach involving the self-assembling of so-called Janus particles containing iron oxides/hydroxides from one side and noble metal from the other.<sup>6,7</sup> Au/ $\text{Fe}_3\text{O}_4$  Janus particles were successfully synthesized by several groups and were not yet tested for preferential carbon monoxide oxidation.<sup>6</sup> Optimization of their size and iron content can help to achieve a higher number of Au-Fe or Pt-Fe contacts and thereby achieve carbon monoxide oxidation with a high catalytic rate, potentially with better selectivity.

Hydrogen adsorption on platinum is dissociative, while adsorption of carbon monoxide is not. This implies that stoichiometric or diluted Pt-based alloys (Pt-Cu, Pt-Ag), with no monometallic facets available for hydrogen dissociation, would selectively adsorb carbon monoxide, and dissociation of hydrogen would be limited.<sup>8,9</sup> Combination of these alloys with the  $\text{FeO}_x(\text{OH})_y$  would greatly benefit high PROX activity. Optimization of iron concentration can help to increase platinum-iron interaction as well.

Theoretical modeling of active intermediates at the  $\text{FeO}_x(\text{OH})_y$ -Pt interface can help to compare activation barriers of hydrogen and carbon monoxide oxidation via different intermediates discussed in this dissertation. Preference should be given to the active sites with high activation energies of hydrogen oxidation. Investigation of the co-adsorption of water, hydrogen, and carbon monoxide on the platinum and gold surfaces could pave the way for new research on water-assisted selective catalytic oxidation.

## References

1. Allian, A. D.; Takanabe, K.; Fujidala, K. L.; Hao, X.; Truex, T. J.; Cai, J.; Buda, C.; Neurock, M. and Iglesia, E. Chemisorption of CO and mechanism of CO oxidation on supported platinum nanoclusters. *J. Am. Chem. Soc.* **2011**, *133*, 4498-4517.
2. Saavedra, J.; Pursell, C.J. and Chandler, B.D. CO oxidation kinetics over Au/TiO<sub>2</sub> and Au/Al<sub>2</sub>O<sub>3</sub> catalysts: evidence for a common water-assisted mechanism. *JACS* **2018**, *140*, 3712-3723.
3. Saavedra, J.; Whittaker, T.; Chen, Z.; Pursell, C.J.; Rioux, R.M. and Chandler, B.D. Controlling activity and selectivity using water in the Au-catalysed preferential oxidation of CO in H<sub>2</sub>. *Nature Chem.* **2016**, *8*, 584-589.
4. Chen, G.; Zhao, Y.; Fu, G.; Duchesne, P. N.; Gu, L.; Zheng, Y.; Weng, X.; Chen, M.; Zhang, P.; Pao, C.; Lee, J. and Zheng, N. Interfacial effects in iron-nickel hydroxide-platinum nanoparticles enhance catalytic oxidation. *Science* **2014**, *344*, 495-499.
5. Prevot, V. and Tokudome, Y. 3D hierarchical and porous layered double hydroxide structures: an overview of synthesis methods and applications. *J. Mater. Sci.* **2017**, *52*, 11229-11250.
6. Landon, P.; Ferguson, J.; Solsona, B.E.; Garcia, T.; Al-Sayari, S.; Carley, A.F.; Herzing, A.A.; Kiely, C.J.; Makkee, M.; Moulijn, J.A. and Overweg, A. Selective oxidation of CO in the presence of H<sub>2</sub>, H<sub>2</sub>O and CO<sub>2</sub> utilising Au/ $\alpha$ -Fe<sub>2</sub>O<sub>3</sub> catalysts for use in fuel cells. *J. Materials Chem.* **2006**, *16*, 199-208.
7. Hu, J.; Zhou, S.; Sun, Y.; Fang, X. and Wu, L. Fabrication, properties and applications of Janus particles. *Chem. Soc. Rev.* **2012**, *41*, 4356-4378.
8. Liu, Y.; Zhang, A.; Xue, L.; Zhang, H.; Hao, Y.; Wang, Y.; Wu, J. and Zeng, S. Dual active sites of CO adsorption and activation over PtCu alloy nanocages for preferential oxidation of carbon monoxide. *ACS Appl. Energ. Mater.* **2021**, *5*, 604-614.
9. Hua, M.; Tian, X.; Li, S.; Shao, A. and Lin, X. Theoretical design of platinum-silver single atom alloy catalysts with CO adsorbate-induced surface structures. *Phys. Chem. Chem. Phys.* **2022**, *24*, 19488-19501.



## 7 Materials and Methods

### 7.1 Gases

Gas bottles containing pure carbon dioxide (CO<sub>2</sub> 4.8, Carbagas AG), 2 vol.% CO 4.7 in He 5.0 (Messer Schweiz AG), 10 vol.% CO 4.7 in He 5.0 (Messer Schweiz AG), 5 vol.% O<sub>2</sub> 5.0 in He 5.0 (Messer Schweiz AG), 40 vol.% O<sub>2</sub> 5.0 in He 5.0 (Messer Schweiz AG), 100 % H<sub>2</sub> 5.0 (Messer Schweiz AG) and 20 vol.% H<sub>2</sub> 5.0 in He 5.0 (Messer Schweiz AG) were used for catalytic experiments with helium (He 6.0, Carbagas AG) as a carrier gas. Gas bottles containing 2 vol.% CO 4.7 in Ar 5.0 (Messer Schweiz AG), 5 vol.% O<sub>2</sub> 5.0 in Ar 5.0 (Messer Schweiz AG), and 5 vol.% H<sub>2</sub> 5.0 in Ar 5.0 (Messer Schweiz AG) were used for the experiments with argon (Ar 5.0, PanGas AG) as the carrier gas. Two dedicated gas mixtures containing 1000.0 ppm CO<sub>2</sub> 4.8 and 1000.0 ppm O<sub>2</sub> 4.8 in He 5.0 (Carbagas AG) and 1 vol.% CO<sub>2</sub> 4.8 in Ar 5.0 (Messer Schweiz AG), respectively, were used for CO<sub>2</sub> and O<sub>2</sub> calibration. All gas concentrations correspond to volumetric percentages. Helium and argon were additionally purified using an oxygen/water filter (Restek). All gas lines and the operando cell were additionally tested for leaks, carbon monoxide, oxygen, and hydrogen sensors were installed to ensure safe operation.

### 7.2 Catalysts Supports

#### Al<sub>2</sub>O<sub>3</sub>

$\gamma$ -Al<sub>2</sub>O<sub>3</sub> support was obtained by calcination of boehmite ( $\gamma$ -AlOOH) powder (Catapal® C1 alumina, Sasol Chemicals) at 873 K for 12 h. The resulting specific surface area determined by the Brunauer-Emmett-Teller (BET) method was 180 m<sup>2</sup>·g<sup>-1</sup>.

#### SiO<sub>2</sub>

Amorphous SiO<sub>2</sub> support (Fluka) was dried at 393 K for 2 h before impregnation. The surface area measured by the BET method was 280 m<sup>2</sup>·g<sup>-1</sup>.

### 7.3 Main Characterization Methods

Below we described the analytical methods used across Chapters 3, 4, and 5.

#### 7.3.1 Elemental Analysis

The catalysts elemental composition was determined by the inductively coupled plasma-optical emission spectrometry (ICP-OES) using Horiba Ultra 2 instrument. The catalysts were dissolved in *aqua regia* in the proportion of 150 mg of catalyst per 50 ml and stirred at 353 K until full dissolution. Concentrations of analytes in a blank experiment were below the detection limit.

#### 7.3.2 Carbon Monoxide Chemisorption

To estimate the surface area of metallic platinum in the catalysts, we performed carbon monoxide chemisorption experiments. The measurement was performed using the Autochem instrument (Micromeritics). About 150 mg of a catalyst was pre-reduced under the same conditions as before the operando experiments either under 100 % or 5 vol.% H<sub>2</sub> by heating with a 10 K·min<sup>-1</sup> ramp to either 473 or 673 K (depending on the pretreatment protocol) and dwelling for 20 min. Then it was cooled down to 313 K and flushed with helium. After stabilization of the thermal conductivity detector signal,

the 10% CO mixture was automatically pulsed (0.171 ml per pulse) into the reactor until the carbon monoxide saturation was reached. The amount of surface platinum atoms and the dispersion were estimated from the total amount of adsorbed carbon monoxide using 3Flex V 4.04 software assuming adsorption of one carbon monoxide molecule per one surface atom of platinum.

### 7.3.3 Electron Microscopy

The platinum particle size distribution was determined using high-angle annular dark field scanning transmission electron microscopy (HAADF-STEM). Sieved catalysts containing particles below 40  $\mu\text{m}$  were deposited onto a perforated carbon foil supported on a copper grid. The grid was mounted on a single tilt holder of the dedicated aberration-corrected STEM microscope HD-2700CS (Hitachi), which was operated at an acceleration potential of 200 kV (cold field emitter). The high resolution below ca. 0.1 nm is achieved by a probe corrector (CEOS) that is incorporated in the microscope column between the condenser lens and the probe-forming objective lens.<sup>1</sup> The HAADF-STEM images (1024  $\times$  1024 pixels) were generated by measuring incoherently scattered electrons, which leads to an intensity significantly increasing with the atomic number (Z-contrast). The recording time was varied between 10 and 30 s. The elemental composition was determined using an energy-dispersive X-ray spectrometer (EDXS, EDAX) attached to the microscope column. We calculated the particle size distribution by measuring the longest edge-to-edge distance for at least 100 particles using the ImageJ software.<sup>2</sup> The mean particle size ( $d$ ) was estimated by a log-normal distribution fit. TEM-derived dispersions (DTEM) were obtained in the approximation of the spherical nanoparticles using equation 1:<sup>3,4</sup>

$$(1) D_{TEM} = 1.483 \frac{\langle d^2 \rangle}{\langle d^3 \rangle} - 0.733 \frac{\langle d \rangle}{\langle d^3 \rangle} + \frac{0.121}{\langle d^3 \rangle}.$$

### 7.3.4 X-ray Absorption Spectroscopy

The X-ray absorption spectroscopy (XAS) measurements were performed at the SuperXAS beamline at the Swiss Light Source (SLS, PSI, Villigen, Switzerland). The SLS operates at 2.4 GeV and 400 mA, where a 2.9 T superbend magnet provides the polychromatic X-ray beam. Silicon-coated (for Fe K-edge) and rhodium-coated (for Pt L<sub>3</sub>-edge) collimating mirrors at 2.5 mrad were used for collimation and harmonics rejection. Both Fe K and Pt L<sub>3</sub>-edges were measured using a Si(111) channel-cut QuickXAS monochromator.<sup>5</sup> The monochromator was operated at 1 Hz frequency, resulting in one spectrum (in the direction of increasing energy) per 1 s. The X-ray beam size on the sample was tuned by a rhodium-coated toroidal mirror located after the monochromator. For the calibration of the incident beam energy, we measured iron (Fe K-edge at 7112 eV) foil before each Fe K-edge experiment by moving the sample away from the beam or by measuring it simultaneously with the sample in the transmission mode. Platinum foil (Pt L<sub>3</sub>-edge at 11564 eV) was measured in transmission mode simultaneously with the sample. All of the oxide reference samples were pressed into pellets to obtain an optimal edge jump for transmission detection.

In situ/operando Pt L<sub>3</sub>-edge XAS signal of the catalysts was measured in transmission mode using 20 cm long N<sub>2</sub>-filled ionization chambers. The majority of in situ/operando XAS data Fe K-edge were collected in total fluorescence yield mode using a PIPS diode (PD1200-25-500AM, Mirion Technologies), or in a transmission mode.<sup>6</sup> For fluorescence measurements, the PIPS diode was placed at a 20° angle with respect to the incident beam perpendicular to the operando plug flow reactor cell window. X-ray beam damage tests were performed in a transmission geometry.

A homemade python-based “ProQEXAFS” v.2.39 software was used to import, calibrate, normalize and average all Pt L<sub>3</sub>- and Fe K-edge XAS data.<sup>7</sup> Linear combination fitting was performed using the same software.

### 7.3.5 In situ Fourier Transform Infrared Spectroscopy

For studying the adsorption of carbon monoxide on the catalysts, we used a custom-made quartz low-temperature in situ infrared cell enabling a high-temperature pretreatment. The infrared data were collected in a transmission geometry using a Nicolet iS50 FTIR spectrometer (Thermo Fischer Scientific). The instrument was equipped with a deuterated triglycine sulfate (DTGS) detector. About 20 mg of the catalyst powder was pressed into a self-supported disc (2 cm<sup>2</sup>) and placed into the FTIR cell. The catalysts were initially activated in a vacuum at 673 K, followed by the reduction in either 100 % (1 bar) or 5 vol.% (50 mbar) H<sub>2</sub> at 673 or 473 K for 1 h and subsequent evacuation at 423 K to remove water formed during reduction. After cooling down to ambient temperature under vacuum, small doses of carbon monoxide were introduced into the cell while acquiring IR spectra until complete saturation of the catalyst. The OMNIC 9.3 (Thermo Fischer Scientific) software was used to process the collected spectra and to extract the baseline (polynomial function).

### 7.3.6 Conversion and Selectivity Estimation

Carbon monoxide conversion was estimated from the outlet concentration of carbon dioxide, selectivity to carbon monoxide (CO selectivity) and CO conversion were estimated using the following equations:

$$(1) \quad \text{CO conversion (\%)} = \frac{[CO_2]_{in} - [CO_2]_{out}}{[CO]_{in}} 100\%$$

$$(2) \quad \text{CO selectivity (\%)} = \frac{[CO_2]_{out}}{[CO_2]_{out} + [H_2O]_{out}} 100\%$$

[CO]<sub>in</sub>, [CO]<sub>out</sub>, [O<sub>2</sub>]<sub>in</sub>, and [O<sub>2</sub>]<sub>out</sub> are the concentrations of CO and O<sub>2</sub> at the inlet and the outlet of the operando cell, respectively.

## 7.4 References

1. Krumeich, F.; Müller, E.; Wepf, R. A. and Nesper, R. Characterization of catalysts in an aberration-corrected scanning transmission electron microscope. *J. Phys. Chem. C* **2011**, *115*, 1080-1083.
2. Schneider, C. A.; Rasband, W. S. and Eliceiri, K. W. NIH Image to ImageJ: 25 years of image analysis. *Nat. Methods* **2012**, *9*, 671-675.
3. Larsson, M. I. U.S. Patent 7,813,523 B1, **2010**.
4. Allian, A. D. and Takanabe, K. Chemisorption of CO and mechanism of CO oxidation on supported platinum nanoclusters. *J. Am. Chem. Soc.* **2011**, *133*, 4498-4517.
5. Müller, O.; Nachttegaal, M.; Just, J.; Lützenkirchen-Hecht, D. and Frahm, R. Quick-EXAFS setup at the SuperXAS beamline for in situ X-ray absorption spectroscopy with 10 ms time resolution. *J. Synchrotron Radiat.* **2016**, *23*, 260-266.
6. Clark, A. H.; Steiger, P.; Bornmann, B.; Hitz, S.; Frahm, R.; Ferri, D. and Nachttegaal, M. Fluorescence-detected quick-scanning X-ray absorption spectroscopy. *J. Synchrotron Radiat.* **2020**, *27*, 681- 688.
7. Clark, A. H.; Imbao, J.; Frahm, R. and Nachttegaal, M. ProQEXAFS: A highly optimized parallelized rapid processing software for QEXAFS data. *J. Synchrotron Radiat.* **2020**, *27*, 551- 557.

## Supporting Information

---

## S1. Time-Resolved XAS Study of Carbon Monoxide Oxidation over a Bimetallic $\gamma$ -Al<sub>2</sub>O<sub>3</sub>-Supported Pt-Fe Catalyst (Chapter 3)

The Supporting Information S1 is based on the article from Ilia I. Sadykov, Maxim Zabilskiy, Adam H. Clark, Frank Krumeich, Vitaly L. Sushkevich, Jeroen A. van Bokhoven, Maarten Nachtegaal and Olga V. Safonova, *ACS Catal.*, **2021**, *11*, *18*, 11793-11805.

## Catalysts (Chapter 3)

### Pt<sub>2.0</sub>-Al<sub>2</sub>O<sub>3</sub>-673-5

1.20 g of  $\gamma$ -Al<sub>2</sub>O<sub>3</sub> was impregnated with an aqueous solution of 0.05 g Pt(NH<sub>3</sub>)<sub>4</sub>(NO<sub>3</sub>)<sub>2</sub> (99.995% purity, Sigma-Aldrich) and then mixed for 10 min. The volume of the metal salt solution was equal to that of the pore volume of the support. After drying for 1 h, the catalyst was calcined for 2 h at 473 K and then for 2 h at 673 K.

### Pt<sub>2.1</sub>Fe<sub>0.7</sub>-Al<sub>2</sub>O<sub>3</sub>-673-5

1.17 g of  $\gamma$ -Al<sub>2</sub>O<sub>3</sub> was first impregnated with 0.05 g Pt(NH<sub>3</sub>)<sub>4</sub>(NO<sub>3</sub>)<sub>2</sub> and calcined in the same way as Pt/Al<sub>2</sub>O<sub>3</sub>. After subsequent impregnation with an aqueous solution of 0.05 g Fe(NO<sub>3</sub>)<sub>3</sub>·9H<sub>2</sub>O and drying for 1 h at 393 K, the obtained catalyst was calcined for 2 h at 473 K and then for 2 h at 673 K.

### Fe<sub>0.6</sub>-Al<sub>2</sub>O<sub>3</sub>-673-5

1.12 g of  $\gamma$ -Al<sub>2</sub>O<sub>3</sub> was impregnated with an aqueous solution of 0.0494 g Fe(NO<sub>3</sub>)<sub>3</sub>·9H<sub>2</sub>O and calcined for 2 h at 473 K and then for 2 h at 673 K.

Readers are referred to supporting information for details on sample characterization and gas compositions.

## Methods (Chapter 3)

### In situ X-ray Powder Diffraction

The X-ray powder diffraction (XRD) patterns were recorded on the D8 Advance Bruker diffractometer equipped with a goniometer and Cu K $\alpha$  X-ray source with a K $\beta$  filter. All diffraction patterns were recorded at  $20^\circ \leq 2\theta \leq 75^\circ$ . The data were analyzed with the TOPAS software (Bruker). A catalyst was placed in the in situ reactor chamber XRK 900 (Anton Paar, Austria) and reduced with 5% H<sub>2</sub> in argon (50 ml·min<sup>-1</sup>) by heating to 673 K and dwelling for 20 min. After such a pretreatment, a catalyst was cooled down to 423 K and the in situ XRD pattern was recorded. The heating and cooling ramps were always of 10 K min<sup>-1</sup>.

### Catalysts Activity Measurements

To understand whether the operando cell is suitable for the catalytic activity measurements, we firstly compared the activity of about 12-20 mg of the catalyst in the operando cell<sup>1</sup> diluted with Al<sub>2</sub>O<sub>3</sub> (the same as the support) in 1:1 ratio with its activity in a dedicated tubular plug-flow reactor diluted in 1:40 ratio. The total flow was 45 ml·min<sup>-1</sup> for the operando cell and 80 ml·min<sup>-1</sup> for the tubular reactor, carrier gas was helium in both cases. At first, the catalysts were reduced in situ in 5 vol.% H<sub>2</sub> by heating up to 673 K with the ramp rate of 10 K·min<sup>-1</sup> and holding for 20 min. After that, the catalysts were exposed to 1 vol.% CO and 1 vol.% O<sub>2</sub> in helium gas mixture and kept for 1 h at 383 K to stabilize the activity, which was estimated using mass spectrometer (OmniStar GSD 320 O1, Pfeiffer). When using helium as a carrier gas, the rate of carbon dioxide concentration was calculated from the ratio between the mass-to-charge (m/z) signals of 44 (CO<sub>2</sub>) and 4 (He). We found that catalyst activity for both reactors even with different dilution ratios was similar (**Fig. S1-8d**).

We used different concentrations of oxygen and carbon monoxide to measure the reaction orders in a tubular reactor (**Fig. S1-8 a-c**). Reactants partial pressure was calculated taking into account both ambient pressure and the pressure drop before the catalyst bed, which was about 110 mbar. The mass spectrometer was calibrated immediately after the catalytic tests, using a bypass line with the same pressure drop value

controlled by an additional needle valve. The conversion was always kept below 15%, which allowed us to accurately extract the catalytic reaction rates. The reaction temperature was determined as the temperature of the thermocouple inserted in a catalyst bed.

#### In situ Raman Spectroscopy

Raman spectra were recorded using a Kaiser RamanRXN-1 analyzer equipped with a fiber optics probe and a 785-nm laser at 100 mW laser power and 0.5 s exposure time. The Raman probe was mounted above the custom built in situ spectroscopic cell with the catalyst sample.<sup>1</sup> Catalyst cell was heated up to 673 K under 5 vol.% H<sub>2</sub> for an initial reduction and then different gas mixtures were sent through the catalyst including 1 vol.% CO. Results are presented in **Fig. S1-16**.



## Figures and Tables to S1 (Chapter 3)

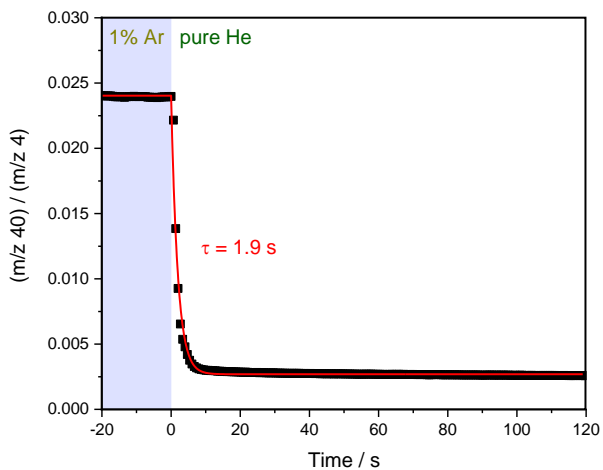


**Figure S1-1.** Ratio between mass-to-charge ratio signals 40 and 4 during argon cut-off experiment and determined operando cell residence time. Pressure drop was 105 mbar, operando cell was filled with sieved (75-100  $\mu\text{m}$ )  $\gamma\text{-Al}_2\text{O}_3$ . Total flow was  $45\text{ ml}\cdot\text{min}^{-1}$ . Gas concentrations are shown as vol.%.

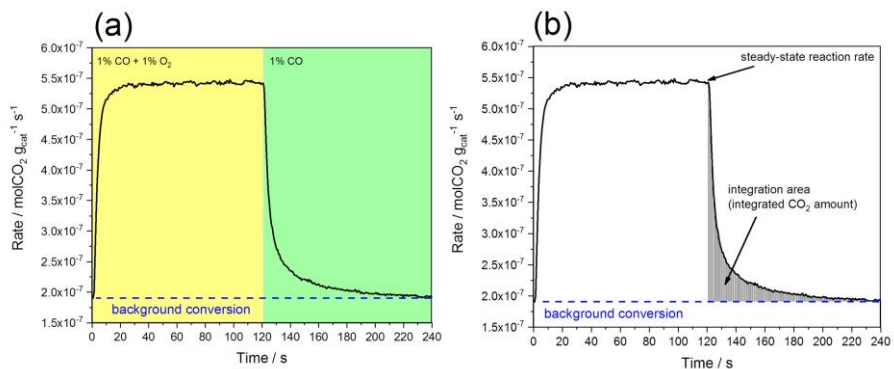


**Figure S1-2.** (a) Rate of carbon dioxide formation monitored by in-line mass-spectrometer during the single operando Fe K-edge XAS oxygen cut-off cycle at 353 K (experiment 4) and (b) calculation of the integrated carbon dioxide amount after the cut-off. Gas concentrations are shown as vol.%.

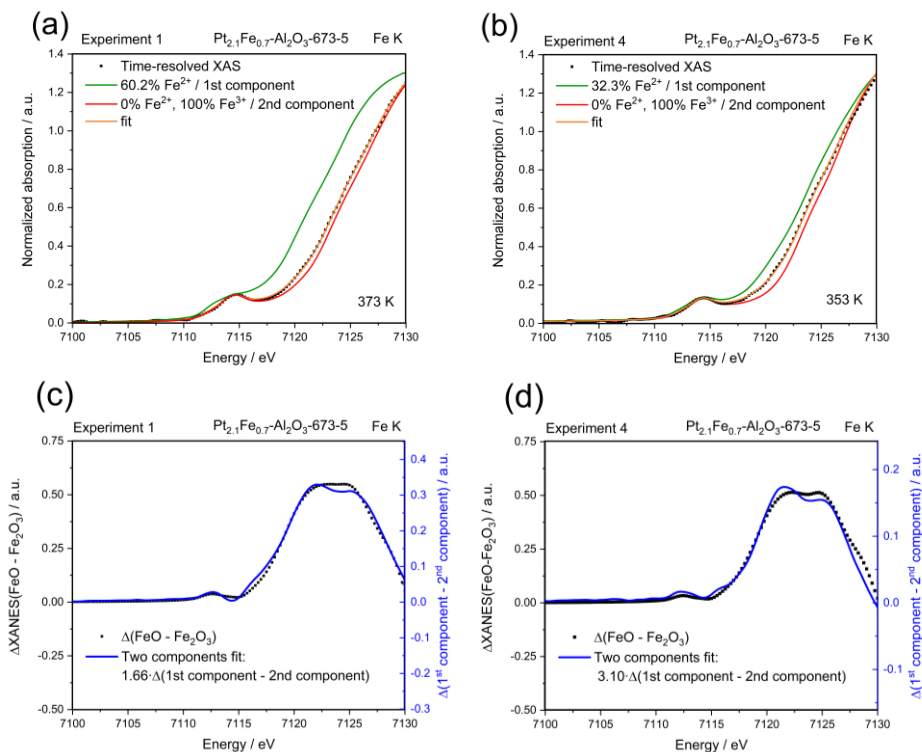


**Figure S1-3.** An example of the Fe K-edge XANES linear combination fitting for  $\text{Pt}_{2.1}\text{Fe}_{0.7}\text{Al}_2\text{O}_3$ -673-5 at 373 K during the experiment 1 (a) and the experiment 4 (b); difference between FeO and  $\text{Fe}_2\text{O}_3$  references spectra for the experiment 1 (c) and the experiment 4 (d) fitted with difference between the 1<sup>st</sup> (the most reduced state) and the 2<sup>nd</sup> component (the most oxidized state) for each experiment. Obtained multiplication coefficients allow to calculate the percentage of  $\text{Fe}^{2+}$  in the 1<sup>st</sup> component (the most reduced state) for each experiment.

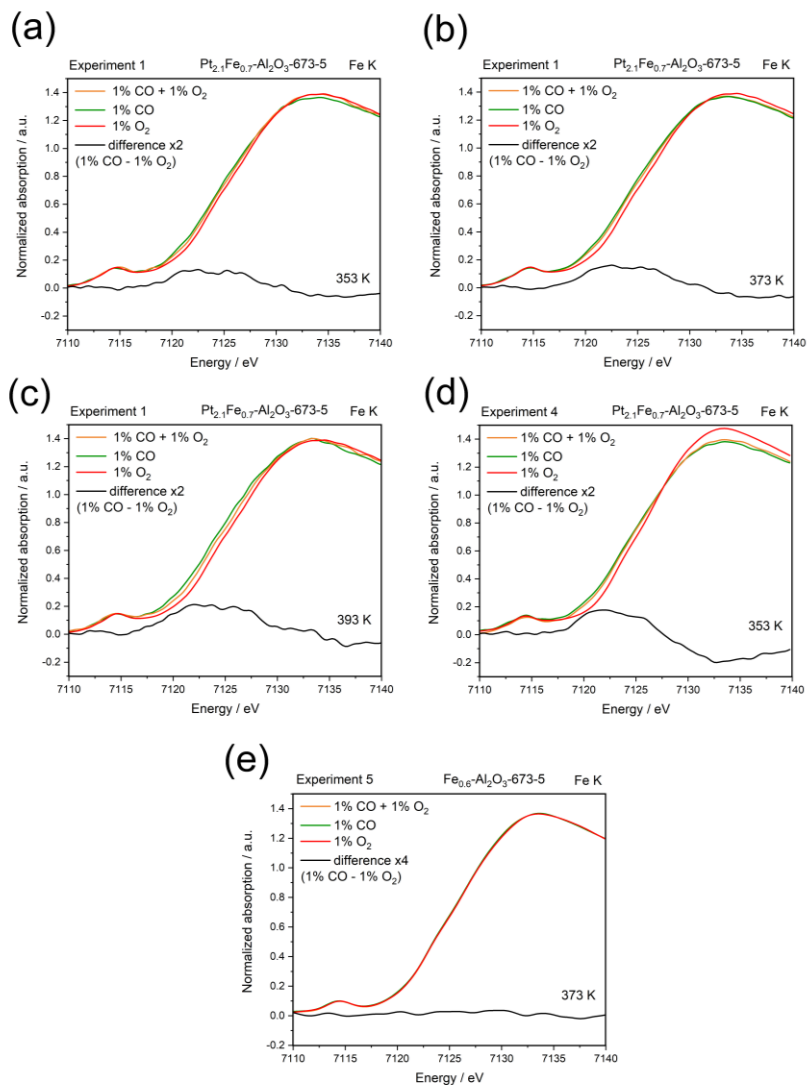


**Figure S1-4.** Operando Fe K-edge XAS spectra of  $\text{Pt}_{2.1}\text{Fe}_{0.7}\text{-Al}_2\text{O}_3\text{-673-5}$  under different gas mixtures at 353 K (a), 373 K (b), 393 K (c) during the experiment 1 and (d) at 353 K during the experiment 4; (e) operando Fe K-edge XAS spectra of  $\text{Fe}_{0.6}\text{-Al}_2\text{O}_3\text{-673-5}$  under different gas mixtures at 373 K during the experiment 5. The black line demonstrates the difference between the spectra of  $\text{Pt}_{2.1}\text{Fe}_{0.7}\text{-Al}_2\text{O}_3\text{-673-5}$  under 1 vol.% CO and 1 vol.%  $\text{O}_2$  multiplied by a certain coefficient. All gas concentrations are shown as vol.%.

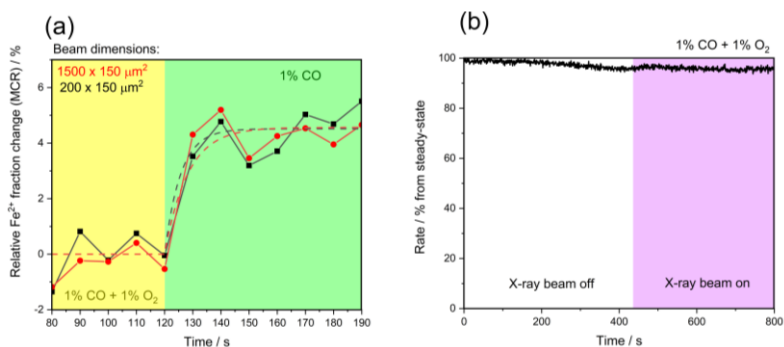


**Figure S1-5.** (a) Reversible  $\text{Fe}^{2+}$  reduction as a function of the dimensions of the beam focus applied for  $\text{Pt}_{2.1}\text{Fe}_{0.7}\text{-Al}_2\text{O}_3\text{-673-5}$  at 363 K; (b) carbon dioxide formation rate before and after opening the X-ray beam shutter for Fe K-edge XAS measurements for  $\text{Pt}_{2.1}\text{Fe}_{0.7}\text{-Al}_2\text{O}_3\text{-673-5}$  at 373 K. Gas concentrations are shown as vol.%.

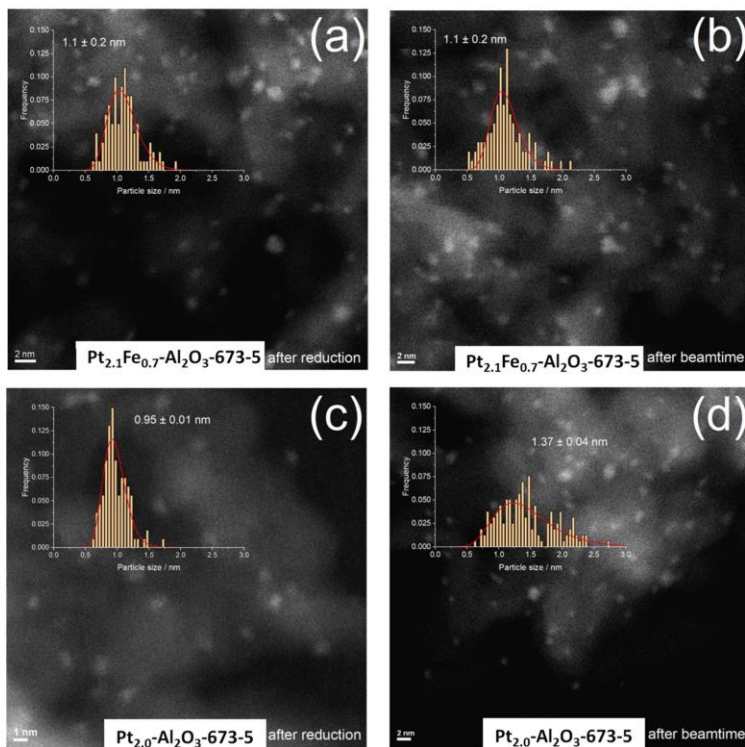


**Figure S1-6.** HAADF-STEM images and derived platinum particle size distributions of  $\text{Pt}_{2.1}\text{Fe}_{0.7}\text{-Al}_2\text{O}_3\text{-673-5}$  after reduction (a) and after operando XAS measurements (b), HAADF-STEM images and derived platinum particle size distributions of  $\text{Pt}_{2.0}\text{-Al}_2\text{O}_3\text{-673-5}$  after reduction (c) and after operando XAS measurements (d).

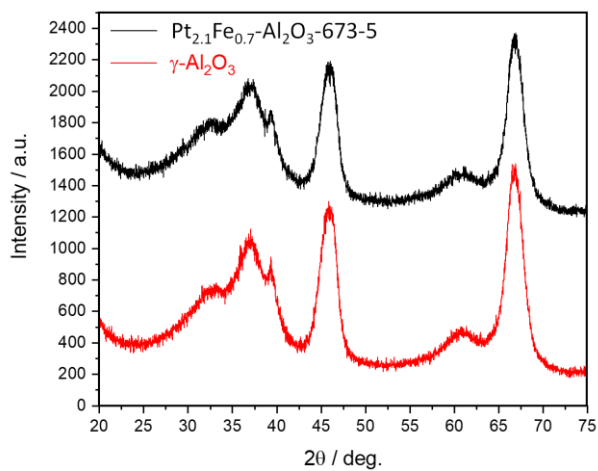


**Figure S1-7.** In situ XRD patterns of Pt<sub>2.1</sub>Fe<sub>0.7</sub>-Al<sub>2</sub>O<sub>3</sub>-673-5 and pure Al<sub>2</sub>O<sub>3</sub> support measured at 423 K after reduction.

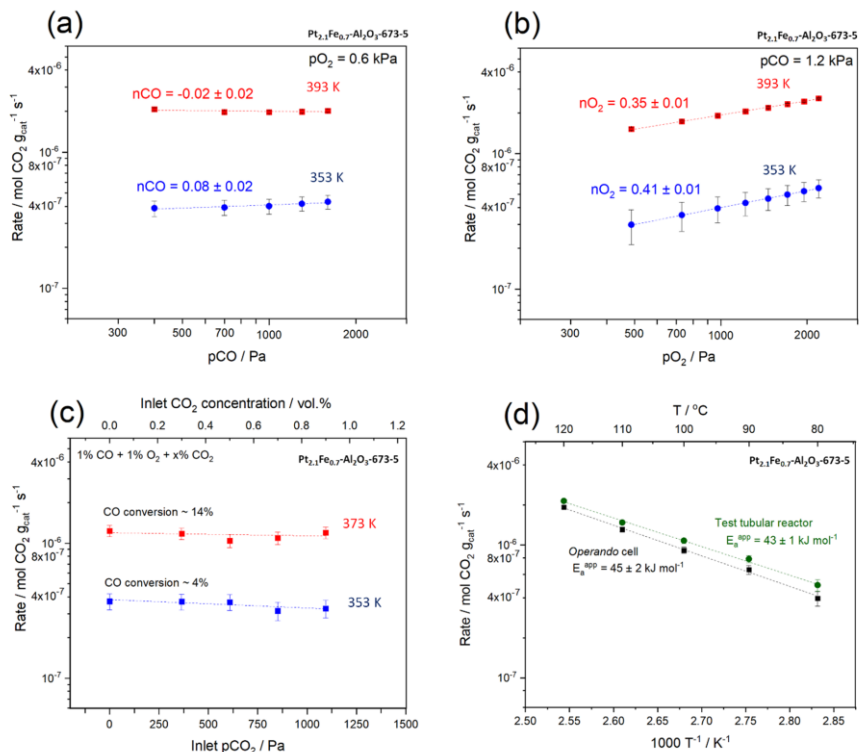


**Figure S1-8.** Double-logarithmic plots of the dependence of the rate of carbon dioxide formation on additional carbon monoxide (a), oxygen (b), carbon dioxide (c) added to the reaction mixture with constant total pressure for the  $\text{Pt}_{2.1}\text{Fe}_{0.7}\text{-Al}_2\text{O}_3\text{-673-5}$  at different reactor temperatures; (d) comparison of carbon dioxide formation rate during the 1<sup>st</sup> operando Fe K edge XAS experiment and during the kinetic tests in a tubular plug flow reactor for  $\text{Pt}_{2.1}\text{Fe}_{0.7}\text{-Al}_2\text{O}_3\text{-673-5}$ . Gas concentrations are shown as vol.%.



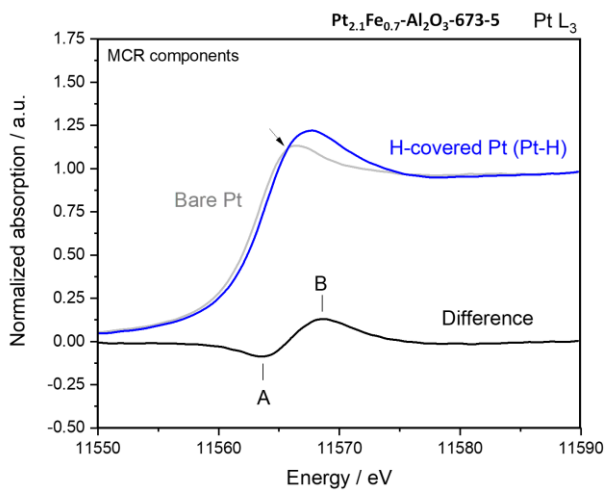


**Figure S1-9.** Comparison of two in situ Pt  $L_3$ -edge XANES MCR-ALS components of  $\text{Pt}_{2.1}\text{Fe}_{0.7}\text{-Al}_2\text{O}_3\text{-673-5}$  extracted during temperature programmed reduction.

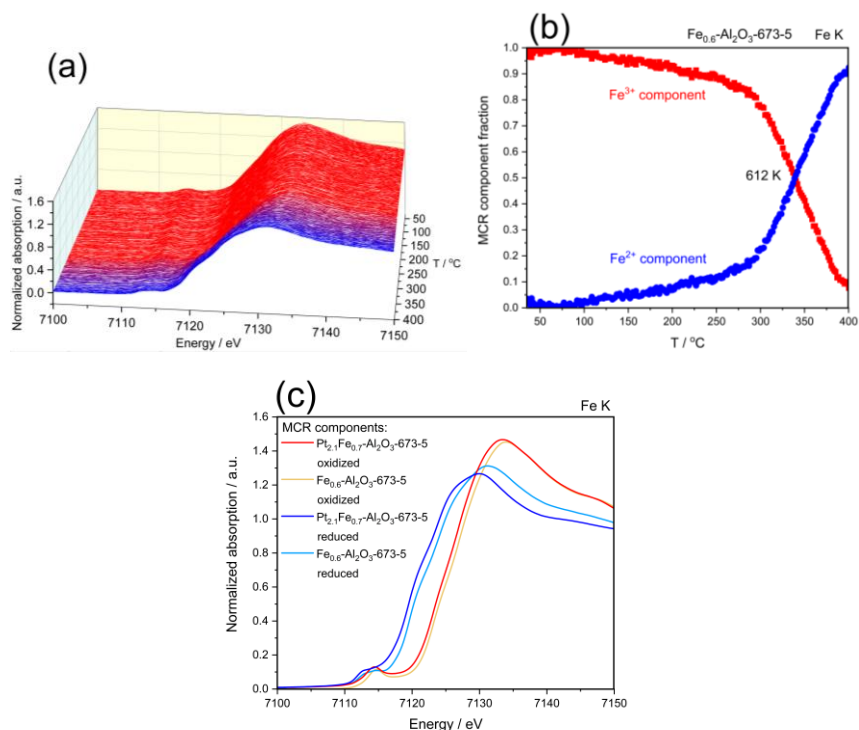


**Figure S1-10.** Time-resolved in situ Fe K-edge XANES spectra of  $\text{Fe}_{0.6}\text{-Al}_2\text{O}_3\text{-673-5}$  during the temperature programmed reduction (a) and Fe speciation (b); comparison of oxidized/reduced MCR-ALS components for  $\text{Pt}_{2.1}\text{Fe}_{0.7}\text{-Al}_2\text{O}_3\text{-673-5}$  and  $\text{Fe}_{0.6}\text{-Al}_2\text{O}_3\text{-673-5}$  extracted from in situ Fe K edge XANES during temperature programmed reduction.

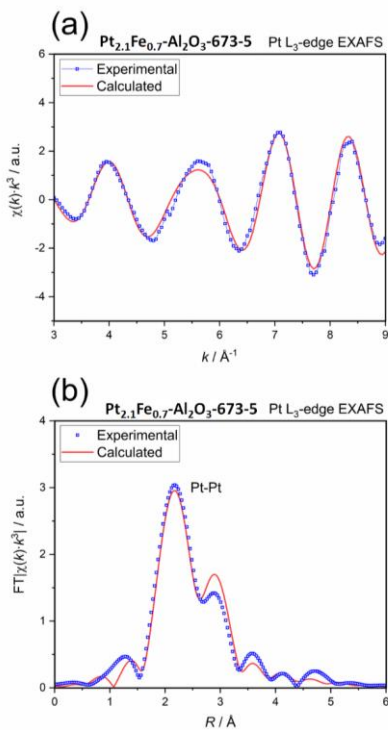


**Figure S1-11.** (a)  $k^3$ -weighted  $\chi(k)$  Pt  $L_3$ -edge EXAFS data for  $\text{Pt}_{2.1}\text{Fe}_{0.7}\text{Al}_2\text{O}_3\text{-673-5}$  under 5 vol.%  $\text{H}_2$  at 303 K after temperature programmed reduction and its fit; (b) corresponding FT EXAFS spectrum and its fit.

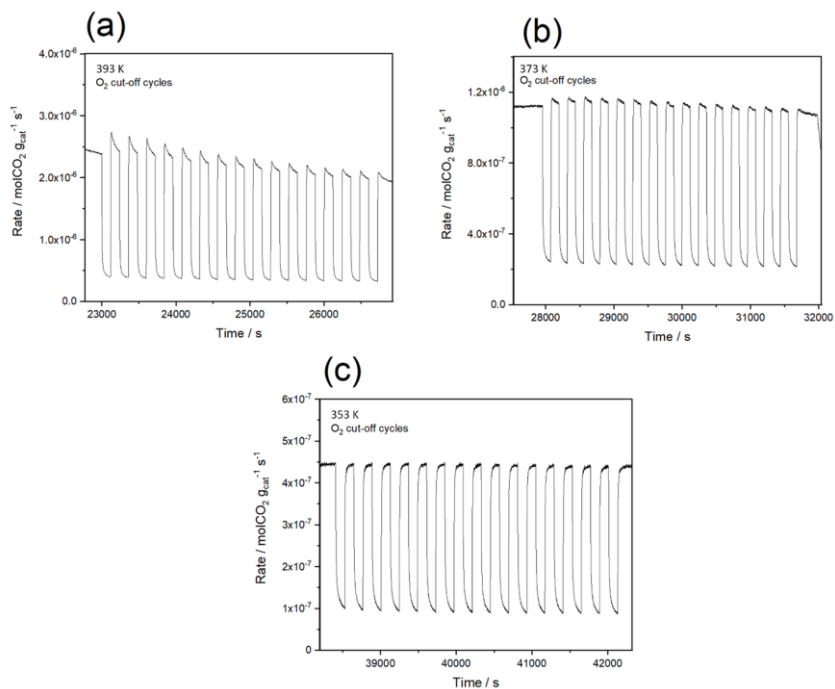


**Figure S1-12.** Rate of carbon dioxide formation monitored by the in-line mass-spectrometer during operando Pt L<sub>3</sub>-edge XAS oxygen cut-off cycles (experiment 2).

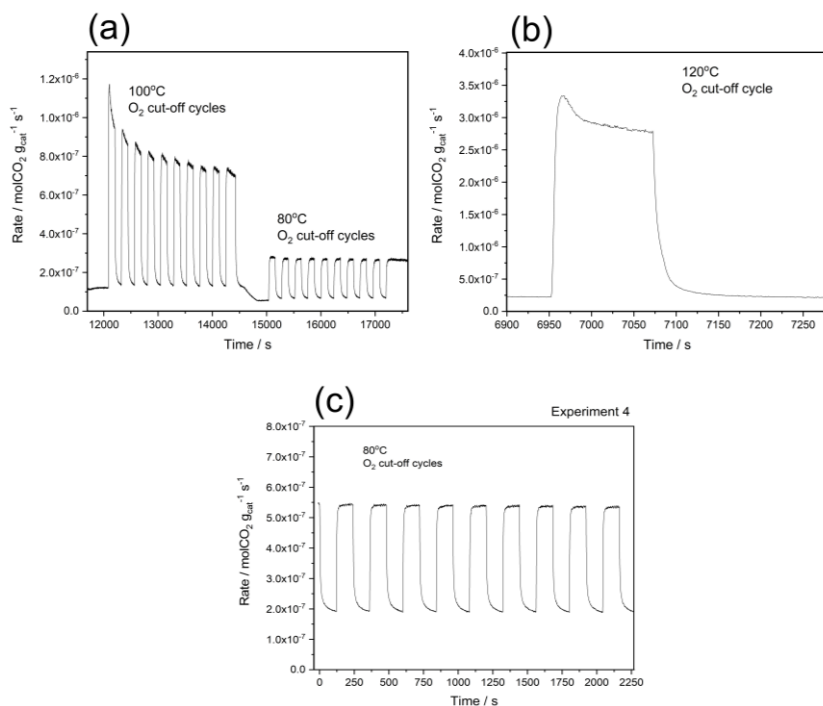


**Figure S1-13.** Rate of carbon dioxide formation monitored by the in-line mass-spectrometer during operando Fe K-edge XAS oxygen cut-off cycles for the experiments number 1(a, b), and 4 (c).

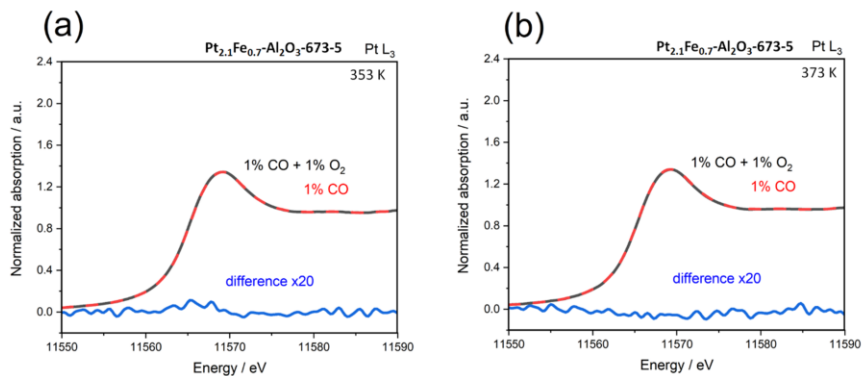


**Figure S1-14.** Operando Pt L<sub>3</sub> edge XANES spectra of Pt<sub>2.1</sub>Fe<sub>0.7</sub>-Al<sub>2</sub>O<sub>3</sub>-673-5 under 1 vol.% CO + 1 vol.% O<sub>2</sub> and 1 vol.% CO gas mixtures at 353 K (c) and 373 K (d). Gas concentrations are shown as vol.%.

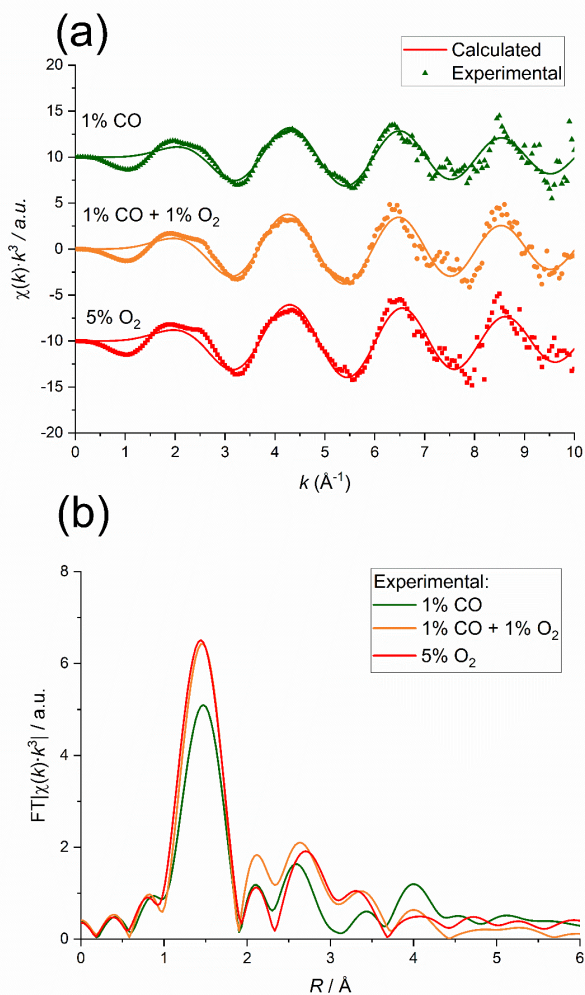


**Figure S1-15.** (a)  $k^3$ -weighted  $\chi(k)$  Fe K-edge EXAFS data for Pt<sub>2.1</sub>Fe<sub>0.7</sub>-Al<sub>2</sub>O<sub>3</sub>-673-5 under 5 vol.% H<sub>2</sub> at 303 K after TPR and their fits; (b) the corresponding FT EXAFS data. Gas concentrations are shown as vol.%.

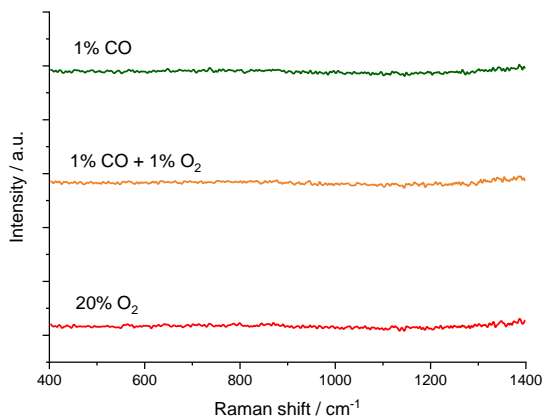


**Figure S1-16.** In situ Raman spectra of Pt<sub>2.1</sub>Fe<sub>0.7</sub>-Al<sub>2</sub>O<sub>3</sub>-673-5 under (a) 1 vol.% CO + 1 vol.% O<sub>2</sub>, (b) 1 vol.% CO, and 20 vol.% O<sub>2</sub> gas mixtures.

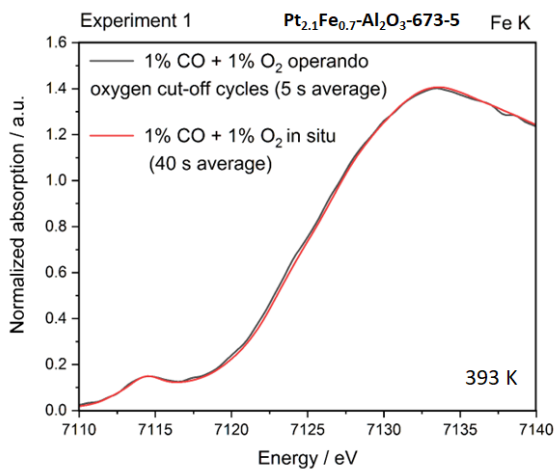


**Figure S1-17.** Comparison of operando Fe K-edge XAS spectrum measured during oxygen cut-off cycles averaged for 5 s with an in situ Fe K-edge XAS spectrum both collected under reaction conditions 1 vol.% CO + 1 vol.% O<sub>2</sub>, both at 393 K.



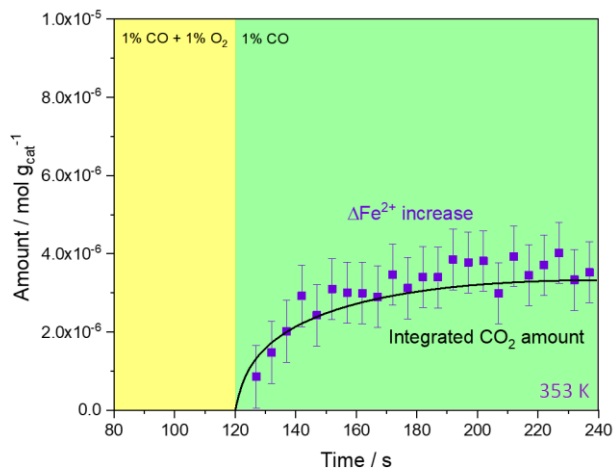


**Figure S1-18.** Comparison of amounts of produced carbon dioxide vs produced Fe<sup>2+</sup> after oxygen cut-off extracted from operando Fe K edge operando XAS / MS data for Pt<sub>2.1</sub>Fe<sub>0.7</sub>-Al<sub>2</sub>O<sub>3</sub>-673-5 at 353 K averaged over all cut-off cycles for the experiment number 4 with a helium carrier gas. Gas concentrations are shown as vol.%.

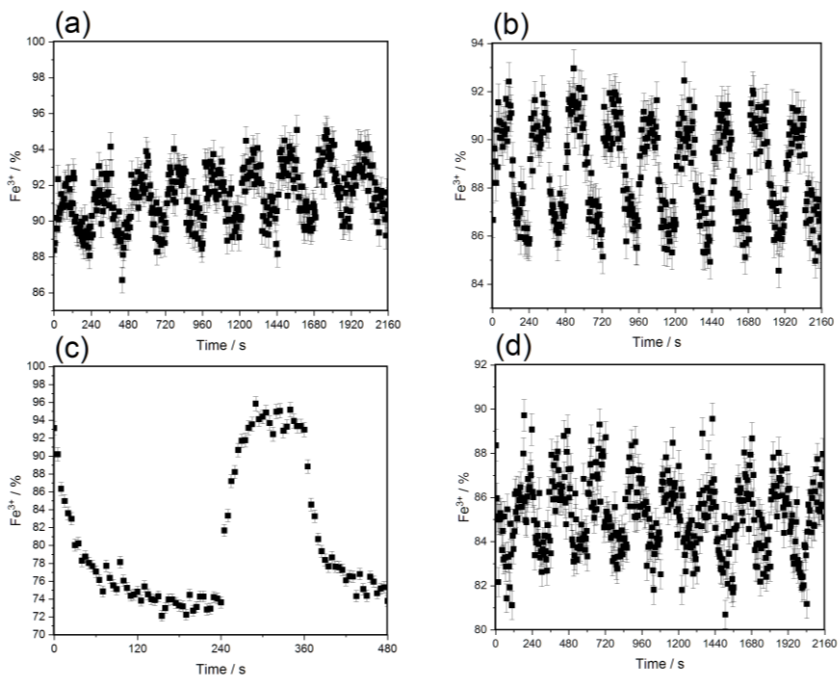


**Figure S1-19.** Reversible change of Fe<sup>3+</sup> concentration in Pt<sub>2.1</sub>Fe<sub>0.7</sub>-Al<sub>2</sub>O<sub>3</sub>-673-5 after multiple switching from 1 vol.% CO + 1 vol.% O<sub>2</sub> to 1 vol.% CO gas mixtures at 353-393 K before further averaging for the experiment 1 (a-c) and the experiment 4 (d).

**Table S1-1.** Experimental conditions of all XAS experiments.

Experiment number	Experiment type	Sample	Experiment description	XAS measurement mode	Carrier gas
1	Fe K-edge XAS	Pt <sub>2.1</sub> Fe <sub>0.7</sub> -Al <sub>2</sub> O <sub>3</sub> -673-5	TPR, steady-state experiments, oxygen cut-off cycles	fluorescence yield	argon
2	Pt L <sub>3</sub> -edge XAS	Pt <sub>2.1</sub> Fe <sub>0.7</sub> -Al <sub>2</sub> O <sub>3</sub> -673-5	TPR, steady-state experiments, oxygen cut-off cycles	transmission	helium
3	Pt L <sub>3</sub> -edge XAS	Pt <sub>2.0</sub> -Al <sub>2</sub> O <sub>3</sub> -673-5	steady-state experiments	transmission	helium
4	Fe K-edge XAS (reproduce the 1 <sup>st</sup> experiment)	Pt <sub>2.1</sub> Fe <sub>0.7</sub> -Al <sub>2</sub> O <sub>3</sub> -673-5	oxygen cut-off cycles (reproduce experiment 1)	fluorescence yield	helium
5	Fe K-edge XAS	Fe <sub>0.6</sub> -Al <sub>2</sub> O <sub>3</sub> -673-5	TPR, steady-state experiments, oxygen cut-off cycles	transmission	helium
6	Fe K-edge XAS (beam damage study)	Pt <sub>2.1</sub> Fe <sub>0.7</sub> -Al <sub>2</sub> O <sub>3</sub> -673-5	oxygen cut-off cycles	transmission	helium
7	Fe K-edge EXAFS	Pt <sub>2.1</sub> Fe <sub>0.7</sub> -Al <sub>2</sub> O <sub>3</sub> -673-5	TPR, steady-state in situ EXAFS	transmission	helium

**Table S1-2.** Optimized parameters of the Pt L<sub>3</sub>-edge EXAFS fit. *N*: coordination number, *R*: internuclear distance,  $\sigma^2$ : disorder parameter,  $\Delta E_0$ : energy shift.

	Model	Bond	<i>N</i>	<i>R</i> / Å	$\sigma^2$ / Å <sup>2</sup>	$\Delta E_0$ / eV
<b>Pt foil</b>	Pt	Pt-Pt	12.00 (fixed)	2.76 ± 0.06	0.0049 ± 0.0003	4.8 ± 0.8
<b>Pt<sub>2.1</sub>Fe<sub>0.7</sub>- Al<sub>2</sub>O<sub>3</sub>-673-5 reduced</b>	Pt	Pt-Pt	8.0 ± 1.1	2.70 ± 0.01	0.011 ± 0.002	3.8 ± 1.0

**Table S1-3.** Optimized parameters of the Fe K-edge EXAFS fit. N: coordination number, R: interatomic distance,  $\sigma^2$ : disorder parameter,  $\Delta E_0$ : energy shift.

	Model	Bond	N	R / Å	$\sigma^2 / \text{Å}^2$	$\Delta E_0 / \text{eV}$
<b>Fe foil</b>	Fe	Fe-Fe	8.00 (fixed)	$2.47 \pm 0.008$	$0.005 \pm 0.001$	$-1.4 \pm 1.5$
	Fe	Fe-Fe	6.00 (fixed)	$2.85 \pm 0.009$	$0.005 \pm 0.002$	$-1.4 \pm 1.5$
<b>Pt<sub>2.1</sub>Fe<sub>0.7</sub>- Al<sub>2</sub>O<sub>3</sub>-673-5 1 vol.% CO</b>	Fe <sub>2</sub> O <sub>3</sub>	Fe-O	$3.5 \pm 0.4$	$1.94 \pm 0.02$	$0.005 \pm 0.001$	$-2.2 \pm 2.2$
<b>Pt<sub>2.1</sub>Fe<sub>0.7</sub>- Al<sub>2</sub>O<sub>3</sub>-673-5 1 vol.% CO + 1 vol.% O<sub>2</sub></b>	Fe <sub>2</sub> O <sub>3</sub>	Fe-O	$4.3 \pm 0.5$	$1.94 \pm 0.01$	$0.005 \pm 0.001$	$-4.0 \pm 2.2$
<b>Pt<sub>2.1</sub>Fe<sub>0.7</sub>- Al<sub>2</sub>O<sub>3</sub>-673-5 5 vol.% O<sub>2</sub></b>	Fe <sub>2</sub> O <sub>3</sub>	Fe-O	$4.5 \pm 0.4$	$1.92 \pm 0.01$	$0.005 \pm 0.001$	$-4.7 \pm 1.9$

**Table S1-4.** Elemental composition and Pt dispersion of all used materials.

Catalyst	Elemental composition (ICP-OES)		Pt dispersion (CO chemisorption) after reduction, $D_{CO}$	Pt dispersion (Electron microscopy) after reduction, $D_{TEM}$
	Pt content / wt. %	Fe content / wt. %		
<b>Pt<sub>2.0</sub>-Al<sub>2</sub>O<sub>3</sub>-673-5</b>	2.0 ± 0.1	0	0.58	0.82
<b>Pt<sub>2.1</sub>Fe<sub>0.7</sub>-Al<sub>2</sub>O<sub>3</sub>-673-5</b>	2.09 ± 0.08	0.65 ± 0.06	0.56	0.69
<b>Fe<sub>0.6</sub>-Al<sub>2</sub>O<sub>3</sub>-673-5</b>	0	0.61 ± 0.06	-	-
<b>Al<sub>2</sub>O<sub>3</sub></b>	0	0	-	-

**Table S1-5.** Fe<sup>2+</sup> formation rates and carbon dioxide production rates for Pt<sub>2.1</sub>Fe<sub>0.7</sub>-Al<sub>2</sub>O<sub>3</sub>-673-5 during operando XAS oxygen cut-off experiments and preliminary catalytic tests. Calculations for operando oxygen cut-off experiments were performed after merging all subsequent cycles with a period of 240 s at each temperature.

Experiment 1				
Temperature / K	Operando Fe K-edge XAS			
	Fe <sup>2+</sup> formation rate / molFe <sup>2+</sup> s <sup>-1</sup> g <sub>cat</sub> <sup>-1</sup>	Steady-state reaction rate during oxygen cut-off cycles / molCO <sub>2</sub> s <sup>-1</sup> g <sub>cat</sub> <sup>-1</sup>	Steady-state reaction rate during oxygen cut-off cycles - background rate / molCO <sub>2</sub> s <sup>-1</sup> g <sub>cat</sub> <sup>-1</sup>	Number of oxygen cut-off cycles
393	1.07·10 <sup>-6</sup> (±4.8%)	2.78·10 <sup>-6</sup> (±11.9%)	2.56·10 <sup>-6</sup> (±12.9%)	1
373	2.42·10 <sup>-7</sup> (±8.2%)	7.70·10 <sup>-7</sup> (±22.3%)	6.42·10 <sup>-7</sup> (±26.7%)	9
353	1.12·10 <sup>-7</sup> (±25.0%)	2.69·10 <sup>-7</sup> (±2.6%)	2.00·10 <sup>-7</sup> (±3.5%)	9
Experiment 2				
Temperature / K	Operando Pt L <sub>3</sub> -edge XAS			
	-	Steady-state reaction rate during oxygen cut-off cycles / molCO <sub>2</sub> s <sup>-1</sup> g <sub>cat</sub> <sup>-1</sup>	Steady-state reaction rate during oxygen cut-off cycles - background rate / molCO <sub>2</sub> s <sup>-1</sup> g <sub>cat</sub> <sup>-1</sup>	Number of oxygen cut-off cycles
393	-	2.17·10 <sup>-6</sup> (±12.4%)	1.82·10 <sup>-6</sup> (±14.9%)	15
373	-	1.12·10 <sup>-6</sup> (±1.8%)	8.94·10 <sup>-7</sup> (±2.2%)	15
353	-	4.39·10 <sup>-7</sup> (±1.1%)	3.50·10 <sup>-7</sup> (±1.4%)	15
Experiment 4				
Temperature / K	Operando Fe K-edge XAS			
	Fe <sup>2+</sup> formation rate / molFe <sup>2+</sup> s <sup>-1</sup> g <sub>cat</sub> <sup>-1</sup>	Steady-state reaction rate during oxygen cut-off cycles / molCO <sub>2</sub> s <sup>-1</sup> g <sub>cat</sub> <sup>-1</sup>	Steady-state reaction rate during oxygen cut-off cycles - background rate / molCO <sub>2</sub> s <sup>-1</sup> g <sub>cat</sub> <sup>-1</sup>	Number of oxygen cut-off cycles
353	1.60·10 <sup>-7</sup> (±10.7%)	5.36·10 <sup>-7</sup> (±1.7%)	3.45·10 <sup>-7</sup> (±2.6%)	9

Catalytic tests before beamtime (tubular reactor)	
Temperature / K	Steady-state reaction rate / molCO <sub>2</sub> s <sup>-1</sup> g <sub>cat</sub> <sup>-1</sup>
393	2.15·10 <sup>-6</sup> (±0.4%)
383	1.48·10 <sup>-6</sup> (±0.4%)
373	1.08·10 <sup>-6</sup> (±0.4%)
363	7.84·10 <sup>-7</sup> (±0.4%)
353	5.00·10 <sup>-7</sup> (±0.4%)



**Table S1-6.** The maximal values of integrated amount of produced carbon dioxide and  $\Delta\text{Fe}^{2+}$  after 120 s exposure to 1 vol.% CO measured during operando Fe K-edge XAS oxygen cut-off cycles. Calculations were performed after merging all subsequent cycles with a period of 240 s at each temperature.

Experiment 1			
Temperature / K	Operando Fe K-edge XAS		
	Maximal $\Delta\text{Fe}^{2+}$ increase (after the oxygen cut-off) / $\text{molFe}^{2+} \text{ g}_{\text{cat}}^{-1}$	Maximal integrated $\text{CO}_2$ amount (after the oxygen cut-off) / $\text{molCO}_2 \text{ g}_{\text{cat}}^{-1}$	Ratio between maximal integrated $\text{CO}_2$ and $\Delta\text{Fe}^{2+}$ amounts
393	$2.17 \cdot 10^{-5} (\pm 2.2\%)$	$2.40 \cdot 10^{-5} (--)$	$1.06 \pm (0.02)$
373	$5.15 \cdot 10^{-6} (\pm 3.6\%)$	$6.51 \cdot 10^{-6} (\pm 13.4\%)$	$1.26 \pm 0.21$
353	$3.61 \cdot 10^{-6} (\pm 10.1\%)$	$2.78 \cdot 10^{-6} (\pm 4.7\%)$	$0.77 \pm 0.11$
Experiment 2			
Temperature / K	Operando Fe K-edge XAS		
	Maximal $\Delta\text{Fe}^{2+}$ increase (after the oxygen cut-off) / $\Delta\text{molFe}^{2+} \text{ g}_{\text{cat}}^{-1}$	Maximal integrated $\text{CO}_2$ amount (after the oxygen cut-off) / $\text{molCO}_2 \text{ g}_{\text{cat}}^{-1}$	Ratio between maximal integrated $\text{CO}_2$ and $\Delta\text{Fe}^{2+}$ amounts
353	$3.69 \cdot 10^{-6} (\pm 4.6\%)$	$3.33 \cdot 10^{-6} (\pm 11.3\%)$	$0.90 \pm 0.14$

## References

1. Chiarello, G. L.; Nachtegaal, M.; Marchionni, V.; Quaroni, L. and Ferri, D. Adding diffuse reflectance infrared Fourier transform spectroscopy capability to extended x-ray-absorption fine structure in a new cell to study solid catalysts in combination with a modulation approach. *Rev. Sci. Instrum.* **2014**, 85.

## S2. An Operando XAS Study of Preferential Carbon Monoxide Oxidation over $\gamma$ -Al<sub>2</sub>O<sub>3</sub> and SiO<sub>2</sub>-Supported Pt-Fe Catalysts Active at Ambient Temperature (Chapter 4)

The Supporting Information S2 is based on the article from Ilia I. Sadykov, Vitaly L. Sushkevich, Frank Krumeich, Rob Jeremiah G. Nuguid, Jeroen A. van Bokhoven, Maarten Nachtegaal and Olga V. Safonova, *Angew. Chem. Int. Ed.*, **2023**, *135*, e2022140.

## Catalysts and References (Chapter 4)

### Pt<sub>2.0</sub>-Al<sub>2</sub>O<sub>3</sub>-673-100

1.20 g of  $\gamma$ -Al<sub>2</sub>O<sub>3</sub> was impregnated with an aqueous solution of 0.05 g Pt(NH<sub>3</sub>)<sub>4</sub>(NO<sub>3</sub>)<sub>2</sub> (99.995% purity, Sigma-Aldrich) and then mixed for 10 min. The volume of the metal salt solution was equal to that of the pore volume of the support. After drying for 1 h, the catalyst was calcined for 2 h at 473 K and then for 2 h at 673 K. Catalyst was reduced before each experiment in situ for 1 h under 100 vol.% H<sub>2</sub> at 673 K.

### Pt<sub>2.1</sub>Fe<sub>1.1</sub>-Al<sub>2</sub>O<sub>3</sub>-673-100; Pt<sub>2.1</sub>Fe<sub>1.1</sub>-Al<sub>2</sub>O<sub>3</sub>-673-5; Pt<sub>2.1</sub>Fe<sub>1.1</sub>-Al<sub>2</sub>O<sub>3</sub>-473-100

1.17 g of  $\gamma$ -Al<sub>2</sub>O<sub>3</sub> was first impregnated with 0.05 g Pt(NH<sub>3</sub>)<sub>4</sub>(NO<sub>3</sub>)<sub>2</sub> and dried for 1 h at 393 K. After subsequent impregnation with an aqueous solution of 0.25 g Fe(NO<sub>3</sub>)<sub>3</sub>·9H<sub>2</sub>O and drying for 1 h at 393 K, the obtained catalyst was calcined for 2 h at 473 K and then for 2 h at 673 K. Calcined powder was split into two parts. Calcined powder was reduced in situ before each experiment at 473 or 673 K either under 5 vol.% H<sub>2</sub> (50 mbar), or under 100 vol.% H<sub>2</sub> (1 bar), respectively. All heating rates were 10 K min<sup>-1</sup>.

### Pt<sub>2.0</sub>Fe<sub>1.4</sub>-SiO<sub>2</sub>-473-100; Pt<sub>2.0</sub>Fe<sub>1.4</sub>-SiO<sub>2</sub>-673-100

1.10 g of SiO<sub>2</sub> was first impregnated with 0.05 g Pt(NH<sub>3</sub>)<sub>4</sub>(NO<sub>3</sub>)<sub>2</sub> and dried for 1 h at 393 K. After subsequent impregnation with an aqueous solution of 0.25 g Fe(NO<sub>3</sub>)<sub>3</sub>·9H<sub>2</sub>O and drying for 1 h at 393 K, the obtained catalyst was calcined for 2 h at 473 K and then for 2 h at 673 K. Calcined powder was split into two parts. Calcined powder was reduced in situ before each experiment under 100 vol.% H<sub>2</sub> (1 bar) either at 473 or 673 K, respectively. All heating rates were 10 K min<sup>-1</sup>.

### Pt-Fe/C Reference Alloy

1 g of carbon black with the specific BET surface area of 150 m<sup>2</sup> g<sup>-1</sup> was impregnated in 50:50: water-ethanol solution of 0.43 g Fe(NO<sub>3</sub>)<sub>3</sub>·9H<sub>2</sub>O and 0.23 g of Pt(NH<sub>3</sub>)<sub>4</sub>(NO<sub>3</sub>)<sub>2</sub>. Resulting material was dried for 1 h and calcined on air for 2 h at 473 K. It was then reduced in situ under 2 bar of pure hydrogen at 873 K in 2 mm quartz capillary and sealed for further investigation. The resulting material contained 5.2 wt.% Fe and 10 wt.% Pt as it had been determined by ICP-OES (**Table S2-1**). Ex situ STEM measured after air exposure, showed that platinum and iron had formed relatively large agglomerated nanoparticles (**Figure S2-21**). Pt L<sub>3</sub>-edge XAS confirmed alloy formation (**Figure S2-22**, **Table S2-5**).

## Methods (Chapter 4)

### In situ FTIR Fitting

The OMNIC 9.3 (Thermo Fischer Scientific) software was used to process the collected spectra and to extract the baseline (polynomial function). Fitting of the main band associated with the carbon monoxide linearly adsorbed to platinum was performed for all catalysts employing the fitting range of 2120-2040  $\text{cm}^{-1}$  using three pseudo-Voigt functions in Origin software (OriginLab Corp.). Peak positions, area, profile shape factor (fraction of the Lorentz function contribution), and full width at half maximum (FWHM) for each of the three peaks were used as free variables. The baseline was constrained to be a straight line with the height corresponding to the signal at 2120  $\text{cm}^{-1}$ . For fit details reader is referred to **Table S2-4** and **Figure S2-4**. The Pseudo-Voigt function used for the fit is the following:

$$y = y_0 + A \left[ m_u \frac{2}{\pi} \frac{w}{4(x - x_c)^2 + w^2} + (1 - m_u) \frac{\sqrt{4 \ln 2}}{\sqrt{\pi} w} e^{-\frac{4 \ln 2}{w^2}(x - x_c)^2} \right]$$

, where  $y_0$  - baseline offset,  $A$  - peak area,  $m_u$  - profile shape factor (fraction of the Lorentz function contribution),  $w$  - full width at half maximum (FWHM),  $x_c$  - peak center.

The fit of  $\text{Pt}_{2.1}\text{Fe}_{1.1}\text{-Al}_2\text{O}_3\text{-673-100}$ , and  $\text{Pt}_{2.1}\text{Fe}_{1.1}\text{-Al}_2\text{O}_3\text{-673-5}$  using the same 2092, 2079, and 2063  $\text{cm}^{-1}$  peaks with the same FWHM and profile shape factors as for  $\text{Pt}_{2.0}\text{Fe}_{1.4}\text{-SiO}_2\text{-473-100}$  is shown in **Figure S2-4d,e** and **Table S2-4**. Clearly, FTIR peak components from  $\text{Pt}_{2.0}\text{Fe}_{1.4}\text{-SiO}_2\text{-473-100}$  are different from that of alumina-supported Pt-FeO<sub>x</sub> catalysts and do not effectively describe those. For technical details readers are referred to Chapter 7.

### Catalysts Activity Measurements

All samples were measured in the operando cell in the same way as during the following operando experiments.<sup>1</sup> Catalysts activities were calculated only after 1 h to achieve stable conversion for the reaction orders measurements and the temperature ramp. We used different concentrations of oxygen, carbon monoxide, water, and hydrogen to measure reaction orders keeping the total pressure and flow rate the same. Reactants partial pressures were calculated taking into account both ambient pressure and the pressure drop before the catalyst bed, which was about 200 mbar. The mass spectrometer was calibrated immediately after the catalytic tests. The conversion was always kept below 15%, which allowed us to accurately extract the catalytic reaction rates. The reaction temperature was determined as the temperature of the thermocouple inserted in a catalyst bed. Water was produced using a custom-made water generator filled with 5 g of 5 wt.% Pt/Al<sub>2</sub>O<sub>3</sub> (J&M, sieved) and connected to one of the supply lines. Water was produced by hydrogen oxidation with a small amount of oxygen up to 1 vol.% O<sub>2</sub>. During all water addition tests, the total flow rate was kept at 180 ml min<sup>-1</sup>, pressure drop was 150 mbar. PROX reaction mixture composition was 2 vol.% O<sub>2</sub> + 5 vol.% CO + 40 vol.% H<sub>2</sub> in He.

A mass spectrometer (MS, OmniStar GSD 320 O1, Pfeiffer) was connected to the outlet of the operando cell to measure the composition of the feed and catalyst activity. Carbon dioxide concentration was calculated from the 44 (m/z) / 4 (m/z) ratio through a preliminary calibration with the mixture of 1000.0 ppm CO<sub>2</sub> 4.8 and 1000.0 ppm O<sub>2</sub> 4.8 in He 5.0 (Carbagas AG) diluted with helium (He 6.0, Carbagas AG) supplied to the MS through the bypass line with the same pressure drop and total flow rate as in the operando cell. Undesirable hydrogen oxidation was estimated from the 18 (m/z) / 4 (m/z) ratio through a preliminary calibration with water vapor in the concentration range of 0.01 - 2 vol.% H<sub>2</sub>O.

About 7 mg of fresh catalyst diluted with 15 mg of silica (Fluka, 99.999% purity silica) was used in each experiment to ensure the conversion of carbon monoxide was below 15% and oxygen selectivity to carbon monoxide oxidation (CO selectivity) was close to 100% ( $\pm 2\%$ ). The differential reactor model was used to calculate specific rates.

### Time-on-stream Activity in the Tubular Reactor

In order to compare the activity of the most active catalysts: Pt<sub>2.0</sub>Fe<sub>1.4</sub>-SiO<sub>2</sub>-473-100 and Pt<sub>2.1</sub>Fe<sub>1.1</sub>-Al<sub>2</sub>O<sub>3</sub>-673-100 with the literature references, we used a tubular fixed-bed reactor connected to the same gas supply system and the same on-line mass-spectrometer as during the operando XAS experiments and kinetic studies. Mass-spectrometer was further recalibrated to adequately determine conversion and selectivity at each specific flow rate. The differential reactor model was used to calculate specific rates.

We studied the activity of the two aforementioned catalysts under the same conditions as in the paper by Qiao et al.<sup>2</sup> Namely, 4.00 mg of the catalyst was diluted with 150 mg SiC both sieved to the pellet size of 200 mesh and placed in the tubular reactor between two quartz wool plugs. The reactor temperature was controlled using a K-type thermocouple to be the same (<1 K difference) across the entire length of the catalysts bed. After cooling down to 353 K (80°C) under 100 vol.% H<sub>2</sub> from a specific reduction temperature used for the pretreatment, the reaction mixture of 1 vol.% O<sub>2</sub> + 2 vol.% CO + 40 vol.% H<sub>2</sub> in He was supplied to the catalyst with the velocity of 180 ml min<sup>-1</sup>. CO oxidation rates at 20 minutes, 40 minutes, and 60 minutes under this reaction mixture were averaged and used to calculate the specific rate as in the cited paper.<sup>2</sup>

To reproduce the time-on-stream PROX activity tests at high conversion performed by Qiao et al., we diluted 9.8 mg of the catalyst with 150 mg of SiC both sieved to the pellet size of 200 mesh, and supplied the reaction mixture of 1 vol.% O<sub>2</sub> + 2 vol.% CO + 40 vol.% H<sub>2</sub> in He at 9.8 ml min<sup>-1</sup> to achieve the space velocity of 2.1 × 10<sup>6</sup> ml gPt<sup>-1</sup> h<sup>-1</sup> equal to that of the original paper.<sup>2</sup>

### In situ/operando XAS Experiments

We performed a series of in situ/operando XAS experiments at the Fe K and Pt L<sub>3</sub>-edges using the operando reactor cell connected to two separate gas feeds.<sup>1</sup> Each gas feed was controlled using four gas mass flow controllers (Bronkhorst). Fast switching between the two gas feeds was realized using two three-way solenoid switching valves (Parker, Series 9). While one gas mixture was flowing to the cell, the other was directed via a bypass to the outlet. A mass spectrometer (MS, OmniStar GSD 320 O1, Pfeiffer) was connected to the outlet of the operando cell to measure the composition of the feed and catalyst activity. All the other conditions, including the pressure and the catalyst mass, were as during the preliminary experiments. Using a needle valve on the bypass line, we reduced the back-pressure difference between the cell and the bypass line down to 5 mbar. All of this allowed us to perform transient experiments following kinetics on a scale of seconds. Linear combination fitting of Fe K-edge XANES was performed on the spectra averaged over 150 s. During the fast switching cut-off experiments, Fe K-edge XANES spectra were averaged every 10 s. CO and O<sub>2</sub> conversions during operando XAS experiments were both below 15%. The differential reactor model was used to calculate specific rates.

### EXAFS Processing

A homemade python-based “ProQEXAFS” v.2.39 software was used for initial Fe and Pt L<sub>3</sub>-edge XAS data importing, energy calibration, averaging, background subtraction, and normalization to an edge-step of one.<sup>3</sup> Linear combination fitting of Fe K-edge XANES data was performed using the same software. A sum of all components fractions was constrained to unity. Examples of the linear combination fit for operando Fe K-edge XANES spectra averaged over 150 s are shown in **Figure S2-6**. Linear combination fit during oxygen and hydrogen cut-off experiments (**Figures S2-20; S2-21**) was performed with the averaging spectra every 10 s.

Fe K-edge EXAFS, initially processed with “ProQEXAFS” v.2.39, was fitted using the Demeter software package.<sup>4</sup> We extracted the amplitude reduction factor from the fitting of the reference iron foil (0.75). Then we performed EXAFS fitting using multiple k weightings of 1-3 within the k-range of 3.0-9.5 Å<sup>-1</sup> and an R-range of 1.0-4.0 Å. All fitting parameters are summarized in **Table S2-6**. The EXAFS fitting models were goethite and a DFT model of FeO<sub>x</sub>/Pt described by Y. Wang et al.<sup>5</sup> Goethite can adequately describe

surface iron oxidic species because of its low-density structure. The number of independent points was  $N_{\text{ind}} > 9$ . The Fe K-edge EXAFS fit for all samples is shown in **Figure S2-14**.

Pt L<sub>3</sub>-edge EXAFS spectra collected under steady-state conditions were used for the EXAFS analysis. The amplitude reduction factor ( $S_0^2$ ) was estimated from the fitting of the reference Pt foil EXAFS to be 0.84.

For all the alumina-supported under study, the fit was performed in R-space in the range of 1.0-3.5 Å, employing the k-range of 3.0-9.0 Å<sup>-1</sup> for the Fourier transform (FT). Datasets were fitted simultaneously with multiple k weightings of 1-3, so as to reduce correlations between the fitting parameters. All fitting parameters are summarized in **Table S2-5**. The number of independent points was  $N_{\text{ind}} > 7$ . The Pt L<sub>3</sub>-edge EXAFS fit for all samples is shown in **Figure S2-5**.

EXAFS of Pt<sub>2.0</sub>Fe<sub>1.4</sub>-SiO<sub>2</sub>-473-100 was fitted using the R-space range of 1.0-3.5 Å and the k-range of 3.0-13.0 Å<sup>-1</sup>. The PtFe/C reference EXAFS was fitted using the R-space range of 1.0-3.5 Å and the k-range of 3.0-16.0 Å<sup>-1</sup>. The EXAFS fit for the PtFe/C reference is shown in **Figure S2-23**.

#### Estimation of Platinum Particle Size from Pt L<sub>3</sub>-edge EXAFS

Extracted from Pt L<sub>3</sub>-edge EXAFS fit platinum mean Pt-Pt coordination numbers and average Pt-Pt distances were compared with the electron microscopy-derived coordination numbers. Two models were employed, the first one proposed by Calvin et al., which estimates the mean Pt-Pt coordination number in a spherical nanoparticle ( $n_{\text{nano}}$ ) using the following equation:<sup>6</sup>

$$n_{\text{nano}} = \left[ 1 - \frac{3}{4} \left( \frac{r}{R} \right) + \frac{1}{16} \left( \frac{r}{R} \right)^3 \right] n_{\text{bulk}}$$

, where  $r$  is the distance between the nearest-neighbor platinum atoms from EXAFS (**Table S2-5**),  $R$  is the particle radius,  $n_{\text{bulk}} = 12$  is the nearest-neighbor coordination number for bulk platinum.

The second model proposed by Frenkel et al., on the contrary, uses EXAFS-derived Pt-Pt average distance to estimate the number of platinum layers for the entire particle size distribution derived from TEM.<sup>7</sup> First, we extract the number of platinum layers, assuming a cuboctahedral shape of the particles:  $L = D/2r$ , where  $D$  is the particle diameter and  $r$  is the Pt-Pt distance in the first coordination sphere. Particle size distribution can be expressed as the platinum layers distribution approximated by the Gaussian function:

$$\rho(L) = \exp\left(\frac{-(L - L_{\text{av}})^2}{2\sigma_s^2}\right)$$

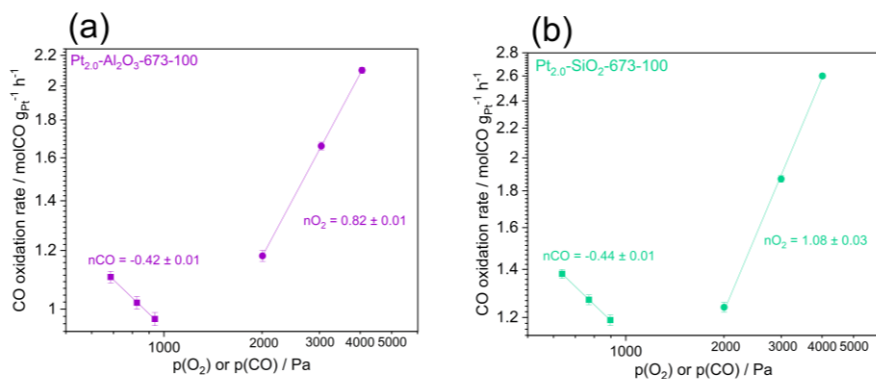
, where  $L_{\text{av}}$  is the average number of platinum layers and  $\sigma_s$  is the standard deviation in  $L$ . Then one is able to compare the theoretical coordination numbers in a cuboctahedral cluster of a certain order; the average coordination numbers are calculated over all clusters with the size distribution  $\rho(L)$ :

$$n_{\text{app}} = \frac{\int_0^{\infty} \rho(L)N(L)n(L)dL}{\int_0^{\infty} \rho(L)N(L)dL}$$

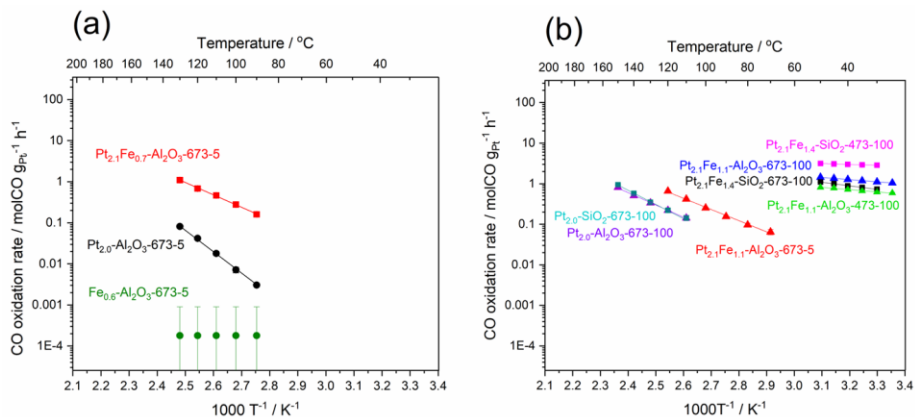
, where  $N(L)$  is the number of atoms in an octahedral cluster of a certain size and  $n(L)$  is the number of atoms in each cluster, which for an octahedral cluster equals:

$$n(L) = \frac{24L(5L^2 + 3L + 1)}{10L^3 + 15L^2 + 11L + 3}$$

## Figures and Tables to S2 (Chapter 4)

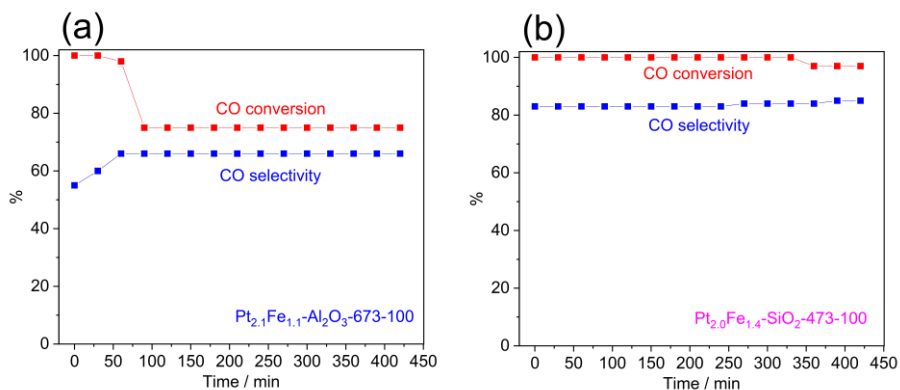


**Figure S2-1.** Double-logarithmic plots of the dependence of the PROX rate on partial carbon monoxide and oxygen pressures at 313 K for  $\text{Pt}_{2.0}\text{-Al}_2\text{O}_3\text{-673-100}$  (a) and  $\text{Pt}_{2.0}\text{-SiO}_2\text{-673-100}$  (b).

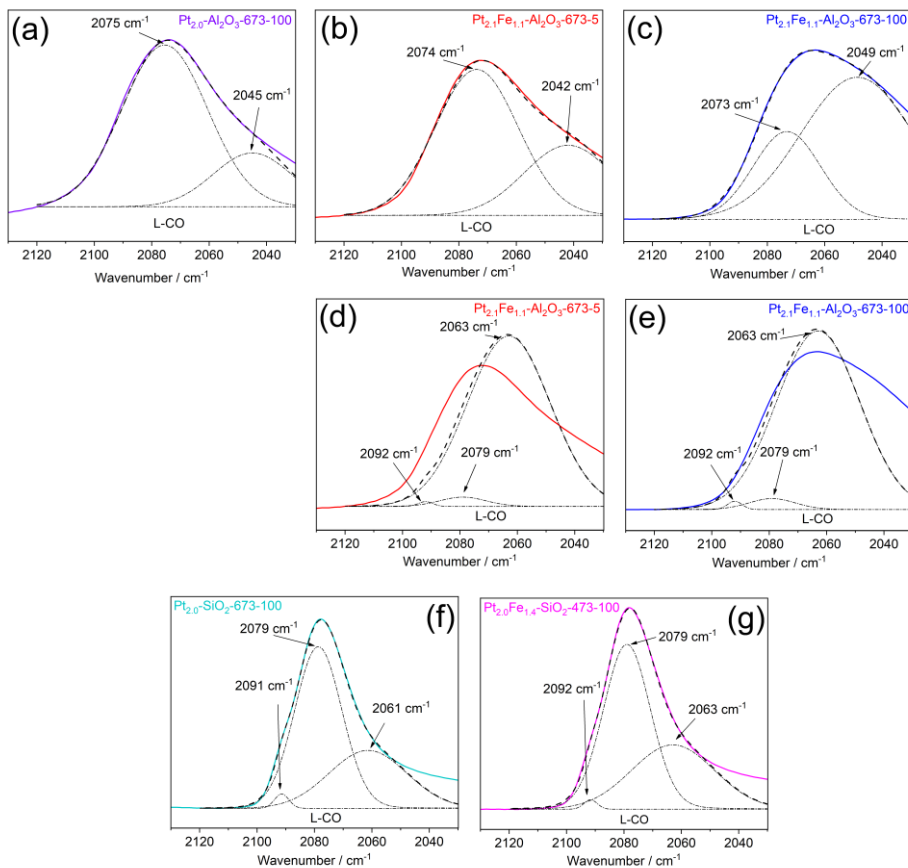


**Figure S2-2.** Arrhenius plots of the carbon monoxide oxidation activity of the catalysts from (a) Chapter 3 measured under 1 vol.% CO + 1 vol.%  $\text{O}_2$  in He, (b) Chapter 4 measured under 1 vol.%  $\text{O}_2$  + 2 vol.% CO + 40 vol.%  $\text{H}_2$  in He.

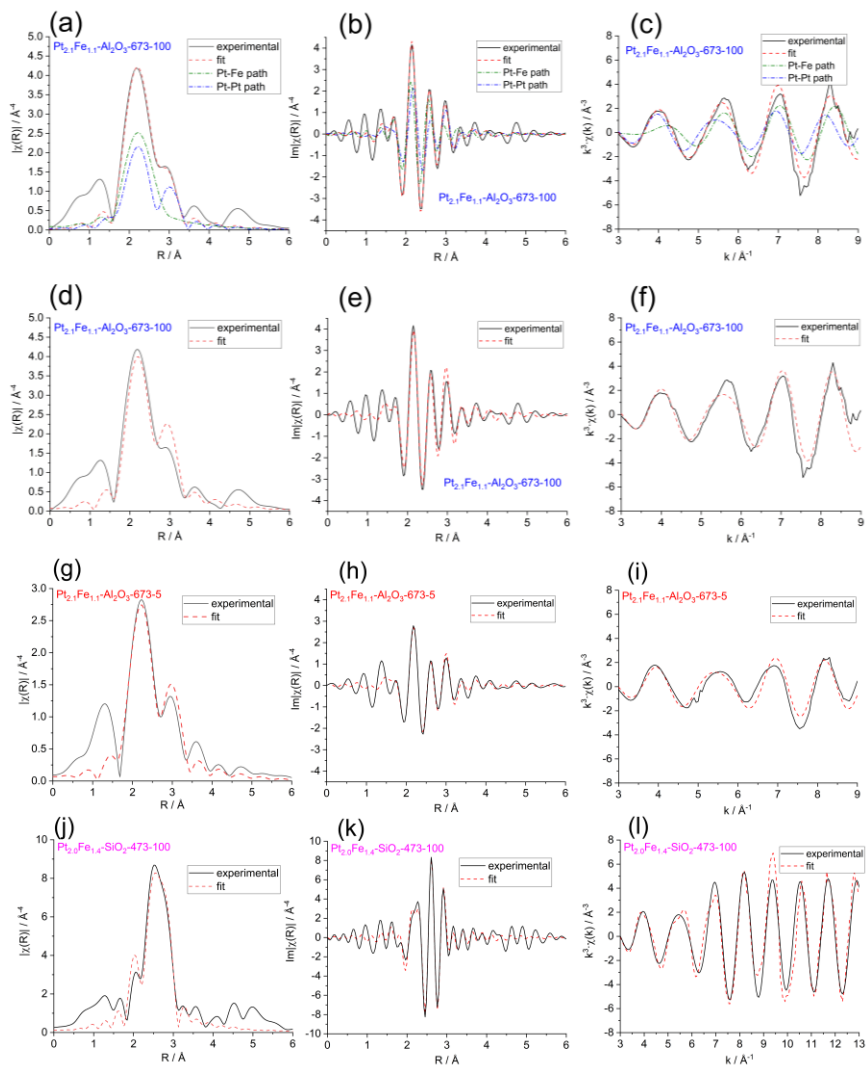




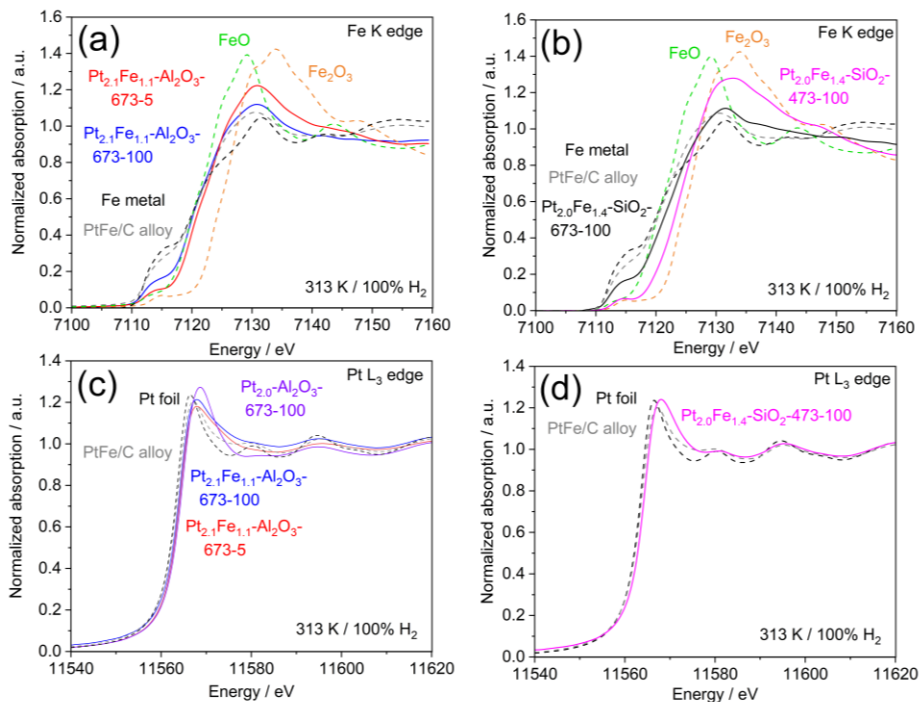
**Figure S2-3.** Carbon monoxide conversion (red) and selectivity to carbon monoxide oxidation (blue, CO selectivity) for  $\text{Pt}_{2.1}\text{Fe}_{1.1}\text{-Al}_2\text{O}_3\text{-673-100}$  (a) and  $\text{Pt}_{2.0}\text{Fe}_{1.4}\text{-SiO}_2\text{-473-100}$  (b) catalysts during the time-on-stream PROX reaction at 353 K (80 °C). The feed gas composition was 40 vol%  $\text{H}_2$ , 1 vol% CO, 1 vol%  $\text{O}_2$  and balance He. Space velocities were  $2.1 \times 10^6 \text{ ml} \cdot \text{g}_{\text{Pt}}^{-1} \text{ h}^{-1}$ .



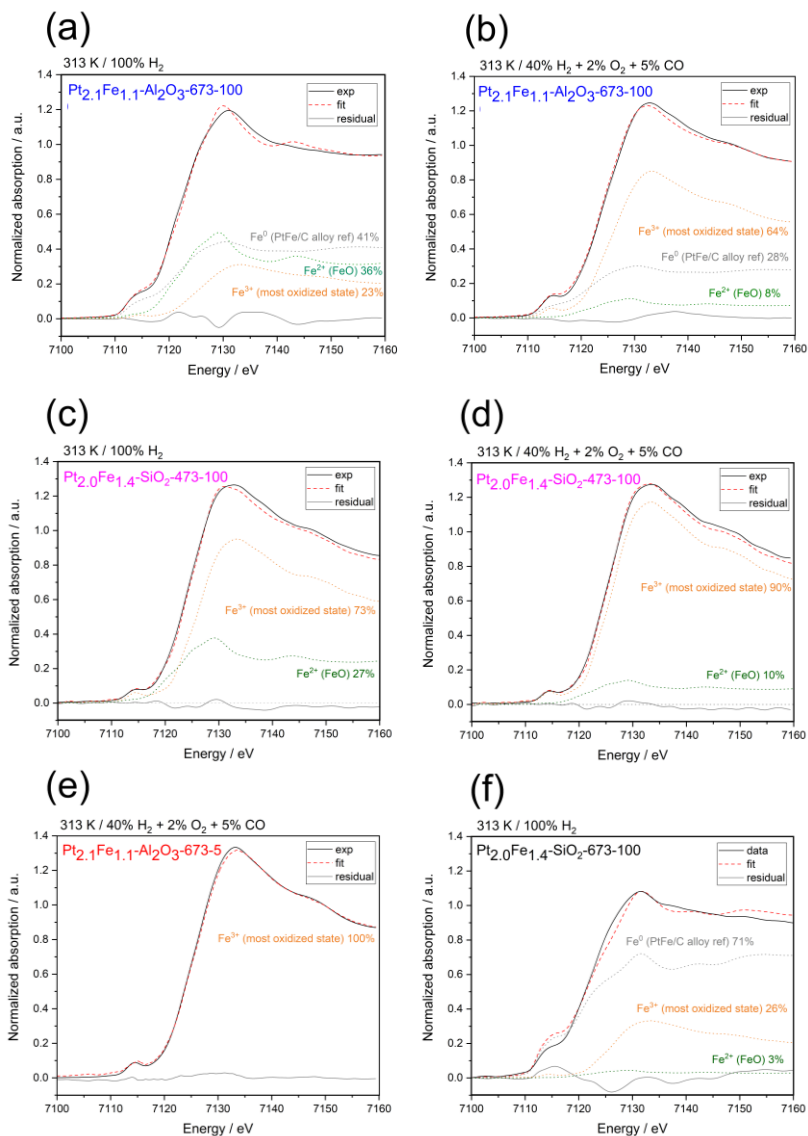
**Figure S2-4.** Fitted in situ FTIR spectra of carbon monoxide adsorption at 300 K on  $\text{Pt}_{2.0}\text{-Al}_2\text{O}_3\text{-673-100}$  (a),  $\text{Pt}_{2.1}\text{Fe}_{1.1}\text{-Al}_2\text{O}_3\text{-673-5}$  (b - successful fit, d - unsuccessful fit),  $\text{Pt}_{2.1}\text{Fe}_{1.1}\text{-Al}_2\text{O}_3\text{-673-100}$  (c - successful fit, e - unsuccessful fit),  $\text{Pt}_{2.0}\text{-SiO}_2\text{-673-100}$  (f), and  $\text{Pt}_{2.0}\text{Fe}_{1.4}\text{-SiO}_2\text{-473-100}$  catalysts (g); solid line - experimental data, dashed line - fit, dashed-dotted line - separate fit components. For details on fit parameters reader is referred to **Table S2-4**.



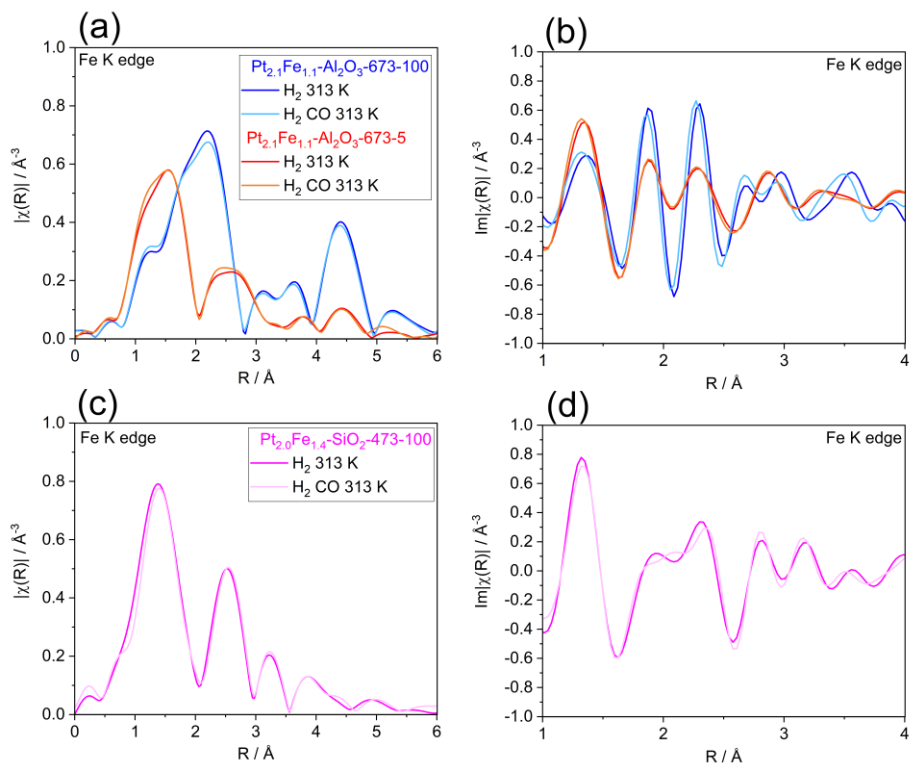
**Figure S2-5.** Fit of the Fourier-transformed  $k^3$ -weighted Pt  $L_3$ -edge EXAFS modulus (a,d,g,j) and imaginary (b,e,h,k) parts, as well as the fit of the real part of the  $\chi(k)$  (c,f,i,l) measured at 313 K under hydrogen for  $Pt_{2.1}Fe_{1.1}Al_2O_3-673-100$  (a-c, alloy model),  $Pt_{2.1}Fe_{1.1}Al_2O_3-673-100$  (d-f, no alloy),  $Pt_{2.1}Fe_{1.1}Al_2O_3-673-5$  (g-i, no alloy), and  $Pt_{2.0}Fe_{1.4}SiO_2-473-100$  (j-l, no alloy). Black solid line - experimental data, red dashed line - fit, dashed-dotted lines show individual path signals.



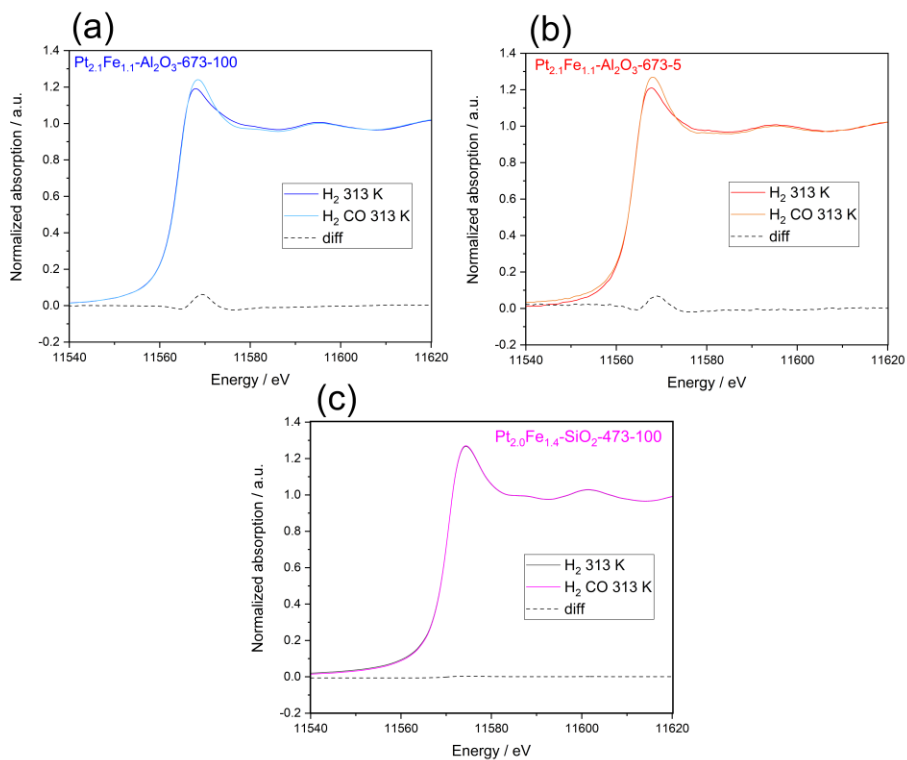
**Figure S2-6.** In situ Fe K-edge (a), (b) and Pt L<sub>3</sub>-edge (c), (d) XANES of as-reduced catalysts (solid) and multiple references (dashed) under 1 bar hydrogen (100 vol.%  $\text{H}_2$ ) at 313 K.



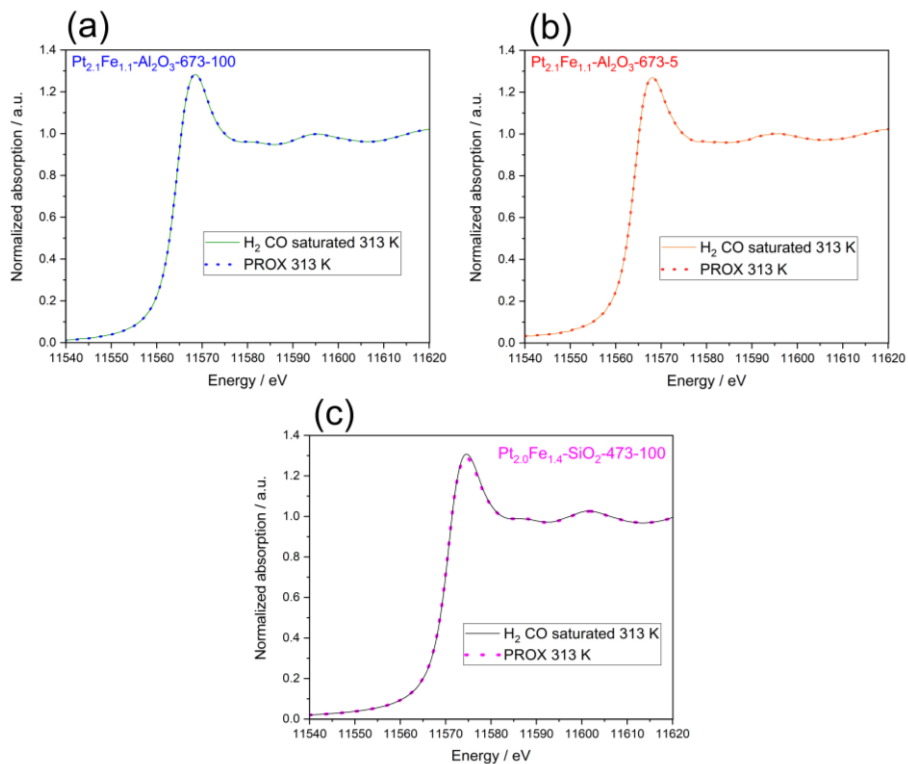
**Figure S2-7.** Examples of the linear combination fit of operando Fe K-edge XANES spectra of  $\text{Pt}_{2.1}\text{Fe}_{1.1}\text{-Al}_2\text{O}_3\text{-673-100}$  (a) -650 s during experiment 3; (b) 1900 s during experiment 3;  $\text{Pt}_{2.0}\text{Fe}_{1.4}\text{-SiO}_2\text{-473-100}$  (c) -388 s during the experiment, (d) 2090 s during the experiment;  $\text{Pt}_{2.1}\text{Fe}_{1.1}\text{-Al}_2\text{O}_3\text{-673-5}$  (e) 300 s during the experiment;  $\text{Pt}_{2.0}\text{Fe}_{1.4}\text{-SiO}_2\text{-673-100}$  (f); under 100 vol.%  $\text{H}_2$  (a), (c), (f) or under the PROX mixture: 40 vol.%  $\text{H}_2$  + 5 vol.%  $\text{CO}$  + 2 vol.%  $\text{O}_2$  (b), (d), (e) gas mixtures at 313 K. Each figure shows a spectrum averaged over 150 s.



**Figure S2-8.** Modulus (a,c) and imaginary (b,d) parts of the Fourier-transformed Fe K-edge EXAFS spectra of Pt<sub>2.1</sub>Fe<sub>1.1</sub>-Al<sub>2</sub>O<sub>3</sub>-673-100, Pt<sub>2.1</sub>Fe<sub>1.1</sub>-Al<sub>2</sub>O<sub>3</sub>-673-5 (a,b) and Pt<sub>2.0</sub>Fe<sub>1.4</sub>-SiO<sub>2</sub>-473-100 (c-d) immediately after reduction under 100 vol.% H<sub>2</sub> and under 40 vol.% H<sub>2</sub> + 5 vol.% CO at 313 K.

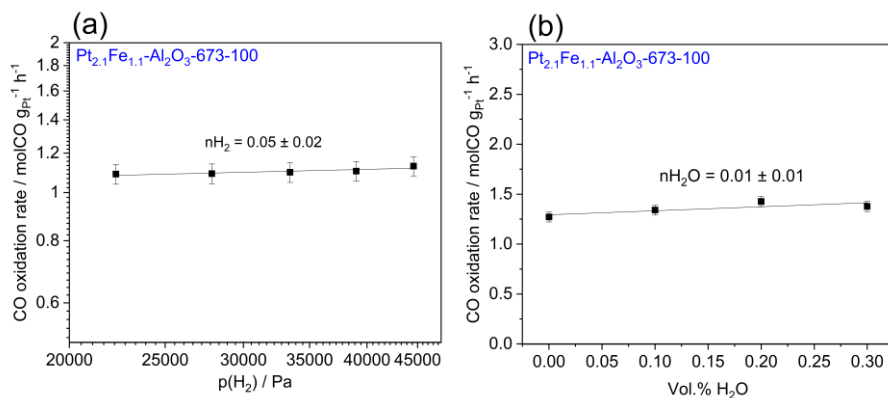


**Figure S2-9.** The difference between the Pt L<sub>3</sub>-edge XANES spectra of reduced (under 100 vol.% H<sub>2</sub>) and carbon monoxide-covered platinum (under 40 vol.% H<sub>2</sub> + 5 vol.% CO) components at 313 K for Pt<sub>2.1</sub>Fe<sub>1.1</sub>-Al<sub>2</sub>O<sub>3</sub>-673-100 H<sub>2</sub> (a), Pt<sub>2.1</sub>Fe<sub>1.1</sub>-Al<sub>2</sub>O<sub>3</sub>-673-5 (b) and Pt<sub>2.0</sub>Fe<sub>1.4</sub>-SiO<sub>2</sub>-473-100 (c).

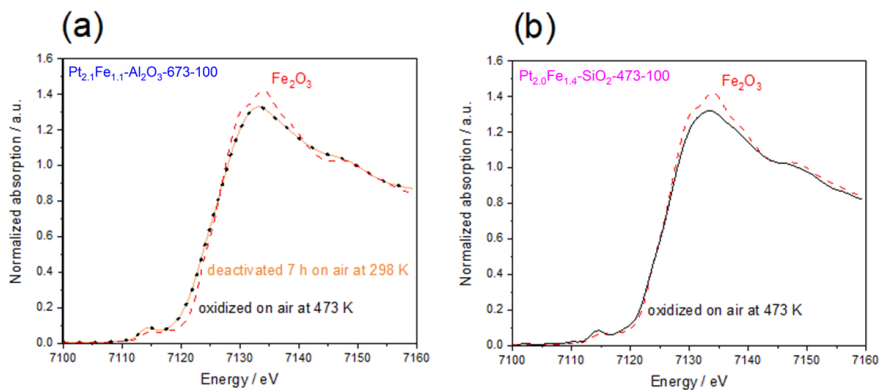


**Figure S2-10.** Comparison of operando Pt L<sub>3</sub>-edge XANES spectra of Pt<sub>2.1</sub>Fe<sub>1.1</sub>-Al<sub>2</sub>O<sub>3</sub>-673-100 (a), Pt<sub>2.1</sub>Fe<sub>1.1</sub>-Al<sub>2</sub>O<sub>3</sub>-673-5 (b), and Pt<sub>2.0</sub>Fe<sub>1.4</sub>-SiO<sub>2</sub>-473-100 (c) under 40 vol.% H<sub>2</sub> + 5 vol.% CO + 2 vol.% O<sub>2</sub> (dashed) and 40 vol.% H<sub>2</sub> + 5 vol.% CO (solid) gas mixtures at 313 K after 30 min under reaction conditions.

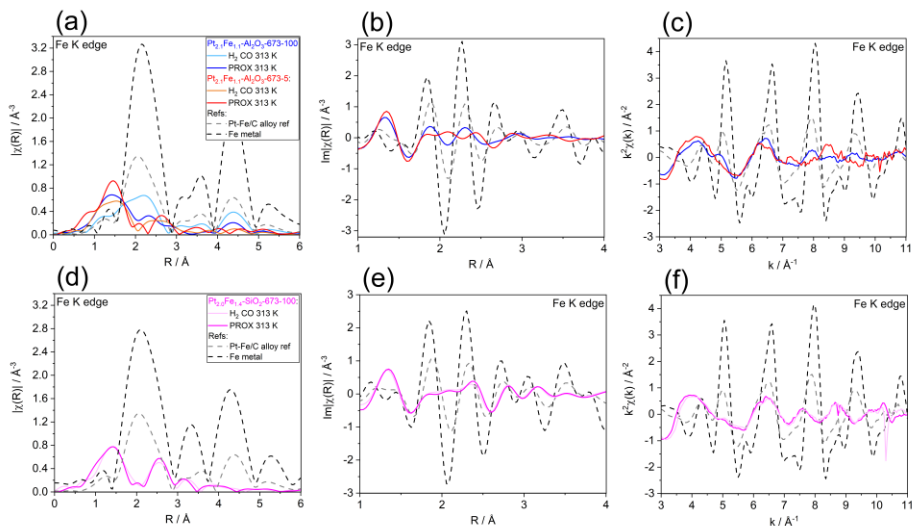




**Figure S2-11.** (a) Double-logarithmic plot of the dependence of the PROX rate over  $\text{Pt}_{2.1}\text{Fe}_{1.1}\text{-Al}_2\text{O}_3\text{-673-100}$  on varying hydrogen partial pressure while keeping total pressure constant; (b) an influence of water concentration on PROX rate over  $\text{Pt}_{2.1}\text{Fe}_{1.1}\text{-Al}_2\text{O}_3\text{-673-100}$ . PROX gas mixture is 40(x) vol.%  $\text{H}_2$  + 5 vol.%  $\text{CO}$  + 2 vol.%  $\text{O}_2$  + y vol.%  $\text{H}_2\text{O}$ . All measurements were done after activity stabilization for 1 h under PROX conditions at 313 K.

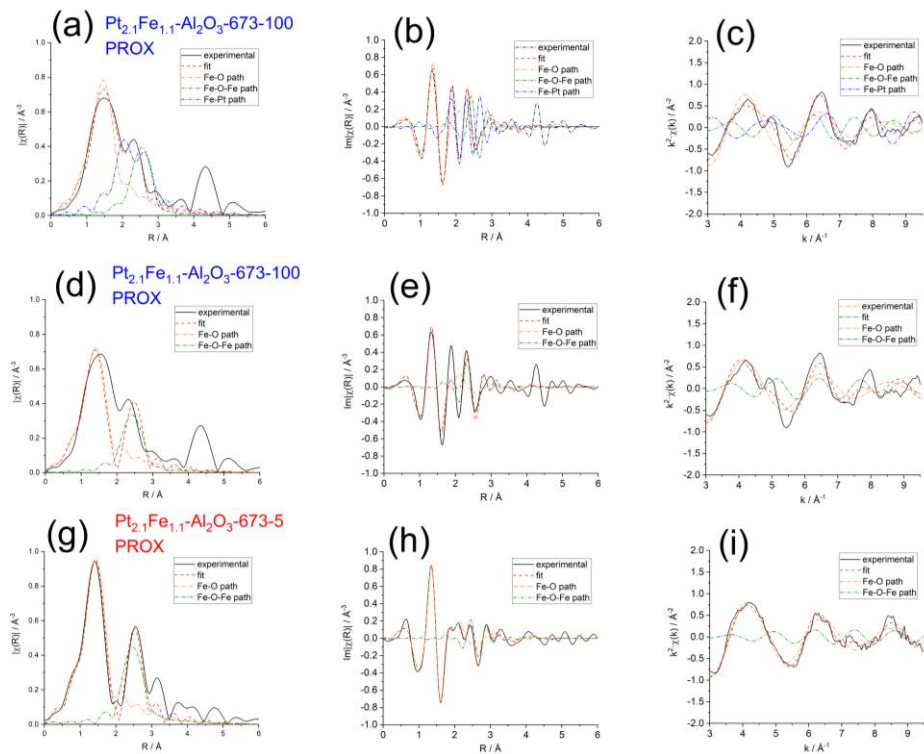


**Figure S2-12.** Fe K-edge XANES of  $\text{Pt}_{2.1}\text{Fe}_{1.1}\text{-Al}_2\text{O}_3\text{-673-100}$  (a) and  $\text{Pt}_{2.0}\text{Fe}_{1.4}\text{-SiO}_2\text{-473-100}$  (b) catalysts after deactivation on air for 7 h and after the temperature programmed oxidation at 473 K ( $10\text{ K min}^{-1}$  heating rate), XANES of the  $\text{Fe}_2\text{O}_3$  reference.



**Figure S2-13.** Modulus (a,d) and imaginary (b,e) parts of the Fourier-transformed Fe K-edge EXAFS of  $Pt_{2.1}Fe_{1.1}-Al_2O_3-673-100$ ,  $Pt_{2.1}Fe_{1.1}-Al_2O_3-673-5$ , and  $Pt_{2.0}Fe_{1.4}-SiO_2-473-100$  (solid lines), as well as references: Pt-Fe/C and Fe (dashed lines); (c,f) Fe K-edge EXAFS in  $k$ -space of  $Pt_{2.1}Fe_{1.1}-Al_2O_3-673-100$ ,  $Pt_{2.1}Fe_{1.1}-Al_2O_3-673-5$ , and  $Pt_{2.0}Fe_{1.4}-SiO_2-473-100$  (solid lines), as well as references: Pt-Fe/C and Fe (dashed lines). All spectra were measured right after reduction under 40 vol.%  $H_2$  + 5 vol.% CO or under PROX: 40 vol.%  $H_2$  + 5 vol.% CO + 2 vol.%  $O_2$  after 30 min of reaction (experiment 1) at 313 K.





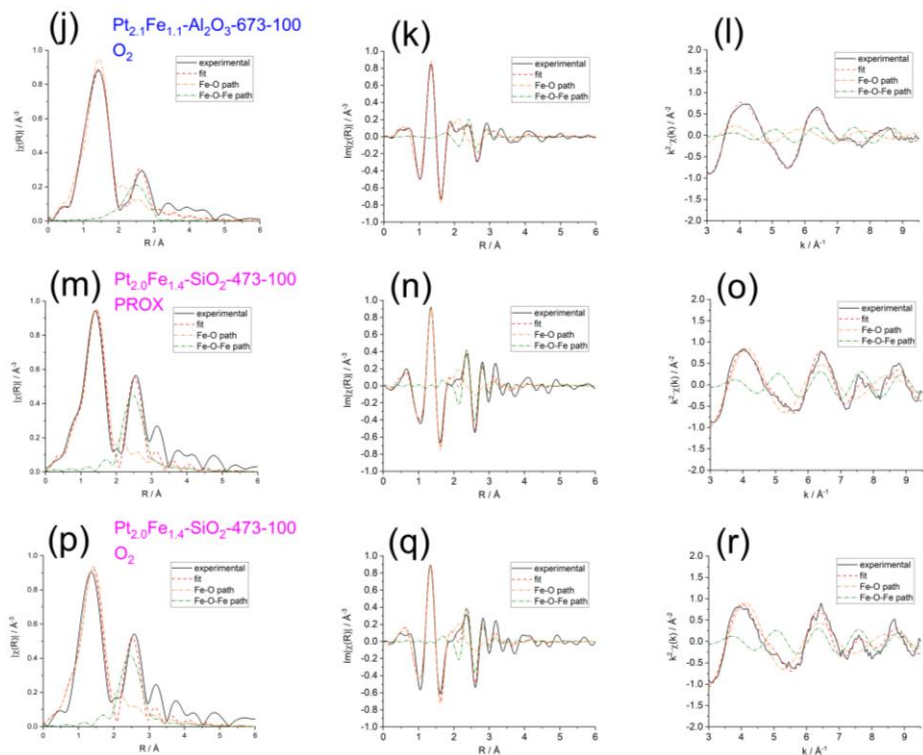


**Figure S2-14.** Fit of the Fourier-transformed  $k^2$ -weighted Fe K-edge EXAFS modulus (a,d,g,j,m,p) and imaginary (b,e,h,k,n,q) parts, as well as the fit of the real part of the  $\chi(k)$  (c,f,i,l,o,r) for  $\text{Pt}_{2.1}\text{Fe}_{1.1}\text{-Al}_2\text{O}_3\text{-673-100}$  (a-c - alloy model; d-f - no alloy model),  $\text{Pt}_{2.1}\text{Fe}_{1.1}\text{-Al}_2\text{O}_3\text{-673-5}$  (no alloy), and  $\text{Pt}_{2.0}\text{Fe}_{1.4}\text{-SiO}_2\text{-473-100}$  (no alloy). Black solid line - experimental data, red dashed line - fit, dashed-dotted lines show individual path signals. All spectra were measured either under PROX: 40 vol.%  $\text{H}_2$  + 5 vol.%  $\text{CO}$  + 2 vol.%  $\text{O}_2$  after 30 min of reaction (experiment 1 for  $\text{Pt}_{2.1}\text{Fe}_{1.1}\text{-Al}_2\text{O}_3\text{-673-100}$ ) at 313 K (a-i, m-o) or after complete oxidation (most oxidized state).

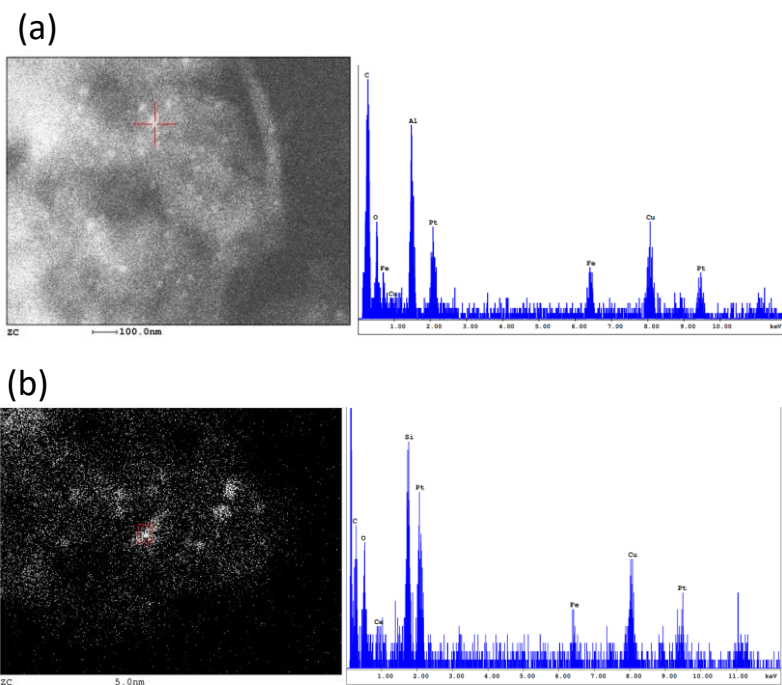


**Figure S2-15.** Ex situ STEM images of Pt<sub>2.1</sub>Fe<sub>1.1</sub>-Al<sub>2</sub>O<sub>3</sub>-673-100 (a) and Pt<sub>2.0</sub>Fe<sub>1.4</sub>-SiO<sub>2</sub>-473-100 (b) with the corresponding EDX X-ray spectra showing the signals of both iron and platinum signals at the red spot, together with the alumina or silica and oxygen from the support and copper from the TEM grid.

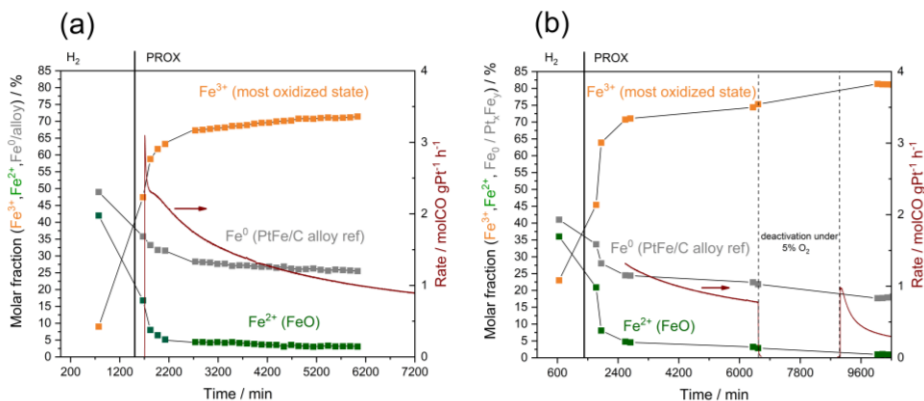


**Figure S2-16.** Operando XAS vs MS data following deactivation of Pt<sub>2.1</sub>Fe<sub>1.1</sub>-Al<sub>2</sub>O<sub>3</sub>-673-100 during experiments 2 (a) and 3 (b) at 313 K under 100 % H<sub>2</sub> and PROX 40 vol.% H<sub>2</sub> + 5 vol.% CO + 2 vol.% O<sub>2</sub> gas mixtures. Activity recording in experiment 3 was delayed. Gas concentrations are shown as vol.%.

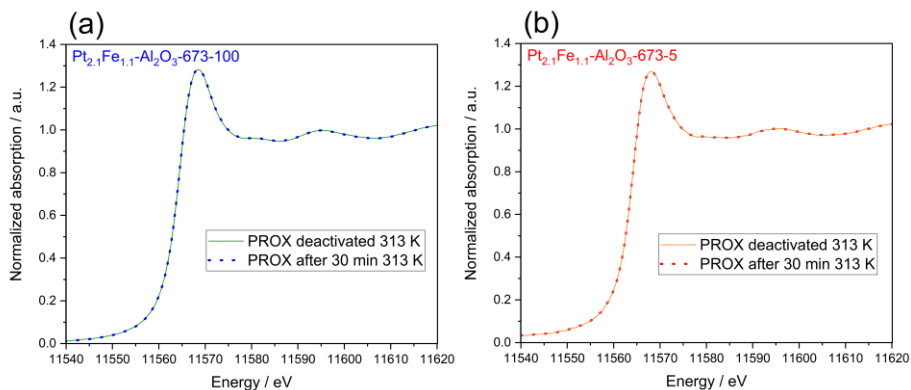


**Figure S2-17.** Comparison of operando Pt L<sub>3</sub>-edge XANES spectra of Pt<sub>2.1</sub>Fe<sub>1.1</sub>-Al<sub>2</sub>O<sub>3</sub>-673-100 (a) and Pt<sub>2.1</sub>Fe<sub>1.1</sub>-Al<sub>2</sub>O<sub>3</sub>-673-5 (b) under 40 vol.% H<sub>2</sub> + 5 vol.% CO + 2 vol.% O<sub>2</sub> gas mixture at 313 K after 30 min under reaction conditions (dashed) and after the deactivation under 5% O<sub>2</sub> (solid). Gas concentrations are shown as vol.%.

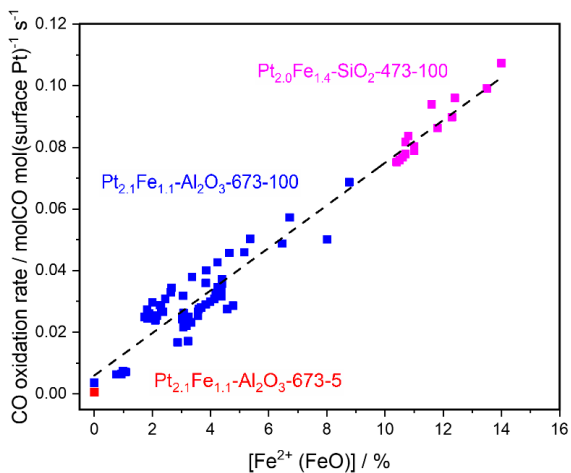


**Figure S2-18.**  $\text{Fe}^{2+}$  - activity (per surface platinum) correlation at 313 K during PROX. Red colored dot presents  $\text{Pt}_{2,1}\text{Fe}_{1,1}\text{-Al}_2\text{O}_3\text{-673-5}$ .

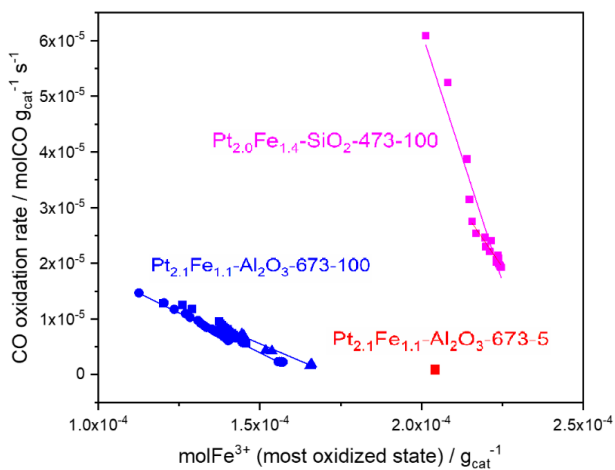


**Figure S2-19.**  $\text{Fe}^{3+}$  - activity correlation at 313 K during PROX.



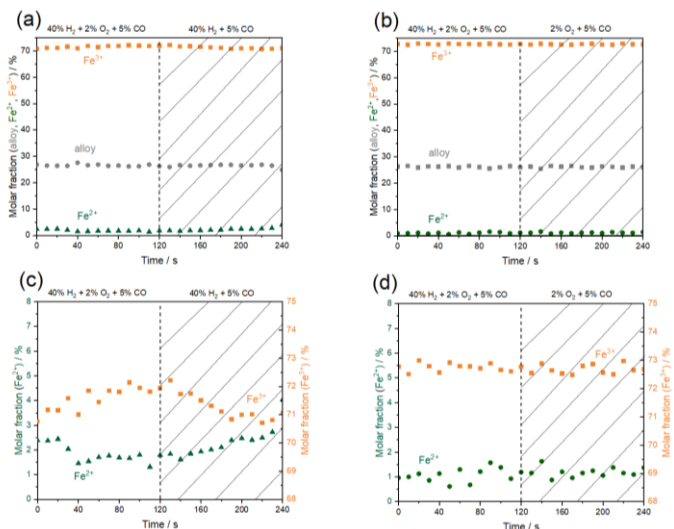


**Figure S2-20.** Iron speciation during operando oxygen (a),(c) and hydrogen (b),(d) cut-off cycles (experiment 4) at 313 K over Pt<sub>2.1</sub>Fe<sub>1.1</sub>-Al<sub>2</sub>O<sub>3</sub>-673-100.

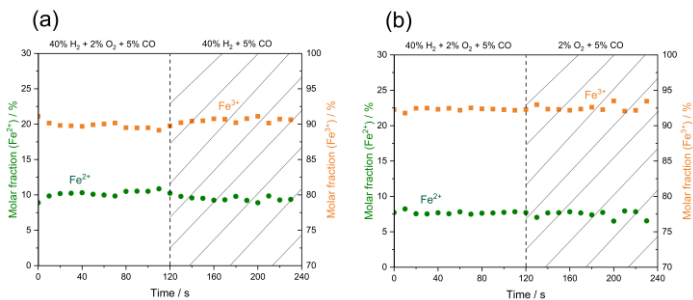


**Figure S2-21.** Iron speciation during operando oxygen (a) and hydrogen (b) cut-off cycles at 313 K for Pt<sub>2.0</sub>Fe<sub>1.4</sub>-SiO<sub>2</sub>-473-100.

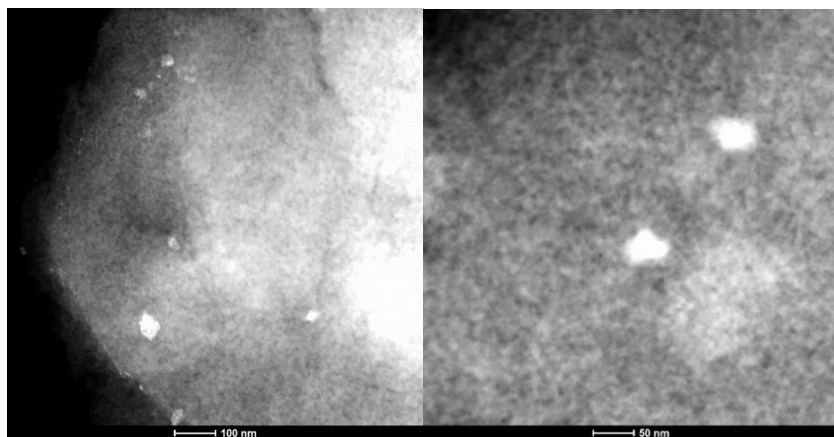


**Figure S2-22.** Ex situ STEM images of the PtFe/C reference.

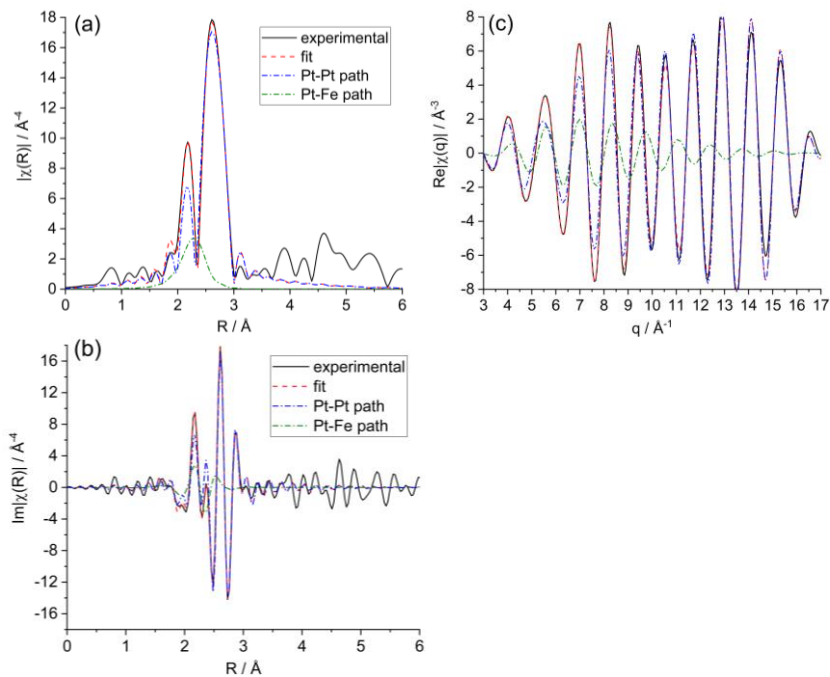


**Figure S2-23.** Fit of the Fourier-transformed  $k^3$ -weighted Pt  $L_3$ -edge EXAFS modulus (a) and imaginary (b) parts, as well as the fit of the real part of the  $\chi(k)$  (c) for the PtFe/C alloy reference.

**Table S2-1.** Elemental composition and Pt dispersion of all used materials.

Catalyst	Elemental composition (ICP-OES)		Pt dispersion (CO chemisorption) after reduction, $D_{CO}$	Pt dispersion (ex situ electron microscopy) after reduction, $D_{TEM}$
	Pt content / wt. %	Fe content / wt. %		
Pt <sub>2.0</sub> -Al <sub>2</sub> O <sub>3</sub> -673-100	2.0 ± 0.1	0	0.6	0.8
Pt <sub>2.1</sub> Fe <sub>1.1</sub> -Al <sub>2</sub> O <sub>3</sub> -673-100	2.1 ± 0.1	1.14 ± 0.07	0.3	0.4
Pt <sub>2.1</sub> Fe <sub>1.1</sub> -Al <sub>2</sub> O <sub>3</sub> -673-5	2.1 ± 0.1	1.14 ± 0.07	0.6	0.7
Pt <sub>2.0</sub> -SiO <sub>2</sub> -473-100	2.0 ± 0.1	0	0.4	0.4
Pt <sub>2.0</sub> Fe <sub>1.4</sub> -SiO <sub>2</sub> -473-100	2.0 ± 0.1	1.4 ± 0.1	0.4	0.3
Pt-Fe/C alloy	10 ± 0.2	5.2 ± 0.2	-	-

**Table S2-2.** Kinetic parameters of the preferential carbon monoxide oxidation reaction for the previously published catalysts and catalysts under study. Catalytic activity of the catalysts under study was characterized under the same conditions as during the operando XAS experiments in the operando cell: 5 vol.% CO + 2 vol.% O<sub>2</sub> + 40 vol.% H<sub>2</sub>, He balance, total flow 180 ml min<sup>-1</sup>.

Catalyst	Estimated activity (T, K) / molCO gPt <sup>-1</sup> h <sup>-1</sup>	O <sub>2</sub> reaction order (T, K)	CO reaction order (T, K)	Effective activation energy / kJ mol <sup>-1</sup>	Ref
Pt <sub>2.0</sub> Fe <sub>1.4</sub> -SiO <sub>2</sub> -473-100	2.8 (303 K, 1 h on stream)	1.00 (313 K)	0.06 (313 K)	10	current study
Pt <sub>2.0</sub> Fe <sub>1.4</sub> -SiO <sub>2</sub> -673-100	0.7 (303 K, 1 h on stream)	-	-	16	current study
Pt <sub>2.1</sub> Fe <sub>1.1</sub> -Al <sub>2</sub> O <sub>3</sub> -473-100	0.6 (303 K, 1 h on stream)	-	-	11	current study
Pt <sub>2.1</sub> Fe <sub>1.1</sub> -Al <sub>2</sub> O <sub>3</sub> -673-100	1.1 (303 K, 1 h on stream)	0.79 (313 K)	0.06 (313 K)	10	current study
0.25 wt.% Pt 0.072% Fe / Al <sub>2</sub> O <sub>3</sub> (no hydrogen in the feed)	1.5 (298 K)	0.9 (298 K)	0.09 (298 K)	9.2	8
7.2 wt.% Pt, 0.6 wt.% Fe Pt/Fe(OH) <sub>x</sub> /TiO <sub>2</sub>	0.2 (313 K)	1.17 (313 K)	0.16 (313 K)	16	9
3.6 wt.% Pt, 0.1 wt.% Fe / SiO <sub>2</sub>	5.21 (300 K)	-	-	-	10
2.3 wt.% Pt / Fe <sub>2</sub> O <sub>3</sub>	0.258 (300 K)	-	-	-	11
0.17 wt.% Pt / Fe <sub>2</sub> O <sub>3</sub>	0.676 (300 K)	-	-	-	2

**Table S2-3.** Comparison of the carbon monoxide oxidation rates for the catalysts under study and the Pt/FeO<sub>x</sub> catalysts published by Qiao et al.<sup>2</sup> Catalytic activity of the catalysts under study was measured in the tubular reactor at 353 K (80°C) under 2 vol.% CO + 1 vol.% O<sub>2</sub> + 40 vol.% H<sub>2</sub>, He balance, total flow 100 ml min<sup>-1</sup>, reader is referred to the experimental description for more details.

Catalyst	Estimated activity/ molCO gPt <sup>-1</sup> h <sup>-1</sup>	Ref.
Pt <sub>2.0</sub> Fe <sub>1.4</sub> -SiO <sub>2</sub> -473-100	8.4	current study
Pt <sub>2.1</sub> Fe <sub>1.1</sub> -Al <sub>2</sub> O <sub>3</sub> -673-100	4.6	current study
0.17 wt.% Pt / Fe <sub>2</sub> O <sub>3</sub>	0.68	2
2.5 wt.% Pt / Fe <sub>2</sub> O <sub>3</sub>	0.36	2
4.4 wt.% Au/ Fe <sub>2</sub> O <sub>3</sub>	0.80	2

**Table S2-4.** Results of the Gauss fit of the in situ FTIR of the catalysts under study. Fitting range: 2120-2040  $\text{cm}^{-1}$ , peak positions, area, profile shape factor, and full width at half maximum (FWHM) are used as free variables. Profile shape factor shows the fraction of the Lorentz component.

Sample / ambient temperature	Peak number	Peak position / $\text{cm}^{-1}$	FWHM / $\text{cm}^{-1}$	Area	Profile shape factor
Pt <sub>2.0</sub> -Al <sub>2</sub> O <sub>3</sub> -673-100 CO-saturated	1	-	-	0 ± 0	-
	2	2075 ± 47	35 ± 84	9 ± 37	0 ± 2
	3	2045 ± 119	32 ± 110	3 ± 47	0 ± 18
Pt <sub>2.1</sub> Fe <sub>1.1</sub> -Al <sub>2</sub> O <sub>3</sub> -673-5 CO-saturated	1	-	-	0 ± 0	-
	2	2074 ± 47	34 ± 78	8 ± 34	0 ± 2
	3	2042 ± 86	36 ± 140	4 ± 43	0 ± 10
Pt <sub>2.1</sub> Fe <sub>1.1</sub> -Al <sub>2</sub> O <sub>3</sub> -673-5 CO-saturated "bad fit"	1	2092 / fixed	6 / fixed	0.05 ± 0.07	0 / fixed
	2	2079 / fixed	19 / fixed	0.3 ± 0.2	0.1 / fixed
	3	2063 / fixed	34 / fixed	10.4 ± 0.2	0 / fixed
Pt <sub>2.1</sub> Fe <sub>1.1</sub> -Al <sub>2</sub> O <sub>3</sub> -673-100 CO-saturated	1	-	-	0 ± 0	-
	2	2073.2 ± 0.4	28 ± 2	4 ± 1	0.0 ± 0.2
	3	2049 ± 2	46 ± 2	11 ± 1	0.00 ± 0.07
Pt <sub>2.1</sub> Fe <sub>1.1</sub> -Al <sub>2</sub> O <sub>3</sub> -673-100 CO-saturated "bad fit"	1	2092 / fixed	6 / fixed	0.09 ± 0.07	0 / fixed
	2	2079 / fixed	19 / fixed	0.4 ± 0.2	0.1 / fixed
	3	2063 / fixed	34 / fixed	10.6 ± 0.2	0 / fixed
Pt <sub>2.0</sub> -SiO <sub>2</sub> -673-100 CO-saturated	1	2091 ± 2	6 ± 2	0.1 ± 0.2	0 ± 3
	2	2078.7 ± 0.6	19 ± 2	5 ± 2	0.1 ± 0.3
	3	2061 ± 6	32 ± 3	3 ± 2	0.0 ± 0.6
Pt <sub>2.1</sub> Fe <sub>1.4</sub> -SiO <sub>2</sub> -473-100 CO-saturated	1	2092 ± 3	6 ± 2	0.1 ± 0.2	0 ± 5
	2	2079.0 ± 0.4	19 ± 2	5 ± 2	0.1 ± 0.4
	3	2063 ± 7	34 ± 3	3 ± 2	0.0 ± 0.6

**Table S2-5.** Optimized parameters of the Pt L<sub>3</sub>-edge EXAFS fit. *N*: coordination number, *R*: internuclear distance,  $\sigma^2$ : disorder parameter,  $\Delta E_0$ : energy shift, “\*” - fixed parameters. For all the alumina-supported under study the fit was performed in R-space in the range of 1.0-3.5 Å, employing the k-range of 3.0-9.0 Å<sup>-1</sup> for the Fourier transform (FT). Pt<sub>2.0</sub>Fe<sub>1.4</sub>-SiO<sub>2</sub>-473-100 EXAFS was fitted using the R-space range of 1.0-3.5 Å and the k-range of 3.0-13.0 Å<sup>-1</sup>. The PtFe/C reference EXAFS was fitted using the R-space range of 1.0-3.5 Å and the k-range of 3.0-16.0 Å<sup>-1</sup>.

Sample	Model	Bond	<i>N</i> / <i>N</i> <sub>0</sub>	<i>R</i> / Å	$\Delta\sigma^2$ / Å <sup>2</sup>	<i>E</i> <sub>0</sub> / eV
Pt foil	Pt	Pt-Pt	12*	2.76 ± 0.02	0.0048 ± 0.0001	6 ± 1.7
Pt <sub>2.1</sub> Fe <sub>1.1</sub> -Al <sub>2</sub> O <sub>3</sub> -673-100 under H <sub>2</sub>	Pt + PtFe	Pt-Fe Pt-Pt	2 ± 1.3 10 ± 5.1	2.61 ± 0.03 2.76 ± 0.09	0.006 ± 0.008 0.017 ± 0.005	5 ± 4.0
Pt <sub>2.1</sub> Fe <sub>1.1</sub> -Al <sub>2</sub> O <sub>3</sub> -673-100 under H <sub>2</sub> “bad fit”	Pt	Pt-Pt	11 ± 2.9	2.72 ± 0.02	0.011 ± 0.003	4 ± 1.9
Pt <sub>2.1</sub> Fe <sub>1.1</sub> -Al <sub>2</sub> O <sub>3</sub> -673-5 under H <sub>2</sub>	Pt	Pt-Pt	10 ± 2.0	2.76 ± 0.01	0.013 ± 0.002	5 ± 1.5
Pt <sub>2.0</sub> Fe <sub>1.4</sub> -SiO <sub>2</sub> -473-100 under H <sub>2</sub>	Pt	Pt-Pt	10 ± 1.2	2.750 ± 0.007	0.0075 ± 0.0008	5 ± 1.0
PtFe/C reference	Pt + PtFe	Pt-Fe Pt-Pt	2.0 ± 0.5 8.3 ± 0.6	2.631 ± 0.002 2.751 ± 0.009	0.008 ± 0.002 0.0052 ± 0.0003	6.2 ± 0.4



**Table S2-6.** Optimized parameters of the Fe K-edge EXAFS fit. N: coordination number, R: interatomic distance,  $\sigma^2$ : disorder parameter,  $\Delta E_0$ : energy shift, “\*” - fixed parameters. We performed EXAFS fitting using multiple k weightings of 1-3 within the k-range of 3.0-9.5  $\text{\AA}^{-1}$  and an R-range of 1.0-4.0  $\text{\AA}$ .

Sample	Model	Bond	N / N <sub>0</sub>	R / $\text{\AA}$	$\Delta\sigma^2 / \text{\AA}^2$	E <sub>0</sub> / eV
Fe foil	$\alpha$ -Fe	Fe-Fe Fe-Fe	8* 6*	2.48 $\pm$ 0.02 2.86 $\pm$ 0.02	0.0055 $\pm$ 0.0009 0.0055 $\pm$ 0.0009	-2 $\pm$ 1.7
Pt <sub>2.1</sub> Fe <sub>1.1</sub> -Al <sub>2</sub> O <sub>3</sub> -673-100 under PROX	goethite + FeO <sub>x</sub> /Pt <sup>9</sup>	Fe-O Fe-Pt Fe-(O)-Fe	5 $\pm$ 1.3 2 $\pm$ 1.4 3 $\pm$ 1.8	1.94 $\pm$ 0.03 2.44 $\pm$ 0.02 3.01 $\pm$ 0.03	0.011 $\pm$ 0.004 0.003 $\pm$ 0.006 0.010 $\pm$ 0.009	-3 $\pm$ 3.1
Pt <sub>2.1</sub> Fe <sub>1.1</sub> -Al <sub>2</sub> O <sub>3</sub> -673-100 under PROX “bad fit”	goethite	Fe-O Fe-(O)-Fe	4 $\pm$ 2.8 2 $\pm$ 2.9	1.93 $\pm$ 0.05 2.92 $\pm$ 0.07	0.01 $\pm$ 0.01 0.01 $\pm$ 0.02	-7 $\pm$ 6.6
Pt <sub>2.1</sub> Fe <sub>1.1</sub> -Al <sub>2</sub> O <sub>3</sub> -673-5 under PROX	goethite	Fe-O Fe-(O)-Fe	4 $\pm$ 0.3 1 $\pm$ 0.4	1.946 $\pm$ 0.007 3.02 $\pm$ 0.01	0.007 $\pm$ 0.001 0.003 $\pm$ 0.003	-4 $\pm$ 1.0
Pt <sub>2.1</sub> Fe <sub>1.1</sub> -Al <sub>2</sub> O <sub>3</sub> -673-100 oxidized on air	goethite	Fe-O Fe-(O)-Fe	5 $\pm$ 0.7 3 $\pm$ 2.5	1.94 $\pm$ 0.01 3.01 $\pm$ 0.03	0.009 $\pm$ 0.002 0.018 $\pm$ 0.009	-5 $\pm$ 2.0
Pt <sub>2.0</sub> Fe <sub>1.4</sub> -SiO <sub>2</sub> -473-100 under PROX	goethite	Fe-O Fe-(O)-Fe	5 $\pm$ 1.3 2 $\pm$ 1.3	1.94 $\pm$ 0.02 2.94 $\pm$ 0.03	0.007 $\pm$ 0.004 0.004 $\pm$ 0.006	-6 $\pm$ 2.9
Pt <sub>2.0</sub> Fe <sub>1.4</sub> -SiO <sub>2</sub> -473-100 oxidized on air	goethite	Fe-O Fe-(O)-Fe	6 $\pm$ 2.1 2 $\pm$ 1.9	1.94 $\pm$ 0.03 2.95 $\pm$ 0.04	0.010 $\pm$ 0.005 0.006 $\pm$ 0.008	-6 $\pm$ 3.9

**Table S2-7.** Linear combination fitting of operando Fe K-edge XANES spectra of the catalysts under indicated gas mixtures at 313 K.

Sample	Experiment number (Figure reference)	Gas mixture	Time / s	Fe <sup>2+</sup> / fraction	Fe <sup>3+</sup> / fraction	Fe <sup>0</sup> / fraction	Averaging time / s
Pt <sub>2.1</sub> Fe <sub>1.1</sub> -Al <sub>2</sub> O <sub>3</sub> -673-100	1 (Figure 6a)	100% H <sub>2</sub>	-812	0.290	0.100	0.610	150
		40% H <sub>2</sub> + 5% CO	-262	0.290	0.130	0.580	
		40% H <sub>2</sub> + 5% CO + 2% O <sub>2</sub>	88	0.211	0.360	0.428	
			238	0.088	0.548	0.361	
			388	0.067	0.586	0.343	
			538	0.054	0.601	0.341	
			688	0.046	0.618	0.331	
			838	0.042	0.626	0.328	
			988	0.038	0.646	0.320	
			1138	0.034	0.641	0.321	
			1288	0.038	0.645	0.312	
			1438	0.027	0.652	0.319	
			1588	0.026	0.659	0.312	
			1738	0.031	0.660	0.305	
			1888	0.024	0.674	0.306	
			2038	0.020	0.669	0.307	
			2188	0.023	0.671	0.301	
			2338	0.023	0.675	0.297	
			2488	0.018	0.675	0.302	
			2638	0.024	0.679	0.292	
2788	0.019	0.679	0.297				
2938	0.021	0.692	0.291				
3088	0.017	0.684	0.294				
3238	0.018	0.682	0.295				
3388	0.021	0.685	0.290				
Pt <sub>2.1</sub> Fe <sub>1.1</sub> -Al <sub>2</sub> O <sub>3</sub> -673-100	2 (Figure S15a)	100% H <sub>2</sub>	772	0.420	0.090	0.490	150
		40% H <sub>2</sub> + 5% CO + 2% O <sub>2</sub>	1672	0.168	0.474	0.358	
			1822	0.080	0.588	0.332	
			1972	0.065	0.618	0.318	
			2122	0.052	0.632	0.316	
			2735	0.044	0.673	0.283	
			2885	0.044	0.675	0.281	
			3035	0.042	0.677	0.280	
			3185	0.044	0.680	0.276	
			3335	0.042	0.682	0.277	
			3485	0.044	0.686	0.270	
			3635	0.041	0.687	0.272	
			3785	0.040	0.688	0.272	
			3935	0.038	0.693	0.269	
			4085	0.037	0.695	0.268	
4235	0.036	0.696	0.268				

Sample	Experiment number (Figure reference)	Gas mixture	Time / s	Fe <sup>2+</sup> / fraction	Fe <sup>3+</sup> / fraction	Fe <sup>0</sup> / fraction	Averaging time / s
			4385	0.036	0.700	0.265	
			4535	0.031	0.701	0.268	
			4685	0.036	0.702	0.262	
			4835	0.032	0.707	0.260	
			4985	0.031	0.708	0.261	
			5135	0.030	0.707	0.263	
			5285	0.032	0.710	0.259	
			5435	0.033	0.711	0.256	
			5585	0.031	0.709	0.260	
			5735	0.032	0.711	0.258	
Pt <sub>2.1</sub> Fe <sub>1.1</sub> -Al <sub>2</sub> O <sub>3</sub> -673-100	3 (Figure S15b)	100% H <sub>2</sub>	650	0.360	0.230	0.410	150
		40% H <sub>2</sub> + 5% CO + 2% O <sub>2</sub>	1750	0.209	0.454	0.337	
			1900	0.081	0.639	0.280	
			2615	0.048	0.707	0.245	
			2765	0.046	0.710	0.244	
			6400	0.032	0.744	0.224	
			6550	0.029	0.753	0.218	
			10090	0.010	0.813	0.177	
			10240	0.011	0.812	0.177	
		10390	0.009	0.812	0.179		
10540	0.008	0.811	0.182				
Pt <sub>2.1</sub> Fe <sub>1.1</sub> -Al <sub>2</sub> O <sub>3</sub> -673-100	4, oxygen cut-off cycles (Figure S19a,c)	40% H <sub>2</sub> + 5% CO + 2% O <sub>2</sub>	0	0.024	0.708	0.268	10
			10	0.024	0.712	0.265	
			20	0.024	0.712	0.264	
			30	0.020	0.716	0.264	
			40	0.015	0.710	0.275	
			50	0.015	0.718	0.266	
			60	0.017	0.714	0.268	
			70	0.018	0.719	0.264	
			80	0.017	0.718	0.265	
			90	0.017	0.721	0.262	
		40% H <sub>2</sub> + 5% CO	100	0.018	0.719	0.263	
			110	0.013	0.718	0.269	
			120	0.018	0.719	0.263	
			130	0.018	0.722	0.259	
			140	0.016	0.717	0.267	
			150	0.019	0.717	0.264	
			160	0.019	0.715	0.266	
			170	0.020	0.713	0.267	
			180	0.021	0.711	0.268	
			190	0.024	0.708	0.268	
			200	0.025	0.710	0.265	
			210	0.024	0.710	0.266	
220	0.025	0.707	0.268				

Sample	Experiment number (Figure reference)	Gas mixture	230	0.027	0.708	0.265	Averaging time / s
			Time / s	Fe <sup>2+</sup> / fraction	Fe <sup>3+</sup> / fraction	Fe <sup>0</sup> / fraction	
Pt <sub>2.1</sub> Fe <sub>1.1</sub> -Al <sub>2</sub> O <sub>3</sub> -673-100	4, hydrogen cut-off cycles (Figure S19b,d)	40% H <sub>2</sub> + 5% CO + 2% O <sub>2</sub>	0	0.00964	0.72778	0.26258	10
			10	0.01	0.72511	0.26489	
			20	0.01125	0.72992	0.25883	
			30	0.00857	0.72787	0.26356	
			40	0.01133	0.72563	0.26304	
			50	0.00611	0.72916	0.26474	
			60	0.013	0.72789	0.25911	
			70	0.00677	0.72784	0.26539	
			80	0.01213	0.72718	0.26069	
			90	0.01572	0.72886	0.25543	
		100	0.01383	0.72655	0.25963		
		110	0.00925	0.72605	0.26469		
		120	0.01192	0.7277	0.26038		
		130	0.0116	0.72547	0.26293		
		140	0.0163	0.7288	0.2549		
		150	0.00876	0.72638	0.26486		
		160	0.01207	0.72533	0.26261		
		170	0.00962	0.72481	0.26557		
		180	0.01157	0.72799	0.26044		
		190	0.01249	0.72863	0.25887		
		200	0.01057	0.72567	0.26376		
		210	0.01379	0.72495	0.26126		
		220	0.01158	0.7297	0.25873		
230	0.01096	0.72652	0.26253				
Pt <sub>2.0</sub> Fe <sub>1.4</sub> -SiO <sub>2</sub> -473-100	(Figure 6b)	100% H <sub>2</sub>	388	0.270	0.730	0.000	10
		40% H <sub>2</sub> + 5% CO	938	0.230	0.770	0.000	
		40% H <sub>2</sub> + 5% CO + 2% O <sub>2</sub>	1440	0.140	0.860	0.000	
			1490	0.135	0.865	0.000	
			1540	0.124	0.876	0.000	
			1590	0.116	0.884	0.000	
			1640	0.123	0.877	0.000	
			1690	0.118	0.882	0.000	
			1740	0.108	0.892	0.000	
			1790	0.107	0.893	0.000	
			1840	0.110	0.890	0.000	
			1890	0.110	0.890	0.000	
			1940	0.107	0.893	0.000	
			1990	0.106	0.894	0.000	
			2040	0.105	0.895	0.000	
2090	0.104	0.896	0.000				

Sample	Experiment number (Figure reference)	Gas mixture	Time / s	Fe <sup>2+</sup> / fraction	Fe <sup>3+</sup> / fraction	Fe <sup>0</sup> / fraction	Averaging time / s
Pt <sub>2.0</sub> Fe <sub>1.4</sub> -SiO <sub>2</sub> -473-100	oxygen cut-off cycles (Fig. S20a)	40% H <sub>2</sub> + 5% CO + 2% O <sub>2</sub>	0	0.089	0.91099	0.000	10
			10	0.099	0.901	0.000	
			20	0.102	0.898	0.000	
			30	0.102	0.898	0.000	
			40	0.103	0.897	0.000	
			50	0.101	0.899	0.000	
			60	0.100	0.900	0.000	
			70	0.098	0.902	0.000	
			80	0.105	0.895	0.000	
			90	0.105	0.895	0.000	
			100	0.105	0.895	0.000	
		110	0.109	0.891	0.000		
		40% H <sub>2</sub> + 5% CO	120	0.102	0.898	0.000	
			130	0.098	0.902	0.000	
			140	0.096	0.904	0.000	
			150	0.095	0.905	0.000	
			160	0.093	0.907	0.000	
			170	0.093	0.907	0.000	
			180	0.098	0.902	0.000	
			190	0.092	0.908	0.000	
			200	0.089	0.911	0.000	
			210	0.098	0.902	0.000	
			220	0.093	0.907	0.000	
230	0.094		0.906	0.000			
Pt <sub>2.0</sub> Fe <sub>1.4</sub> -SiO <sub>2</sub> -473-100	hydrogen cut-off cycles (Figure S20b)	40% H <sub>2</sub> + 5% CO + 2% O <sub>2</sub>	0	0.077	0.922	0.000	10
			10	0.082	0.918	0.000	
			20	0.075	0.925	0.000	
			30	0.075	0.925	0.000	
			40	0.077	0.923	0.000	
			50	0.076	0.924	0.000	
			60	0.078	0.922	0.000	
			70	0.075	0.925	0.000	
			80	0.076	0.924	0.000	
			90	0.077	0.923	0.000	
			100	0.077	0.923	0.000	
		110	0.078	0.922	0.000		
		5% CO + 2% O <sub>2</sub>	120	0.077	0.923	0.000	
			130	0.070	0.930	0.000	
			140	0.077	0.923	0.000	
			150	0.077	0.923	0.000	
			160	0.078	0.92	0.000	
			170	0.077	0.923	0.000	
			180	0.074	0.926	0.000	
			190	0.077	0.923	0.000	
			200	0.065	0.935	0.000	

			210	0.079	0.921	0.000	
			220	0.078	0.922	0.000	
			230	0.065	0.935	0.000	
Sample	Experiment number (Figure reference)	Gas mixture	Time / s	Fe <sup>2+</sup> / fraction	Fe <sup>3+</sup> / fraction	Fe <sup>0</sup> / fraction	Aver-aging time / s
Pt <sub>2.1</sub> Fe <sub>1.1</sub> -Al <sub>2</sub> O <sub>3</sub> -673-5	(Figure S6e)	40% H <sub>2</sub> + 5% CO + 2% O <sub>2</sub>	300	0.000	1.000	0.000	150
Pt <sub>2.0</sub> Fe <sub>1.4</sub> -SiO <sub>2</sub> -673-100	(Figure S6f)	100% H <sub>2</sub>		0.030	0.260	0.710	150

## References

1. Chiarello, G.L.; Nachtegaal, M.; Marchionni, V.; Quaroni, L. and Ferri, D. Adding diffuse reflectance infrared Fourier transform spectroscopy capability to extended X-ray-absorption fine structure in a new cell to study solid catalysts in combination with a modulation approach. *Rev. Sci. Instrum.* **2014**, *85*, 074102.
2. Qiao, B.; Wang, A.; Yang, X.; Allard, L. F.; Jiang, Z.; Cui, Y.; Liu, J.; Li, J. and Zhang, T. Single-atom catalysis of CO oxidation using Pt1/FeO<sub>x</sub>. *Nature Chem.* **2011**, *3*, 634-641.
3. Clark, A. H.; Imbao, J.; Frahm, R. and Nachtegaal, M. ProQEXAFS: a highly optimized parallelized rapid processing software for QEXAFS data. *J. Synchrotron Radiat.* **2020**, *27*, 551-557.
4. Ravel, B. and Newville, M. ATHENA , ARTEMIS , HEPHAESTUS : data analysis for X-ray absorption spectroscopy using IFEFFIT. *J. Synchrotron Radiat.* **2005**, *12*, 537-541.
5. Wang, Y.; Zhang, H.; Yao, X and Zhao, H. Edges of FeO/Pt(111) interface: a first-principle theoretical study. *J. Phys. Chem. C.* **2013**, *117*, 1672-1676.
6. Calvin, S.; Miller, M. M.; Goswami, R.; Cheng, S. F.; Mulvaney, S. P.; Whitman, L. J. and Harris, V. G. J. Determination of crystallite size in a magnetic nanocomposite using extended X-ray absorption fine structure. *J. Appl. Phys.* **2003**, *94*, 778-783.
7. Frenkel, A. I.; Yevick, A.; Cooper, and Vasic, C. R. Modeling the structure and composition of nanoparticles by extended X-ray absorption fine-structure spectroscopy. *Annu. Rev. Anal. Chem.* **2011**, *4*, 23-39.
8. Tomita, A.; Shimizu, K.; Kato, K. and Tai, Y. Pt/Fe-containing alumina catalysts prepared and treated with water under moderate conditions exhibit low-temperature CO oxidation activity. *Catal. Comm.* **2012**, *17*, 194-199.
9. Chen, G.; Zhao, Y.; Fu, G.; Duchesne, P.N.; Gu, L.; Zheng, Y.; Weng, X.; Chen, M.; Zhang, P.; Pao, C.W. and Lee, J.F. Interfacial effects in iron-nickel hydroxide-platinum nanoparticles enhance catalytic oxidation. *Science* **2014**, *344* (6183), 495-499.
10. Cao, L.; Liu, W.; Luo, Q.; Yin, R.; Wang, B.; Weissenrieder, J.; Soldemo, M.; Yan, H.; Lin, Y.; Sun, Z. and Ma, C. Atomically dispersed iron hydroxide anchored on Pt for preferential oxidation of CO in H<sub>2</sub>. *Nature* **2019**, *565* (7741), pp.631-635.
11. Qiao, B.; Wang, A.; Li, L.; Lin, Q.; Wei, H.; Liu, J. and Zhang, T. Ferric oxide-supported Pt subnano clusters for preferential oxidation of CO in H<sub>2</sub>-rich gas at room temperature. *ACS Catal.* **2014**, *4*, 2113-2117.

## S3. Role of Water in the Promotion of Preferential Carbon Monoxide Oxidation over $\gamma$ -Al<sub>2</sub>O<sub>3</sub>- and SiO<sub>2</sub>-Supported Platinum-Iron Catalysts (Chapter 5)

The Supporting Information S3 contains scientific contributions from Ilia I. Sadykov, Frank Krumeich, Dennis Palagin, Davide Ferri, Igor V. Plokhikh, Jeroen A. van Bokhoven, Maarten Nachttegaal, and Olga V. Safonova.



## Catalysts (Chapter 5)

### Al<sub>2</sub>O<sub>3</sub>-Based Catalysts

5.85 g of  $\gamma$ -Al<sub>2</sub>O<sub>3</sub> was first impregnated with 0.25 g Pt(NH<sub>3</sub>)<sub>4</sub>(NO<sub>3</sub>)<sub>2</sub> and dried for 1 h at 393 K. After subsequent impregnation with an aqueous solution of 3.55 g Fe(NO<sub>3</sub>)<sub>3</sub>·9H<sub>2</sub>O and drying for 1 h at 393 K, the obtained catalyst was calcined on air for 2 h at 473 K and then for 2 h at 673 K. ICP-OES described in Chapter 7, helped to determine metal concentrations after calcination. For pure platinum or iron compositions, either platinum or iron impregnation step was omitted. The as-calcined powder was used for further pretreatments.

### SiO<sub>2</sub>-Based Catalysts

The preparation of SiO<sub>2</sub>-based catalysts is described in Supporting information S2, Chapter 4. PtFe-SiO<sub>2</sub>-473-100 is the exact catalyst described in Chapter 4.

Below we describe various in situ reduction pretreatment protocols used to obtain actual catalysts under investigation. The heating rate was 10 K min<sup>-1</sup>, total volumetric flow was 100 ml min<sup>-1</sup>.

### Pt<sub>2,0</sub>-Al<sub>2</sub>O<sub>3</sub>-473-100, Pt<sub>2,0</sub>-SiO<sub>2</sub>-473-100

The as-calcined powder (supported on Al<sub>2</sub>O<sub>3</sub> or SiO<sub>2</sub>) without iron was reduced in situ for 1 h under 100 % H<sub>2</sub> at 473 K and cooled down under the same gas mixture.

### Pt<sub>2,0</sub>-Al<sub>2</sub>O<sub>3</sub>-473-100-steam, Pt<sub>2,0</sub>-SiO<sub>2</sub>-473-100-steam

The as-calcined powder (supported on Al<sub>2</sub>O<sub>3</sub> or SiO<sub>2</sub>) without iron was reduced in situ for 1 h under 98 % H<sub>2</sub> + 2 vol.% H<sub>2</sub>O at 473 K and cooled down under the same gas mixture.

### Fe<sub>3,4</sub>-Al<sub>2</sub>O<sub>3</sub>-473-100

The as-calcined powder (supported on Al<sub>2</sub>O<sub>3</sub>) without platinum was reduced in situ for 1 h under 100 % H<sub>2</sub> at 473 K and cooled down under the same gas mixture.

### Pt<sub>2,1</sub>Fe<sub>3,6</sub>-Al<sub>2</sub>O<sub>3</sub>-473-100

The as-calcined bimetallic powder (supported on Al<sub>2</sub>O<sub>3</sub>) was reduced in situ for 1 h under 100 % H<sub>2</sub> at 473 K and cooled down under the same gas mixture.

### Pt<sub>2,1</sub>Fe<sub>3,6</sub>-Al<sub>2</sub>O<sub>3</sub>-wet-473-100, Pt<sub>2,1</sub>Fe<sub>3,6</sub>-Al<sub>2</sub>O<sub>3</sub>-wet-373-100

The as-calcined bimetallic powder (supported on Al<sub>2</sub>O<sub>3</sub>) was impregnated with liquid water. The water volume was equal to the pore volume of the support. Obtained wetted material was reduced in situ for 1 h under 100 % H<sub>2</sub> at 473 K or 373 K and cooled down under the same gas mixture.

### Pt<sub>2,1</sub>Fe<sub>3,6</sub>-Al<sub>2</sub>O<sub>3</sub>-473-100-steam

The as-calcined bimetallic powder (supported on Al<sub>2</sub>O<sub>3</sub>) was reduced in situ for 1 h under 98 % H<sub>2</sub> + 2 vol.% H<sub>2</sub>O at 473 K and cooled down under the same gas mixture.

### Pt<sub>2,0</sub>Fe<sub>1,4</sub>-SiO<sub>2</sub>-473-100

The same catalyst as described in Chapter 4.

### Pt<sub>2,0</sub>Fe<sub>1,4</sub>-SiO<sub>2</sub>-473-100-deh, Pt<sub>2,1</sub>Fe<sub>3,6</sub>-Al<sub>2</sub>O<sub>3</sub>-473-100-deh

The as-calcined powder (supported on SiO<sub>2</sub> or Al<sub>2</sub>O<sub>3</sub> as described in Chapter 4) without platinum was reduced in situ for 1 h under 100 % H<sub>2</sub> at 473 K. Helium gas replaced hydrogen and the material was heated to 673 K, where it was kept for another 1 h. This dehydrated catalyst was then cooled down under helium.

## Methods (Chapter 5)

### In situ/Operando XAS and Kinetic Experiments

We performed a series of in situ / operando XAS experiments at the Fe K-edge using the operando reactor cell (the same as described in Chapters 3 and 4) installed into the PROX setup (**Figure S3-2**).<sup>1-3</sup> During these experiments, 7 mg of the catalyst diluted with 20 mg of SiO<sub>2</sub> was placed into the operando cell, with the volumetric flow being 180 ml min<sup>-1</sup>. A mass spectrometer (MS, OmniStar GSD 320 O1, Pfeiffer) was connected to the outlet of the operando cell to measure the composition of the products and catalyst activity and selectivity. This mass spectrometer was calibrated immediately after the catalytic tests. The conversion was always kept below 20%, which allowed us to accurately extract the catalytic reaction rates. PROX setup had two separate supply lines, one of which was either used as a bypass or a water-supply line. Water generator based on the hydrogen oxidation reactor operating at 473 K filled with 1 g of the commercial 5 wt.% Pt/Al<sub>2</sub>O<sub>3</sub> (Johnson Matthey) was used to supply water directly into the feed through this bypass line during water-addition experiments. All gas lines were additionally heated to ensure no water condensation. Calibration of the water concentration in the feed (**Figure S3-18**) was done using the water generator.

Each gas feed was controlled using four gas mass flow controllers (Bronkhorst). Fast switching between the two gas feeds was realized using two three-way solenoid switching valves (Parker, Series 9). The total pressure drop during all experiments was ca. 250 mbar.

Fe K-edge XAS spectra were collected in transmission geometry. Linear combination fitting of Fe K-edge XANES was performed on the spectra averaged over 100 s. CO and O<sub>2</sub> conversions during operando XAS experiments were both below 20%.

Reaction orders, as well as water-addition experiments (**Figure S3-13**), were performed after the XAS experiments by varying concentrations of the feed gases keeping total flow at 180 ml min<sup>-1</sup>. Water vapor was cut off or added into the feed to observe how catalysts behave with and without steam (**Figure 5-3**). During all water addition and fast switching experiments, helium gas flow was adapted to keep the total volumetric flow the same.

An additional time-on-stream experiment observed the behavior of the most active catalyst (Pt<sub>2,1</sub>Fe<sub>3,6</sub>-Al<sub>2</sub>O<sub>3</sub>-473-98-steam) under the simulated reformate mixture: 5 vol.% CO + 40 vol.% H<sub>2</sub> + 10 vol.% O<sub>2</sub> + 2 vol.% H<sub>2</sub>O / He. The total volume flow rate during this experiment was 180 ml min<sup>-1</sup>, catalyst mass was 7 mg (**Figure S3-3**), catalyst was diluted with 15 mg of amorphous silica.

### Temperature-programmed Desorption of Water

Temperature-programmed desorption of water from  $\gamma$ -Al<sub>2</sub>O<sub>3</sub> and amorphous SiO<sub>2</sub> supports was carried out in the operando XAS cell. In each experiment, 25 mg of the support was placed into the operando cell connected to the standard reactor setup (**Figure S3-2**). Before the temperature-programmed desorption, some samples were pretreated with water according to the experimental protocols (**Table S3-2**). Water adsorbed on the supports was removed by heating the supports to 750 K (**Figure S3-1**) with the rate of 10 K min<sup>-1</sup> under the flow of 100 ml min<sup>-1</sup> helium. The amount of desorbed water was calculated using the water calibration of the normalized water signal in the mass spectrometer (**Figure S3-18**) and normalized by the surface area of the support (nm<sup>2</sup> g<sup>-1</sup>).

### EXAFS Processing

Fe K-edge EXAFS, initially processed with “ProQEXAFS” v.2.39, was fitted using the Demeter software package.<sup>4</sup> We extracted the amplitude reduction factor from the fitting of the reference iron foil (0.91, **Table S3-4**). Subsequently, we performed EXAFS fitting using multiple k weightings of 1-3 within the k-range of 3.0-9.5 Å<sup>-1</sup> and an R-range of 1.0-3.5 Å using a goethite ( $\alpha$ -FeOOH) model. All fitting parameters are summarized in **Table S3-4**. The number of independent points was N<sub>ind</sub> > 10. The Fe K-edge EXAFS fit for all samples is shown in **Figures S3-11-1, S3-11-2**.

### Operando Diffuse Reflectance Infrared Fourier Transform Spectroscopy

Diffuse reflectance infrared Fourier transform (DRIFTS) spectra were measured using a Vertex 70 spectrometer (Bruker) equipped with a liquid nitrogen-cooled mercury-cadmium-telluride detector and a Praying Mantis mirror unit (Harrick). The homemade DRIFTS cell was equipped with a flat CaF<sub>2</sub> window (d = 25 mm; 2 mm thick) and was connected to gas supply lines.<sup>5</sup> All samples were loaded into the cell and pretreated in situ the same way as during all other experiments. Background spectra were collected under 100 % Ar at 313 K right before reduction. Space velocity and catalyst mass were the same as during operando XAS measurements. All operando DRIFT spectra were obtained by accumulating and averaging 10 interferograms at 4 cm<sup>-1</sup> resolution and 80 kHz scanner velocity (0.9 s per spectrum) within 1000 - 4000 cm<sup>-1</sup>. The same experimental setup and pretreatment strategies used for operando XAS experiments were also employed for operando DRIFTS (**Figure S3-2**). Solenoid valves were operated by the OPUS software (Bruker).

Fast cut-off experiments were performed after the samples were equilibrated under PROX mixture 40 vol.% H<sub>2</sub> + 5 vol.% CO + 2 vol.% O<sub>2</sub> for 500 s. After measuring the background under the PROX mixture, we either cut off all reaction gases replacing them with an equal flow of 100 % Ar (**Figure 5-7a,b**), or cut off only the oxygen gas (**Figures 5-7c-f; S3-15**). Oxygen gas was returned back into the equilibrated mixture after 140 s of the oxygen cut-off. Intensities of DRIFTS bands were normalized by the energy window, and these normalized intensities were used to compare the behavior of different bands as shown in **Figures 5-7b,d,f; S3-15b**.

### <sup>18</sup>O Isotope-labeling Experiments

Isotope labeling experiments were performed in the operando reactor cell for XAS experiments with the same setup described in **Figure S3-2** with the water generator exchanged with a water bubbler.<sup>1-3</sup> Reaction products were analyzed using the same mass spectrometer (OmniStar GSD 320 O1, Pfeiffer). Two types of experiments were performed: either an impregnation of the samples with H<sub>2</sub><sup>18</sup>O/H<sub>2</sub><sup>16</sup>O before the reduction pretreatment or an addition of a standard or <sup>18</sup>O-labelled water into the reaction mixture through the water bubbler. The water bubbler was filled with 1 ml of either normal deionized water or isotopically labeled water (H<sub>2</sub><sup>18</sup>O/H<sub>2</sub><sup>16</sup>O, 80% <sup>18</sup>O, Sigma Aldrich).

The first set of experiments involved an impregnation of samples with the standard H<sub>2</sub>O or H<sub>2</sub><sup>18</sup>O/H<sub>2</sub><sup>16</sup>O using the same experimental protocol as during the operando and kinetic tests. H<sub>2</sub>O or H<sub>2</sub><sup>18</sup>O-impregnated catalysts were first reduced under 100 % H<sub>2</sub> at a specific temperature. As-reduced catalysts were saturated with 40 vol.% H<sub>2</sub> + 5 vol.% CO in helium at 318 K for 300 s and then exposed to the PROX mixture 40 vol.% H<sub>2</sub> + 5 vol.% CO + 2 vol.% O<sub>2</sub> as shown in **Figures 5-4a,b; S3-7a**. An additional blank experiment to test possible isotopic exchange between oxygen and adsorbed H<sub>2</sub><sup>18</sup>O is shown in **Figure S3-7b**.

The second set of experiments involved a direct addition of 2 vol.% O<sub>2</sub> and H<sub>2</sub><sup>18</sup>O/H<sub>2</sub><sup>16</sup>O into the 40 vol.% H<sub>2</sub> + 5 vol.% CO mixture passing through the catalyst bed. The total flow was always balanced by helium to 180 ml min<sup>-1</sup>. O<sub>2</sub>-He mixture was first saturated with H<sub>2</sub><sup>18</sup>O from the water bubbler conditioned at 300 K. This mixture was then quickly supplied into the operando cell using the set of fast solenoid valves (**Figure S3-2**). Results of these experiments are presented in **Figures 5-4c,d; S3-7d**. 0.03 vol.% CO<sub>2</sub> + 2 vol.% O<sub>2</sub> / He mixture was used in an additional blank test where helium saturated with H<sub>2</sub><sup>18</sup>O/H<sub>2</sub><sup>16</sup>O was quickly added into the reactor in the same manner (**Figure S3-7c**).

### Density Functional Theory Calculations

Ground-state total energy calculations were performed with the all-electron full-potential DFT code FHI-aims within the periodic boundary conditions model.<sup>6,7</sup> Electronic exchange and correlation were treated on the GGA functional level with the PBE functional.<sup>8</sup> All geometry optimization was done with the tier2 atom-centered basis set using tight settings for numerical integrations. All geometries reported herein correspond to the locally optimized, fully periodic configurations. A geometrically optimized cluster of partially reduced iron oxyhydroxide Fe<sub>6</sub>O<sub>14</sub>H<sub>11</sub> (1Fe<sup>2+</sup>/5Fe<sup>3+</sup>) on the surface of double-layered Pt(111) was chosen to represent a catalytically active interface with the platinum nanoparticle. In order to understand the influence of hydroxylation on the stability of this cluster, we compared changes in the cluster total energy after the removal of three or five molecules of water resulting in Fe<sub>6</sub>O<sub>11</sub>H<sub>5</sub>/Pt(111) and Fe<sub>6</sub>O<sub>9</sub>H/Pt(111) clusters, respectively. Energy differences (dE) were calculated from energies (E) of the clusters and energies of individual water molecules, E[H<sub>2</sub>O], as:

$$\begin{aligned} dE [\text{Fe}_6\text{O}_{14}\text{H}_{11}/\text{Pt}(111)] &= E [\text{Fe}_6\text{O}_{14}\text{H}_{11}/\text{Pt}(111)] - E [\text{Fe}_6\text{O}_{14}\text{H}_{11}/\text{Pt}(111)] \\ &= 0 \text{ eV;} \end{aligned}$$

$$\begin{aligned} dE [\text{Fe}_6\text{O}_{11}\text{H}_5/\text{Pt}(111)] &= E [\text{Fe}_6\text{O}_{11}\text{H}_5/\text{Pt}(111)] - (E [\text{Fe}_6\text{O}_{14}\text{H}_{11}/\text{Pt}(111)] - 3 E[\text{H}_2\text{O}]) \\ &= 0.94 \text{ eV;} \end{aligned}$$

$$\begin{aligned} dE [\text{Fe}_6\text{O}_9\text{H}/\text{Pt}(111)] &= E [\text{Fe}_6\text{O}_9\text{H}/\text{Pt}(111)] - (E [\text{Fe}_6\text{O}_{14}\text{H}_{11}/\text{Pt}(111)] - 5 E[\text{H}_2\text{O}]) \\ &= 0.38 \text{ eV.} \end{aligned}$$

Optimized geometries and energies of these clusters are shown in **Figure S3-17**.

## Figures and Tables to S3 (Chapter 5)

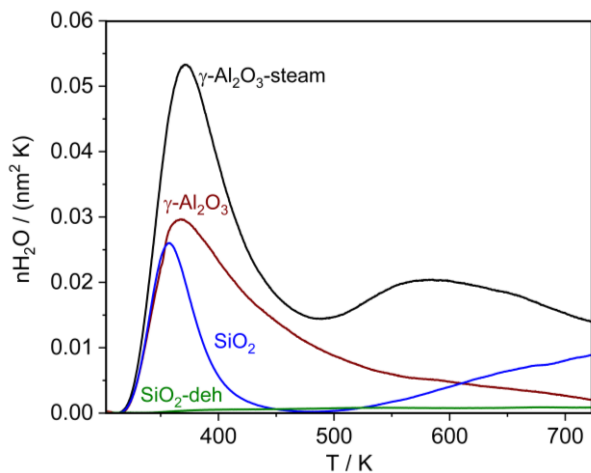


**Figure S3-1.** Temperature-programmed desorption of water from  $\gamma\text{-Al}_2\text{O}_3$  (brown), steam-treated  $\gamma\text{-Al}_2\text{O}_3$  (black),  $\text{SiO}_2$  (blue), and  $\text{SiO}_2$  dehydrated at 673 K (green) supports. The main axis shows the rate of water desorption per temperature unit per  $\text{nm}^2$ .

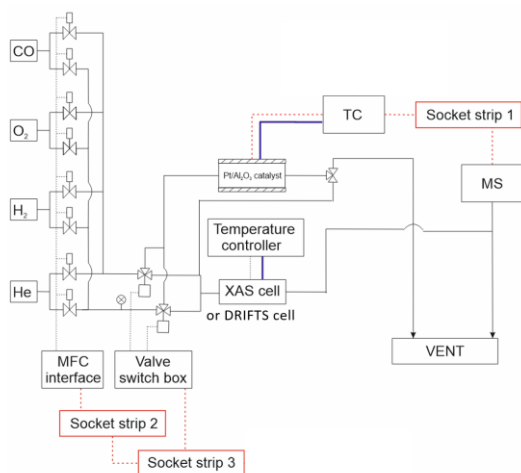


**Figure S3-2.** Scheme of the reactor setup. “Central distribution” indicates power supply through socket strips, “TC” is a temperature controller, and “MS” is the mass spectrometer. “Pt/Al<sub>2</sub>O<sub>3</sub>” catalyst is used for water generation through controlled hydrogen oxidation.

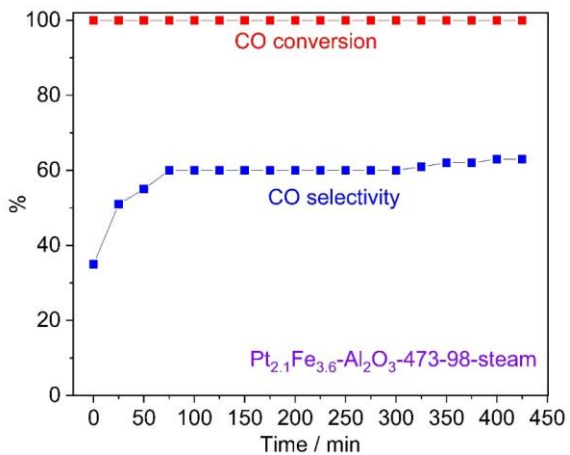


**Figure S3-3.** Stability test of PROX catalyst Pt<sub>2.1</sub>Fe<sub>3.6</sub>-Al<sub>2</sub>O<sub>3</sub>-473-98-steam under 5 vol.% CO + 40 vol.% H<sub>2</sub> + 10 vol.% O<sub>2</sub> + 2 vol.% H<sub>2</sub>O / He. Conversion corresponds to an estimated average rate of 15.5 molCO g<sub>Pt</sub><sup>-1</sup> h<sup>-1</sup>, CO selectivity represents oxygen selectivity towards the carbon monoxide oxidation. The total volume flow was 180 ml min<sup>-1</sup>, catalyst mass was 7 mg.

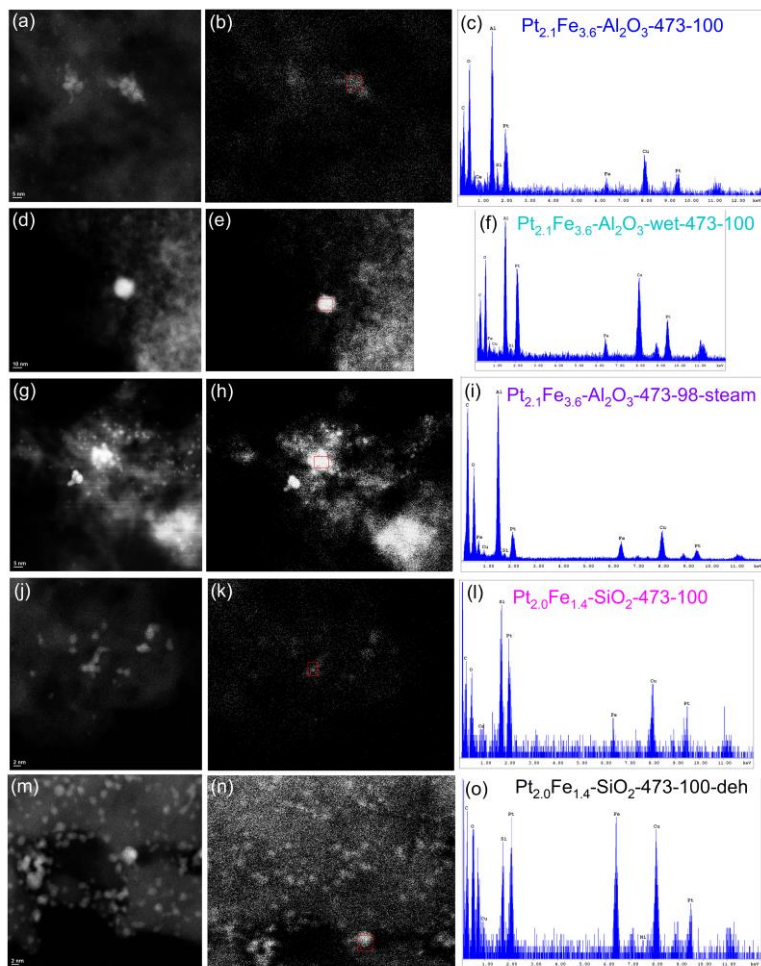


**Figure S3-4.** (a,d,g,j,m) Ex situ STEM images of indicated reduced catalysts; (b,e,h,k,n) low-resolution STEM images used for EDX analysis with the red frame indicating EDX collection region; (c,f,i,l,o) corresponding EDX spectra with indicated X-ray fluorescence peaks of indicated elements.



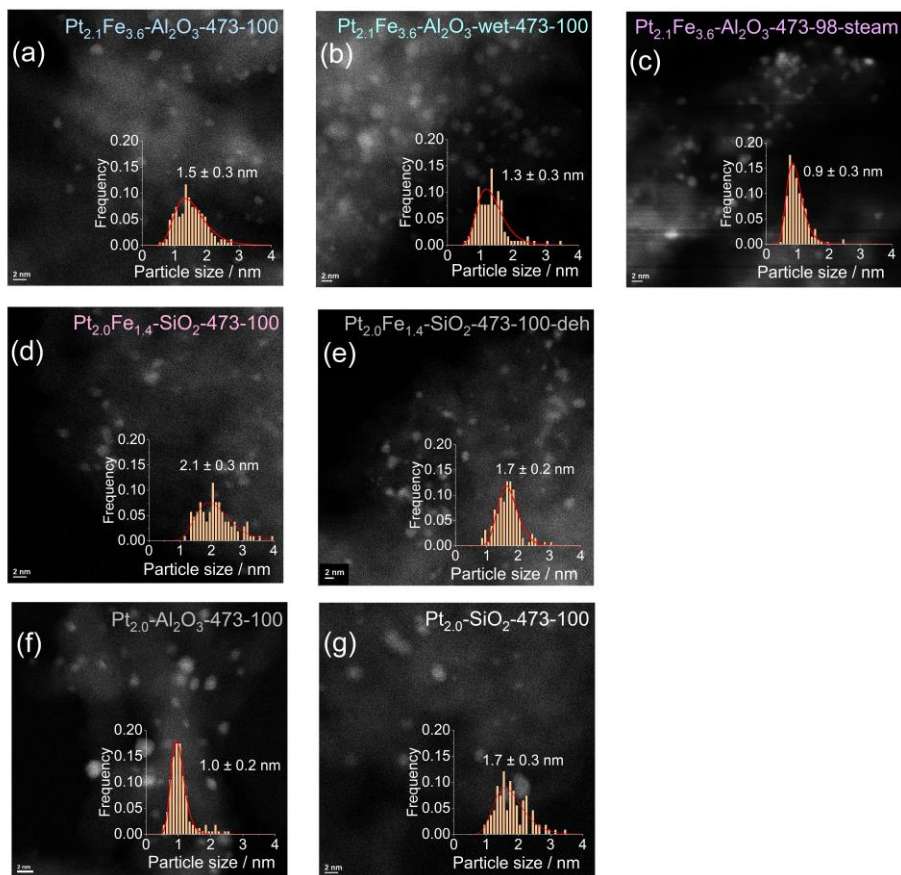
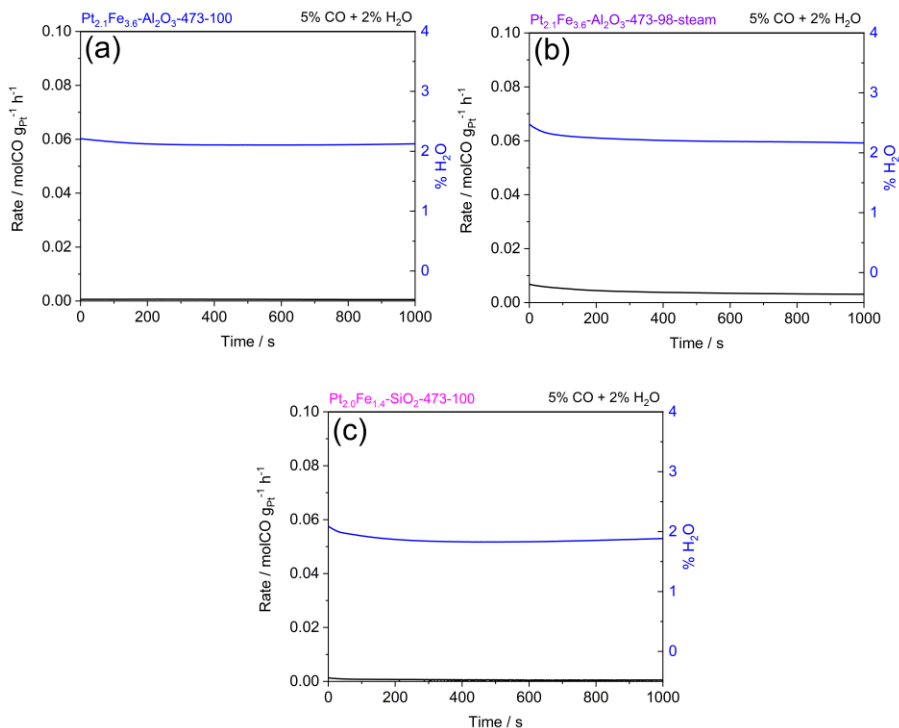
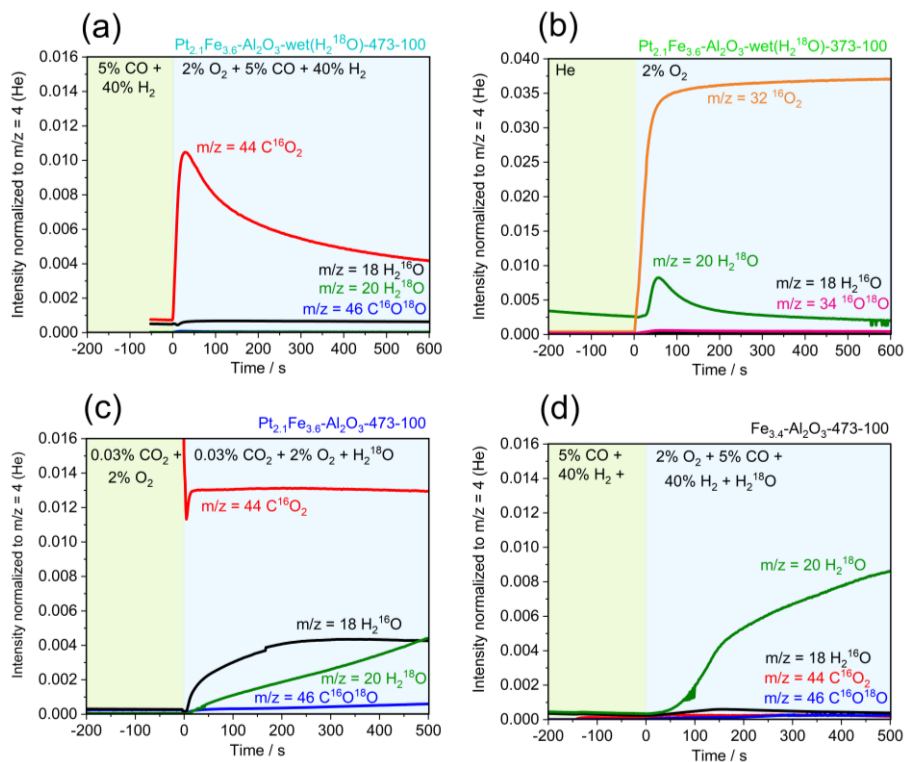


Figure S3-5. STEM images and particle size distributions for the reduced catalysts.



**Figure S3-6.** Tests for water-gas shift reaction at 313 K after in situ reduction over Pt<sub>2.1</sub>Fe<sub>3.6</sub>-Al<sub>2</sub>O<sub>3</sub>-473-100 (a), Pt<sub>2.1</sub>Fe<sub>3.6</sub>-Al<sub>2</sub>O<sub>3</sub>-473-98-steam (b), and Pt<sub>2.0</sub>Fe<sub>1.4</sub>-SiO<sub>2</sub>-473-100 (c). The black curve shows the estimated rate of carbon monoxide consumption due to the water-gas shift reaction. Oxygen concentration was below the detection limit of 5 ppm. Total volumetric flow 180 ml min<sup>-1</sup>. Gas composition was 5 vol.% CO + 2 vol.% H<sub>2</sub>O / He. Gas concentrations are shown in vol. %.



**Figure S3-7.** Helium-normalized MS signals of reaction gases at 313 K during oxygen addition into PROX mixture over  $Pt_{2.1}Fe_{3.6}-Al_2O_3-wet-473-100$  catalyst soaked with  $H_2^{18}O$  before reduction (a); (b) during isotopic exchange tests with oxygen addition into inert carrier gas over  $PtFe-Al_2O_3-wet-373-100$  catalyst soaked with  $H_2^{18}O$  before reduction; (c) during isotopic exchange tests with  $H_2^{18}O$  pulses added into 0.03 vol.%  $CO_2$  + 2 vol.%  $O_2$  / He over  $Pt_{2.1}Fe_{3.6}-Al_2O_3-473-100$  (d) or added into 5 vol.% CO + 40 vol.%  $H_2$  / He together with 2 vol.%  $O_2$  over  $Fe_{3.4}-Al_2O_3-473-100$ . Gas concentrations are shown in vol. %.

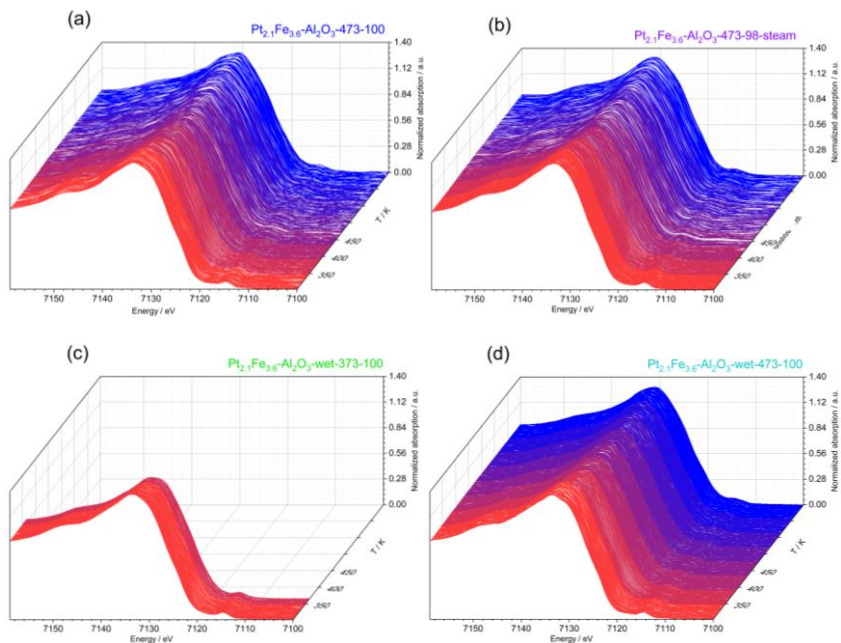


**Figure S3-8.** In situ Fe K-edge XAS during temperature programmed reduction for Pt<sub>2.1</sub>Fe<sub>3.6</sub>-Al<sub>2</sub>O<sub>3</sub>-473-100 (a), Pt<sub>2.1</sub>Fe<sub>3.6</sub>-Al<sub>2</sub>O<sub>3</sub>-473-98-steam (b), Pt<sub>2.1</sub>Fe<sub>3.6</sub>-Al<sub>2</sub>O<sub>3</sub>-wet-373-100 (c), and Pt<sub>2.1</sub>Fe<sub>3.6</sub>-Al<sub>2</sub>O<sub>3</sub>-wet-473-100 (d).

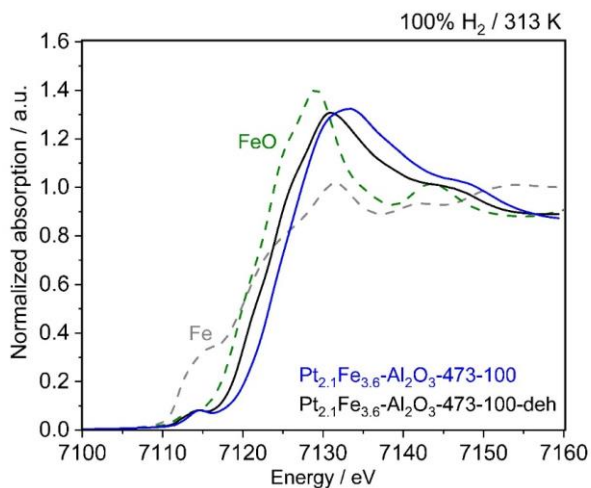


**Figure S3-9.** Results of auto-reduction of Pt<sub>2.1</sub>Fe<sub>3.6</sub>-Al<sub>2</sub>O<sub>3</sub>-473-100-deh (black) during dehydration at 673 K under He atmosphere; Pt<sub>2.1</sub>Fe<sub>3.6</sub>-Al<sub>2</sub>O<sub>3</sub>-473-100 (blue) is shown for comparison. Fe K-edge XAS spectra were measured under 100% H<sub>2</sub> at 313 K. Dashed lines represent spectra of FeO (green) and Fe foil (grey) references.

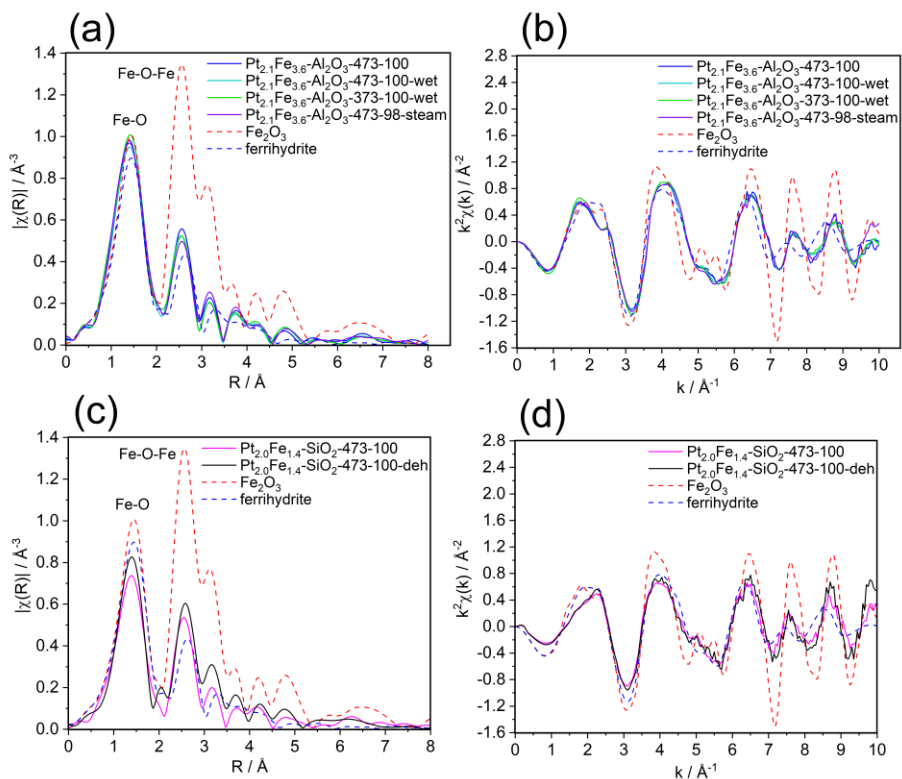


**Figure S3-10.** Fourier-transformed Fe K-edge EXAFS for alumina- (a) and silica-supported catalysts;  $k^2$ -weighted  $k$ -space EXAFS for alumina- (b) and silica-supported catalysts (d). Datapoints were averaged over 200 - 500 s under 2 vol.%  $\text{O}_2$  + 40 vol.%  $\text{H}_2$  + 5 vol.%  $\text{CO}$  at 313 K. Dashed lines represent  $\text{Fe}_2\text{O}_3$  (red) and ferrihydrite (blue) references.

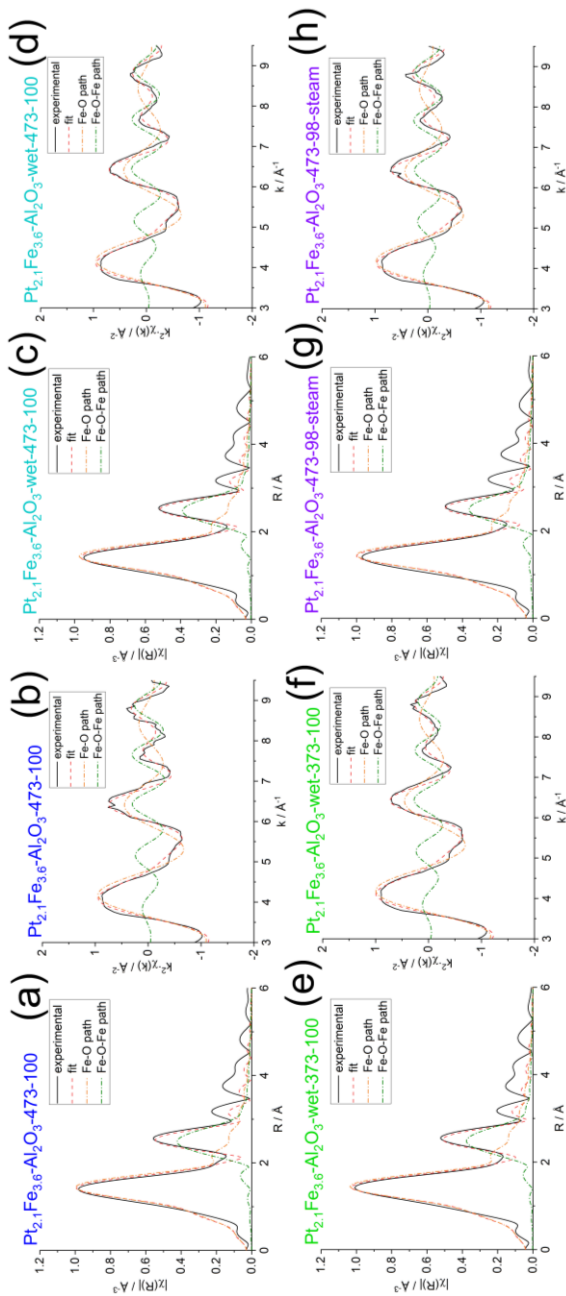


**Figure S3-11-1.** The fit of the Fourier-transformed  $k^2$ -weighted Fe K-edge EXAFS modulus (a,c,e,g), as well as the fit of the real part of the  $\chi(k)$  (b,d,f,h) for  $\text{Pt}_{2.1}\text{Fe}_{3.6}\text{Al}_2\text{O}_3$ -473-100 (a,b),  $\text{Pt}_{2.1}\text{Fe}_{3.6}\text{Al}_2\text{O}_3$ -wet-473-100 (c,d),  $\text{Pt}_{2.1}\text{Fe}_{3.6}\text{Al}_2\text{O}_3$ -wet-373-100 (e,f) and  $\text{Pt}_{2.1}\text{Fe}_{3.6}\text{Al}_2\text{O}_3$ -473-98-steam (g,h). Black solid line - experimental data, red dashed line - fit, dashed-dotted lines show individual path signals. All spectra were measured under 200 - 500 s under PROX mixture: 40 vol.%  $\text{H}_2$  + 5 vol.%  $\text{CO}$  + 2 vol.%  $\text{O}_2$  at 313 K.

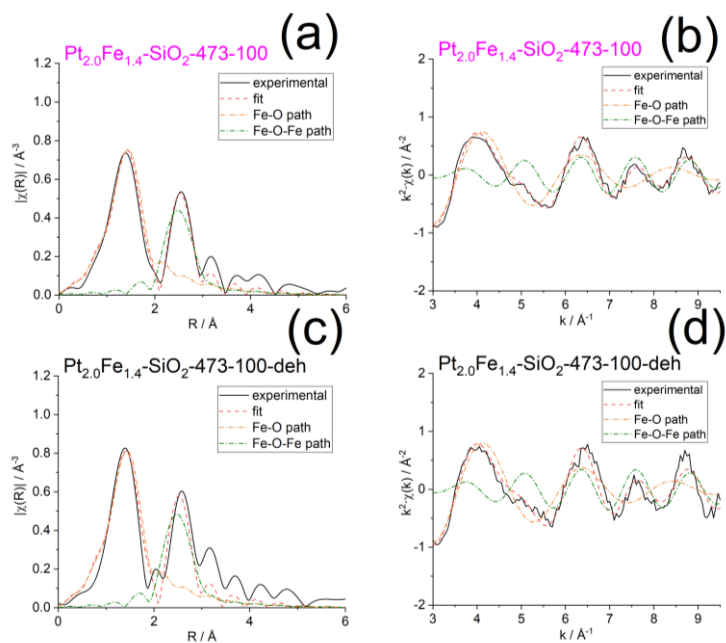


**Figure S3-11-2.** The fit of the Fourier-transformed  $k^2$ -weighted Fe K-edge EXAFS modulus (a,c), as well as the fit of the real part of the  $\chi(k)$  (b,d) for  $\text{Pt}_{2.0}\text{Fe}_{1.4}\text{-SiO}_2\text{-473-100}$  (a,b) and  $\text{Pt}_{2.0}\text{Fe}_{1.4}\text{-SiO}_2\text{-473-100-deh}$  (c,d). Black solid line - experimental data, red dashed line - fit, dashed-dotted lines show individual path signals. All spectra were measured under 200 - 500 s under PROX mixture: 40 vol.%  $\text{H}_2$  + 5 vol.%  $\text{CO}$  + 2 vol.%  $\text{O}_2$  at 313 K.



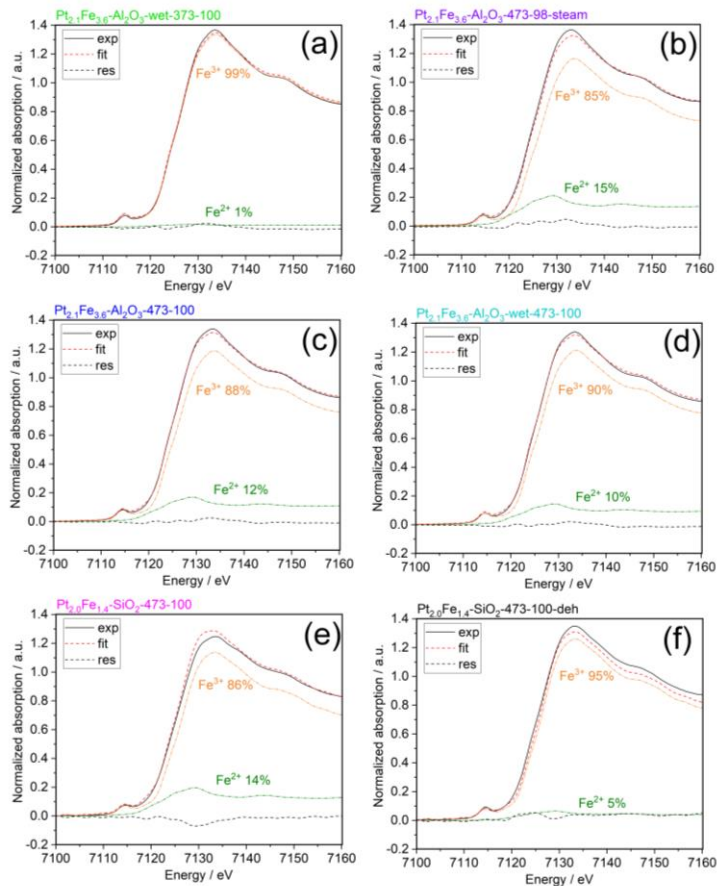


**Figure S3-12.** Linear combination fit of operando Fe K-edge XANES spectra of various catalysts averaged over 200-500 s under 2 vol.% O<sub>2</sub> + 40 vol.% H<sub>2</sub> + 5 vol.% CO at 313 K. Fe<sup>3+</sup> is the state of the catalysts after TPO, Fe<sup>2+</sup> is the FeO reference.

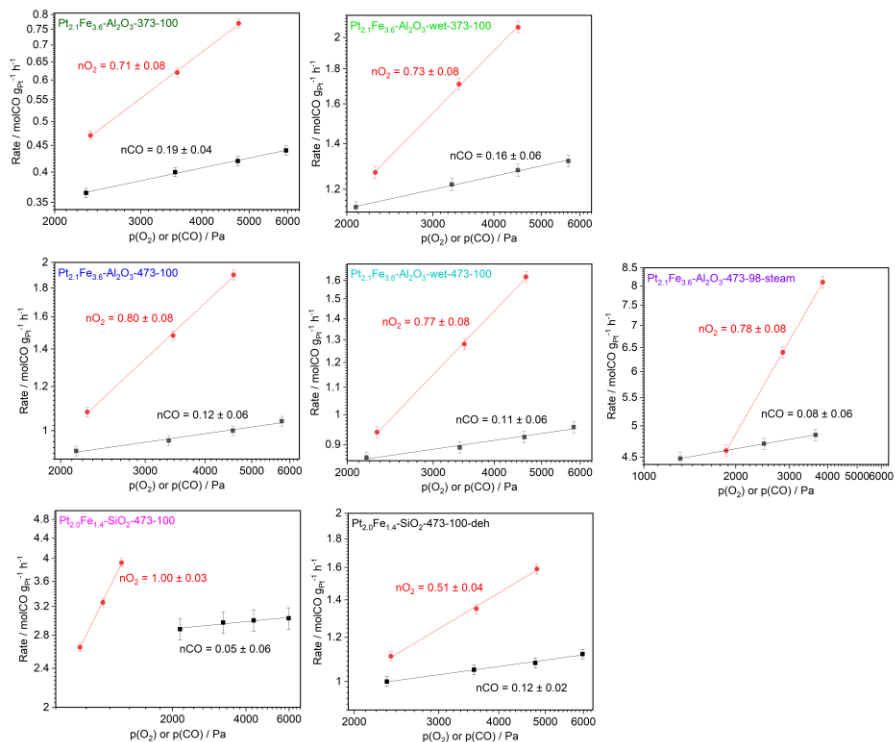


**Figure S3-13.** Double-logarithmic plots of the PROX activity versus the partial pressures of carbon monoxide and oxygen at 313 K. The corresponding reaction orders are given next to the lines.

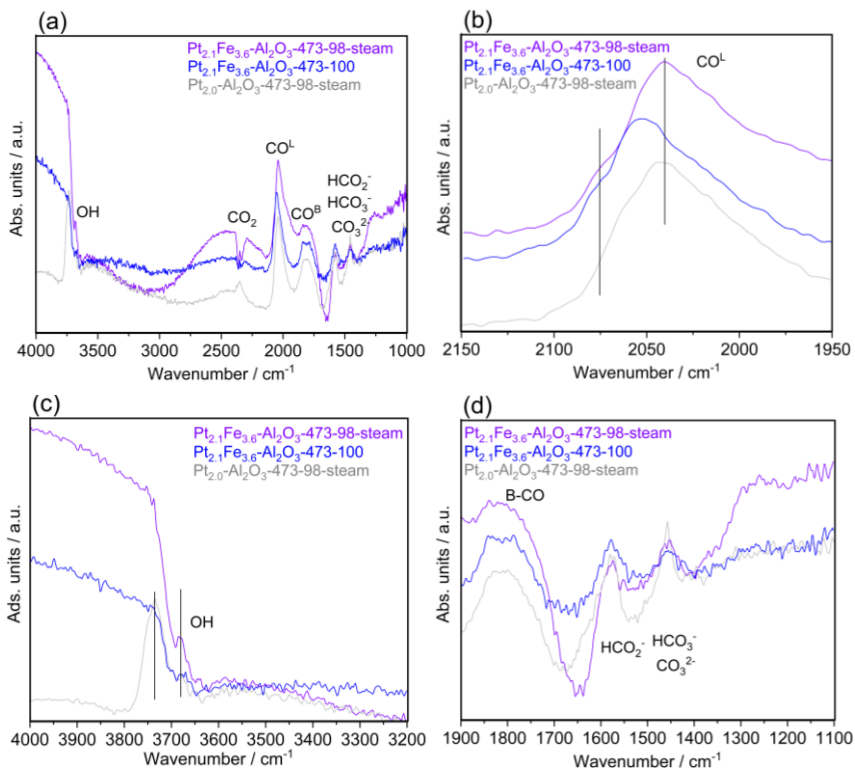


**Figure S3-14.** In situ DRIFTS spectra of PtFe-Al<sub>2</sub>O<sub>3</sub>-473-98-steam (purple), Pt<sub>2.1</sub>Fe<sub>3.6</sub>-Al<sub>2</sub>O<sub>3</sub>-473-100 (blue), and Pt<sub>2.0</sub>-Al<sub>2</sub>O<sub>3</sub>-473-98-steam (grey) measured during 200-500 s in 2 vol.% O<sub>2</sub> + 40 vol.% H<sub>2</sub> + 5 vol.% CO at 313 K. The entire spectrum (a) and various spectral regions (b-d) are shown.

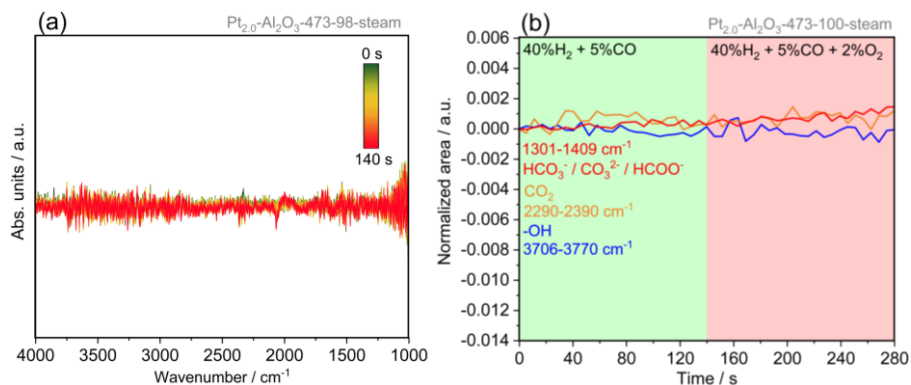


**Figure S3-15.** In situ DRIFTS spectra measured during the oxygen cut-off over  $\text{Pt}_{2.0}\text{-Al}_2\text{O}_3\text{-473-98-steam}$  at 313 K (a); corresponding changes in the normalized area of DRIFTS peaks during alternate oxygen cut-off during 0-140 s and oxygen addition during 140-280 s (b).

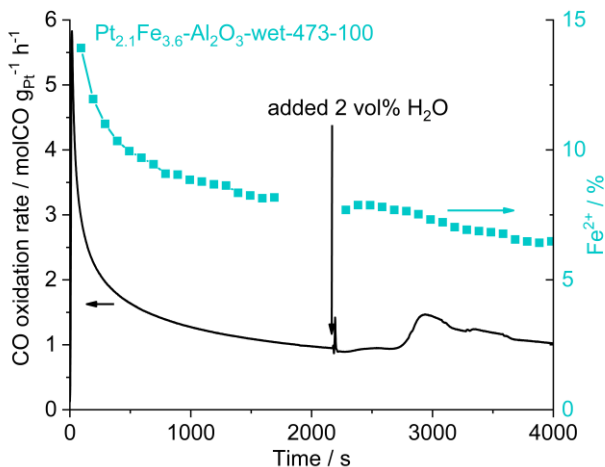


**Figure S3-16.** Operando  $\text{Fe}^{2+}$  concentrations during PROX over  $\text{Pt}_{2.1}\text{Fe}_{3.6}\text{-Al}_2\text{O}_3\text{-wet-473-100}$  (a). Correlation between the concentrations of  $\text{Fe}^{2+}$  and PROX activity (b), data points are averaged every 100 s. The black arrow indicates when water vapors pulse (2 vol.%  $\text{H}_2\text{O}$ ) was added into the reaction stream. Reaction performed at 313 K.

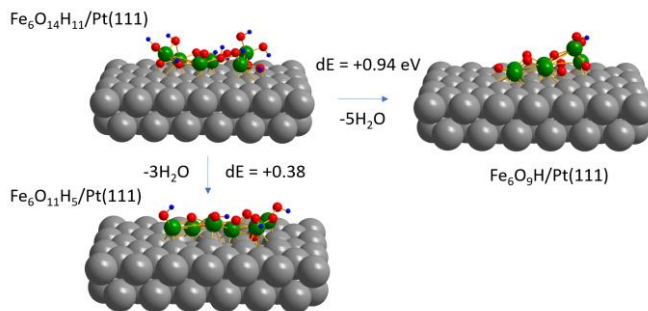


**Figure S3-17.** Optimized structure of theoretical clusters calculated using the density functional theory. Atom colors: Pt - gray, O - red, Fe - green, and H - blue. “dE” indicates an energy difference.

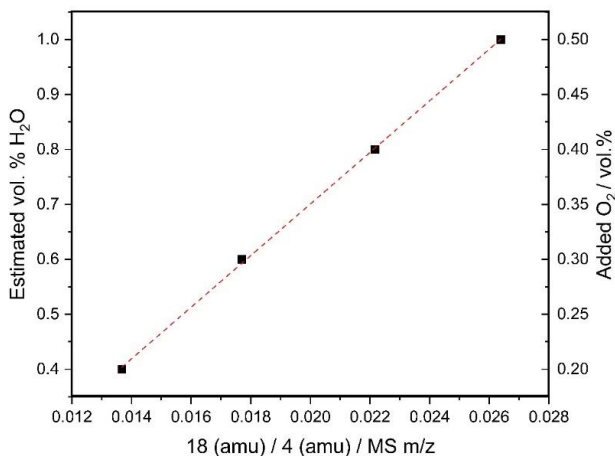


**Figure S3-18.** Calibration of the water content was performed with the water generator operating with the hydrogen excess (40-41 vol.%  $\text{H}_2$  + 0-0.5 vol.%  $\text{O}_2$  / He before the water generator). The mass spectrometer signal of water (18 amu) was normalized by the signal of helium (4 amu).

**Table S3-1.** Pretreatment protocols used to obtain catalysts under study.

Sample name	Support	Initial treatment before reduction	Reduction temperature, K	Gas composition during reduction, vol.%	Additional treatment after reduction
<b>Pt<sub>2.0</sub>-Al<sub>2</sub>O<sub>3</sub>-473-100</b>	$\gamma$ -Al <sub>2</sub> O <sub>3</sub>	none	473	100 vol.% H <sub>2</sub>	none
<b>Pt<sub>2.0</sub>-Al<sub>2</sub>O<sub>3</sub>-473-98-steam</b>	$\gamma$ -Al <sub>2</sub> O <sub>3</sub>	none	473	98 vol.% H <sub>2</sub> + 2 vol.% H <sub>2</sub> O	none
<b>Pt<sub>2.0</sub>-SiO<sub>2</sub>-473-100</b>	SiO <sub>2</sub>	none	473	100 vol.% H <sub>2</sub>	none
<b>Pt<sub>2.0</sub>-SiO<sub>2</sub>-473-98-steam</b>	SiO <sub>2</sub>	none	473	98 vol.% H <sub>2</sub> + 2 vol.% H <sub>2</sub> O	none
<b>Pt<sub>2.1</sub>Fe<sub>3.6</sub>-Al<sub>2</sub>O<sub>3</sub>-473-100</b>	$\gamma$ -Al <sub>2</sub> O <sub>3</sub>	none	473	100 vol.% H <sub>2</sub>	none
<b>Pt<sub>2.1</sub>Fe<sub>3.6</sub>-Al<sub>2</sub>O<sub>3</sub>-473-98-steam</b>	$\gamma$ -Al <sub>2</sub> O <sub>3</sub>	none	473	98 vol.% H <sub>2</sub> + 2 vol.% H <sub>2</sub> O	none
<b>Pt<sub>2.1</sub>Fe<sub>3.6</sub>-Al<sub>2</sub>O<sub>3</sub>-wet-473-100</b>	$\gamma$ -Al <sub>2</sub> O <sub>3</sub>	impregnated with H <sub>2</sub> O	473	100 vol.% H <sub>2</sub>	none
<b>Pt<sub>2.1</sub>Fe<sub>3.6</sub>-Al<sub>2</sub>O<sub>3</sub>-wet-373-100</b>	$\gamma$ -Al <sub>2</sub> O <sub>3</sub>	impregnated with H <sub>2</sub> O	373	100 vol.% H <sub>2</sub>	none
<b>Pt<sub>2.1</sub>Fe<sub>3.6</sub>-Al<sub>2</sub>O<sub>3</sub>-473-100-deh</b>	$\gamma$ -Al <sub>2</sub> O <sub>3</sub>	none	473	100 vol.% H <sub>2</sub>	dehydrated under 100% He or Ar at 673 K
<b>Pt<sub>2.0</sub>Fe<sub>1.4</sub>-SiO<sub>2</sub>-473-100</b>	SiO <sub>2</sub>	none	473	100 vol.% H <sub>2</sub>	none
<b>Pt<sub>2.0</sub>Fe<sub>1.4</sub>-SiO<sub>2</sub>-473-100-deh</b>	SiO <sub>2</sub>	none	473	100 vol.% H <sub>2</sub>	dehydrated under 100% He or Ar at 673 K

**Table S3-2.** Integrated amounts of water molecules present on pure supports after different treatments calculated from temperature programmed desorption of water. Original data are shown in Figure S3-1.

Support	Pretreatment	Desorption temperature range	Water molecules desorbed from 1 nm <sup>2</sup>
$\gamma$ -Al <sub>2</sub> O <sub>3</sub>	no	303 - 873 K	3.9
		473 - 873 K	1.2
	2% H <sub>2</sub> O / He (steam) at 473 K	303 - 873 K	9.5
		473 - 873 K	5.2
SiO <sub>2</sub>	no	303 - 873 K	3.0
		473 - 873 K	1.7
	dehydrated at 673 K under He	303 - 873 K	0.3
		473 - 873 K	0.3

**Table S3-3.** Comparison of the carbon monoxide oxidation rates after 20 min under PROX mixture for the Pt-Fe catalysts from Chapter 4 and Chapter 5 at 313 K. PROX mixture composition was 40 vol.% H<sub>2</sub> + 5 vol.% CO + 2 vol.% O<sub>2</sub> in He in all cases, volumetric flow was 180 ml min<sup>-1</sup>.

Catalyst	Estimated activity / molCO gPt <sup>-1</sup> h <sup>-1</sup>	Ref.
<b>Pt<sub>2.0</sub>Fe<sub>1.4</sub>-SiO<sub>2</sub>-473-100</b>	3.27	Chapter 4 / Chapter 5
<b>Pt<sub>2.1</sub>Fe<sub>1.1</sub>-Al<sub>2</sub>O<sub>3</sub>-673-100</b>	1.62	Chapter 4
<b>Pt<sub>2.1</sub>Fe<sub>3.6</sub>-Al<sub>2</sub>O<sub>3</sub>-473-98-steam</b>	6.93	Chapter 5
<b>Pt<sub>2.1</sub>Fe<sub>3.6</sub>-Al<sub>2</sub>O<sub>3</sub>-wet-473-100</b>	1.45	Chapter 5
<b>Pt<sub>2.1</sub>Fe<sub>3.6</sub>-Al<sub>2</sub>O<sub>3</sub>-wet-373-100</b>	2.03	Chapter 5
<b>Pt<sub>2.1</sub>Fe<sub>3.6</sub>-Al<sub>2</sub>O<sub>3</sub>-473-100</b>	1.60	Chapter 5

**Table S3-4.** Thermodynamic stabilities of various iron oxides and hydroxides towards reduction by hydrogen measured as the standard free Gibbs energy of reduction reaction.

Reaction / 298 K	$\Delta_r G^\circ / \text{kJ mol}_{\text{Fe}}^{-1}$
$1/2\text{Fe}_2\text{O}_3 + 1/6\text{H}_2 = 1/3\text{Fe}_3\text{O}_4 + 1/6\text{H}_2\text{O}(\text{g})$	-5.38
$\text{Fe}(\text{OH})_3 + 1/2\text{H}_2 = \text{FeO} + 2\text{H}_2\text{O}(\text{g})$	-4.91
$\gamma\text{-FeOOH} + 1/2\text{H}_2 = \text{FeO} + \text{H}_2\text{O}(\text{g})$	0.11
$1/2\text{Fe}_2\text{O}_3 + 1/2\text{H}_2 = \text{FeO} + 1/2\text{H}_2\text{O}(\text{g})$	5.51
$\alpha\text{-FeOOH} + 1/2\text{H}_2 = \text{FeO} + \text{H}_2\text{O}(\text{g})$	8.60



**Table S3-5.** Optimized parameters of the Fe K-edge EXAFS fit. N: coordination number, R: interatomic distance,  $\sigma^2$ : disorder parameter,  $\Delta E_0$ : energy shift, “\*” - fixed parameters. We performed EXAFS fitting using multiple k weightings of 1-3 within the k-range of 3.0-9.5  $\text{\AA}^{-1}$  and an R-range of 1.0-3.5  $\text{\AA}$ .

Sample	Bond	N / N <sub>0</sub>	R / $\text{\AA}$	$\Delta\sigma^2 / \text{\AA}^2$	E <sub>0</sub> / eV
Fe foil	Fe-Fe	8*	2.48 ± 0.02	0.0069 ± 0.0009	-4 ± 1.8
	Fe-Fe	6*	2.86 ± 0.02	0.0079 ± 0.0009	
<b>Pt<sub>2.1</sub>Fe<sub>3.6</sub>-Al<sub>2</sub>O<sub>3</sub>-473-100</b> 200 - 500 s under PROX	Fe-O Fe-(O)-Fe	4.7 ± 1.0 1.3 ± 0.8	1.95 ± 0.02 2.94 ± 0.02	0.010 ± 0.004 0.003 ± 0.006	-4 ± 2.3
<b>Pt<sub>2.1</sub>Fe<sub>3.6</sub>-Al<sub>2</sub>O<sub>3</sub>-wet-473-100</b> 200 - 500 s under PROX	Fe-O Fe-(O)-Fe	5.0 ± 0.8 1.3 ± 0.7	1.95 ± 0.01 2.94 ± 0.02	0.012 ± 0.003 0.004 ± 0.005	-3 ± 1.8
<b>Pt<sub>2.1</sub>Fe<sub>3.6</sub>-Al<sub>2</sub>O<sub>3</sub>-wet-373-100</b> 200 - 500 s under PROX	Fe-O Fe-(O)-Fe	5.1 ± 0.9 1.5 ± 0.8	1.95 ± 0.01 2.94 ± 0.02	0.011 ± 0.003 0.005 ± 0.005	-3 ± 1.8
<b>Pt<sub>2.1</sub>Fe<sub>3.6</sub>-Al<sub>2</sub>O<sub>3</sub>-473-98-steam</b> 200 - 500 s under PROX	Fe-O Fe-(O)-Fe	5.2 ± 1.1 0.9 ± 0.7	1.95 ± 0.02 2.94 ± 0.02	0.011 ± 0.004 0.002 ± 0.007	-5 ± 2.4
<b>Pt<sub>2.0</sub>Fe<sub>1.4</sub>-SiO<sub>2</sub>-473-100</b> 200 - 500 s under PROX	Fe-O Fe-(O)-Fe	4.0 ± 0.8 1.5 ± 0.6	1.96 ± 0.02 2.96 ± 0.02	0.011 ± 0.003 0.004 ± 0.003	-5 ± 1.8
<b>Pt<sub>2.0</sub>Fe<sub>1.4</sub>-SiO<sub>2</sub>-473-100-deh</b> 200 - 500 s under PROX	Fe-O Fe-(O)-Fe	4.2 ± 0.9 1.6 ± 0.7	1.95 ± 0.02 2.95 ± 0.02	0.011 ± 0.003 0.004 ± 0.003	-5 ± 1.8

## References

1. Chiarello, G. L.; Nachtegaal, M.; Marchionni, V.; Quaroni, L. and Ferri, D. Adding diffuse reflectance infrared Fourier transform spectroscopy capability to extended x-ray-absorption fine structure in a new cell to study solid catalysts in combination with a modulation approach. *Rev. Sci. Instrum.* **2014**, *85*, 074102.
2. Sadykov, I.I.; Zabilskiy, M.; Clark, A.H.; Krumeich, F.; Sushkevich, V.L.; van Bokhoven, J.A.; Nachtegaal, M. and Safonova, O.V. Time-resolved XAS provides direct evidence for oxygen activation on cationic iron in a bimetallic Pt-FeO<sub>x</sub>/Al<sub>2</sub>O<sub>3</sub> catalyst. *ACS Catal.*, **2021**, *11*, 11793-11805.
3. Sadykov, I.I.; Sushkevich, V.L.; Krumeich, F.; Nuguid, R.J.G.; van Bokhoven, J.A.; Nachtegaal, M. and Safonova, O.V. Platinum-Iron(II) oxide sites directly responsible for preferential carbon monoxide oxidation at ambient temperature: an operando X-ray absorption spectroscopy study. *Angew. Chem. Int. Ed.*, **2023**, *135*, e2022140.
4. Ravel, B. and Newville, M. ATHENA, ARTEMIS, HEPHAESTUS: data analysis for X-ray absorption spectroscopy using IFEFFIT. *J. Synchrotron Radiat.* **2005**, *12*, 537- 541.
5. Nuguid, R. J. G.; Ferri, D. and Kröcher, O. Design of a reactor cell for modulated excitation Raman and diffuse reflectance studies of selective catalytic reduction catalysts. *Emission Control Sci. Tech.* **2019**, *5*, 307-316.
6. Blum, V.; Gehrke, R.; Hanke, F.; Havu, P.; Havu, V.; Ren, X.; Reuter, K. and Scheffler, M. Ab initio molecular simulations with numeric atom-centered orbitals. *Comp. Phys. Comm.* **2009**, *180*, 2175-2196.
7. Ren, X.; Rinke, P.; Blum, V.; Wieferink, J.; Tkatchenko, A.; Sanfilippo, A.; Reuter, K. and Scheffler, M. Resolution-of-identity approach to Hartree-Fock, hybrid density functionals, RPA, MP2 and GW with numeric atom-centered orbital basis functions. *New J. Phys.* **2012**, *14*, 053020.
8. Perdew, J. P.; Burke, K. and Ernzerhof, M. Generalized Gradient Approximation made simple. *Phys. Rev. Lett.* **1997**, *77*, 3865-3868.

# CURRICULUM VITAE

Name: Iliia Sadykov

Date of Birth: January 7, 1994

## Education

2011-2017 / Lomonosov Moscow State University, Russian Federation

Bachelor of Science in Chemistry / Master of Science in Chemistry (*Summa cum Laude*)

2019-2023 / ETH Zürich, Switzerland

Doctor of Sciences, Institute for Chemical and Bioengineering

## Publications

1. Makarevich, A.M.; Sadykov, I.I.; Sharovarov, D.I.; Amelichev, V.A.; Adamenkov, A.A.; Tsymbarenko, D.M.; Plokhii, A.V.; Esaulkov, M.N.; Solyankin, P.M. and Kaul, A.R. Chemical synthesis of high quality epitaxial vanadium dioxide films with sharp electrical and optical switch properties. *J. Mater. Chem. C* **2015**, 3 (35), 9197-9205.
2. Makarevich, A. M; Sobol, A. G; Sadykov, I. I; Sharovarov, D. I; Amelichev, V. A; Tsymbarenko, D. M; Boytsova, O. V and Kaul, A. R. Delicate tuning of epitaxial VO<sub>2</sub> films for ultra-sharp electrical and intense IR optical switching properties. *J. Alloys and Compounds* **2021**, 853, 157214.
3. Liu, Q.; Meissel, H.; Sadykov, I. I.; Jones, S.; Van Dijk, N.; Rzepka, P.; Artiglia, L.; Ranocchiari, M. and van Bokhoven, J. A. On the Stability of Pt-Based Catalysts in HBr/Br<sub>2</sub> Solution. *Helvetica Chimica Acta* **2021**, 104 (7), e2100082.
4. Kopelent, R.; Tereshchenko, A.; Guda, A.; Smolentsev, G.; Artiglia, L.; Sushkevich, V.L.; Bugaev, A.; Sadykov, I. I.; Baidya, T.; Bodnarchuk, M. and van Bokhoven, J. A. Enhanced reducibility of the ceria–tin oxide solid solution modifies the CO oxidation mechanism at the platinum–oxide interface. *ACS Catal.* **2021**, 11 (15), 9435-9449.
5. Sadykov, I. I.; Zabilskiy, M.; Clark, A. H.; Krumeich, F.; Sushkevich, V.; van Bokhoven, J. A.; Nachttegaal, M. and Safonova, O. V. Time-resolved XAS provides direct evidence for oxygen activation on cationic iron in a bimetallic Pt-FeO<sub>x</sub>/Al<sub>2</sub>O<sub>3</sub> catalyst. *ACS Catal.* **2021**, 11, 11793-11805.

- 
6. Li, X.; Wang, X.; Sadykov, I. I.; Palagin, D.; Safonova, O.V.; Li, J.; Beck, A.; Krumeich, F.; van Bokhoven, J.A. and Artiglia, L. Temperature and reaction environment influence the nature of platinum species supported on ceria. *ACS Catal.* **2021**, *11* (21), 13041-13049.
7. Cannelli, O.; Wiktor, J.; Colonna, N.; Leroy, L.; Puppini, M.; Bacellar, C.; Sadykov, I. I.; Krieg, F.; Smolentsev, G.; Kovalenko, M.V. and Pasquarello, A. Atomic-level description of thermal fluctuations in inorganic lead halide perovskites. *J. Phys. Chem. Lett.* **2022**, *13* (15), 3382-3391.
8. Cannelli, O.; Wiktor, J.; Colonna, N.; Leroy, L.; Puppini, M.; Bacellar, C.; Sadykov, I. I.; Krieg, F.; Smolentsev, G.; Kovalenko, M.V. and Pasquarello, A. Decoupled Structural Responses upon Light and Thermal Functional Activation in CsPbBr<sub>3</sub> Perovskites. In International Conference on Ultrafast Phenomena **2022** (pp. F1A-3). Optica Publishing Group.
9. Lee, J.D.; Qi, Z.; Foucher, A.C.; Ngan, H.T.; Dennis, K.; Cui, J.; Sadykov, I.I.; Crumlin, E.J.; Sautet, P.; Stach, E.A. and Friend, C.M. Facilitating Hydrogen Dissociation over Dilute Nanoporous Ti-Cu Catalysts. *JACS* **2022**, *144* (37), 16778-16791.
10. Sadykov, I.I.; Sushkevich, V.L.; Krumeich, F.; Nuguid, R.J.G.; van Bokhoven, J.A.; Nachttegaal, M. and Safonova, O.V. Platinum-Iron(II) oxide sites directly responsible for preferential carbon monoxide oxidation at ambient temperature: an operando X-ray absorption spectroscopy study. *Angew. Chem. Int. Ed.*, **2023**, *135*, e2022140.
11. Foucher, A.C.; Yang, S.; Rosen, D.J.; Huang, R.; Pyo, J.B.; Kwon, O.; Owen, C.J.; Sanchez, D.F.; Sadykov, I. I.; Grolimund, D. and Kozinsky, B. Synthesis and Characterization of Stable Cu-Pt Nanoparticles under Reductive and Oxidative Conditions, *ChemRxiv* **2023**.